VARIATION OF THE PLASMASPHERIC FIELD-ALIGNED ELECTRON DENSITY AND ION COMPOSITION AS A FUNCTION OF GEOMAGNETIC STORM ACTIVITY

By

Amani Reddy

RECOMMENDED:

Dr. Seta Bogosyan

Dr. Joseph G. Hawkins

Dr. Brenton Watkins

Dr. Vikas S. Sonwalkar
Advisory Committee Chair

Dr. Charles E. Mayer
Chair, Department of Electrical and Computer Engineering

APPROVED:

Dr. Douglas Goering
Dean, College of Engineering and Mines

Dr. John C. Eichelberger
Dean of the Graduate School

11 August 2015
Date

VARIATION OF THE PLASMASPHERIC FIELD-ALIGNED ELECTRON DENSITY AND ION COMPOSITION AS A FUNCTION OF GEOMAGNETIC STORM ACTIVITY

A

THESIS

Presented to the Faculty
of the University of Alaska Fairbanks

in Partial Fulfillment of the Requirements
for the Degree of

DOCTOR OF PHILOSOPHY

By

Amani Reddy, B.Tech., M.S.

Fairbanks, Alaska

August 2015

Abstract

Whistler mode (WM) radio sounding is a powerful new method that provides measurement of both field-aligned electron and ion densities from the satellite altitude (<5,000 km) down to 90 km. Using radio sounding data from the Radio Plasma Imager (RPI) onboard the IMAGE (Imager for Magnetosphere-to-Aurora Global Exploration) satellite, this thesis presents a systematic and efficient approach to implement the whistler mode radio sounding method and discusses the uncertainties in the measured plasma parameters. The sounding method is applied to obtain the first measurements of plasmaspheric field-aligned electron density and ion composition as a function of geomagnetic storm activity during the mid-August to September 2005 period. This period included several geomagnetic storms of varying strength that occurred in succession. The plasmapause was located at L$\sim$2.4 during the onset and main phases of the storms. The whistler mode sounding results were augmented by measurements from the CHAMP and DMSP satellites, and ground ionosonde stations during the same period. On the day-side, at L$\sim$2, as a function of storm activity the following general results were found: (1) The electron density, relative ion concentrations, and O^+/H^+ transition height underwent temporal changes as a function of geomagnetic storm activity, and each species had different temporal behavior thus indicating different recovery times. (2) O^+/H^+ transition height increased by $\sim$200-300 km during the onset, main and early recovery phases of the storms. (3) Variation in the electron density below the O^+/H^+ transition height was different than that above. (4) Electron density at F2 peak increased during the onset or main phase of storms followed by a decrease in the recovery phase. (5) Electron density above O^+/H^+ transition height increased either in the onset or on the first day of recovery phase followed by a decrease. (6) α_{H^+} decreased during the onset, main and/or early recovery phases of storms; α_{O^+} increased in the early recovery phases of the storms; α_{He^+} varied in a complex manner but in general there was an increase in α_{He^+} during the onset phases and decrease in α_{He^+} during the recovery phases of the storms. (7) When storms occurred in succession in an interval of roughly less than a day, the latter storms had little or no effect on the electron density and/or ion composition. On the night-side, WM sounding data was sparse. In the case of one moderate storm, we found that 3 days after the storm, at L$\sim$2.3, electron density at F2 peak and relative ion concentrations (at all altitudes) were comparable to those before the storm, whereas electron density above O^+/H^+ transition height decreased. WM sounding results for the day-side and night-side were in

agreement with measurements from CHAMP (∼350 km) and DMSP (∼850 km). Whistler mode sounding results coupled with physics-based models will allow: (a) investigation of the role of thermospheric winds, dynamo electric fields, and storm time electric fields in causing the variations in electron and ion densities and (b) testing of current theories and validating physics-based models of the thermosphere-ionosphere-magnetosphere.

Table of Contents

List of Figures

Page

Page

Page

Page

List of Tables

Page

Acknowledgements

First and foremost I would like to thank my advisor, Prof. Vikas S. Sonwalkar. I appreciate his constructive criticism and all his contributions of time, ideas, and funding to make my Ph.D. experience productive and stimulating. He taught me how to think about complex things in simpler ways and how to improve the quality of research by questioning and critical thinking. He has helped me come up with this thesis topic. During the most difficult times when writing this thesis, he gave me the moral support and the freedom I needed. It was a privilege and real education for me to work under his guidance.

I have performed the research presented in this thesis under the guidance and in collaboration with my advisor, Professor Vikas S. Sonwalkar. Throughout this thesis "we" refers to this collaboration. Professor Donald L. Carpenter of Stanford University contributed to the initial research on the whistler mode radio sounding technique presented in Chapter 2. That part of the research is published in the Journal of Geophysical Research. Throughout the thesis-writing I have received critical comments and advice from my advisor, but I am the senior author and I take the full responsibility for the writing.

I thank my graduate advisory committee members Dr. Seta Bogosyan, Dr. Joseph G. Hawkins and Dr. Brenton Watkins for taking time to read my thesis and sharing their views. I would also like to thank Dr. Richard Wies for serving as a proxy for Prof. Bogosyan at my thesis defense and insightful questions and Dr. Chung-Sang Ng for serving as an external examiner for my thesis defense.

I am grateful to Dr. Donald L. Carpenter for many useful discussions related to whistler mode sounding and for his interest in my thesis research. When he visited University of Alaska Fairbanks the time he spent in our lab, sharing his knowledge on the measurements of electron density and history of VLF group is greatly appreciated. I thank Dr. Robert F. Benson for discussing my thesis research when we met at AGU conferences. I would also like to thank Dr. George. V. Khazanov for his interest on my thesis research and discussions on the importance of field-aligned measurements of plasma parameters.

I want to acknowledge Dr. Dennis L. Gallagher for helping me with compiling GCPM code and running test programs, and Dr. Hairston for supplying me with perl script files that saved me time and made it easier for me to download DMSP spacecraft data. I also want to acknowledge Dr.

Joseph D. Huba and Dr. Jonathan Krall for aiding me in understanding SAMI2 parameters and for their suggestions on modifying SAMI2 so it can be applied to simulate whistler mode sounding results.

During the final stages of my PhD I was blessed with a handsome son, Virat. My parents, husband, parents-in law, and brother stepped in to help and made it possible for me to devote time towards my thesis. This thesis could not have been accomplished without their constant support, encouragement, and understanding. I wish to give my heart felt thanks to my husband for his patience and sticking with me through all the good and bad times. I owe a lot of fun time to my son. He gave me happiness, taught me to be patient, and organize myself.

I would like to thank the UAF graduate school for funding me through graduate fellowship (3 semesters) and thesis completion fellowship (2 semesters). I would also like to thank the ECE department for offering me a teaching assistantship for the Fall 2009 and Spring 2010 semesters.

The research presented in this thesis is based upon work supported by the National Science Foundation under Grant No. AGS-1212593 and National Aeronautics and Space Administration under Grant No's. NNX08AN51A and NNX14AE02G. Any opinions, findings, and conclusions or recommendations expressed in this material are those of the author(s) and do not necessarily reflect the views of the National Science Foundation or National Aeronautics and Space Administration.

Chapter 1
Introduction

1.1 Objectives

The objectives of this dissertation are: (1) to devise a systematic and efficient iterative procedure to implement the whistler mode radio method of determining field-aligned electron density (N_e), ion effective mass (m_{eff}), and ion densities (H^+, He^+, O^+) using magnetospherically reflected (MR) and specularly reflected (SR) whistler mode (WM) echoes observed on the IMAGE satellite; (2) to estimate uncertainties in the measurement of electron and ion densities and ion effective mass obtained using the whistler mode radio sounding method; (3) to determine plasmaspheric field aligned electron densities and relative ion concentrations as a function of geomagnetic storm activity using whistler mode radio sounding data and other complementary data sets; and (4) to compare WM sounding results of field aligned electron and ion densities with measurements from other satellites and ground-based ionosondes and predictions from empirical models.

1.2 Background and past work

This thesis deals with the measurement and interpretation of the plasmaspheric density and compositional changes along field lines that occur during the onset, main, and recovery phases of geomagnetic storms. These density and compositional changes as a function of storm activity can be used for space weather predictions. Space weather refers to conditions on the Sun and in the solar wind, magnetosphere, ionosphere, and thermosphere that can influence the performance and reliability of space-borne and ground-based technological systems and can endanger human life or health [Moldwin, 2008]. Adverse conditions in the space environment can cause disruption of satellite operations, communications, navigation, and electric power distribution grids, leading to a variety of socioeconomic losses. Intense changes in solar activity leading to coronal mass ejections (CME), large solar flares, and high–speed solar wind streams can severely influence the behavior of magnetospheric plasma and cause great variation in the motion and quantity of the energetic particles within the magnetosphere. This disturbs the Earth's magnetosphere, dramatically leading to geomagnetic storms and substorms. The inner magnetospheric plasma parameters including plasma density and composition are profoundly affected by the geomagnetic activity.

These density and compositional changes have implications on magnetospheric processes such as ring current and can influence magnetosphere dynamics by modifying wave particle interactions [e.g., Daglis, 1997; Daglis et al., 1999b; Nose et al., 2011].

In the following a brief review of past work upon which this dissertation is built is provided.

1.2.1 The Earth's magnetosphere

The Earth's upper atmosphere comprises the Earth's ionosphere and magnetosphere and consists of cold and hot plasma, plasma waves, and geomagnetic field.

Immediately surrounding the Earth is the non-conducting atmosphere, roughly 60-80 km thick and transparent to the propagation of radio waves. The next layer above the neutral atmosphere is called the ionosphere, which extends up to $\sim$1000 km, completely encircles the Earth, and then merges into the magnetosphere. The boundary between the ionosphere and the neutral atmosphere below it is called the Earth-ionosphere boundary. The region between this boundary and the Earth is called the Earth-ionosphere waveguide. The topside ionosphere starts at the F2 layer peak at approximately 300 km and extends upward. Below the F2 peak, the electron density increases with altitude and above it decreases. The topside ionosphere extends up to transition height where heavier ions (O^+) become less numerous than lighter ions (H^+ and He^+) [Schunk and Nagy, 2000; Kelley, 2009].

The magnetosphere extends upward from the ionosphere. The magnetosphere is defined as that region of space where the behavior of the plasma is controlled primarily by the geomagnetic field. In the absence of the interplanetary plasma, the Earth's dipole field would extend symmetrically in all directions. But in reality the solar wind exerts pressure on the dipole field, compressing it on the sun side (thus creating the boundary known as the magnetopause) at $\sim$10 R_E (1 $R_E \simeq 6370$ km) and extending it into a long tail on the night side that blends gradually into the background interplanetary field at $>$60 R_E.

The inner magnetosphere, called the plasmasphere, is a high-density (100–1000 el/cc) cold plasma region consisting mainly of electrons and H^+ ions, and a smaller population of He^+ and O^+ ions. The plasma in this region co-rotates with the Earth and can also flow along the field lines from one hemisphere to the other. It is believed that cold plasma of ionospheric origin flows along the field lines to fill the plasmasphere. The plasmasphere extends from above the ionosphere

to anywhere between 2-8 R_E in the equatorial plane, depending on the geomagnetic activity. The boundary of the plasmasphere is called the plasmapause. The cold plasma density measured at the geomagnetic equator gradually decreases with increasing distance from the Earth up to the plasmapause at which the electron density drops by as much as one or two orders of magnitude. The location of the plasmapause is often near L = 4-5 during quiet geomagnetic conditions. The distribution of plasma within the plasmasphere can be roughly described by a diffusive equilibrium model [Angerami and Thomas 1964]. More recently, Ozhogin et al. [2014] evaluated diffusive equilibrium models and found the representation of the real plasmasphere using diffusive equilibrium model questionable. Outside the plasmasphere the plasma density continues to decrease, generally following a R^{-N} drop off in density, where N$\sim$3–5. In addition to cold plasma, the inner magnetosphere also contains two zones of energetic particles, the Van Allen radiation belts.

Whistler mode echoes that are analyzed in this thesis were observed inside the plasmasphere and below 4000 km altitude.

1.2.2 Measurement of electron and ion densities in the magnetosphere

Measurement of plasma density and composition along the field line ($\mathbf{B_0}$) is critical to understanding the dynamic processes that determine the distribution of plasma along a flux tube and testing predictions from various physics-based models. In the past it was nearly impossible to obtain direct measurements of field-aligned plasma distribution. Our knowledge on the ionospheric and the overlaying plasmaspheric/magnetospheric electron density (N_e) has been obtained mainly from topside or bottomside sounding using radio waves in the high frequency (HF) range [e.g., Hunsucker and Hargreaves, 2003; and references therein] or incoherent scatter radars [e.g., Foster et al., 2004] or in situ satellite measurements using plasma density probes [Kletzing et al., 1998] or plasma resonances [e.g., Benson et al., 2003] or plasma wave cutoffs [e.g., Persoon et al., 1983; Benson et al., 2004] or natural whistlers [Storey, 1953; Helliwell, 1965; Smith, 1960; Edgar, 1976; Clilverd et al., 1991]. While the spacecraft measurements are either limited to high altitudes (>5000 km) or along the satellite track, the bottomside sounding measurements are limited altitudes less than roughly 300 km. In order to obtain information on plasma distribution as a function of altitude covering both the bottomside and topside ionosphere, it was necessary to piece together data obtained on multiple satellites and from the ground [e.g., Persoon et al., 1983; Horwitz et

al., 1990; Carpenter and Anderson, 1992; Gallagher et al., 2000; Goldstein et al., 2001; Denton et al., 2001]. Most such information is statistical in nature, because the conjunctions between two satellites or between satellite and a specific ground station are infrequent.

The effective ion mass and ion densities of the plasmasphere are not as well known [Lemaire and Gringauz, 1998; Bilitza and Reinisch, 2008]. Our knowledge of plasmaspheric effective ion mass and ion densities has mainly come from in situ measurements from satellites [e.g., Taylor et al., 1965; Brinton et al., 1969; Horwitz et al., 1984; Farrugia et al., 1989; Baugher et al., 1980; Craven et al., 1997] or field-line resonance frequencies measured using ground magnetometers [e.g., Schulz, 1996; Denton and Gallagher, 2000; Berube et al., 2003], lower hybrid waves [e.g., Brice and Smith 1965; Barrington et al., 1965; Kougblenou et al., 2011], ion whistlers [e.g., Barrington et al., 1966; Gurnett and Shawhan, 1966; Shawhan and Gurnett, 1966], and theoretical modeling involving relation of ion composition to electron density and temperature [e.g., Webb et al., 2006]. In situ ion density measurements using particle detectors have large uncertainties because of problems such as spacecraft potential that afflict the particle detectors [Lemaire and Gringauz, 1998]. Other measurements using field-line resonances and lower hybrid waves provide effective ion mass either at the equator or locally. Theoretical modeling of ion densities [e.g., Webb et al., 2006] need to be substantiated with observations.

1.2.3 Effect of geomagnetic storms on the ionosphere

The ionosphere is the main source of plasma in the magnetosphere. The ionosphere is known to be highly variable. The ionospheric density and its variability have been mainly studied with bottom and topside sounding of the ionosphere using radio waves in the HF range [e.g., Kelley, 2009; and references therein; Benson, 2010; and references therein] or from in situ satellite measurements using plasma density probes [e.g., De La Beaujardiere et al., 2004, and new technology of the GPS ground and satellite receivers for TEC measurements [Klobuchar, 1997; Mendillo, 2006 and references therein; Siefring et al., 2009]. The sources of ionospheric variability include solar EUV radiation, thermospheric winds, E$\times$B drifts, and thermospheric composition [e.g., Kelley, 2009; Hargreaves 1992; Danilov 2001]. Solar EUV radiation is responsible for the diurnal and solar cycle variations of the ionosphere. Thermospheric winds can move the ionospheric ions and electrons in the direction of the geomagnetic field. Electrodynamic (E$\times$B) plasma drifts control the distribution

and composition of the ionospheric plasma and strongly affect the generation of plasma waves and density structures with a large range of scale sizes. Thermospheric composition affects the rate at which ions and electrons recombine. It influences the electron concentration in the F2 region. Electron density at the F2 layer peak at mid-latitudes can vary by a factor of 10 from day to day and by a factor of 5 with solar cycle.

Geomagnetic storms can dramatically alter F2 region density in the ionosphere [e.g., Liu et al., 2010; Mansilla, 2007; Danilov, 2001; and references therein]. The maximum electron density at the F2 peak, NmF2, may increase or decrease during these geomagnetic disturbances. The increase in F2 peak is termed as positive ionospheric storm and the decrease in F2 peak is termed as negative ionospheric storm [Mansilla, 2007]. The reaction of the ionosphere as seen at different ionospheric stations may be quite different during the same storm depending on the station coordinates, local time, and other parameters. While negative ionospheric storms are almost always observed at high latitudes, positive ionospheric storms tend to occur at middle and low latitudes. As for the seasonal preference, negative ionospheric storms dominate in all seasons except winter, when positive ionospheric storms are more probable [e.g., Liu et al., 2010]. The recovery period of the ionosphere is shorter compared to that of the plasmasphere and does not show any latitudinal dependence [e.g., Park 1974; Liu et al., 2010; Reinisch et al., 2004].

Although the sources of ionospheric variability are well known [Hargreaves, 1992; Schunk and Nagy, 2000; Kelly, 2009], the role of various sources, e.g., thermospheric winds, dynamo electric fields, electric fields during storms, compositional changes, in modifying the ionosphere during geomagnetic disturbances, and how ionospheric density varies with disturbance magnitude, remains as an important unsolved problem in upper atmosphere [Kintner et al., 2008, and references therein]. The problem is: (1) global distribution of thermospheric winds over the disturbance time scale is not known, (2) the relative importance of the wind and electric field of solar-magnetospheric origin in determining the ionospheric disturbance is not known, (3) thermospheric ion composition is not well known.

1.2.4 Erosion and refilling of the plasmasphere

One of the fundamental and difficult problems of plasmaspheric dynamics is the study of plasmasphere refilling. The plasmasphere is known to be highly dynamic. It quickly shrinks during

periods of enhanced geomagnetic activity and slowly grows or refills during recovery times. In the aftermath of strong magnetic activity, the plasmapause may be located at L=2, and the plasmaspheric plasma may extend globally beyond L=6 after several days of low magnetic activity [Carpenter and Anderson, 1992]. The outer regions of the plasmasphere can be stripped away during geomagnetic storms to form plumes which convect through the dayside magnetosphere toward the magnetopause, where the plasma is believed to be lost. Inside the plasmasphere there can be significant loss of plasma through flow along the flux tubes to the underlying ionosphere. With decreasing geomagnetic activity, depleted flux tubes are subsequently replenished from the underlying ionosphere (i.e., they refill).

1.2.4.1 Electron density flux during quiet and disturbed time

Plasmasphere refilling has been studied since the 1970s. In the following, we focus on the handful of studies that are closely related to the work presented in this thesis (low to mid latitudes). We first discuss electron and ion flux from the ionosphere under quiet time geomagnetic conditions then the refilling rate under disturbed geomagnetic conditions.

Earlier, Park [1970] and Tarcsai [1985] used whistler observations to determine the electron flux to and from the ionosphere over L=3.5-5.0 and L=2.0-2.8, respectively. Park found that under quiet geomagnetic conditions this was $\sim 3\times10^8$ el cm^{-2} s^{-1} (referenced to 1000 km altitude) upward on the day-side and $\sim 1.5\times10^8$ el cm^{-2} s^{-1} downward on the night-side. Tarcsai reported that fluxes were usually $<6\times10^8$ el cm^{-2} s^{-1} and mostly downward from 1700–0400 LT. Saxton and Smith, [1989] also used whistler observations and estimated that the daytime upward flux at L=2.5 was 1-3$\times10^8$ el cm^{-2} s^{-1}.

Evans and Holt [1978] used incoherent scatter measurements to investigate electron density and H^+ and O^+ fluxes at L=3.2. They concluded that the upward daytime H^+ flux is $\sim 5\times10^7$ el cm^{-2} s^{-1} near sunspot maximum and 10^8 el cm^{-2} s^{-1} near sunspot minimum. The flux remains upward at night in summer near sunspot maximum but is downward before sunrise at sunspot minimum. Ground based measurements (via cross-phase analysis) of ultra low frequency (ULF) field line resonances (FLRs) have also been used to estimate the upward plasma flux at L=2 (but mapping to the outer plasmasphere) during the recovery phase of a large storm [Chi et al., 2000]. This was found to be $\sim 6\times10^8$ amu cm^{-2} s^{-1}.

Using measurements of the electron density found from passive radio wave observations by the IMAGE spacecraft Radio Plasma Imager (RPI) instrument on consecutive passes through the magnetosphere Denton et al. [2012] calculated the long-term (>1day) refilling rate of equatorial electron density from L = 2 to 9 during geomagnetically quiet time. They found that the refilling rate is greater at solar maximum for small L<4, about the same at solar maximum and solar minimum for L=4.2 to 5.8, and larger at solar minimum for large L>5.8, such as at geostationary orbit (L$\sim$6.8) (at least to L of about 8).

Whistler observations were also used to determine the electron flux during disturbed periods. Park [1970] found the refilling rate over L = 3.5-5.0 to be 3.5-5.8$\times 10^7$ el cm^{-2} s^{-1}. Park [1974] also used whistler observation and reported that recovery time strongly depends on plasmaspheric tube volume. It varies from $\sim$1 day at L=2.5 to $\sim$8 days at L=4. Chappell [1974] states that the refilling rate for N_e can reach 50 cm^{-3}/day based on measurements by the OGO 5 spacecraft at L=4. Carpenter et al. [1993] used measurement of ion density from the DE-1 spacecraft and found an N_e refilling rate of 80 cm^{-3}/day at L=4.5 for an event observed during the summer of 1982.

Chi et al. [2000] investigated plasma depletion and refilling at L=2 using ground magnetometer data for an event in September 1998. They found that even at such low latitudes the plasma density dropped significantly to $\sim$1/4 of the pre-storm value. They estimated the refilling rate to be $\sim$ 647 amu/cm^3/day.

Dent et al. [2006] used ground-based magnetometer cross-phase and the IMAGE satellite in situ RPI data for monitoring of plasma depletion and refilling for two cold plasma depletion episodes during May 2001. Their results suggested a dependence on both L and the time taken for depletion to complete. They also found an enhanced heavy ion population in the inner plasmatrough during an active refilling interval.

Sandel and Denton [2007] used data from the IMAGE Extreme Ultraviolet Imager (EUV) instrument to calculate local time averaged refilling rates of He^+ for moderate geomagnetic conditions in June 2001. With certain assumptions, they found a refilling rate for He^+ of roughly 1 cm^{-3}/hr at L=3.3, and 7×10^{-2} cm^{-3}/hr at L=6.3.

Obana et al. [2010] used crossphase analysis of magnetometer array data to determine the equatorial mass density during three moderate geomagnetic storms in March 2004 and June and April of 2001. They concluded that it took two to three days for L=2.3 flux tubes, three days at

L=2.6, and over four days for L> 3.3. They also found that plasmaspheric refilling progressed with a clear diurnal variation associated with linearly increasing plasma density in the daytime and decreasing plasma density at nighttime. The daytime increases in plasma mass density related to refilling rates ranging from ~250 to ~13 amu cm^{-3} h^{-1} over L=2.3-3.8. The resultant upward plasma flux at the 1000 km level was in the range of 0.9-5.2×108 amu cm^{-2} s^{-1}. The daily averaged refilling rate, including the nighttime downward flux, was found to be ~420 amu cm^{-3} d^{-1} at L=2.9-3.1. Using EUV/IMAGE and VLF whistler data, they estimated the plasma composition and found that the O^+ proportion was on the order of 3%–7% at L=2.3 and 6%–13% at L=3.0.

Reinisch et al. [2004] used sounding measurements from the RPI experiment on the IMAGE spacecraft and a plasma density inversion algorithm to derive the field-aligned electron density profile for a range of L shells during a large geomagnetic storm (Dst<-350 nT). The authors found that during the main phase of the storm more than two thirds of the quiet time plasma content was depleted at the L=2.8 flux tubes near local noon in <5 h , while at L=2.3 there was almost no depletion. They also found that L=2.5-3.3 flux tubes were refilled to near full values within 28 hrs. The refilling rate was at least 470 cm^{-3}/day at L=3 for one event in April 2000.

Although in most cases depletion of the plasmasphere was reported due to geomagnetic storms, Chi et al. [2005], used ground magnetometer data and TEC observations and reported enhancement in electron density at mid latitudes in the plasmasphere after the 2003 Halloween storm.

1.2.4.2 Variation of ion densities during geomagnetic storms

Geomagnetic storms are also known to cause dramatic changes in the plasmaspheric ion composition. These compositional changes have implications on magnetospheric processes such as ring current, and they can influence magnetosphere dynamics by modifying wave-particle interactions.

In the past couple of decades, growing experimental evidence, including ground based radar observations, field line resonances, and satellite observations has suggested an increase in mass density/thermal heavy ion population at low-mid latitudes [e.g., Yeh and Foster, 1990; Berube et al., 2005; Horwitz et al., 1984; Grew et al., 2007].

Yeh and Foster [1990] used the Millstone Hill incoherent scatter radar to monitor upward O^+ outflow during a February 1986 storm and found an increase in O^+ flux at mid latitudes. They

stated that these ions constituted a significant source of 1 eV O^+ ions to the overlying magnetosphere during such intervals.

Horwitz et al. [1984] used DE-1 thermal ion composition measurements and reported that in the aftermath of a storm, O^+ density could become comparable to H^+ density in the plasmasphere (November 1981 storm).

Berube et al. [2005] determined plasmaspheric mass density between L=1.7 and L=3.2 from pairs of stations in the MEASURE array of ground magnetometers during quiet and disturbed periods. They used the RPI electron density database in conjunction with mass density measurements and found that average ion mass is greatest under the most disturbed conditions. Their results indicated that heavy ion concentrations (percent by number) are enhanced during large geomagnetic disturbances. They also found that the average ion mass increases with increasing L (below L=3.2), indicating the presence of a heavy ion torus during disturbed times.

Dent et al. [2006] reported that on L shells between 2.39 and 6.54 in May 2001 comparisons between time dependent ground-based magnetometer cross-phase and IMAGE RPI determined plasma mass density profile evolution implied the presence of an enhanced heavy ion population in the inner plasma trough during an active refilling interval.

Takahashi et al. [2006] used field-line resonances recorded by ground magnetometers at L=1.32-1.41 during the Halloween storm and found an increase in the mass density along the field lines during the magnetic storm relative to the pre-storm value. He also reported that the mass density returned to its pre-storm value within 6 hours. He noted that the ionospheric plasma number density, obtained from TEC, during this storm was similar to that during quiet times.

Grew et al. [2007] studied the equatorial plasma density and composition at L = 2.5 during an extended disturbed interval, Sep–Oct 2002, using field line resonance measurements, naturally and artificially stimulated VLF whistlers, and IMAGE EUV observations. He found that during the storm the plasmapause moved to L<2.5. In the plasmasphere and plasmatrough the H^+: He^+: O^+ composition by number was 82:15:3. Just outside the plasmapause he found that the O^+ concentration exceeded 50%, which suggested the presence of an oxygen torus.

1.2.5 Effect of geomagnetic storms on ring current and its composition

In addition to changes in thermal ion compositions in the ionosphere/magnetosphere, geomagnetic storms are also known to increase energetic ion population in ring current. For example, comparing the storm time ring current composition with the quiet time composition and protons (90% in number density), Balsiger et al. [1980] pointed out that the storm time magnetosphere has abundant O^+ ions (75% in number density) in the region 6<L<8 and in the energy range of less than 16 keV. Young et al. [1982] pointed out that it must be O^+ ions (E<50 keV) that influence the decay process because of their long lifetime. Hamilton et al. [1988] found greatly increased concentrations of O^+ in the ring current during disturbed periods. Grande et al. [1996] presented survey plots of magnetospheric ion composition spectrometry (MICS) data for the whole CRRES mission and showed that ionospheric material concentrated at low altitude during the storm's main phase and moved to higher L shells during the recovery phase. Daglis [1997] examined five events by using the MICS data on CRRES, and his results showed that the energy densities of O^+ ions in the outer range of the ring current ($5< L <7$) were extraordinarily high. Daglis et al. [1999a, 1999b] showed that ionospheric origin ions contribute to large part of ring current during major storms. Fu et al. [2001] using CRRES data for four selected storms found energetic particle enhancements at very low equatorial altitudes (L=3-4) during major storms with significant delays relative to the sudden storm commencement times. They also found that fractional number density of O^+ ions increases with the intensity of the storm. Nose et al. [2011] proposed that the ring current, rich in O^+, is formed in a recurrent process in which the oxygen torus, the plasmasphere, and the ring current interact. It is speculated by Nose et al. [2011] that the source of O^+ in ring current is the ionosphere and that the energy is of solar origin. Observing the spatial and temporal variations of the density of ions (H^+, He^+, O^+) is important to understanding the source region of the ions and the role the ions play in controlling the properties of the ring current and the radiation belt [Takahashi et al., 2008; Nose et al., 2011].

In the past, geomagnetic storm influence on the ionosphere was mostly studied separately from its influence on the plasmasphere. But to better understanding magnetosphere-ionosphere coupling during storm time, we need combined information on plasmaspheric density and composition, ionospheric density and composition, and solar and interplanetary conditions. The WM sounding from IMAGE provided an excellent opportunity to study this. Whistler mode radio sounding pro-

vides electron density, effective ion mass, ion composition, and density irregularities along field lines from 90 km to $\sim$ 4000 km, which includes the F2 peak [Sonwalkar et al., 2011a; 2011b].

1.3 Problem statement and approach

This thesis is built upon the work published in Sonwalkar et al. [2001]; Sonwalkar et al. [2004]; Sonwalkar et al. [2011a]; and Sonwalkar et al. [2011b] papers. Part of this thesis work has already appeared in two Journal of Geophysical Research-space physics publications [Sonwalkar, Carpenter, Reddy et al., 2011a; Sonwalkar, Reddy, and Carpenter, 2011b]. More recent thesis work was presented and published at AGU conferences [Reddy and Sonwalkar, 2011, 2012, Sonwalkar et al., 2013, 2014c], a COSPAR conference [Sonwalkar et al., 2012], and the URSIGA conference [Sonwalkar et al., 2014a]. This thesis work seeks to answer the following questions:

(1) How do we systematically and efficiently determine the field-aligned electron density, effective ion mass, and ion composition given whistler mode echo dispersion and cutoffs?

(2) What is the uncertainty in the measurement of electron density, ion effective mass and ion composition obtained using the whistler mode radio sounding method?

(3) How do the electron and ion densities in the ionosphere and the overlying plasmasphere on the day-side and night-side change as a function of geomagnetic activity?

(4) How does the response obtained from WM sounding compare with those from in situ measurements from other satellites, ground-based ionosondes, and empirical models?

(5) What is the role of thermospheric winds in determining ionospheric storm time variability?

1.4 Contributions of this thesis work

Several contributions were made in the course of this work. They are summarized below:

(1) Development of a systematic and efficient iterative procedure for the whistler mode radio sounding method that allows determination of the field-aligned electron density, ion effective mass, ion composition (with certain assumptions), and field-aligned density irregularities using WM echo observations and ray tracing calculations.

(2) Methodology to determine the field-aligned irregularities, their location and scale sizes using WM echo observations and ray tracing calculations.

(3) Comparison of the whistler mode radio sounding results with in situ measurements from the DMSP and CHAMP satellites, bottomside sounding results, and predictive values from IRI 2012, GCPM and Ozhogin et al. [2012] empirical models.

(4) Estimation of uncertainties in the measured field-aligned electron density, ion effective mass and ion composition using the whistler mode radio sounding method.

(5) Application of the whistler mode radio sounding method to determine for the first time plasmaspheric field-aligned electron and ion densities during the onset, main, and recovery phases of storms.

1.5 Organization of thesis

The present work is organized into four chapters. Chapter 1 provides thesis objectives, background for the work done in this thesis, problem statement and approach, and contributions of this thesis work. Chapter 2 presents observations and interpretations of whistler mode echoes, devises a systematic and efficient iterative procedure to implement the whistler mode radio sounding method, and provides estimates of uncertainties in the measurement of plasma density, composition, and ion effective mass. Chapter 3 includes analysis of whistler mode echoes observed on the IMAGE satellite during quiet and disturbed periods to determine field-aligned electron density and relative ion concentrations on day-side and night-side as a function of geomagnetic storm activity. Chapter 3 also presents the response of electron and ion densities to geomagnetic storm activity, as obtained from the in situ measurements from other satellites, bottomside sounding, and empirical model predictions. Chapter 4 gives a summary, concluding remarks, and suggestions for a possible future work.

Chapter 2

Whistler Mode Radio Sounding on IMAGE of Field-Aligned Electron Density, Ion Composition, and Field Aligned Density Irregularities

The objectives of this chapter are: (1) to devise a systematic and efficient approach to implement whistler mode radio sounding technique to determine field-aligned electron density, ion effective mass and ion densities in the magnetosphere; (2) to discuss uncertainties in the measurement of electron and ion densities and ion effective mass; (3) to compare the whistler mode sounding results of field-aligned electron and ion densities with those from other satellites, bottomside sounding results, and predictions from other empirical models; and (4) to augment whistler mode radio sounding results with those from other satellites and ground-based ionosonde stations.

2.1 Introduction to whistler mode echoes

Whistler mode is a cold plasma wave mode. Whistler mode waves propagate in the magnetosphere at a frequency (f) below either the electron plasma frequency (f_{pe}) or the electron gyro frequency (f_{ce}), whichever is lower. These waves are found in all parts of the magnetosphere. Because of their large refractive index that varies over three to four orders of magnitude (>1–10,000), slow phase and group velocities, and their accessibility to most parts of the magnetosphere, WM waves play an important role in magnetospheric physics and have proved to be a powerful tool for magnetospheric cold and hot plasma diagnostics [Storey, 1953; Helliwell 1965; Carpenter, 1966; Helliwell, 1988; Carpenter et al., 1997; Sonwalkar et al., 1997]. Whistler-mode waves are also known to influence the distribution, acceleration, and loss of energetic particles in the radiation belts [e.g., Kennel and Petschek, 1966; Lyons and Williams, 1984; Liemohn and Chan, 2007].

In the past, observations of WM waves included either ground signals from lightning or transmitters with injection into the magnetosphere with vertical wave normal angles (because of Snell's law and $\mu_{iono} >> 1$; where $\mu iono$ is the refractive index at the ionosphere) or signals from magnetospheric sources (e.g., hiss, chorus) with unknown initial wave normal angle and source location. Attempts to inject WM waves from space from the Activny satellite in the early nineties failed [Inan et al., 1981]. The Radio Plasma Imager (RPI) aboard the IMAGE satellite is the first successful whistler mode radio sounder in space. For the first time, WM waves were successfully

injected into the magnetosphere in all directions from a known source within the magnetosphere and were received back after a certain time. Since WM waves propagate close to the geomagnetic field line, WM echoes observed on IMAGE allow remote sensing along the field line.

2.1.1 Types of WM echo reflections

There are two distinct types of echo reflection that depend upon spatial changes in the refractive index along ray paths below or above the satellite.

(1) Magnetospheric reflection: The generation of magnetospherically reflected whistler mode echoes is schematically illustrated in Figure 2.1a. For a wave injected close to the resonance cone angle in frequency range $f_{lh} < f < f_{lh,max}$, where f_{lh} is the local lower hybrid frequency and $f_{lh,max}$ is the maximum lower hybrid frequency along the field line passing through the satellite magnetospheric reflection (MR) occurs at an altitude where the refractive index surface changes from an open to a closed topology (Figure 2.1a ray path C, C′). This can happen in a smoothly varying medium when the wave encounters the condition $f_{lh} \sim f$, [Kimura, 1966; Smith and Angerami, 1968; Edgar, 1976]. At reflection (properly viewed as a process of refraction), the ray direction becomes transverse to $\mathbf{B_0}$ as it changes from downward (upward) to upward (downward), thus describing a loop as the echo returns to the satellite [Sonwalkar et al., 2011a]. Because the MR echo path is a loop, it may be traversed in either direction. The dashed red curves in Figure 2.1a indicate MR echo traversed in reverse direction.

The expression for f_{lh}, which plays a key role in WM propagation, reflection, and echo formation, is given below for a magnetospheric plasma composed of electrons, protons (H^+), and helium (He^+) and oxygen (O^+) ions.

$$\frac{1}{f_{lh}^2} = \left(\frac{m_p}{m_e} m_{eff}\right)\left(\frac{1}{f_{pe}^2} + \frac{1}{f_{ce}^2}\right) \tag{2.1}$$

where $m_p/m_e \approx 1836$ is the ratio of the proton mass to the electron mass, f_{pe} and f_{ce} are the electron plasma and gyro frequencies, and m_{eff} is the effective ion mass, defined below.

$$\frac{1}{m_{eff}} = \frac{\alpha_{H^+}}{1} + \frac{\alpha_{He^+}}{4} + \frac{\alpha_{O^+}}{16}, \tag{2.2}$$

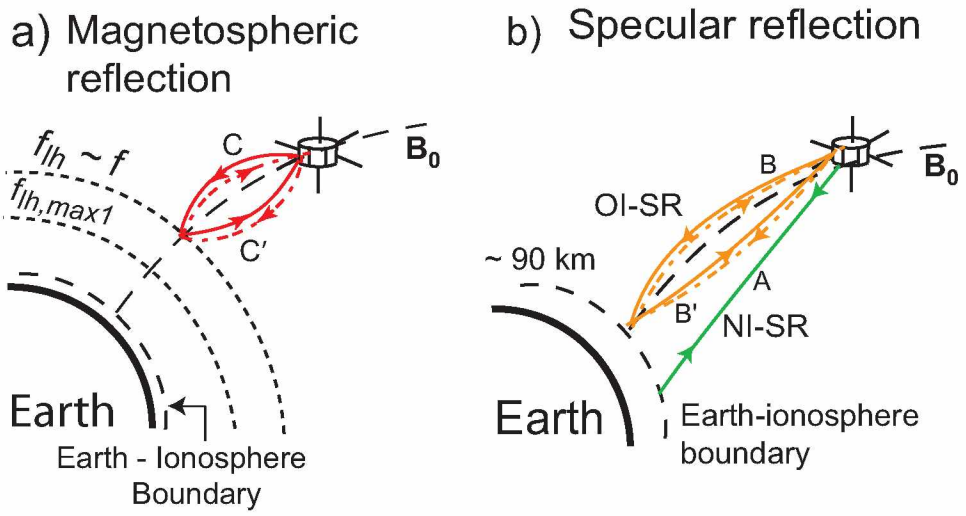

Figure 2.1. Schematics showing whistler mode echo reflections. (a) Magnetospheric reflection. (b) Specular reflection [adapted from Sonwalkar et al., 2011a].

where $\alpha_{H^+} = N_{H^+}/N_e$, $\alpha_{He^+} = N_{He^+}/N_e$, $\alpha_{O^+} = N_{O^+}/N_e$, are the fractional ion abundances, and N_e, N_{H^+}, N_{He^+}, and N_{O^+} are the densities of electrons, H^+, He^+, and O^+ ions, respectively.

The charge neutrality of the plasma requires

$$\alpha_{H^+} + \alpha_{He^+} + \alpha_{O^+} = 1 \tag{2.3}$$

(2) Specular reflection: The generation of specularly reflected whistler mode echoes is schematically illustrated in Figure 2.1b. For a wave at frequency f, propagating at small or large wave normal angles, specular reflection (SR) occurs at the earth-ionosphere boundary near 90 km for that wave that has not undergone a magnetospheric reflection discussed above. Near 90 km, the refractive index governing this wave undergoes an 'abrupt' change from the magnetized-plasma conditions of the bottomside ionosphere to the essentially free-space conditions of the earth-ionosphere wave guide [Helliwell, 1965]. Note Muldrew [1969] from soundings between $\sim$ 200 and 800 kHz on Alouette II, identified that whistler mode echoes on a limited number of ionograms recorded at high latitudes in early morning had reflected at the Earth's surface [Sonwalkar et al., 2011a].

Incident upon the earth-ionosphere boundary, which need not be horizontally stratified, there will generally be a distribution of wave-normals and ray directions that depend on the amount of ray bending that has occurred as the waves (launched at various angles and hence onto various ray paths) penetrated the dense F layer. There may then occur two types of SR echo reflections:

one involving a ray for which the wave-normal is normally incident on the boundary (the NI echo; Figure 2.1b green curve, ray path A) and the other a ray whose wave-normal is obliquely incident (the OI echo; Figure 2.1b gold curves, ray path B B′). In the NI case, both the incident and reflected wave-normal angles are perpendicular to the boundary, and during reflection the ray direction is reversed such that the echo retraces its path to the satellite. For the OI case, in which the incident and reflected angles differ from one another (because of the anisotropy of the medium), the incident and reflected wave-normal angles are oblique, as are the incident and reflected ray directions. Thus the echo path to the satellite forms a loop. Because the OI-SR echo path is a loop, it may be traversed in either direction. The dashed gold color curves in Figure 2.1b indicate an OI-SR echo traversed in reverse direction. Although called specular, SR reflection may be understood to include penetration of the ionospheric lower boundary by a fraction of the incident wave energy. All waves that start from the satellite eventually undergo MR or SR reflection, but only a subset of them return in the form of observable echoes [Sonwalkar et al., 2011a]. [For further details on the generation mechanisms of MR, NI-SR, and OI-SR whistler mode echoes, see Sonwalkar et al., 2011b.]

2.2 Observations and interpretation

This section gives brief introduction to the RPI instrument aboard the IMAGE satellite. It presents the observations and interpretation of a variety of magnetospherically and specularly reflected whistler mode echoes observed by RPI/IMAGE during the August to September 2005 period. It discusses a method to obtain local electron density and ion effective mass from the lower cutoff of MR echoes. The occurrence patterns of MR and SR echoes is also presented.

2.2.1 Instrument description

The IMAGE satellite was launched on 25 March 2000 into an elliptical polar orbit with apogee at $\sim$ 8 RE, perigee at $\sim$ 1000 km altitude, and initial latitude of apogee 40° N. The RPI instrument aboard the IMAGE satellite is a multi-mode instrument [Reinisch et al., 2000] in which sounding and listening frequencies, range detection, pulse characteristics, and repetition rate are adjustable parameters over a wide range of values. The instrument covers the frequency range from 3 kHz to 3 MHz with a receiver bandwidth of 300 Hz. There are three orthogonal thin-wire antennas, two

500-m tip-to-tip dipoles in the spin plane (X and Y), and a 20-m tip-to-tip dipole along the spin axis (Z). The long dipoles are used for transmission, and all three antennas are used for reception. The nominal radiated power from the RPI, variable (in terms of free-space-mode excitation) from 0.1 mW at low frequencies to $\approx$ 10 W per dipole at 200 kHz, was reduced by 3 dB on 8 May 2000 when the power supply for the Y-axis transmitter failed. A further reduction occurred on 3 October 2000, when one of the X-axis monopoles was partially severed, apparently by a micro-meteorite, reducing the dipole length to 340 m. On 18 September 2001 an unknown (presumably small and negligible) section of the Y antenna was lost. On 30 September 2004, as a result of an unknown failure of the Y-antenna/receiver system, the signal strength received by the Y-antenna was reduced substantially. The failure of the Y-antenna/receiver system in September 2004 led to an unexpected benefit: it permitted detection of diffuse MR-WM echoes that in a large number of instances could not be recognized on the X and Z antennas because of receiver saturation (see Sonwalkar et al. [2011a] for details and examples of MR and SR echoes observed on three antennas). In spite of difficulties with antennas, excellent whistler mode sounding data and passive recordings of background whistler mode waves were acquired over the 5.8 year lifetime of IMAGE, which ended on 18 December 2005 due to loss of telemetry.

The RPI instrument could be operated in two modes: active sounding and passive recording. Figure 2.2a shows the IMAGE orbit in 2005, a schematic of active sounding (left) and the passive recording experiment (right). In the sounding mode, RPI transmits a sequence of narrow radio pulses of a few milliseconds to a few hundred milliseconds duration in 3 kHz to 3 MHz range in various frequency-time formats called programs. Figure 2.2b shows a schematic of a sounding program. During typical RPI operations, a sounding program lasting $\sim$10–100 seconds is repeated at intervals of 2–10 minutes within a schedule containing other programs such as thermal noise (passive recordings). The satellite only listens to the thermal noise in space during passive recordings. These recordings are used to determine local plasma parameters [Reinisch et al., 2000].

At low altitude ($< 5,000$–$10,000$ km) the RPI on IMAGE has observed a variety WM echoes at all latitudes at frequencies up to 300 kHz [Sonwalkar et al., 2004]. A survey of WM echoes observed in January–August 2004, January 2005, and August–December 2005 during 3.2 ms pulse transmissions in the 6–63 kHz range, with a step frequency of 0.3 kHz (program #38; Figure 2.2c), has led to the discovery of magnetospherically reflected WM echoes [Sonwalkar et al., 2011a].

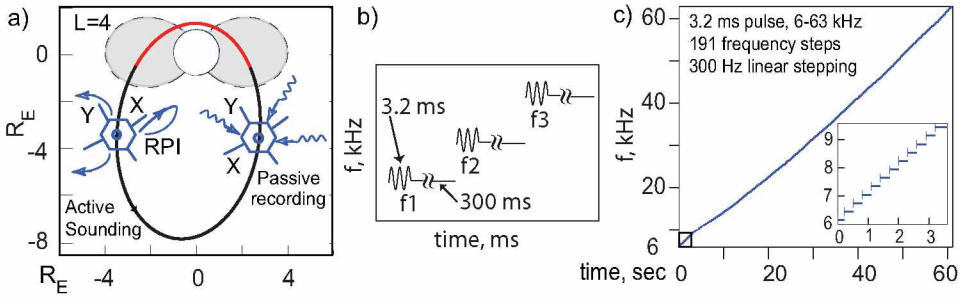

Figure 2.2. Schematic showing the active (sounding) and passive (thermal noise) measurements using Radio Plasma Imager (RPI) on the IMAGE satellite. (a) The IMAGE polar orbit and antenna geometry. (b) Schematic of a sounding program. (c) The frequency step and time step of transmitted signal in active sounding program 38. The inset shows the details of the program.

2.2.2 Examples of specularly reflected and magnetospherically reflected whistler mode echoes and their interpretation

Figures 2.3 and 2.4, respectively, show examples of typical specularly reflected and magnetospherically reflected WM echoes observed on IMAGE during active sounding experiments. Figure 2.5 schematically shows propagation mechanisms of various types of WM echoes [Sonwalkar et al., 2004; Sonwalkar et al., 2011a].

Figure 2.3a shows a plasmagram (time delay versus frequency plot) displaying discrete SR whistler mode (WM) echoes above $\approx$ 10 kHz, with time delay decreasing with frequency and with relatively small spreading in time delays at each frequency. The generation of SR echoes is schematically illustrated in Figure 2.5a. The echoes shown in Figure 2.3a result from RPI signals propagating downwards in a relatively smooth magnetosphere, specularly reflecting, either normally incident (Figure 2.5a, ray path A) or obliquely incident (Figure 2.5a, ray path B, B$'$), at the earth-ionosphere boundary, and returning to the satellite. Because the SR echo path is a loop, it may be traversed in either direction.

Figure 2.4a shows a plasmagram displaying discrete MR whistler mode (WM) echoes below $\approx$ 12 kHz with time delay increasing with frequency and with relatively small spreading ($\sim$3-6 ms) in time delays at each frequency. The MR-WM echo has a lower ($f_{min,MR}$) and upper cutoff ($f_{max,MR}$) frequency and a distinguishing shape on a plasmagram. Horizontal traces below about 40 ms time delay are proton cyclotron (PC) echoes [Carpenter et al., 2007]. The arrows on frequency axes indicate the lower cutoff frequency of MR WM echoes, identified as the local lower hybrid

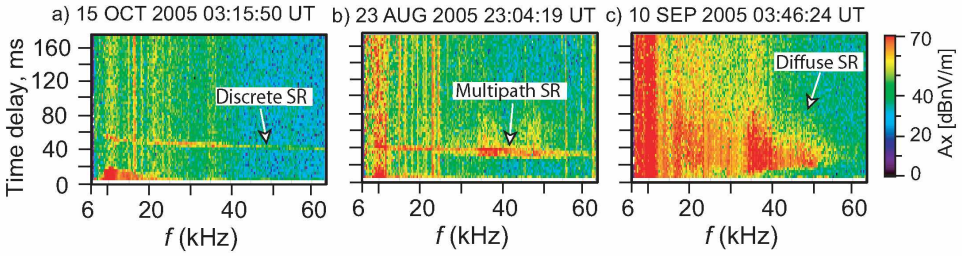

Figure 2.3. Plasmagrams showing examples of the variety of spectral forms of SR echoes received during RPI soundings. (a) Discrete SR echoes observed on 15 October 2005, (1776 km, $\lambda_m = 56^\circ$ N, L= 4.14, MLT=11.7) resulting from propagation in a smooth magnetosphere. (b) Discrete multipath echoes observed on 23 August 2005 (1915 km, $\lambda_m = 59.7^\circ$ N, L= 5.1, MLT=4.16), possibly resulting from refraction of RPI signals by large scale irregularities. There is also evidence of diffuse forward scattered SR echoes between 32 and 50 kHz. (c) Diffuse SR echoes observed on 10 September 2005 (1855 km, $\lambda_m = 76.91^\circ$ N, MLT=4.3), possibly resulting from scattering by small scale irregularities. [Reproduced from Sonwalkar et al., 2011a.]

frequency (f_{lh}). The generation of MR echoes is schematically illustrated in Figure 2.5d. The echoes shown in Figure 2.4a result from RPI signals propagating downwards in a relatively smooth magnetosphere and reflecting at an altitude where $f \sim f_{lh}$ (Figure 2.5d, ray path C, C′) when the WM refractive index surface changes from open to closed topology [Kimura, 1966]. Because the MR echo path is a loop, it may be traversed in either direction. This mechanism, involving the MR process, is limited to frequencies less than the maximum f_{lh} 10-15 kHz in the ionosphere [Sonwalkar et al., 2011a].

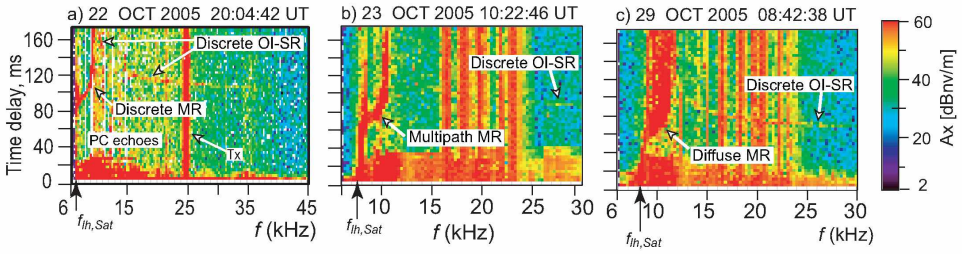

Figure 2.4. These RPI plasmagrams illustrate various features of MR echoes seen on the IMAGE satellite. The arrows on the frequency axes indicate the lower cutoffs $f_{min,MR} \sim f_{lh,Sat}$ of MR echoes. (a) Discrete MR echo (Altitude=3404 Km, $\lambda_m = 31.9^\circ$ N, L=2.13, MLT= 11.2). (b) Discrete multipath MR echo (2654 km, $\lambda_m = 39.24^\circ$ N, L=2.36 ,MLT= 12.3). (c) Diffuse MR echo (2490 km, $\lambda_m = 38.52^\circ$ N, L= 2.27, MLT= 11.9). [Adapted from Sonwalkar et al., 2011a.]

Whistler mode echo propagation paths and echo characteristics are profoundly affected by the presence of plasma density irregularities (or field-aligned irregularities, FAIs)along their ray paths. Field-aligned irregularities can be broadly categorized [Sonwalkar, 2006] as small or large scale based on $\lambda_{\perp,IRREG} << \lambda$ or $\lambda_{\perp,IRREG} >> \lambda$, where $\lambda_{\perp,IRREG}$ and λ, respectively, are the irregularity scale size in the direction perpendicular to the field line and the WM wavelength. Large scale irregularities in the propagation paths of WM waves can lead to refraction whereas small scale irregularities lead to scattering of WM waves. These refracted and scattered waves can reach back to the satellite giving multiple time delays at each frequency.

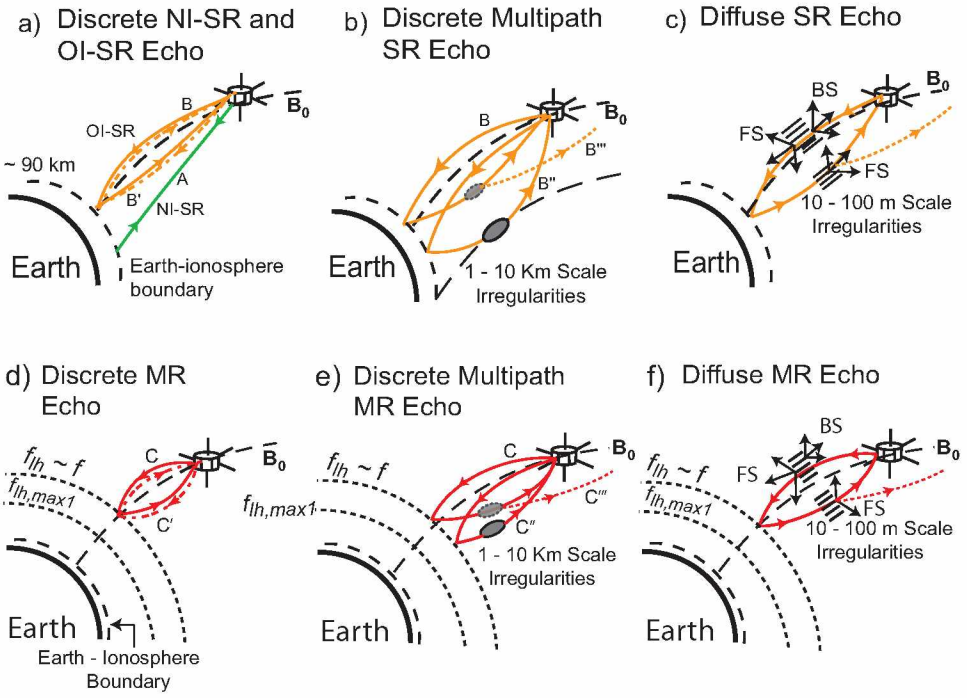

Figure 2.5. Schematic showing various propagation scenarios that may lead to specularly reflected (SR) and magnetospherically reflected (MR)whistler mode echoes observed on the IMAGE satellite. (a) Discrete SR echoes due to propagation in a smooth magnetosphere. (b) Discrete multipath SR and/or patchy SR echoes due to propagation along multiple paths to IMAGE in the presence of large scale irregularities (1–10 km). (c) Diffuse SR echoes due to scattering of signals by small scale (10 m–100 m) irregularities. (d) Discrete MR echoes due to propagation in a smooth magnetosphere. (e) Discrete multipath MR and/or patchy MR echoes due to propagation along multiple paths in the presence of large scale irregularities. (f) Diffuse MR echoes due to scattering of whistler mode signals by small scale irregularities. [Adapted from Sonwalkar et al., 2011a.]

Figures 2.3b and 2.4b, respectively, show examples of multipath SR and MR echoes. The vertical traces above 15 kHz covering the entire time delay axis range are ground transmitter sig-

nals. Magnetospherically and specularly reflected waves encountering large scale FAIs (1–10 km) following reflection can lead to propagation along multiple closely spaced paths (Figure 2.5b ray paths B and B$''$ and Figure 2.5e ray paths C and C$''$) and hence to the reception of what we call multipath echoes with medium spread time delays ($\sim$10–20 ms) at each frequency. Large scale FAIs can also lead to no detection of SR or MR echoes by affecting the echo raypath (Figure 2.5b, path BB$'''$ and Figure 2.5e ray path C C$'''$). In the absence of FAI, the ray would have returned to the satellite.

Figures 2.3c and 2.4c, respectively, show examples of diffuse SR and MR echoes. Small scale FAIs (1–10m) in the propagation paths of MR and SR waves can lead to backward or forward scattering (Figures 2.5c and 2.5f). FAIs scatter WM waves by linear and nonlinear mechanisms, resulting in spreading of wavenormal angles such that some are close to the resonance cone angle [James, 1978; Bell et al., 1983; Titova et al., 1984; Groves et al., 1988; Bell and Ngo, 1988; Sonwalkar and Harikumar, 2000]. Whistler mode waves with different wave normal angles then reach IMAGE with different time delays, leading to a large time delay spread (>60 ms) at each frequency and diffuse appearance on a plasmagram. Sonwalkar et al. [2011a] presented variety of diffuse WM echo examples and a more detailed discussion of effect of FAIs on WM echoes. See Sonwalkar et al. [2011a] for details on how most of the diffuse MR echoes were identified.

2.3 Obtaining plasmapause location and local electron density from upper hybrid frequency measurements

Figure 2.6 shows an example of RPI dynamic spectra made from passive measurements that are interspersed with active sounding along an entire orbit. These passive measurements provide information on local plasma density, plasmapause location, natural plasma wave activity, and reception of the ground transmitter signals. The upper hybrid emission provides a measure of f_{pe} [Benson et al., 2004]. At altitudes $<$ 5000 km where MR echoes are observed, f_{ce} can be obtained within 5% from the IGRF model [Li, 2004]. Dynamic spectra such as those shown in Figure 2.6, typically showed naturally occurring upper hybrid emissions with upper cutoff at $f_{uh} = \sqrt{f_{pe}^2 + f_{ce}^2}$. Measurement of f_{uh} along with f_{ce} from the model thus provides f_{pe}. The values of f_{pe} from the dynamic spectra are available before and after the transmissions of program #38 and can be used to determine f_{pe} at the time of the f_{lh} observation by interpolation.

For example, note the 22 Oct 2005 2004:42 UT case. From the IGRF model, f_{ce} ≈322 kHz; from the dynamic spectra (Figure 2.6); and by the method described above, we obtain f_{pe} at the times before and after the program #38 transmissions. At 2004:12 UT, when the satellite was at 3466 km and λ_m = 31.06°, the measured upper hybrid frequency from the dynamic spectrum of Figure 2.6 was ∼ 640-653 kHz, f_{ce} from IGRF was 312, and thus f_{pe} ∼ 559-573 kHz. At 2006:57 UT, when the satellite was at 2984 km and λ_m=38.01°, the measured f_{uh} was ∼ 750 − 765 kHz, f_{ce} from IGRF was 396 kHz, and thus f_{pe} ∼637-654 kHz. Interpolating, we get that at the time of f_{lh} measurement (2004:42 UT) f_{pe} ∼ 569-584 kHz,.

The sudden drop in the upper hybrid emission frequency can be used to determine the plasmapause location. Under disturbed conditions, the dynamic spectra can show large scale plasma density irregularities, which commonly occur near the plasmapause [Carpenter and Anderson, 1992]. The plasmapause locations as estimated from f_{uh} measurements for the case of 22 Oct 2005 are L=5.5 (day-side) and L=4.5 (night-side).

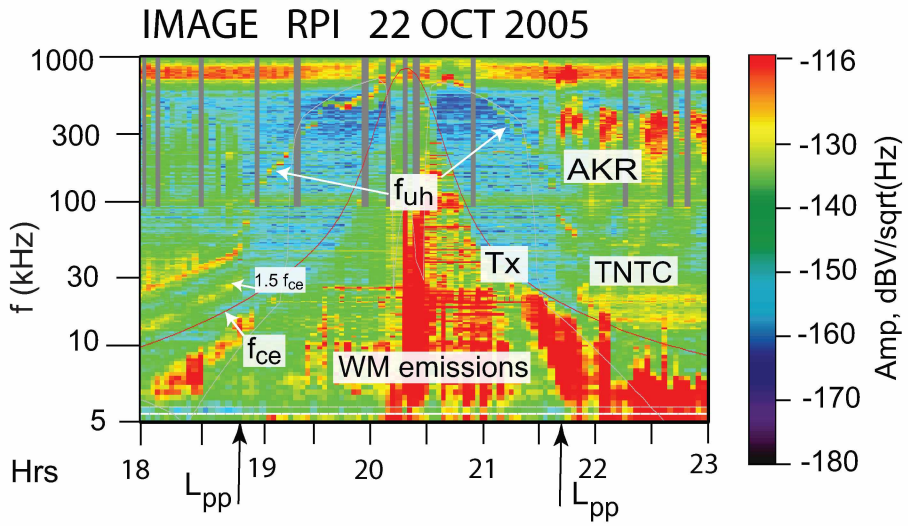

Figure 2.6. Dynamic spectra from RPI passive recordings on 22 October 2005 showing various naturally occurring plasma waves and VLF ground transmitter **(Tx)** signals.

2.4 Determination of local electron density and effective ion mass from the lower cutoff of MR echoes

The lower cutoff of MR echo $f_{MR,min} = f_{lh}$ and Equation (2.1) provide a method to measure m_{eff}, if independent measures of f_{pe} (N_e) and f_{ce} are available. As an example, consider the case of 22 October 2005, when IMAGE was located at 3403 km and $\lambda_m = 31.8^\circ$. The Figure 2.4a shows that $f_{MR,min}$ <6.6 kHz. Unfortunately for this particular transmission the data was missing at 6.3 kHz. By comparing the minimum frequency of the MR echo in Figure 2.4a with that of other examples (e.g., Figure 2.4b), which show that the minimum frequency of an MR echo generally occupies two bins, we estimate that $f_{MR,min}$=6.3$\pm$0.15 kHz (Δf = 300 Hz). With this value of f_{lh} at the satellite location, we can estimate m_{eff} as follows. From the IGRF model, $f_{ce} \approx$ 322 kHz and from the dynamic spectra $f_{pe} \sim 569 - 584$ kHz. Taking $f_{pe} \sim$ 576 kHz and $f_{ce} \sim$ 322 kHz at the satellite, we obtain $m_{eff} \approx 1.138$ with $f_{lh} = 6.15$ kHz and $m_{eff} \approx 1.034$ with $f_{lh} = 6.45$ kHz. If we assume that at the satellite the principal contribution to m_{eff} was from H^+ and He^+, we obtain He^+/H^+ ~0.19 for f_{lh}=6.15 kHz and $He^+/H+$ ~0.05 for f_{lh}=6.45 kHz. The uncertainty in the m_{eff} and He^+/H^+ measurement is the result of limitations on frequency resolution ($\Delta f = 300$ Hz) for f_{lh} measurement and uncertainties in f_{pe} and f_{ce}.

The calculation can be turned around to focus on obtaining f_{pe} from the MR data. At high altitudes (> 2000 km) the main constituent ion is H^+, and therefore $m_{eff} \approx 1$. Local plasma density can be obtained from Equation (2.1) by using the measured values of $f_{MR,min}$ and f_{ce} either measured or calculated from a model [Sonwalkar et al., 2011a]. In the 22 Oct 2005 case, for example, $f_{ce,IGRF}$=322 kHz. From Equation (2.1) we obtain f_{pe}=459 kHz and 539 kHz, for f_{lh}=6.15 and 6.45 kHz, respectively. Note that this range of f_{pe} is smaller than the range 569-584 kHz obtained from the dynamic spectra. This is expected because $m_{eff} > 1$ and it is assumed to be 1 in the calculation of f_{pe}.

2.4.1 Occurrence pattern of MR and SR echoes

Probabilities of echo occurrence depend on many factors: radiated power and pattern, antenna orientation, frequency, distance traveled and spreading losses, efficiency of reflection, losses due to absorption (D region), and the presence of FAIs along the signal ray paths. Figure 2.7 shows the occurrence patterns along the IMAGE orbit in the geomagnetic meridional plane of various

types of WM echoes observed during the transmissions of program #38 in January-August 2004 and August-December 2005. There were fewer MR echoes in 2004 because of fewer program #38 transmissions. Most echoes were observed at less than 5000 km altitude. We believe this limitation was a result of experimental constraints: power transmitted and the maximum time delay limitation of program #38. The occurrence pattern of MR and SR echoes was reported earlier by Sonwalkar et al. [2004] and Sonwalkar et al. [2011a]. The data set used for the occurrence patterns shown in Figure 2.7 is the same as that used by Sonwalkar et al. [2011a]. Along with the summary from Sonwalkar et al. [2011a], additional aspects on occurrence patterns of WM echoes that were not reported in Sonwalkar et al. [2011a] are presented here. Specularly reflected echoes were observed (discrete, multipath, or diffuse) during ~23% of the transmissions below 5000 km and on at least 50% of the orbits. When observed, such echoes tended to appear on more than one sounding, which were typically spaced by ~2000 km along an orbit (program # 38 was transmitted every ~ 4 minutes). Discrete SR echoes were observed during 14% of the transmissions, multipath SR echoes during 2%, and diffuse SR echoes during 7% of the transmissions. Magnetospherically reflected echoes (discrete, multipath, or diffuse) were observed during 20% of the transmissions below 5000 km and on at least 50% of the orbits. Discrete MR echoes were observed during 5% of the transmissions, multipath MR echoes during 1% of the transmissions, and diffuse MR echoes during 14% of the transmissions. Though all types of SR echoes were observed at all latitudes, the largest fraction of discrete echoes was observed at the lower latitudes and the largest fraction of diffuse echoes at higher latitudes. Similarly, all types of MR echoes were observed at all latitudes, but the largest fraction of discrete and multipath MR echoes was observed at the lower latitudes. Diffuse MR echoes were found in large numbers at all latitudes.

2.5 Whistler mode radio sounding method

Whistler mode radio sounding from IMAGE has been studied since 2001 [Sonwalkar et al., 2001; Sonwalkar et al., 2004; Sonwalkar et al., 2011a; Sonwalkar et al., 2011b]. Sonwalkar et al., 2001 discusses the feasibility of conducting whistler-mode wave-injection experiments within and near the plasmasphere and the potential of such experiments to address certain science questions. Sonwalkar et al., 2004 and Sonwalkar et al., 2011a give a general introduction to whistler mode radio sounding. Sonwalkar et al., 2004 presents observations and interpretation of SR whistler mode

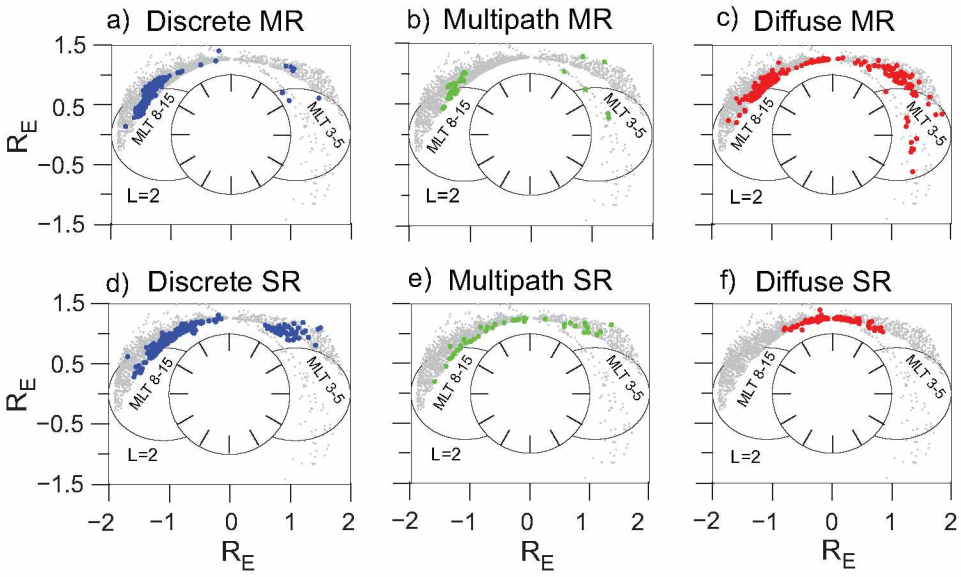

Figure 2.7. Occurrence pattern of MR-WM echoes (a-c) and SR-WM echoes (d-f) in magnetic meridional plane. Also shown are the satellite orbits and MLT. (a) Discrete MR-WM echoes. (b) Multipath MR-WM echoes. (c) Diffuse MR-WM echoes. (d) Discrete SR-WM echoes. (e) Multipath SR-WM echoes. (f) Diffuse SR-WM echoes. From Sonwalkar et al. [2011a].

echoes. It also presents a method for remote sensing of field-aligned N_e and density irregularities from the observed dispersion of whistler mode echoes. Sonwalkar et al., 2011a presents observations and interpretation of MR, OI-SR, and NI-SR whistler mode echoes. It also introduces the idea of remote sensing of field-aligned electron and ion densities and effective ion mass from the observed properties of WM echoes. Sonwalkar et al., 2011b presents whistler mode radio sounding method to determine field-aligned electron density, effective ion mass, relative ion composition and density irregularities. This section provides details of the WM radio sounding method that were not given in Sonwalkar et al., 2011b.

Sonwalkar et al. [2011b] discusses the "direct" problem of WM radio sounding: given a typical magnetospheric plasma distribution, determine the type and characteristics of the WM echoes that can be observed on the satellite as well as the "inverse" problem: given the characteristics/properties of observed WM echoes, determine the magnetospheric plasma distribution along the echo ray paths. Authors use ray tracing as part of the inverse problem of inferring properties of the plasma medium from observed properties of the data. With two case studies, the authors illustrate the new radio sounding method for the remote determination of electron density, ion effective mass, ion densities, and scale sizes and locations of density irregularities along the field

line passing through IMAGE. They also a present a brief discussion of uncertainties in the WM sounding method. Various aspects of WM radio sounding method including Landau damping, hot plasma effects, issues of wavelength and irregularity scale sizes, issues of antenna radiation, limits on spatial resolution, WM echo ray paths in 3-dimensional magnetosphere are also discussed in Sonwalkar et al., 2011b.

This section provides a systematic and efficient iterative procedure of implementing WM radio sounding method that was not discussed in Sonwalkar et al., 2011b. It discusses how adjustments to the raytracing density model are made during the iterative process until a "final" model that explains the observed features of MR and SR echoes is obtained. This procedure is illustrated with a case study; a similar procedure can be employed to the analysis of any WM echo observed on IMAGE. The uncertainties in the measurement of electron density, effective ion mass, and relative ion concentrations using the WM radio method are discussed. A comparison of WM sounding results with in situ measurements from other satellites, bottomside sounding results, and predictions from empirical models is provided. Augmentation of WM radio sounding results, when needed, with in situ measurements from other satellites and bottomside sounding results is presented. Whistler mode radio sounding method is applied to two cases, one observed during geomagnetically quiet condition and the other during geomagnetically disturbed conditions.

2.5.1 Formulation of WM radio sounding problem and iterative procedure to determine field-aligned electron density and ion composition

The problem of whistler mode radio sounding is to determine the plasma distribution along the echo propagation path from the measured echo dispersion and cutoffs. The spatially varying, unknown plasma distribution, characterized by electron density (N_e), fractional ion abundance (α_i), and the geomagnetic field (**B**), must satisfy the following constraints [Sonwalkar et al., 2011b]:

$$f_{lhSat} \backsimeq f_{MR,min} \tag{2.4}$$

$$f_{lhmax1} \gtrsim f_{MR,max} \text{ and } f_{lhmax1} \approx f_{OI,min} \tag{2.5}$$

$$\oint_{\text{MR Echopath}} ds/v_g(f,\theta,\mathbf{B},N_e,m_{eff}) = t_{g,avg}(f/MR)$$
$$f_{MR,min} < f < f_{MR,max} \tag{2.6}$$

$$\oint_{\text{NI Echopath}} ds/v_g(f,\theta,\mathbf{B},N_e,m_{eff}) = t_{g,avg}(f/NI)$$
$$f_{NI,min} < f < f_{NI,max} \tag{2.7}$$

$$\oint_{\text{OI Echopath}} ds/v_g(f,\theta,\mathbf{B},N_e,m_{eff}) = t_{g,avg}(f/OI)$$
$$f_{OI,min} < f < f_{OI,max} \tag{2.8}$$

where variable s denotes the distance along the ray path, v_g is the group velocity along the ray path, $t_{g,avg}(f/MR)$, $t_{g,avg}(f/NI)$, and $t_{g,avg}(f/OI)$ are the measured average time delays for MR, NI, OI echoes, respectively. The integral $\oint ds/v_g$ gives the total round trip echo propagation time (time delay). The integral is evaluated along the echo ray paths, which are distinct for MR, NI, and OI echoes. The group velocity is a function of wave frequency (f), wave-normal angle (θ), and medium parameters $\mathbf{B}$, N_e, and m_{eff}.

In Equations (2.6) to (2.8) we have described the v_g dependence on m_{eff} and not on individual ion concentrations. For whistler mode propagation at frequencies well above local ion gyrofrequencies (f_{ci}), the refractive index depends on the ion effective mass, not on the relative concentrations of the individual ions (See Appendix-B of Sonwalkar et al., 2011b). Thus sounding at frequencies $f >> f_{ci}$ can in principle provide remote sensing of N_e and m_{eff}. Further assumptions are required in order to obtain the fractional abundances of individual ions.

Because constraints (2.6) to (2.8) are integral equations, the inverse problem of determining the plasma distribution is ill-posed. Infinitely many plasma distributions can satisfy these equations as long as the boundary conditions given by (2.4) and (2.5) are satisfied. We also note that while equation (2.5) provides the approximate value of $f_{lh,max1}$ along the MR and OI echo ray paths, or essentially along $\mathbf{B_0}$ (because the MR and OI ray paths lie close to $\mathbf{B_0}$), the equation does not provide the altitude of $f_{lh,max1}$.

A general procedure to solve an ill-posed problem of this kind is to assume a parametric model for the density and then determine the parameters of that model that are consistent with experimental measurements. This procedure has been used for radio sounding of the bottomside and topside ionosphere using cold plasma R-X, L-O, and Z modes [Benson, 2010 and references therein]. The parametric model is chosen so as to be flexible enough to encompass a large variety of the past plasma density and composition measurements at a wide range of locations within the magnetosphere.

Our specific method of analysis is based on ray tracing calculation of WM propagation in a magnetosphere described by a parametric diffusive equilibrium density model and a dipole magnetic field. Our first step is to choose parameters such that the resulting density model satisfies constraints given by equations (2.4) and (2.5). With this model, ray tracings are then carried out to simulate MR, OI, and NI echoes. The calculated time delays are compared with the measured ones. Based on the discrepancies, a new density model is built and the entire process is repeated until a model is found for which the calculated and measured time delays agree within the experimental uncertainties.

2.5.1.1 The Stanford 2-D ray tracing program

As noted above, the Stanford 2-D ray tracing program is a tool used as part of the WM radio sounding method for inferring properties of the plasma medium from observed properties of the data. The Stanford 2-D ray tracing program solves Haselgrove equations [Haselgrove, 1955] in order to determine the ray path in the magnetic meridional plane assuming a magnetospheric density model. Both group time delay and wave normal angle can be calculated along ray paths for rays injected at arbitrary latitudes and altitudes. The reflections at the earth-ionosphere boundary are modeled as specular reflections at a specified altitude, typically 90 km [Sonwalkar et al., 2004].

The wave normal direction of the wave reflected is obtained by applying the Snell's law (Poeverlein construction) at the boundary.

The Stanford ray tracer employs a dipole field model. The dipole field model is characterized by a single assignable parameter, $f_{ce,Eq}$, the gyrofrequency at the geomagnetic equator at the earth's surface. The gyrofrequency at a general point is given by

$$f_{ce} = f_{ce,Eq}\left(\frac{r_e^3}{r^3}\right)\sqrt{1+3\sin^2\lambda_m}, \tag{2.9}$$

where r is the geocentric distance, r_e the radius of the earth, and λ_m the geomagnetic latitude. Along a field line described by L, we have

$$r = r_e L\cos^2\lambda_m \tag{2.10}$$

The ray tracing program uses a density model that assumes the plasma is composed of electrons and H^+, He^+, O^+ ions, and is described by a diffusive equilibrium density model inside the plasmasphere [Angerami and Thomas, 1964]. Outside the plasmasphere, the density model is multiplied by a plasmapause factor that includes an (R^{-n}) density falloff outside the plasmasphere.

The electron density $N_e(r,L)$ at any point is given by [Sonwalkar et al., 2011b]

$$N_e(r,L) = N_b\, N_{DE}(r)\, N_{LI}(r)\, N_{PL}(r,L), \tag{2.11}$$

where r and L are, respectively, the geocentric distance (in km) to and the L-shell of the point where the density is evaluated. N_b is the reference electron density at the base of the diffusive equilibrium model inside the plasmasphere.

N_{DE} is the factor due to the diffusive equilibrium model.

$$N_{DE}(r) = \sqrt{\left[\sum_{i=1}^{3}\alpha_i e^{-\frac{(r-r_b)}{H_i}}\right]}, \tag{2.12}$$

where r_b is the geocentric distance (in km) to the base of the diffusive equilibrium model; α_i are the relative ionic species at r_b, where $i = 1,\ 2,\ 3$ represents H^+, He^+, and O^+, respectively. The scale height H_i for $i = 1,\ 2,\ 3$, is defined as

$$H_i = 1.1506(T)(\frac{r_b}{7370})^2(\frac{r}{r_b})\frac{1}{4^{(i-1)}}, \tag{2.13}$$

where , T is the temperature at the base of the diffusive equilibrium model.

N_{LI} is the factor due to the lower ionosphere:

$$N_{LI}(r) = 1 - e^{-(\frac{r-r_0}{H_{Bot}})^2}, \tag{2.14}$$

where r_0 is the geocentric distance in km to the level of the bottom of the ionosphere where the density goes to zero and H_{Bot} is the scale height of the bottom side of the ionosphere.

N_{PL} is the factor due to the plasmapause. L_p is the location of the plasmapause. This factor is unity for $L \leq L_p$. For $L > L_p$,

$$\begin{aligned} N_{PL}(r,L) &= e^{-\frac{(L-L_p)^2}{(W_p)^2}} + (1 - e^{-\frac{(L-L_p)^2}{(W_p)^2}})(\frac{r_c}{r})^n \\ &\quad + (1 - (\frac{r_c}{r})^n)e^{-(\frac{r-r_c}{H_S})^2}, \end{aligned} \tag{2.15}$$

where L is the L-value defining the particular field line, W_p is the half width (in L) of the plasmapause boundary, r_c is the geocentric distance to the level at which density outside the plasmapause field line is equal to the density inside, n is the exponent decrease outside the plasmapause, r^{-n}, and H_S is the scale height of the radial density decrease for r$\geq r_c$ and outside the plasmapause.

The ion densities are given by

$$N_i = N_e \frac{\alpha_i e^{-\frac{r-r_b}{H_i}}}{\sum_{i=1}^{3} \alpha_i e^{-\frac{(r-r_b)}{H_i}}}, \tag{2.16}$$

where N_e, $N_1 = N_{H^+}$, $N_2 = N_{He^+}$, $N_3 = N_{O^+}$ are electron, Hydrogen, Helium, and Oxygen ion densities, respectively.

From Equation (2.16), as expected, we note

$$N_e = N_{H^+} + N_{He^+} + N_{O^+}. \tag{2.17}$$

Equations (2.11) to (2.17) show that the density model provides much flexibility to adjust N_e and N_i as a function of altitude.

The diffusive equilibrium density model is characterized by a few key parameters, including electron density N_b and ion composition α_i, i = 1, 2, 3 at the altitude baser_b of the diffusive equilibrium model, and temperature T. The lower ionosphere is characterized by a scale height H_{Bot} and the geocentric distance r_0 to the lower ionosphere where density becomes zero. The plasmapause is characterized by its magnetic shell parameter L_p and width W_p. This factor is unity for $L \leq L_p$.

The lower ionosphere factor N_{LI} decreases to zero at $r_0 \sim 50$–60 km. The scale height $H_{Bot} \sim 120$–160 leads to the F2 peak at ~ 200–300 km. The plasmapause factor, N_{PL} is superposed on the basic diffusive equilibrium model. The plasmapause factor is unity inside the plasmasphere. Typically the plasmapause location, L_p, is estimated from the measurements of upper hybrid or by using an empirical relation based on the value of K_P in the previous 24 hours [Carpenter and Anderson, 1992]. Typical values assigned to n, the factor with which density falls-off outside the plasmapause, and the width of the plasmapause, W_p, are $\sim 4-5$ and $\sim 0.1-0.2$, respectively [Sonwalkar et al., 2004].

2.5.1.2 General features of whistler mode echoes and raytracing density model

Before the details of WM radio sounding method are discussed, it is useful to consider how various types of echoes accumulate their time delays and general features of the raytracing density model. This will help in making adjustments to the density model during the WM radio sounding method iterative process.

The diffusive equilibrium factor, $N_{DE}(r)$, determines the altitude variation of the relative concentration of three ions. The ion composition is prescribed by fractional abundances α_{H^+}, α_{He^+}, α_{O^+}, respectively, of H^+, He^+, and O^+ at r_b. Note that $\alpha_{H^+} + \alpha_{He^+} + \alpha_{O^+} = 1$. From Equation 2.16, it can be seen that the relative concentration of each ion as a function of altitude varies with a scale height H_i, which is proportional to T, r_b, r, and inversely proportional to ion mass. The

exponential term in Equation 2.16, changes its sign at r_b indicating decrease in ion densities above r_b. Furthermore, because of the large differences in the ion masses, above r_b the relative abundance of O^+ as a function of altitude decreases rapidly and that of H^+ decreases slowly. Above r_b, as a result, H^+ quickly becomes the dominant ion species, with He^+ the minor ion species and the concentration of O^+ becomes negligible. Below r_b, the reverse happens: O^+ increases rapidly and becomes the dominant ions species, with H^+ and He^+ minor ion species. As an example, for r_b~1000 km and T ~1600 km, the scale heights of H^+, He^+, and O^+ are 1840 km, 460 km, and 115 km, respectively, at an altitude of 1000 km. The typical range of values of the ray tracing density parameters that give a realistic magnetospheric density are obtained by comparing the ray tracing density models with the past measurements. These values can be used for the initial guess of ray tracing density parameters. For example, the best least square fit of the ray tracing density model to in situ electron density measurements on ISIS-A (apogee 3500 km, perigee 500 km) over a range of invariant latitude gives $r_b \sim 800-1200$, $T \sim 1000-2400$ K [Li, 2004]. This shows that the scale heights can vary by as much as a factor of 3, consistent with previous observations.

The measured $t_g - f$ values of MR echoes, which reflect above $f_{lh,max1}$ altitude ~1400 km, provide information about that part of the magnetosphere that is dominated by light ions H^+ and He^+. The time delays of MR echoes are sensitive to both N_e and m_eff. At any given frequency, two thirds of the MR echo time delay is accrued in the turnaround region where $f_{lh} > f$ and the refractive index surface is closed [Sonwalkar et al., 2011b].

The time delays of OI at frequencies near $f_{lh,max1}$ (where delays rapidly increase with decreasing echo frequency) are sensitive to both N_e and m_eff. Above $f_{lh,max1}$ altitude OI-SR echoes accrue about 50% of their time delay. (At frequencies much greater than $f_{lh,max1}$ the time delays of OI echoes are sensitive to N_e only.) Since OI echoes accumulate a large part of their time delay near $R_{flh,max1}$ and near R_{F2}, they provide information on the lightion dominated region above $f_{lh,max1}$ altitude as well as on the heavy O^+ ion dominated region below [Sonwalkar et al., 2011b].

Thus both MR and OI echoes provide information on the region close to $R_{flh,max1}$, which is a few hundred kilometers above the O^+/H^+ transition height, considered to be the nominal boundary between the ionosphere and the magnetosphere. Combined ray tracing analysis of MR and OI-SR time delays therefore provides information on ion composition from the sounder altitude down to 90 km [Sonwalkar et al., 2011b].

Like OI echoes, NI echoes accrue about 50% of their time delay above $f_{lh,max1}$ altitude and about 50% below. But unlike OI echoes, NI echoes propagate at low wavenormal angles and their delays are not sensitive to ion composition at any altitude. Relative to OI-SR echoes, NI-SR echoes accrue a greater fraction of their time delay near the F2 peak [Sonwalkar et al., 2011b].

When we take into account the propagation characteristics ($t_g - f$) of MR, OI, and NI echoes, it is possible to devise a systematic and efficient procedure that, typically in 2-3 iterations, will lead to a density model that provides a close match between the simulated and observed properties of WM echoes, including time delays and cutoffs.

2.5.1.3 Application of WM sounding Method to echoes observed on 22 October 2005

Figure 2.8 shows MR and OI whistler mode echoes observed (Altitude = 3404 km, $\lambda_m = 31.9°N$, MLT = 11.2, $L = 2.13$) on 22 October 2005. Magnetospherically reflected (6.6–9.3 kHz) and obliquely incident specularly reflected (10.2–33.3 kHz) echoes were observed with time delays ranging between ∼85–180 ms and ∼110–180 ms, respectively. No NI echoes were observed on this day. From the observed MR and OI echoes, $f_{lh,Sat} \backsimeq f_{MR,min}$=6.3–6.6 kHz, $f_{lh,max1} \gtrsim f_{MR,max}$=9.3 kHz and $f_{lh,max1} \approx f_{OI,min} \lesssim$10.2 kHz.

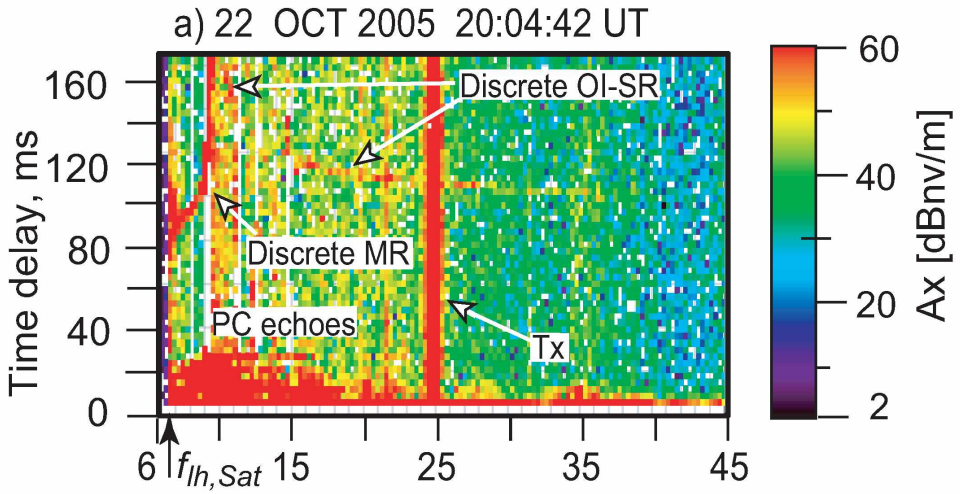

Figure 2.8. Discrete magnetospherically reflected (MR) and specularly reflected whistler-mode echoes received during soundings by RPI on 22 October, 2005 when the satellite was at ∼ 3400 km altitude, above $R_{flh,max1}$. [Adapted from Sonwalkar et al., 2011a.]

On 22 Oct 2005, from dynamic spectra (Figure 2.6) the plasmapause locations as estimated from f_{uh} measurements (dynamic spectra) are L=5.5 (day-side) L=4.5 (night-side); the plasma-

pause locations obtained from maximum K_P in the prior 24 hours are 3.76. When the echoes were observed, IMAGE was on $L = 2.13$ shell and thus well within the plasmasphere. Therefore, the plasmapause factor in the ray tracing density model is $N_{PL} = 1$. Furthermore, ray tracing analysis (time delay) is not sensitive to the precise values of lower ionosphere parameters H_{Bot} and r_0, which determine the scale size of electron density fall-off below the F2 peak and the level at which the electron density reduces to zero.

2.5.1.4 Initial guess for the ray tracing density model

Model-1 is the initial guess. The dipole field parameter $f_{ce,Eq} = 850$ kHz was obtained so that the model f_{ce} at the satellite matches that obtained from the IGRF model at the satellite location ($f_{ce,Sat} = 322$ kHz). We determine Model-1 parameters as follows: assuming a nominal value of 1000 km for r_b and roughly equal proportions of three ions at r_b ($\alpha_{H+} = \alpha_{He+} 0.3$, $\alpha_{O+} = 0.4$), choose N_b and T such that $f_{lh,Sat}$ and $f_{lh,max}$ calculated from the ray tracing density model lie, respectively, within the measured values $f_{lh,Sat} = 6.3 \pm 0.15$ kHz, and $f_{max,MR} = 9.3 \pm 0.15 kHz <$ $f_{lh,max1}$ and $f_{lh,max1} \gtrsim f_{min,SR} = 10.2 \pm 0.15 kHz$. The density model parameters of the initial guess are listed in Table 2.1 under Model-1. Figure 2.9a shows for Model-1 the ion and electron densities along $\mathbf{B_0}$ passing through IMAGE and Figure 2.9b shows the variation along $\mathbf{B_0}$ of f_{ce}, f_{pe}, m_{eff}, and f_{lh} (dotted curves). The black vertical lines near the satellite altitude (arrow near 3400 km) show the range of measured f_{lh}; the black vertical lines near 1300 km show the measured $f_{max,MR}$ and $f_{min,SR}$. The solid green circle in Figures 2.9a and 2.9b show f_{pe} obtained from dynamic spectra. The first column of Table 2.2 lists Model-1 plasma density and composition at certain key altitudes.

Using Model-1, ray tracing was carried at frequencies covering the range of observed MR and SR echoes. Rays are launched at various initial wave-normal angles, and, depending on the frequency, allowed to reflect magnetospherically or at the earth-ionosphere boundary at 90 km before returning to the satellite altitude of $\approx$ 3400 km. The returning ray passing through the satellite location is assumed to simulate the propagation of the observed echo (two closely spaced rays arriving on two sides of the satellite are used to estimate this ray). Figures 2.9c and 2.9d shows examples of MR and SR echo ray propagation paths. The dotted curves in Figures 2.9e and 2.9f show for Model-1 the calculated time delay as a function of frequency for MR and OI-SR echoes.

The measured time delay as a function of frequency is shown by red bars. The comparison of the calculated and the measured echo parameters shows: (1) the calculated time delays of MR echoes for $f < 9$ kHz are ~3–5 ms higher than those measured, (2) the calculated $f_{MR,max}$ agrees with the measured value within experimental uncertainty (yellow box in Figure 2.9c), and (3) the calculated time delays of OI-SR are $\sim 15-20$ ms smaller than those measured.

2.5.1.5 Iterative ray tracing density model

Model-2 is built so that SR echoes time delays are increased but MR echoes time delays are the same as before. In order to increase the calculated time delay for OI-SR echoes, the electron density at lower altitudes (around F2) is increased. This is where SR echoes collects a significant portion of its total time delay. At the same time, the density above $f_{lh,max1}$ altitude ($R_{lh,max1}$) is kept approximately the same as before so that the match between calculated and measured parameters for MR echo is not disturbed.

To increase N_e at lower altitudes and approximately keep same N_e above $R_{lh,max1}$, temperature T is decreased and N_b is increased such that N_e below r_b is increased (because of the reduced oxygen scale height) and N_e above r_b remains approximately the same. In fact, N_b is chosen so that the ray tracing model density at the satellite remains the same as before. The parameters of the new density model, Model-2, are listed in the second column of Table 2.1. The plasma density and composition at certain key altitudes are listed in the second column of Table 2.2. The electron and ion densities for Model-2 are shown by the dashed curves in Figure 2.9a, the characteristic plasma frequencies and m_{eff} by the dashed curved in Figure 2.9b. Ray tracings were performed with Model-2 to simulate MR- and OI-SR echo propagation. The calculated $t_g - f$ for the MR and OI-SR echoes are shown in Figure 2.9c and 2.9d, respectively, by dashed curves. Comparison of the calculated and measured echo parameters shows: (1) the calculated time delays of MR echoes for $f < 9$ kHz are still $\sim 3-5$ ms higher than those measured, (2) the calculated $f_{max,MR} = 9.6$ kHz is now greater than the measured $f_{max,MR} = 9.3 \pm 0.15$ kHz, (3) the calculated $t_g - f$ for OI-SR now match within 1–2 ms with those measured.

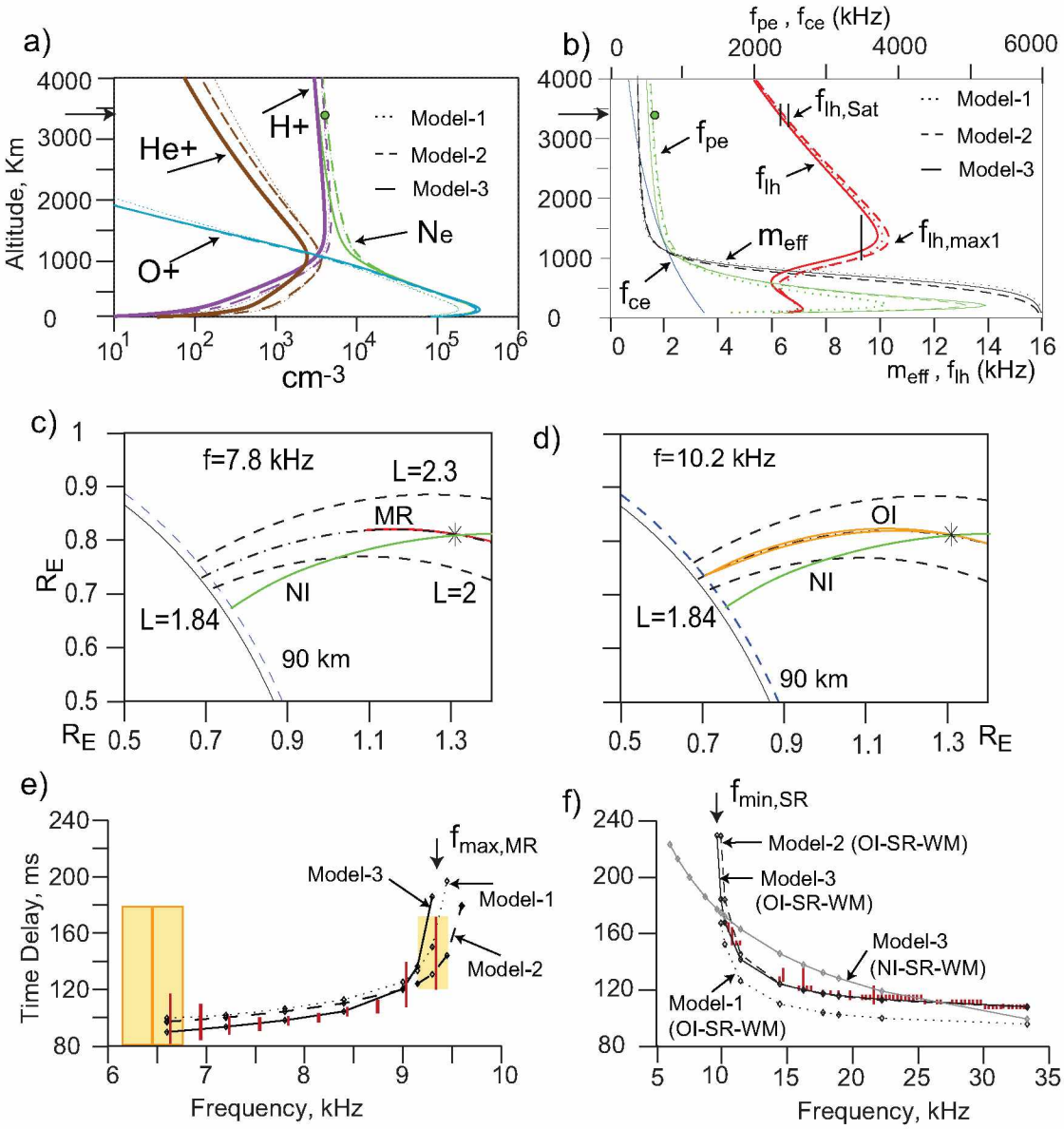

Figure 2.9. Results of ray tracing simulations performed to determine electron density and ion composition along $\mathbf{B_0}$ on 22 October 2005, 20:04:42 UT. (a) Density models along $\mathbf{B_0}$ through the satellite for electron, H^+, He^+, O^+. Models 1 (dotted) and 2 (dashed) are the trial models. Model-3 (solid) is the final model that gives agreement between ray tracing calculations and experimental measurements. The arrow on altitude axis indicates the satellite altitude. (b) Plasma parameters corresponding to three models shown in (a). The parallel vertical lines in black give the range of measured $f_{lh,Sat}$ and the $f_{MR,max}$. (c) Ray tracing examples illustrating ray paths for the MR and NI, and (d) OI and NI echoes. (e) and (f), respectively show comparison of the measured time delays (dark red) of MR echoes and SR with those calculated from ray tracing simulations for MR and OI echoes. In (e) the yellow area centered at 9.3 kHz is shown to indicate the associated uncertainty (0.3 kHz) with measured $f_{max,MR}$. The upper cutoff calculated from ray tracing falls into the yellow area for models 1 and 3 but not for Model-2. Shown in (f) are also the time delays calculated for NI echoes using Model-3. Complete agreement within experimental uncertainty is found between the measured time delays and those calculated for MR and OI echoes using Model-3.

Table 2.1. Ray tracing density model parameters for the case of 22 October 2005. Models 1-3 assume that magnetospheric plasma is composed of three ions. Model-4 assumes that the plasma is composed of two ions.

Parameter	Model-1	Model-2	Model-3	Model-4
$f_{ce,Eq}$	850	850	850	850
L_p	4	4	4	4
W_p	0.1	0.1	0.1	0.1
n	4.5	4.5	4.5	4.5
N_b	1.15×10^4	1.22×10^4	7895	1.57×10^4
r_b	1030	1030	1180	1130
T	1800	1600	1550	2250
$\alpha_{H+}(r_b)$	0.3	0.3	0.45	0.18
$\alpha_{He+}(r_b)$	0.3	0.3	0.3	0
$\alpha_{O+}(r_b)$	0.4	0.4	0.25	0.82
r_0	6420	6420	6420	6420
H_{Bot}	140	140	140	140

2.5.1.6 Final ray tracing density model that represents field-aligned electron density and ion composition on 22 October 2005

The density model is further modified so that calculated $t_g - f$ of OI echoes remain about the same as before, the calculated $t_g - f$ for MR echo is reduced by 3–5 ms, and the calculated $f_{MR,max}$ is reduced from 9.6 to 9.3 kHz. The density model modification required changing r_b, T, α_i, and N_b. The parameters of the new density model are listed under Model-3 in Table 1. The corresponding electron and ion densities are shown by the solid curves in Figure 2.9a, the characteristic plasma frequencies and m_{eff} by the solid curves in Figure 2.9b. Ray tracings were then performed with Model-3 to simulate MR and OI-SR echo propagation. The calculated $t_g - f$ for the MR and OI-SR echoes are shown in Figure 2.9c and 2.9d, respectively, by solid curves. There is now a complete match, within experimental uncertainties, between the calculated and measured MR and OI-SR echo parameters.

As discussed in the previous section, in general there are two possible SR echoes. For Model-3, time delays for NI-SR echoes are also calculated over a 6–33 kHz frequency range. The calculated time delays of NI-SR echoes are shown by the solid gray curve in Figure 2.9d. Comparing the measured SR echo trace time delays with calculated $t_g - f$ of NI-SR echoes, it is clear that the NI-

Table 2.2. Electron density, ion composition, m_{eff}, and f_{lh} at key altitudes obtained from ray tracing analysis

	Model-1 22Oct05	Model-2 22Oct05	Model-3 22Oct05	Model-4 22Oct05
Satellite Altitude (km)	3403	3403	3403	3403
Rbase (km)	1030	1030	1180	1130
Therm (K)	1800	1600	1550	2250
$N_{e,Sat}$(el cm^{-3} at satellite)	4233	4233	3420	4800
α_{H^+} (at satellite)	0.93	0.95	0.96	0.9997
α_{He^+} (at satellite)	0.07	0.05	0.04	0
α_{O^+} (at satellite)	3×10^{-6}	4×10^{-7}	5×10^{-7}	0.0003
M_{eff} (at satellite)	1.040	1.055	1.031	1.0002
$f_{lh,local}$ (kHz)	6.35	6.40	6.25	6.61
$f_{lh,max}$ altitude (km)	1338	1327	1374	1740
$f_{lh,max}$ (kHz)	10.08	10.32	9.90	10.05
N_e (el cm^{-3} at $f_{lh,max}$)	7869	8216	6399	6531
α_{H^+} (at $f_{lh,max}$)	0.56	0.56	0.63	0.837
α_{He^+} (at $f_{lh,max}$)	0.36	0.36	0.30	0
α_{O^+} (at $f_{lh,max}$)	0.08	0.08	0.07	0.163
M_{eff} (at $f_{lh,max}$)	1.529	1.519	1.394	1.18
Transition Height (km)	1070	1066	1108	1411
N_e (el cm^{-3}, at Transition Height)	1.08×10^4	1.14×10^4	8953	8930
α_{H^+} (at Transition Height)	0.34	0.34	0.36	0.5
α_{He^+} (at Transition Height)	0.32	0.32	0.28	0
α_{O^+} (at Transition Height)	0.34	0.34	0.36	0.5
M_{eff} (at Transition Height)	2.269	2.266	2.196	1.88
N_e (el cm^{-3}, 1000 km)	1.21×10^4	1.30×10^4	1.16×10^4	2.21×10^4
α_{H^+} (1000 km)	0.3	0.3	0.27	0.095
α_{He^+} (1000 km)	0.3	0.3	0.23	0
α_{O^+} (1000 km)	0.4	0.4	0.5	0.905
M_{eff} (1000 km)	2.268	2.5	3.05	6.6
N_e (el cm^{-3} at F_2 peak)	1.83×10^5	3.00×10^5	3.36×10^5	2.43×10^5
F_2 peak Altitude (km)	224	216	215	238
α_{H^+}(at F2)	1.2×10^{-3}	5.02×10^{-4}	2.27×10^{-4}	0.0008
α_{He^+} (at F2)	4.3×10^{-3}	2.2×10^{-3}	4.9×10^{-4}	0
α_{O^+} (at F2)	0.991	0.999	0.997	0.9992
N_e (el cm^{-3}, 90 km)	3.52×10^4	6.28×10^4	7.17×10^4	4.04×10^4
α_{H^+} (at 90 km)	3×10^{-4}	1.2×10^{-4}	7×10^{-5}	3×10^{-4}
α_{He^+} (at 90 km)	1.5×10^{-3}	7.1×10^{-4}	3.3×10^{-4}	0
α_{O^+} (at 90 km)	0.9982	0.9992	0.9996	0.9997

SR echoes were not observed on 22 October 2005. If observed, NI-SR echoes should have been be easily noticeable as WM echoes that have no low frequency cutoff and monotonically decreasing time delay. In the WM echoes observed from the transmission of pulses in program #38 format, we have not observed NI-SR echoes. Sonwalkar et al. [2011a] and [2011b] presented the reasons for not seeing NI echoes.

The ray tracing analysis of MR and SR echoes observed on 22 October 2005 shows that the measured parameters of MR and SR echoes are sensitive functions of both electron density and ion composition and that within experimental uncertainties and the limitations of the ray tracing density model electron, H^+, He^+, O^+ densities can be determined from the satellite altitude to the bottom of the ionosphere, including the F2 layer. A complete match between the calculated and measured WM echo parameters confirms our interpretation of MR and OI-SR echoes. We interpret the electron and ion densities represented by Model-3 to be those present on $\mathbf{B_0}$ passing through the satellite.

2.5.1.7 Whistler mode echo ray parameters at initial, reflection and arrival points

In addition to time delays, the ray-tracing simulations provide quantitative information on wave characteristics along the echo ray path including wave-normal angle, refractive index, wavelength, group velocity, amount of group delay accrued as a function of distance along the ray path, MR echo reflection altitude, f_{lh} at this altitude, and details of the magnetospheric and specular reflections. This information, coupled with the satellite motion and the transmission format, explains many features of the observed echoes.

The MR echo raytracings provided the following parameters. In each case the first number refers to 6.6 kHz and the second to 9.3 kHz. Tables A.1–A.3 in Appendix A, respectively, give the parameters at the initial, reflection, and arrival points at each frequency from MR echo ray tracings.

The initial wave normal angles of MR echoes were between 89.43° and 87.97°, which lay within 0.6° of the the resonance cone angles, between 89.56° and 88.56°, and beyond the Gendrin angles, between 89.00° and 87.11°. The corresponding refractive index values varied between 293.6 and 95.3. The refractive index values imply wavelengths of 155 and 338 m for the two frequencies, comparable to the length of the X-antenna. At the reflection points, $\theta = 90°$ and the refractive index values were between 310 and 148. The wave normal angles of the waves returning

to the satellite were between 89.42° and 87.94°, again close to the resonance cone angle. The refractive index values were between 290 and 93. Thus the wave normal angle remained large over the entire echo ray path. The ray direction w.r.to $\mathbf{B_0}$ was small within 0.3–0.9° indicating that the ray propagated close to the field line.

The MR echo ray path lay between 3130 and 1396 km altitude. The MR echo ray path loop is broadest at $f_{lh} = f$ altitude where the ray changes direction and starts moving towards $\mathbf{B_0}$. The lower cutoff, $f_{MR,min} = 6.6kHz$ was reflected at 3130 km where $f_{lh} = 6.75$ kHz altitude. The upper cutoff $f_{MR,max} = 9.3$ kHz was reflected at 1396 km where $f_{lh} = f_{lh,max1} = 9.9$ kHz altitude. The L-shell ranges covered varied between 2.131-2.130 (6.6 kHz) and 2.140–2.128 (9.3 kHz).

The group velocity for MR echoes increased with frequency at the initial point. For all frequencies, it decreased with altitude and was smallest near the reflection altitude. About half to two-thirds of the time delay is accumulated at altitudes where $f < f_{lh}$, that is over the part of the ray path where the refractive index surface is closed. During this part of the trajectory, the group velocity is the smallest. The total length of the ray path increases with frequency. This may explain the sharp rise in tg as frequency approaches $f_{MR,max}$.

The ray tracing analysis of OI-SR echoes in the frequency range 10.2–33.3 kHz observed on 22 October 2005 has provided the following echo parameters. In each case, the first number refers to 10.2 kHz and the second to 33.3 kHz. Tables A.4–A.7 in Appendix A give ray parameters for all frequencies at which raytracings were performed.

Initial wave normal angles of OI-SR echoes varied between 87.72° and 80.01°, which lay beyond the Gendrin angles varying between 86.63° and 76.64°, and within 1–3° of the the resonance cone angles varying between 88.32° and 83.37°. The refractive index values varied between 90 and 21, corresponding to wavelengths of 327 and 429 m, comparable to the length of the X-antenna. At the reflection point at 90 km, the incident wave normal angles varied between 89.6° and 88.4°. These wave normal angles lay outside the transmission cone angles for the WM waves at the earth-ionosphere boundary at 90 km; thus the incident waves were total internally reflected. The transmission cone angle measured with respect to $\mathbf{B_0}$ was between ~25.5° and 32.5°. At the reflection points, the refractive index values for the incident wave varied between 199 and 45, and $\mu \sin\delta$ values varied between 181 and 42, both values greater than unity. The wave normal direction of the reflected wave varied between 88.98 and 84.24 and the corresponding refractive index varied

between 202 and 49 The wave normal direction of the wave returning back to the satellite varied between 87.74° and 80.69°, again close to the resonance cone angle. The refractive index varied between 92 and 23, respectively, corresponding to wavelengths of 156 m and 346 m, again comparable to X-antenna length. Wave normal angles at the F2 layer for downgoing waves were between 86.13° and 65.07°, less than Gendrin angle between 89.28° and 86.89°. The wave normal angles at the F2 layer for up going waves were between 86.52° and 74.92°, again less than the Gendrin angle. The wave normal angles below the F2 layer were less than Gendrin angle throughout.

Ray paths of OI-SR echoes at all frequencies lay between the satellite altitude and 90 km, the specular reflection altitude. The broadest excursion in the L-shell range occurred near F2 altitude where the ray starts moving toward $\mathbf{B_0}$. The L-shell range covered varied between 2.148 to 2.124 for 10.2 kHz and between 2.252 to 2.110 for 33.3 kHz.

Group velocity of OI-SR echoes increased with frequency at the initial point. For frequencies close to $f_{lh,max1}$ ($\lesssim$ 15 kHz) a first minimum in group velocity occurred at $R_{flh,max1}$ and second minimum at F2 peak altitude. At higher frequencies the group velocity steadily decreased, reaching a minimum at the F2 peak where the density was greatest. The time delay accrued between the satellite and $f_{lh,max1}$ altitude was between 49.9 and 24.8 ms. Between $f_{lh,max1}$ and $F2$ peak altitude was between 29.3 and 25.1 ms. Below $F2$ peak altitude was between 12.9 and 8.0 ms. Note that for frequencies close to $f_{lh,max1}$, most of the time delay was accrued below $R_{flh,max1}$ altitude. This is to be expected because the ions significantly affect the WM refractive index surface at large wave normal angles for frequencies close to $f_{lh,max1}$.

As discussed earlier and as shown in Figure 2.9, it is possible to get NI-SR echoes that result from small initial wave normal angle. Though NI echoes were not observed on 22 Oct 2005, the ray tracing calculations of NI-SR echoes for the range of frequencies between 6.0 and 33.3 kHz have provided the following echo parameters. In each case the first number refers to 6.6 kHz and the second to 33.3 kHz. Tables A.7–A.11 in Appendix A give NI echo parameters at initial, reflection, and arrival points for all frequencies at which ray tracings were performed.

Initial wave normal angles varied between 21.92° and 21.20°. The refractive index surface is open with Gendrin angle ranging from 89.01 to 76.64° and resonance cone angle 89.56 to 83.37°, respectively, both much larger than the initial wave normal angles that led to NI-SR echoes. The refractive index values correspond to 12 and 6. These refractive index values imply wavelengths

of 3.8 km and 1.5 km, much larger than the length of the X-antenna. These echoes are reflected at 90 km, where we assume that the lower ionosphere has a sharp boundary. The wave normal angles continue to increase as the waves propagate downwards but remain small (less than Gendrin angle) throughout the WM echo propagation leading to NI-SR echoes. The wave normal angles near the reflection point are 29.00° and 28.18°. These wave normal angles lie inside the transmission cone angle for the WM waves at the earth-ionosphere boundary at 90 km and are thus partially reflected. The range of wave normal angles that lie within the transmission cone is between 26.5° and 32.5°. At the reflection points, the refractive index was 28 and 13 and $\mu \sin\delta = 0$ because of the vertical incidence. The wave normal angles of the waves returning to the satellite were 21.92 and 21.20, again relatively small compared to the resonance cone angles. The refractive index of the returning waves were 12 and 6.

The NI-SR echo ray paths at all frequencies lay between the satellite altitude and 90 km, the specular reflection altitude. At all frequencies the ray moved towards the lower L-shells. The satellite has moved 0.04 L-shells during the time elapsed between the transmission of 6 kHz and 33.3 kHz pulses. If we neglect the motion of the satellite, we note that the ray paths at all frequencies are almost identical. The L-shell range covered by 6.6 kHz is 2.13–1.84 and that by 33.3 kHz is 2.17–1.90.

The group velocity at the satellite increased with frequency and remained roughly the same up to ~1500 km. It then decreased with altitude reaching a minimum at F2 peak. Below F2 peak, group velocity increased up to the reflection altitude of 90 km. The time delay accrued between the satellite and $f_{lh,max1}$ altitude was between 35.0 and 25.4 ms, between $f_{lh,max1}$ and F2 peak altitude was between 42.1 and 24.3, and below F2 peak altitude was between 8.9 and 5.0 ms. In general, the parameters of NI-SR echoes are comparable to those determined in a similar ray tracing analysis of SR echoes observed on 05 May 2000 [Sonwalkar et al., 2004].

2.5.2 Comparison of WM sounding results with in situ measurements from other satellites and bottomside sounding results

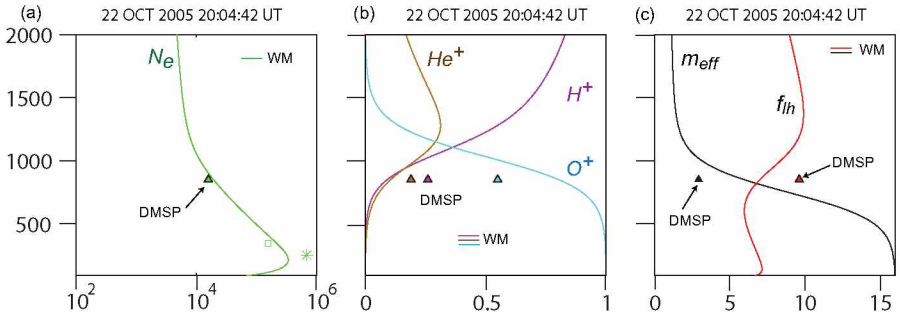

Figure 2.10. Comparison of WM sounding results with in situ measurements from the DMSP and CHAMP satellites, and bottomside sounding results from ionosondes. (a) Electron density. (b) Relative ion concentrations. (c) Lower hybrid frequency and effective ion mass

Whistler mode sounding results are in general agreement with those obtained from in situ measurements from the IMAGE, DMSP-F15, and CHAMP satellites. Relative to whistler mode sounding results, bottomside sounding results from nearby ionosondes overestimate electron density at F2 peak.

Figure 2.10 shows a comparison of whistler mode radio sounding results obtained for the 22 October 2005 case with those obtained from in situ measurements on the IMAGE, DMSP-F15, and CHAMP satellites and bottomside sounding results from nearby ionosonde stations.

For the 22 Oct 2005 case, the local plasma density calculated from upper hybrid emissions is $N_{e,Sat} \approx$ 4000-4200 el/cc, in good agreement with values 3420/cc and 4800/cc obtained from whistler mode radio sounding. The electron density and plasma frequency values for these cases are shown by solid green circles in Figures 2.9a and 2.9b.

The DMSP spacecraft are in circular polar orbits (fixed in local time) sampling the ionospheric plasma at about 850 km. The DMSP-F15 satellite is in a 0930–2130 local time orientation. The SSIES instruments onboard DMSP are used for the measurement of electron density and fractional ion composition [Rich and Hairston, 1994]. The Langmuir probe instrument on SSIES measures the electron density. The retarding potential analyzer (RPA) is used to measure fractional ion composition (H^+, He^+, O^+). For the case of 22 Oct 2005 at 19:52 UT the DMSP-F15 satellite was at MLT = 8.8 (IMAGE MLT = 11.2) and was on the same L-shell as that of IMAGE. The values of the plasma parameters obtained from the DMSP satellite are shown by color coded triangles

in Figure 2.10. Model-3 results are in good agreement with DMSP F-15 measurements. Near simultaneous measurements of in situ ion composition can be used as additional constraints in the WM sounding method.

The CHAMP satellite is in circular near-polar orbit(87° inclination) sampling the ionospheric plasma at ~350 km. The Planar Langmuir Probe instrument onboard CHAMP is used to measure electron density [Cooke et al., 2003; McNamara et al., 2007]. For the 22 October 2005 case, at 20:58 UT the CHAMP satellite was at L=2.31, within 0.2 L-shells of IMAGE and at MLT = 18.8 (IMAGE MLT = 11.2). Electron density obtained from the CHAMP satellite is shown by the green square in Figure 2.10. The values of the plasma density obtained from the CHAMP satellite also show good agreement with sounding results for the 22 October 2005 case.

For the 22 October 2005 case, the footprint of the field line ($\mathbf{B_0}$) passing through IMAGE (L=2.13, MLT =11.2) was in the North Pacific Ocean (Geographic latitude = 41.6°; Geographic longitude = 232.4°). The closest ionosonde station to this location was at Boulder ($\lambda_g = 40°$, $\phi_g = 254.7°$) at L=2.25 and at a distance of 1880 km from the footprint of $\mathbf{B_0}$. The electron density at the F2 peak obtained from the ionosonde is shown by the star in Figure 2.10. The electron density at the F2 peak obtained from bottom side sounding [Reinisch et al., 2004] is about 3 times greater than those obtained from WM sounding.

When MR echoes are not accompanied by SR echoes and vice versa, near simultaneous measurements from DMSP and CHAMP data could be used to augment WM sounding results. This augmentation of WM sounding results is discussed in sections 2.5.6 and 2.5.7.

2.5.3 Uncertainty in the measurement of electron density and effective ion mass resulting from the assumption of number of ion species in the density model

As noted earlier, radio sounding is an ill-posed problem because it involves integral equations and hence does not have a unique solution. The problem is turned into a well-posed problem by assuming a parametric model, in this case a ray tracing density model, for the medium density and composition. In the earlier subsection plasma was assumed to be composed of three ions (H^+, He^+, and O^+). However, plasma can be composed of two or more than three ions. The assumption of number of ions will lead to a different solution or different density model that will explain the observed features of WM echoes.

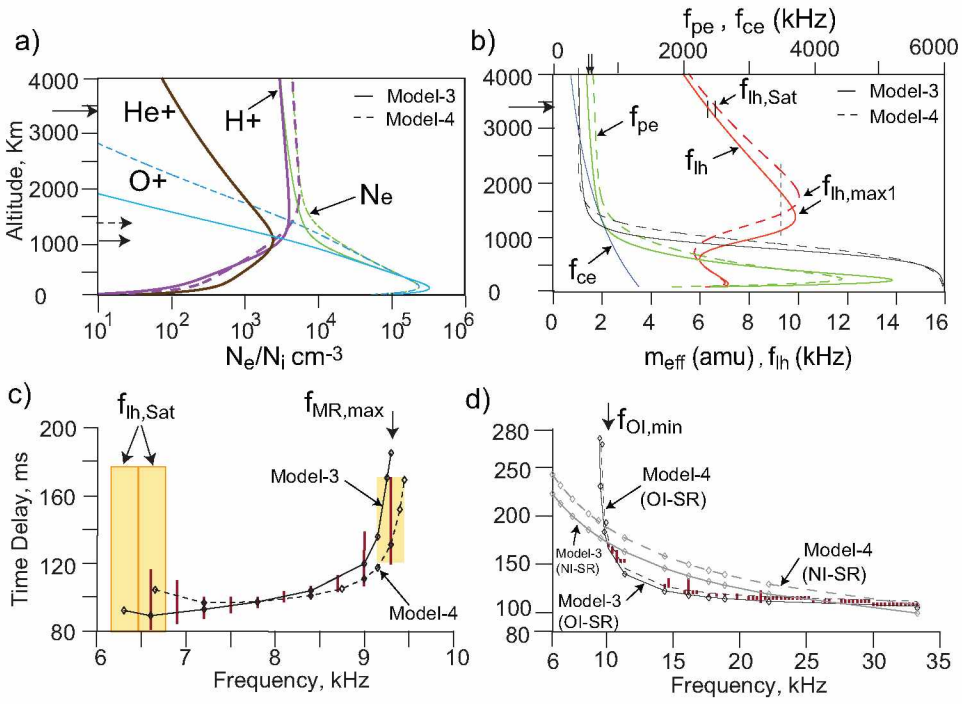

Figure 2.11. Results of ray tracing simulations performed to determine field aligned electron density and ion composition on 22 October 2005, 20:04:42 UT. Simulations are performed for two different models, one assuming that magnetospheric plasma is composed of three ions and the other assuming that plasma is composed of two ions. (a) Density models along $\mathbf{B_0}$ through the satellite for electron (green), H^+ (pink), He^+ (brown), O^+ (cyan). Model-4 (dashed) is a two ion model and Model-3 (solid) is a three ion model. Both Models 3 and 4 give agreement between the ray tracing simulation results and experimental measurement. The arrow on altitude axis indicates the satellite altitude. (b) Plasma parameters corresponding to the two models shown in (a). The parallel vertical lines in black give the range of measured f_{lh} at the satellite altitude, and $f_{MR,max}$ is greater than the upper cutoff of MR echo. (c) Comparison of measured time delays (dark red) of MR echoes with those calculated from ray tracing simulations for Model-3 (solid) and Model-4 (dashed). The yellow area centered at 6.3 and 6.6 kHz is shown to indicate the $f_{lh,Sat} \backsimeq f_{MR,min}$ and the associated uncertainty (0.6 khz). The yellow area centered at 9.3 kHz is shown to indicate the maximum measured frequency ($f_{MR,max}$ indicated by arrow) and the associated uncertainty (0.3 kHz). The lower and upper cutoffs of MR echo calculated from ray tracing falls into the yellow area for both Model-3 and Model-4. (d) Comparison of measured time delays (dark red) of OI echoes with those calculated for OI echoes from ray tracing simulations for Model-3 (solid) and Model-4 (dashed). Also shown are time delays calculated for NI echoes using Models 1 and 2 (gray curves). Complete agreement within experimental uncertainty is found between the measured time delays and those calculated for MR and OI echoes using Models 3 and 4.

Applying the iterative procedure discussed in subsection 2.5.1.3, a two ion density model (H^+ and O^+) that satisfies MR and SR echo dispersion and cutoffs was obtained. The ray tracing density model parameters of this two ion density model (Model-4) are shown in Table 1 column 4. The values of the key plasma parameters as a function of altitude are given in Table 2 column 4. By dashed curves and solid curves, respectively, Figure 2.11(a) shows the plot of electron and ion densities along $\mathbf{B_0}$ for a two ion model (Model-4) as well as a three ion model (Model-3). The arrow on the altitude axis at $\sim$ 3400 km indicates the satellite altitude. The dashed and solid arrows on the altitude axis between $\sim$1000 and 1500 km indicate the $O^+ - H^+$ transition height for Model-3 and Model-4. The characteristic plasma frequencies and m_{eff} for Model-3 and Model-4 are shown in Figure 2.11(b). Ray paths similar to those shown in Figures 2.9c and 2.9d were obtained. Note from Figures 2.9(c) and 2.9(d) that MR and OI echoes are close to the field line, whereas, the NI echo deviates up to 0.3L from the field line. The calculated time delays as a function of frequency for the MR, OI-SR echoes for both models are shown in Figure 2.11(c) and Figure 2.11(d), respectively. The calculated time delays of OI echoes using Model-3 and Model-4 differ by $\sim$ 3 -5 ms in the frequency range 10.2–33.3 kHz, but they are shown slightly more displaced in Figure 2.11(d) for convenience.

From Figures 2.11a and 2.11b and Table 2, clearly that Models 3 and 4 are sufficiently distinct. At the satellite the N_e obtained from Model-4 (4800 el/cc) is $\sim$1.4 times that obtained from Model-3 (3400 el/cc), and at the F2 peak, N_e obtained from Model-3 (2.43×10^5 (238 km)) is $\sim$1.4 times that obtained from Model-4 (3.36×10^5(215 km)). The m_{eff} obtained at the satellite is 1.031 and 1.0002 for Model-3 and Model-4, respectively. The value of $f_{lh,Sat}$ that is related to N_e and m_{eff} is found to be 6.25 kHz for Model-3 and 6.61 kHz for Model-4. The altitude at which m_{eff} rapidly starts changing from low to high values could be described by O-H transition height. The transition height is found to be 1108 km and 1411 km for Model 3 and 4 respectively. Other altitude that is related to the O-H transition height is $R_{flh,max1}$. The maximum in f_{lh} along $\mathbf{B_0}$ is found to be 10.05 and 9.9 kHz, and $R_{flhmax1}$ is 1740 and 1374 km for Model-4 and Model-3, respectively.

Although the raytracing calculations for Models 3 and 4 agree within the experimental limits, note that the answers are not the same. For example, the upper cutoff of MR echo is 9.3 khz for Model-3 and 9.45 kHz for Model-4. The lower cutoff of OI is 9.55 kHz for Model-3 and 9.63 kHz for Model-4. This lower cutoff cannot be discriminated within the 300 Hz boundary. Moreover,

the time delay generated by the OI echo at this frequency exceeds the time delay allowed by the experiment. But it is conceivable that experimental conditions may be different.

As noted earlier, NI echoes were not observed on this day. But in principle, three WM echoes, MR, OI, and NI, are predicted for smooth magnetosphere when the satellite is above or below $R_{flhmax1}$ altitude, except when the satellite is close to the F2 peak ($\sim$ 300 km). The NI echo time delays were calculated for the two models 3 and 4 over the 6–33 kHz frequency range. Figure 2.11(d) shows the time delays calculated for NI echoes (grey curves) for Model-3 (solid) and Model-4 (dashed). From Figure 2.11(d) it can be seen that although both t_g calculated for MR and OI echoes from Model-3 and Model-4 fit with the experimental data, these two models give different time delays for the NI echoes. The difference in the time delays for NI echoes calculated from Model-3 and Model-4 is $\sim$ 20 ms. Had NI echoes been observed with a time delay spread at each frequency less than 20 ms, to choose between the two models we could have used the measured t_g of these two NI echoes.

The reason the time delays for MR and OI echoes are the same for the two models within experimental constraints but are quite different for NI (as much as 20 ms) is that the ray paths are different and the way the time delays are accrued by these three echoes is different. Consider the time delays accrued by MR echoes in Model-3 and Model-4; In Model-3, $R_{flhmax1}$ is lower than that of Model-4, which implies that the echo path length is larger and hence the time delay collected should be more. But this expected increase in time delay is compensated by a lower value of electron density along the ray path. Similarly, Model-4 $R_{flhmax1}$ is higher, which implies the echo path length is smaller, but the electron density is greater compared to that of Model-3, so they compensate each other. The same thing is true for OI echoes. For Model-4 more t_g is collected at higher altitude; in the other case more tg is collected at lower altitude. This explains how these two different models can fit the observed MR and OI echoes.

The NI echo that is generated at small WN angle and traverses a different path ($\sim$ 0.3L away) than those of MR and OI echoes accrues relatively more time delay at lower altitude near F2 peak. The larger time delays collected by the echo because of greater electron density at higher altitudes in Model-2 could not be compensated by the smaller electron density at lower altitude near F2 peak. So although the t_g for MR and OI could be same for the two models, time delays are not the same for the NI. Also note that the NI time delays vary smoothly and monotonically from

frequencies below $f_{lh,max1}$ to above $f_{lh,max1}$. This is because for small wave normal angles the refractive index does not depend on m_{eff} and thus on f_{lh} (see Appendix-B of Sonwalkar et al. [2011b] for details).

The results from the above example indicate that WM radio sounding can provide a unique set of density parameters if all three (MR, OI, and NI) WM echoes were observed and time delay spread at each frequency is small enough (i.e., they are discrete echoes). But, as noted in Sonwalkar et al. [2011a], there are only two observations of three echoes occurring simultaneously. The reasons for this are discussed in Sonwalkar et al. [2011a]. When only two echoes (MR and OI/NI) are observed, this example shows that there can be a different set of electron density and ion effective mass models that will explain the observed WM echo features.

One way to estimate the accuracy of the measured plasma parameters is by comparing all the models considered here for ray tracing analysis. Table 2 shows the electron density, ion composition, m_{eff}, and f_{lh} at certain key altitudes for all four ray tracing models. Because parameters, such as r_b, T, N_b, α_i are different for each model, all four models can be compared at 1000 km to determine the uncertainty in the measured parameters. Note that Model-1 and Model-2 do not provide a complete match between measured and calculated parameters. Model-4 is not realistic since it is known that He^+ is present in the region of interest. Given that only Model-3 provides a complete match between observed and calculated parameters, it can be stated that N_e within $\sim$10-15%, α_{H^+} within 10%, α_{He^+} within 25%, α_{O^+} within 20%, and transition height within 15% have been determined.

2.5.4 Uncertainty in the measurement of ion composition

In this subsection we discuss the uncertainty resulting from the nature of the dependance of whistler mode propagation on ion composition. Despite assuming a parametric model of density and composition (e.g., ray tracing density model), whistler mode radio sounding in the frequency range $f_{ci} << f$ fundamentally limited for determination of ion composition when there are more than two ions. As shown in Appendix B of Sonwalkar et al. [2011b] this limitation is a consequence of the fact that the expression for the whistler mode refractive index depends on f_{pe}, f_{ce}, and m_{eff}, but not on the details of the ion composition. Thus, while WM sounding provides remote sensing of f_{pe} and m_{eff} along the field line, additional assumptions are needed to determine ion composition.

If we assume only H^+ and O^+ ions to be present in the magnetosphere, then we can determine the individual ion densities from the measurement of m_{eff} and Equations (2) and (3).

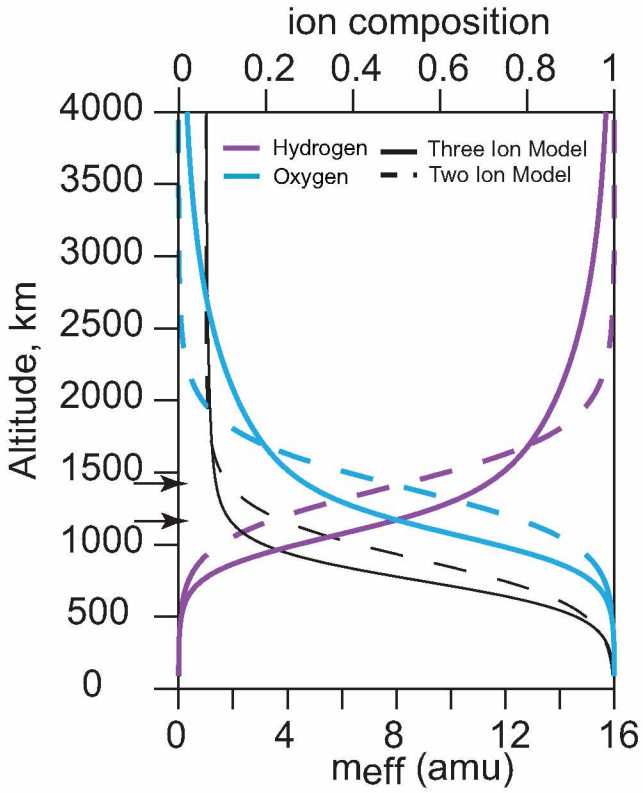

Figure 2.12. Effective ion mass obtained from Model-3 (three ion model) and Model-4 (two ion model). Also shown in the figure are unique values of O^+ and H^+ calculated using the m_{eff} obtained from Model-3 and Model-4 and assuming that magnetospheric plasma is composed of only two ions.

Figure 2.12 shows that if we assume only two ion species, then from the m_{eff} obtained from Model-3 (three ion model) and Model-4 (2 ion model) we get unique values for O^+ and H^+ with each model. Note here that the values of H^+ and O^+ obtained from Model-4 (shown in Figure 2.12) are the same as those shown in Figure 2.11, but the values of H^+ and O^+ obtained from the m_{eff} of Model-3 (shown in Figure 2.12) are different from the values of H^+ and O^+ shown in Figure 2.9. This is because the values of H^+ and O^+ shown in Figure 2.9 are obtained under the assumption of a three ion model, whereas the values shown in Figure 2.11 are obtained using the same m_{eff} of Model-3 but assuming only two ions. These values are calculated using Equations (2.2) and (2.3) and substituting 0 for He^+. The O^+/H^+ transition height from Model-3 is $\sim$1200 and that from Model-4 is $\sim$ 1400. The values of H^+ and O^+ obtained from Model-3 (shown in

Figure 2.12) cannot be obtained within the limitations of ray tracing density parameters. But, such a density model will give us the same solution.

If it is considered that three ion species are present in the magnetosphere, Equations (2.2) and (2.3) are not sufficient to determine the individual densities (or fractional abundances) from the measured m_{eff}. The m_{eff} as calculated from Model-3 and Model-4 gives the range of uncertainties in the measurement of ion composition that are possible in principle based on equations (2.2) and (2.3). The resulting uncertainty places limits on the maximum and minimum fractional abundances of each species. Figure 2.13 shows this uncertainty for the possible range of fractional abundances for H^+, He^+, and O^+ assuming the values of m_{eff} obtained from Model-3 (Figure 2.13a) and Model-4 (Figure 2.13b) above. The uncertainty is smallest for H^+ and greatest for He^+.

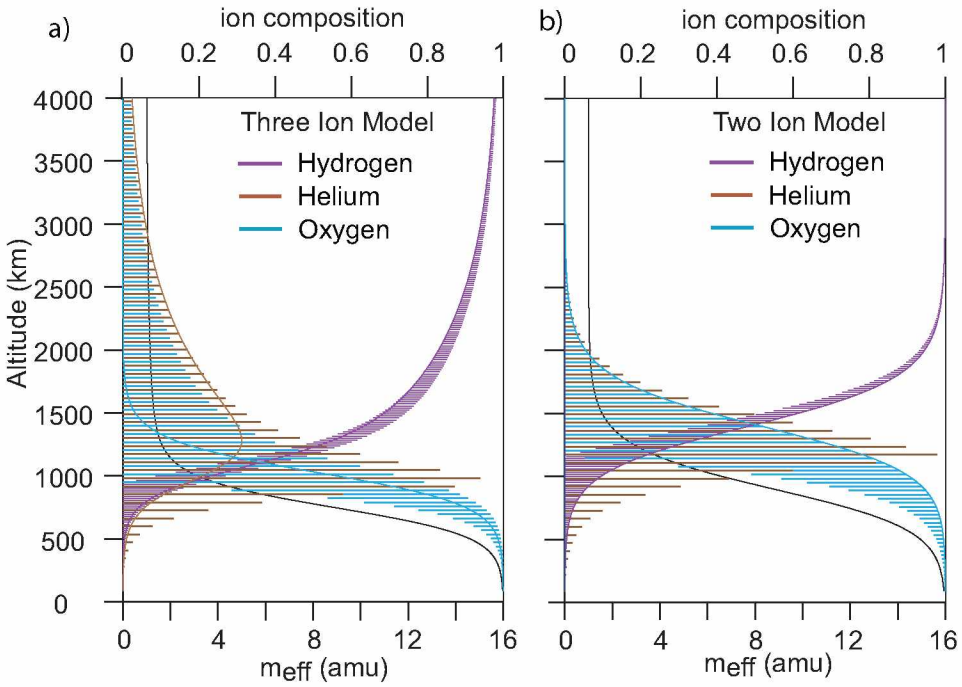

Figure 2.13. Uncertainty in the measurement of relative ion compositions assuming that the magnetospheric plasma is composed of three ions. (a) and (b), respectively, show the uncertainty for the possible range of fractional abundances for H^+, He^+, and O^+ assuming the values of m_{eff} obtained from Model-3 and Model-4

2.5.5 Remote sensing of small scale field-aligned irregularities

The magnetosphere is a highly structured and dynamic system. Field-aligned irregularities of scale sizes from meters to hundreds of kilometers in the direction perpendicular to the geomagnetic field are present in all parts of the magnetosphere [Fejer and Kelley, 1980; Carpenter et al., 2002; Hunsucker and Hargreaves, 2003]. Plasma density and density structures are believed to play an important role in many physical processes at low and high latitudes. In a recent review, Sonwalkar [2006] described how whistler mode waves, both natural in origin and manmade, are profoundly affected by FAIs of scale sizes from meters to tens of kilometers.

This thesis, Figures 2.3 and 2.4, Sonwalkar et al. [2011a] and Sonwalkar et al. [2004] have given many examples of WM echoes whose characteristics are dramatically changed by the presence of FAIs on their propagation paths from IMAGE and back again. FAIs affect propagation of WM signals transmitted by the RPI in a fundamental manner: they modify the accessibility of WM ray paths to different regions of the magnetosphere. This has several consequences: (1) Generation of multipath and diffuse echoes depending on if multiple path propagation resulted from mild refraction of waves by large scale irregularities or resulted from scattering of waves by small scale FAI, (2) Generation of echoes at certain frequencies that in a smooth magnetosphere would not result (bending or rays such that paths return to the satellite). (3) Absence of echoes at all or some (e.g., patchy echoes) of the transmitted frequencies; these echoes would be obtained in a smooth magnetosphere (in the absence of FAIs). (4) Generation of forward scattered echoes that have undergone MR or SR reflections. (5) Generation of back scattered echoes which do not involve reflections. The observed dispersion of echoes is so different from any of the standard echo types, that they cannot be conceived as mere modifications of those types (MR or SR) of echoes. These echoes start with minimum time delays or often do not show a sharp cutoff (for MR) and can be best interpreted as scattering of RPI signal by FAIs close to the satellite.

Sonwalkar et al. [2011b] provides a method to estimate scale sizes of FAIs from the spread in time delays. Application of this method to multipath and diffuse echoes may provide (1) better ways to identify and classify effects of large scale (refraction) and small scale (scattering) FAIs and (2) better ways to determine the distribution of FAI in space and time.

2.5.6 Augmentation of whistler mode sounding results below $f_{lh,max1}$ altitude when only MR echo is observed: 07 September 2005 case

As discussed earlier, when MR echo is observed but not SR echo, plasma density and composition can only be measured from satellite altitude down to $R_{flh,max1}$ ($\sim$ 1500 km). Many ray tracing density models that are significantly different from one another below the $R_{flh,max1}$ could explain MR echo dispersion and cutoffs. For example, in the 22 October 2005 case, if it is assumed that SR echo was not observed, then from Figure 2.9c both Model-1 and Model-3 can explain observed MR time delays. However, the N_e at F2 peak from Model-3 is about twice that from Model-1. In such a case, when only MR echoes were observed, WM sounding results can be augmented with near simultaneous in situ measurements from other satellites and/or bottomside sounding results to determine plasma density below $R_{flh,max1}$ altitude.

Figure 2.14 shows results of ray tracing simulations augmented by DMSP and CHAMP satellite measurements to determine N_e and N_i along $\mathbf{B_0}$ on 07 September 2005, 04:14 UT. Figure 2.14a shows the MR echo, from 6.6–9.6 kHz, observed on 07 September 2005 at 04:14 UT. No SR echo was observed at this time. Using the procedure outlined in subsection 2.5.1.3 a ray tracing density model can be obtained that will explain the observed MR time delays and cutoffs.

For the 07 September 2005 case, at 04:45 UT the DMSP-F13 satellite was at MLT = 17.5 (IMAGE MLT = 14.2) and was on the same L-shell as that of IMAGE. At 04:24 UT, the CHAMP satellite was on the same L-shell as that of IMAGE and at MLT = 11.0 (IMAGE MLT = 14.2). The closest ionosonde station to the footprint of $\mathbf{B_0}$ through IMAGE was at Petropavlovsk ($\lambda_g = 53^\circ$, $\phi_g = 158.7^\circ$) at L=2.06. The station is at a distance of of 471 km from the footprint of $\mathbf{B_0}$ through IMAGE. Earlier work by Sonwalkar et al. [2014a] found that relative to WM sounding results, the F2 peak obtained from ionosondes is almost always greater. Therefore, in the 07 Sep 2005 case, the density model that explains MR echo time delays and cutoffs is further adjusted so that N_e above $R_{flh,max1}$ remains about the same, but N_e below $R_{flhmax1}$ agrees within 20% of plasma density obtained from DMSP and CHAMP satellites.

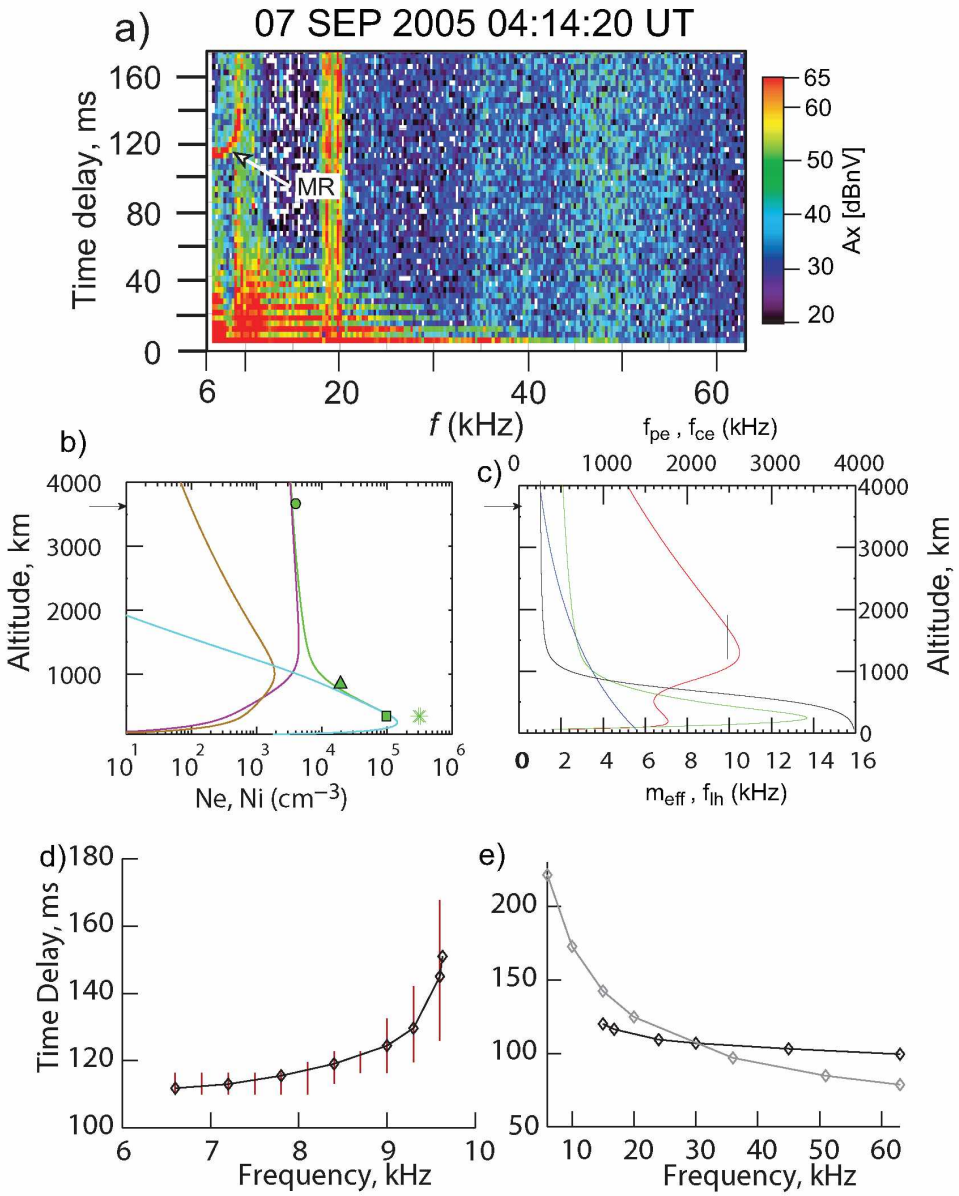

Figure 2.14. Results of ray tracing calculations augmented by the DMSP and CHAMP satellite measurements to determine electron density and ion composition along $\mathbf{B_0}$ on 07 September 2005 at 04:14 UT. (a) Plasmagram showing MR-WM echo observed by RPI. (b) Field-aligned electron (green) and H^+ (pink), He^+ (brown), and O^+ (cyan) ion densities. (c) Plasma parameters corresponding to the model shown in (a): plasma frequency f_{pe} (green), gyrofrequency f_{ce} (blue), effective ion mass m_{eff} (black), lower hybrid frequency f_{lh} (red). The black dashed vertical dashed line shows the measured upper cutoff of the MR echo $f_{MR,max} < f_{lh,max1}$. The solid green circles in (a) and (b), respectively, shows the in situ electron density and plasma frequency obtained from RPI passive recordings. (d) Comparison of the measured time delays (dark red) of the MR echoes with those from the ray tracing calculations (black curve) using the model shown in (a). (e) Calculated time delays for OI (black curve) and NI echoes (gray curve) using the density model shown in (a).

Figures 2.14(b) and 2.14(c), respectively, show the resulting density model and the characteristic plasma frequencies as a function of altitude along the field line passing through IMAGE. Electron density obtained from the DMSP satellite is shown by the green triangle, and that obtained from the CHAMP satellite is shown by the green square in Figure 2.14(b). The electron density at F2 peak from the ionosonde, shown by a star in Figure 2.14(b), is about two times that obtained from WM sounding results augmented by DMSP and CHAMP measurements. The green circle near the satellite altitude in Figure 2.14(b) shows the in situ electron density deduced from the upper hybrid frequency emissions seen at a nearby time. In general, raypaths similar to those shown in Figure 2.9(c) are obtained for the MR echoes. The black curve in Figure 2.14d shows the calculated time delays for simulated MR echoes, the black curve in Figure 2.14(e), the time delays for the simulated OI echo (not observed), and the gray curve in Figure 2.14(e) shows the time delays for an NI echo (not observed). The time delays calculated at specific frequencies are shown by black diamonds. The red vertical bars give the range of the measured time delays for each transmitted frequency at which an echo was observed.

This example demonstrates that WM sounding results augmented by near simultaneous in situ measurement from other satellites and/or bottomside sounding results provide field-aligned plasma density and/or composition measurements from satellite altitude down to 90 km. Chapter 3 of this thesis presents variations of plasma density and composition during storm time. Most of the cases observed during storm time are MR. The approach discussed in this subsection is used to determine field-aligned plasma density and composition and to study their variation.

2.5.7 Determination of field-aligned electron density when only SR echo is observed: 14 September 2005 case

When SR echoes are observed without MR echoes, many ray tracing density models that are significantly different from one another could in principle explain observed SR echo time delays [Li, 2004]. For example, in the 22 October 2005 case, if it is assumed that MR echo was not observed then both Models-2 and Model-3 can explain observed SR time delays (see Figure 2.9(e)). The N_e from these two models is different by $\sim$10–20%. Note that in 22 October 2005 case, N_e at the satellite altitude was constrained so that it agrees with measured f_{lh}. When only SR echoes are observed, there will be more flexibility to choose N_e at the satellite altitude as will be no constraints

on local f_{lh}. Li [2004] has studied various density models that explain observed SR dispersion. He found that the models could be different by as much as 50%. In cases where only SR echoes are observed, WM sounding results can be augmented with near simultaneous in situ measurements from other satellites, and/or bottomside sounding results. The in situ measurements from other satellites, and/or bottomside sounding results can be used to put constraint on the density model that can explain the observed SR echo dispersion.

Figure 2.15 shows results of ray tracing simulations augmented by the DMSP and CHAMP satellite measurements to determine field-aligned N_e on 14 September 2005, 07:08 UT. The SR echo, from ~15-60 kHz, observed on 14 September 2005 at 07:08 UT is shown in Figure 15a. No MR echo was observed. Using the procedure outlined in subsection 2.5.1.3, a ray tracing density model that can explain the observed SR time delays is obtained.

In the 14 Sep Oct 2005 case, at 08:10 UT the DMSP-F13 satellite was at MLT = 17.74 (IMAGE MLT = 14) and was on the same L-shell as that of IMAGE. At 07:28 UT, the CHAMP satellite was on the same L-shell as that of IMAGE and at MLT = 11.0 (IMAGE MLT = 14). The closest ionosonde station to the footprint of the field line passing through IMAGE was Pruhonice ($\lambda_g = 50^\circ$, $\phi_g = 14.6^\circ$) at L=2.38 and at a distance of ~5200 km. Sonwalkar et al. [2014a] found that relative to WM sounding results, the N_e at the F2 peak obtained from ionosondes was almost always greater. Therefore, in the 14 September 2005 case, the density model that explains SR dispersion is further adjusted so that N_e at ~ 850 km and ~300 km, respectively, is within ~20% of that measured by DMSP and CHAMP satellites. Figures 2.15(b) and 2.15(c), respectively, show the resulting density model and the characteristic plasma frequencies as a function of altitude along the field line passing through IMAGE. Electron density obtained from the DMSP satellite is shown by a green triangle, and that obtained from the CHAMP satellite is shown by a green square in Figure 2.15(b). The electron density at the F2 peak from the ionosonde, shown by a star in Figure 2.15(b), is within 20% of that obtained from WM sounding results augmented by DMSP and CHAMP measurements.

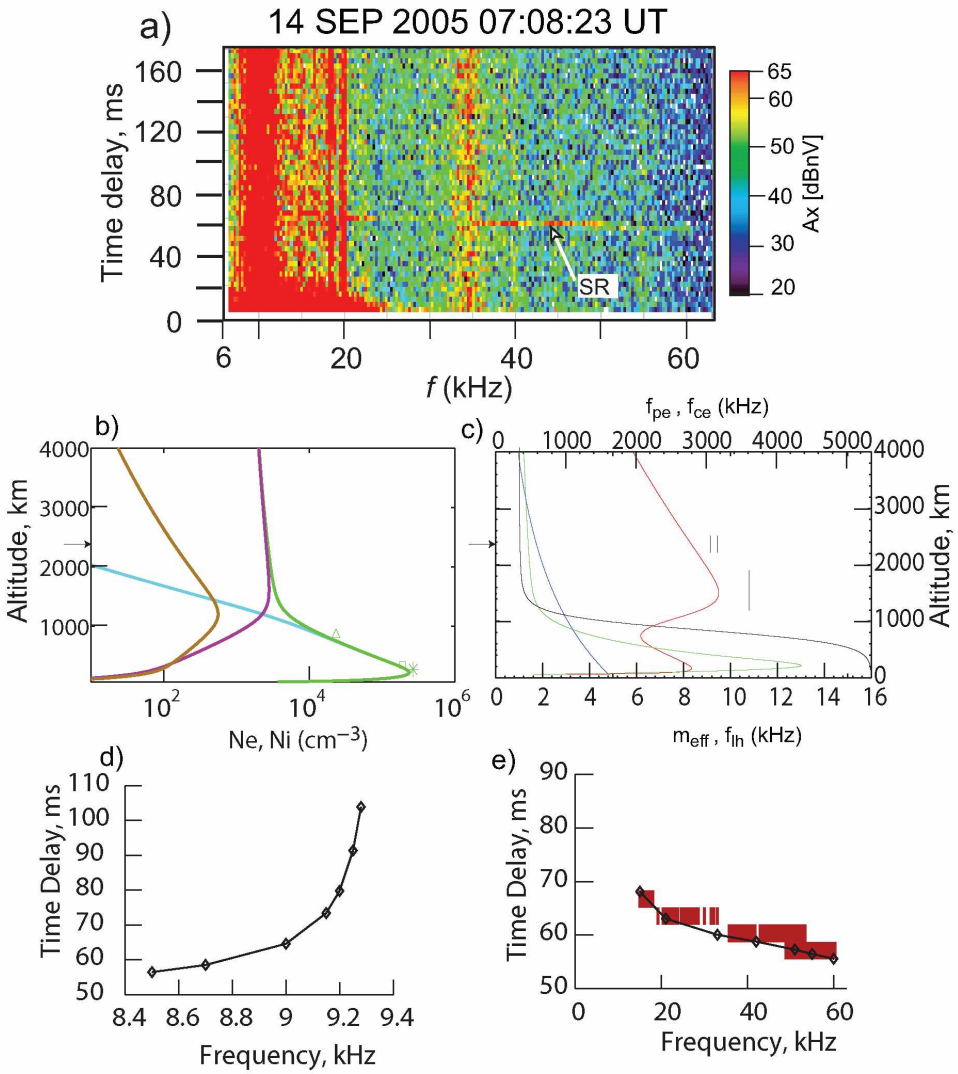

Figure 2.15. Results of ray tracing calculations augmented by DMSP and CHAMP satellite measurements to determine electron density along $\mathbf{B_0}$ on 14 September 2005 at 07:08 UT. (a) Plasmagram showing SR-WM echo observed by RPI. (b) Electron (green) and H^+ (pink), He^+ (brown), and O^+ (cyan) ion densities along $\mathbf{B_0}$ through the satellite. (c) Plasma parameters corresponding to the model shown in (a): plasma frequency f_{pe} (green), gyro frequency f_{ce} (blue), effective ion mass m_{eff} (black), lower hybrid frequency f_{lh} (red). (d) Comparison of the measured time delays (dark red) of the MR echoes with those from the ray tracing calculations (black curve) using the model shown in (a). (e) Calculated time delays for OI (black curve) and NI echoes (gray curve) using the density model shown in (a).

2.5.8 Application of whistler mode sounding method for selected cases: 06 October 2005 and 02 September 2005

Whistler mode radio sounding technique was applied to two cases, one observed during quiet geomagnetic conditions, the other during disturbed geomagnetic conditions. In both cases MR and OI echoes were observed.

Figures 2.16 and 2.17, respectively, show results of ray tracing simulations performed to obtain electron densities for the 06 October 2005 05:40 UT case, a quiet day, and for 02 September 2005 10:25 UT case, a disturbed day. Figure 2.16(a) shows a plasmagram displaying MR (in the frequency range 8.4–10.5 kHz) and SR (frequency range 41.1–54.9 kHz) echoes. The maximum Kp in the past 24 hours was 1.33, indicating very low geomagnetic activity. Figure 2.17(a1) shows a plasmagram displaying MR (in the frequency range 6.6–8.4 kHz) and Figure 2.17(a2) shows a plasmagram displaying SR (frequency range 26.4–37.5 kHz) echoes. There was a major storm on the night of 31 August 2005 (Dst=-128 nT Kp=7). This 02 September 2005 1025 UT case was observed during the 31 August 2005 storm recovery phase.

For both 06 October and 02 September cases two density models one assuming that the plasma is composed of 2 ions and the other assuming three ions that explain observed dispersion cutoffs of WM echoes were obtained. Figures 2.16(b), 2.16(c) and 2.17(b), 2.17(c), respectively, show the resulting density model and the characteristic plasma frequencies as a function of altitude along the field line passing through IMAGE for the 06 October 2005 and 02 September 2005 cases. Solid curves indicate densities and plasma parameters obtained assuming a three ion model. Dashed curves are used for the two ion model. In the 02 September 2005 case, upper hybrid frequency emissions were available. The electron density calculated from these emissions is shown by a green circle in Figure 2.17(c). Also shown in Figures 2.16(c) and 2.17(c) are in situ electron density obtained from DMSP ($\sim$850 km, triangle) and CHAMP satellites ($\sim$350 km, square) and N_e at F2 peak obtained from nearby ionosonde stations (station name=Novosibirsk L-shell=2.05 and station name=Rostov at L=1.85) by a star. In general, ray paths similar to those shown in Figures 2.9(c) and 2.9(d) were obtained for the MR and OI echoes. The red vertical bars in Figures 2.16(d) and 2.17(d) give the range of the measured time delays for transmitted frequency at which an echo was observed. The black curve in Figure 2.16(d) and 2.17(d) shows the calculated time delays for simulated MR echoes. The black curve in Figures 2.16(e) and 2.17(e) shows the time

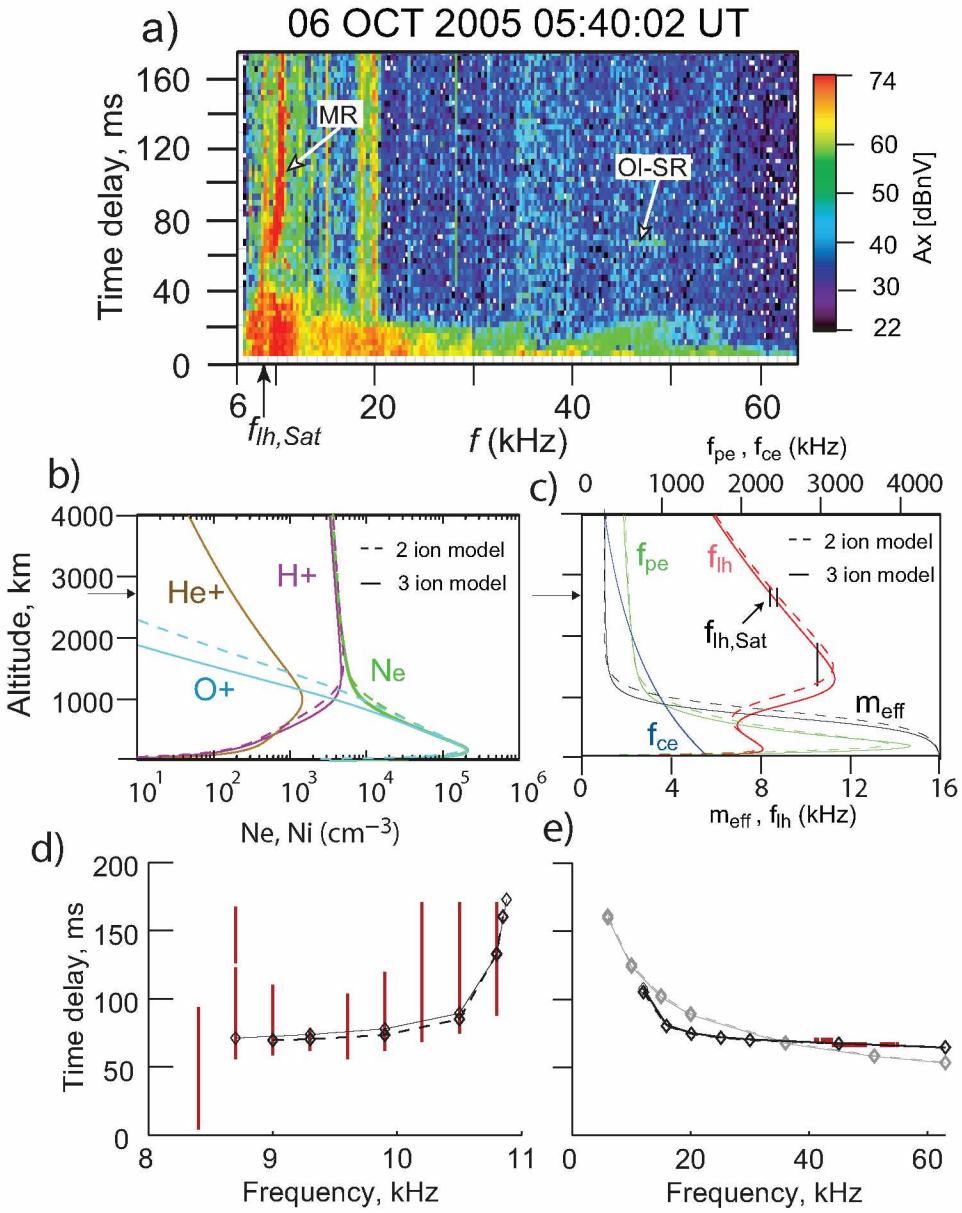

Figure 2.16. Results of ray tracing simulations performed to determine field-aligned electron density and ion composition on 06 October 2005, 0540:02 UT, a quiet day. (a) Plasmagram showing MR and OI-SR echoes observed when satellite was located at Alt=2682 km, Mlat=30.2 ◦ N, L=1.9, and MLT=13. These echoes were observed during quiet geomagnetic conditions. (b) Density models, three ion (solid) and two ion (dashed), along B through the satellite for electron (green), H^+ (pink), He^+ (brown), O^+ (cyan). Both models give agreement between the ray tracing simulation results and experimental measurement. (c) Plasma parameters corresponding to the two models shown in (b). (d) Comparison of the measured time delays (dark red) of MR echoes with those calculated from ray tracing simulations for three ion model(solid) and two ion model (dashed). (e) Comparison of the measured time delays (dark red) of SR echoes with those calculated for OI echoes from ray tracing simulations for three ion model(solid) and two ion model (dashed). Also shown by grey curves (solid and dashed) are time delays obtained for NI echoes from ray tracing calculations.

delays for the simulated OI echo, and a gray curve in Figures 2.16(e) and 2.17(e) the time delays for an NI echo (not observed). Solid curves are time delays obtained using a three ion model and dashed curves show time delays for two ion model. The time delays calculated at specific frequencies are shown by black diamonds.

In the 06 October 2005 0540 UT case, the transition height from the three ion model is 1040 km and that from the two ion model is 1190 km. Electron density obtained from both models is within in 2–3% at altitudes greater than ~1100 km (transition height), and that at F2 peak is within 13%. In the 02 September 2005 1025 UT case, the transition height from the three ion model is 1440 km and that from the two ion model is 1520 km. Electron density obtained from both models is within in 13% at altitudes greater than ~1100 km (transition height), and that at F2 peak is within 2%.

Comparison of the electron and ion densities obtained for the 06 October and 02 September cases shows that (1) at altitudes greater than the transition height (~1500 km), electron density obtained for the 02 September case is about 30% lower than that from the 06 October 2005 case, (2) electron density at F2 peak is almost the same, and (3) transition height in 02 September 2005 case is ~400 km greater than that of 06 October 2005 case. Although both of these cases are at similar L-shells and MLTs, it is suspected that the density models are very different because geomagnetic conditions on both of these days were different. One case was observed during quiet geomagnetic conditions, whereas the other one was observed during the recovery period of a storm. Chapter 3 presents variations of field aligned electron density and ion composition during geomagnetically quiet and disturbed periods.

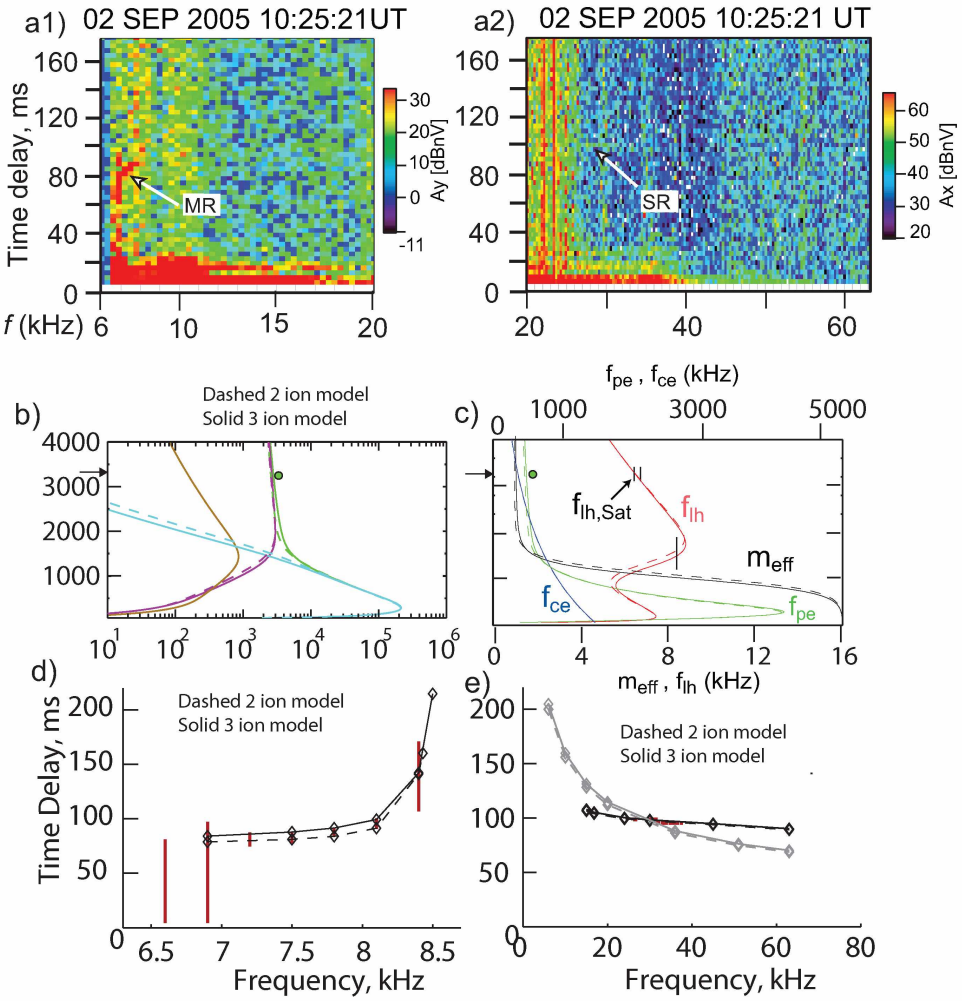

Figure 2.17. Results of ray tracing simulations performed to determine field-aligned electron density and ion composition on 02 September 2005, 1025:21 UT, a disturbed day. (a1, a2) Plasmagrams showing MR and OI-SR echoes observed when satellite was located at Alt=3663 km, Mlat=27.0◦ N, L=1.9, and MLT=14.8. These echoes were observed during the recovery period of a major storm. (b) Density models, three ion (solid) and two ion (dashed), along B through the satellite for electron (green), H^+ (pink), He^+ (brown), O^+ (cyan). Both models give agreement between the ray tracing simulation results and experimental measurement. (c) Plasma parameters corresponding to the two models shown in (b). (d) Comparison of the measured time delays (dark red) of MR echoes with those calculated from ray tracing simulations for three ion model(solid) and two ion model (dashed). (e) Comparison of the measured time delays (dark red) of SR echoes with those calculated for OI echoes from ray tracing simulations for three ion model(solid) and two ion model (dashed). Also shown by grey curves (solid and dashed) are time delays obtained for NI echoes from ray tracing calculations.

2.5.9 Comparison of whistler mode sounding results with empirical models prediction

Figure 2.18 shows a comparison of electron density obtained from WM sounding for the 22 Oct 2005 case with predictions from IRI-2012 [Bilitza et al., 2014], GCPM [Gallagher et al., 2000], and Ozhogin et al. [2012] models. Electron density along the same field line as that of IMAGE (L=2.13) is obtained from these empirical models. Figures 2.18(a) and 2.18(b), respectively, show comparison of electron density obtained using the three ion model (Model-3) and the two ion model (Model-4) with those predicted by empirical models.

The IRI model is based on most of the available and reliable observations of the ionospheric plasma from the ground and from space. It describes monthly averages of electron density, electron temperature, ion temperature, ion composition, and several additional parameters in the altitude range from 60 km to 2000 km. A disadvantage of empirical models is their strong dependence on the underlying database. There is diminished reliability of the model in regions and time periods not well covered by the database [Bilitza et al., 2014].

An issue with IRI-2001 was an overestimation of electron densities in the upper topside (from about 500 km above the F-peak upward) that increases with altitude reaching about a factor of 3 at 1000 km above the peak. This problem was apparently corrected in the IRI-2007 model by incorporating over 150,000 topside profiles from Alouette 1 and 2, and ISIS 1 and 2 [Bilitza and Reinisch, 2008]. The IRI-2012 includes a new model for the region between the F2 and F1 heights [Bilitza et al., 2014]. With the three ion model, we find that the electron density predicted by IRI is greater than that obtained from WM sounding at all altitudes. The difference is greatest at the F2 peak, where the N_e obtained from IRI is roughly three times that from WM sounding. For the two ion model, electron density predicted by IRI agrees well above $\sim$500 km. However, at F2 peak N_e obtained from IRI is roughly three and half times that from WM sounding.

The global core plasma model (GCPM) provides empirically derived core electron and ion densities (H^+, He^+, and O^+) as a function of geomagnetic and solar conditions throughout the inner magnetosphere. The model is based on data from DE/RIMS, DE/PWI, and ISEE/PWI and merges with the International Reference Ionosphere (IRI) at low altitudes. It is composed of separate models for the plasmasphere, plasmapause, trough, and polar cap [Gallagher et al., 2000]. The dashed curves in Figure 2.18 represent N_e predicted by GCPM. At altitudes below 2500 km, the electron density predicted by GCPM is greater than that obtained from WM sounding results using Model-3

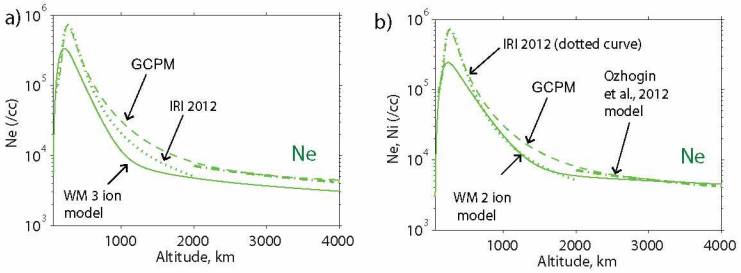

Figure 2.18. Comparison of electron density obtained from Model-3 (a), three ion model, and Model-4 (b), two ion model, for the 22 October 2005 case with GCPM and Ozhogin et al. [2012] empirical models.

(three ion model) and Model-4 (two ion model). The difference is greatest at the F2 peak where the N_e obtained from GCPM is roughly 3–3.5 times that from WM sounding. The GCPM at lower altitudes is expected to overestimate N_e relative to WM sounding results because, as noted above, GCPM merges with IRI at lower altitudes. Above $\sim$ 2500 km, the electron density predicted by GCPM is $\sim$1.4 times greater than that obtained from WM sounding results using Model-3 and it is within $\sim$10% of that obtained from WM sounding results using Model-4.

The Ozhogin et al. [2012] empirical model estimates field-aligned electron density inside the plasmasphere from equator down to 2000 km. This model is based on more than 700 density profiles along field lines derived from active sounding measurements made by the radio plasma imager on IMAGE between June 2000 and July 2005. This model does not include dependence on geomagnetic and solar conditions. The dash dot curves in Figure 2.18 represent N_e obtained from the Ozhogin et al., 2012 model. Note that the N_e predicted by GCPM above 2000 km altitude and Ozhogin et al. [2012] are within 2–3% of each other. The electron density predicted by the Ozhogin et al. [2012] model is $\sim$1.4 times greater than that obtained from WM sounding results using Model-3 and it is within $\sim$10% of that obtained from WM sounding results using Model-4.

Figure 2.19 shows for the 22 October 2005 case a comparison of ion densities obtained from WM sounding using Model-3, three ion model; Figures 2.19(a-c), and Model-4, two ion model; Figures 2.19(d-f), with those predicted by GCPM. The solid curves in Figure 2.19 represent ion densities obtained from ray tracing calculations. As discussed in sections 2.5.3 and 2.5.4, the ion composition obtained from WM sounding is not unique. The dotted curves in Figure 2.19 represent the maximum and minimum ion density possible for the m_{eff} obtained using Model-3 and Model-4. Note that in Figures 2.19(d-f), one of the dotted curves overlaps with the solid curve

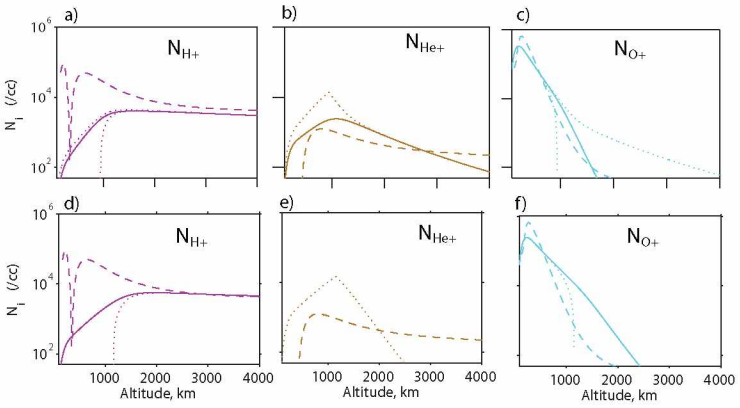

Figure 2.19. Comparison of ion densities N_i obtained from WM sounding with those predicted by GCPM empirical model. (a-c) and (d-f) respectively show comparison of N_i predicted by GCPM with those obtained from WM sounding assuming that magnetospheric plasma is composed of three ions (Model-3) and two ions (Model-4). The solid curves indicate N_i obtained from WM sounding method. The dotted curves indicate the maximum and minimum possible N_i calculated from the m_{eff} obtained form WM sounding. The dotted curves indicate the N_i predicted by GCPM.

because Model-4 is a two ion model and hence the ion composition obtained from ray tracing is maximum H^+ and maximum O^+. In the case of He^+, Figure 2.19(b) and 2.19(e), there is only a dotted curve because the minimum He^+ possible is zero. The dashed curves in Figure 2.19 represent the ion densities predicted by the GCPM empirical model. Relative to the ion densities obtained from WM sounding using both three ion and two ion model: (1)At altitudes lower than ~2000 km GCPM overestimates hydrogen ion density (N_{H^+}). The N_{H^+} predicted by GCPM is more than the maximum possible N_{H+} from WM sounding. (2) Above ~2000 km N_{H^+} from GCPM is comparable. The N_{H^+} predicted by GCPM is within 20–30% and 1–3%, respectively, of that from WM sounding using Model-3 and Model-4. (3)At altitudes below ~500 km, GCPM underestimates N_{He^+} relative to WM sounding of N_{He^+} using Model-3. (4) Above ~500 km, N_{He^+} from GCPM is comparable to that obtained from WM sounding using Model-3. (5) At altitudes below ~500 km, GCPM overestimates oxygen ion density (N_{O^+}). From GCPM N_{O^+} is about 2 times and 3 times, respectively, that from WM sounding using Model-3 and Model-4. (6) Above ~500 km, N_{O^+} from GCPM is comparable to that obtained from WM sounding using Model-3 (Figure 19(c) solid curve). Above ~500 km, N_{O^+} obtained from WM sounding using Model-4 is greater than that predicted by GCPM.

Figure 2.20 shows for 22 Oct 2005 case a comparison of relative ion concentrations obtained from WM sounding using Model-3, three ion model; Figures 2.20(a-c), and two ion model, two ion model; Figures 2.20(d-f), with those predicted by IRI-2012. The solid curves in Figure 2.20 represent ion composition obtained from ray tracing calculations. The dotted curves in Figure 2.20 indicate the maximum and minimum ion concentrations possible for the m_{eff} obtained using Model-3 and Model-4. In Figures 2.20(d) and 2.20(f), the solid curve overlaps with the dotted curve representing the maximum possible α_{H^+} and α_{O^+}. This is because Model-4 is a two ion model and the α_{H^+} and α_{O^+} obtained from Model-4 are already maximized. The dashed curves in Figure 2.20 represent the ion composition predicted by the IRI-2012 empirical model along the same field lines as that of IMAGE. The triangles in Figure 2.20 indicate the DMSP-F15 satellite measurements of relative ion concentrations. The α_{H^+} obtained from the three ion model and that predicted by IRI are in good agreement. At all altitudes, IRI predictions of α_{H^+} are greater than those from the 2 ion model. The IRI model substantially underestimates α_{He^+} at all altitudes. The α_{He^+} from IRI is almost zero at all altitudes and is in agreement with the two ion model. The α_{O^+} predicted by IRI agrees with the maximum O^+ possible from Model-3. The IRI predictions of O^+ lie between the maximum and minimum O+ possible obtained from Model-4. The DMSP measurements of α_{H^+} and α_{O^+} are in general agreement with those measured by the sounder, assuming 3 ions, and predicted by IRI. The DMSP measurements of α_{He^+} are in better agreement with those measured by WM sounding than with those predicted by IRI.

From the above discussion we can say that GCPM overestimates H^+ and O^+ at lower altitudes and that the IRI model substantially underestimates He^+ at all altitudes. On the basis of the work by Craven et al. [1997], GCPM estimates the relative concentrations of H^+, He^+ , and O^+ ions in the plasmasphere. Improvements in the description of ion concentrations in the GCPM can be accommodated in future versions [Gallagher et al., 2000]. The ion composition has been the step-child of IRI development activities, partly because of the limited amount of available data and the still existing discrepancies between ground and space observations, and partly because of the much smaller community of IRI users that require information about the ionospheric ion composition [Bilitza et al., 2014]. WM sounding provides a new method to generate improved empirical models of ion composition.

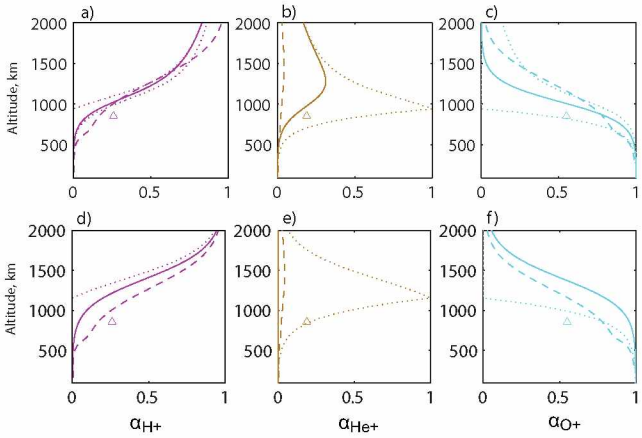

Figure 2.20. Comparison of relative ion concentrations obtained from WM sounding with those predicted by IRI-2012. (a-c) and (d-f) respectively show comparison of α_i predicted by IRI with that obtained from WM sounding assuming that magnetospheric plasma is composed of three ions (Model-3) and two ions (Model-4). The solid curves indicate α_i obtained from WM sounding method. The dotted curves indicate the maximum and minimum possible α_i calculated from the m_{eff} obtained form WM sounding. The dotted curves indicate the α_i predicted by IRI.

2.6 Summary and conclusions

The RPI on IMAGE has observed magnetospherically and specularly reflected whistler mode echoes. The MR echoes are reflected at altitudes where the local lower hybrid frequency ($_{lh}$) is equal to the transmitted pulse frequency f. The SR echoes are reflected at the Earth-ionosphere boundary at 90 km, either with wave vector at normal incidence (the NI echo) or, more commonly at oblique incidence (the OI echo). The MR and SR echoes are further categorized as discrete, multipath, and diffuse echoes based on their spectral forms. The discrete WM echoes with relatively small spreading in time delays (<5–10 ms)at each frequency are a result of WM waves propagating in smooth magnetosphere. The multipath echoes with medium spreading in time delays (∼10–30 ms) at each frequency and diffuse echoes with large spreading in time delays (>30–40 ms) at each frequency are a result of refraction and scattering of WM waves by large and small scale field-aligned irregularities present along the WM echo propagation path.

Magnetospherically and specularly reflected whistler mode echoes were observed at altitudes below 5000 km and at all latitudes. The largest fraction of discrete SR echoes was observed at the lower latitudes; and the largest fraction of diffuse SR echoes at higher latitudes. The largest fraction of discrete and multipath MR echoes was observed at the lower latitudes. Diffuse MR echoes were found in large numbers at all latitudes.

Observed MR echo's lower and upper cutoffs and time delay versus frequency characteristics combined with ray tracing analysis provide measurement of field-aligned electron and ion densities from satellite altitude down to ~1000 km where f_{lh} reaches its maximum along $\mathbf{B_0}$. The observed time delay versus frequency characteristics of SR echo combined with ray tracing analysis provide measurement of field-aligned electron density from satellite altitude down to 90 km. Simultaneously observations of MR and SR echoes allow determination of field aligned electron and ion densities from satellite altitude down to 90 km. When only MR echoes or only SR echoes are observed, WM sounding results can be augmented with in situ measurements from DMSP and CHAMP satellites and/or bottomside sounding results. Analysis of multipath and diffuse echoes provides information on the location and scale sizes of plasma density irregularities over 10 m to 10 km scale sizes.

A systematic and efficient iterative procedure for implementing the WM radio sounding method to determine field-aligned electron and ion densities was discussed. When we consider the propagation characteristics ($t_g - f$) of MR, OI, and NI echoes and the general features of the ray tracing density model, typically, in 2–3 iterations, the procedure leads to a density model that provides a close match between the simulated and observed properties of WM echoes, including time delays and cutoffs. With the help of one case study, this procedure of whistler mode radio sounding of electron density, effective ion mass, and ion composition was illustrated.

The uncertainty in the measurement of N_e, m_{eff} and α_i was discussed with the help of multiple models that can explain observed time delays and cutoffs of observed whistler mode echoes. The measurement of effective ion mass depends on the number of ion species assumed in the ray tracing density model. This assumption leads to uncertainty in the measurement of m_{eff}. The uncertainty in m_{eff} was illustrated with two different density models that explain observed WM echo features. For one model it was assumed that the magnetospheric plasma is composed of three ions (H^+, He^+, and O^+; three ion model). For the other it was assumed that the plasma is composed of two ions (H^+ and O^+; two ion model). Once m_{eff} was obtained, individual ion concentrations were determined using the equation of m_{eff} and that the sum of fractional abundance of all ion species is equal to 1. In the two ion model case, there is no uncertainty in the measurement of ions once m_{eff} is obtained. However, in the three ion model case additional assumptions are needed to determine individual ion concentrations. The uncertainty in the measured ion composition when three ion

species are assumed in the density model is discussed. With the help of the two models, two ion and three ion, the uncertainty in the measurements of electron density is also discussed.

Whistler mode radio method was applied to two selected cases, one observed during quiet geomagnetic conditions and the other during the recovery period of a major storm, to determine field-aligned electron and ion densities and the uncertainty in their measurement. With the help of two case studies, one when only MR echo was observed and the other when only SR echo was observed, augmentation of whistler mode radio sounding results by DMSP, CHAMP satellite data, and/or bottomside sounding results was demonstrated.

Whistler mode sounding results were in agreement with those measured by DMSP and CHAMP satellites. The bottomside sounding results overestimate electron density at F2 peak relative WM sounding results. Whistler mode sounding results are also compared with GCPM, Ozhogin et al. [2012], and IRI-2012 empirical model predictions. Relative to WM sounding results: (1) Both GCPM and IRI models overestimated electron density at lower altitudes; (2) GCPM and Ozhogin et al. [2012] predictions of electron density above 2000 km were comparable; (2) GCPM overestimated H^+ and O^+ at lower altitudes, and IRI substantially underestimated He^+ at all altitudes.

Analysis of whistler mode echoes will lead to new empirical models of plasma density, density structures, and ion composition as functions of geophysical conditions. These new empirical models can be used for gaining new understanding of mechanisms important to magnetosphere-ionosphere coupling, and in space weather predictions.

Chapter 3

Field-Aligned Electron Density and Ion Composition Inside the Plasmasphere as a Function of Geomagnetic Storm Activity

The objectives of this chapter are: (1) to study the signatures of frequency cutoffs, and field-aligned irregularities during geomagnetically quiet and disturbed periods; (2) to determine the variation of average electron density and ion composition along different L-shells during geomagnetically quiet times; (3) to determine using WM radio sounding data from IMAGE how field-aligned electron density and ion composition vary during the onset, main, and recovery phases of geomagnetic storms; and (4) to compare the response of field-aligned electron density and ion composition obtained from WM sounding during quiet and disturbed periods with in situ measurements from other satellites and bottomside sounding results.

3.1 Geomagnetic and solar conditions during IMAGE lifetime: identification of quiet and disturbed periods

Sun is the main source of energy for the processes taking place in the Earth's ionosphere and magnetosphere system and the interaction between the two systems [e.g., Hargreaves, 1992]. The geomagnetic and solar indices provide global and/or specific information on the physical state of the entire system. Solar flux is used as the basic indicator of solar activity, and to determine the level of radiation being received from the Sun. Solar flux measured in solar flux units (SFU), is the amount of radio noise or flux that is emitted at a frequency of 2800 MHz (10.7 cm). The Penticton Radio Observatory in British Columbia, Canada, reports this measure daily at local noon (1700 GMT). It is found that radiation received from the sun increases with sunspot number. Sunspots increase and decrease in number over time in a regular, approximately 11-year cycle, the solar or sunspot cycle.

Solar activity changes the geomagnetic activity. Geomagnetic indices are measures of the geomagnetic activity that occurs, typically over periods of less than a few hours. This activity is recorded by magnetometers at ground-based observatories [Mayaud, 1980]. Geomagnetic indices may be grouped into three categories according to the region from which the records come, namely: (1) auroral zone; (2) mid-latitude; and (3) low-latitude. In these categories, the indices most often

used are: AE (incuding the related indices AU and AL); Kp and Ap; and equatorial Dst. Auroral electrojet or AE was introduced to characterize the auroral zone where the fluctuations of the magnetic field are much stronger that those at mid- and low- latitudes. Planetary-scale magnetic activity is measured by the Kp index. The Kp index is expressed in quasi-logarithmic scale. It is derived from the average of fractional K indices at 13 observatories located in the mid-latitude region in both the northern and the southern hemisphere. Planetary index, Kp can take values between 0 to 9. The time interval for Kp is 3 hrs. The Ap index was introduced to obtain a linear index from Kp. The time interval for Ap is a day. Disturbance storm time or Dst represents the general behavior of a typical geomagnetic storm. The Dst is derived using the horizontal magnetic field component from a network of low-latitude stations. The time interval for Dst is 1 hr.

This chapter mainly deals with analysis of whistler mode echoes observed on the IMAGE satellite in the low to mid latitude region as a function of storm activity. Hence the geomagnetic indices Kp, Ap, and Dst were used as indicators of geomagnetic conditions.

3.1.1 Variation of solar flux and sunspot number during 2000–2005 period

The IMAGE satellite was operational during March 2000 to December 2005. This period approximately covers the last half of the 23rd solar cycle. Figure 3.1 shows the variation of solar flux and sunspot number during those years. Solar activity was high during the years 2000–2002 and it decreased during the years 2003–2005. The average solar flux during 2000–2001 was $\sim$200. It decreased to $\sim$80 in 2005. Sudden increases in solar flux (e.g., year 2003; day 230) indicate intense changes in solar activity leading to coronal mass ejections, large solar flares, or high speed wind streams. The average sunspot number was $\sim$200–250 during the years 2000 and 2001. It decreased to $\sim$60 during 2005. Figure 3.1 shows that during IMAGE's operational period there were periods of high and low solar activity. Analysis of whistler mode echoes observed during this period should provide variations of field-aligned electron density as a function of solar activity.

3.1.2 Variation of Kp, Dst during 2000-2005 period

Figure 3.2 shows the plot of Kp every three hours and hourly Dst for the years 2000–2005. As noted earlier, Kp can take values from 0 to 9. Values of 0–2 indicate that the magnetosphere is relatively quiet; $2 < Kp < 4+$ indicates a moderate geomagnetic activity, -5<Kp<6 indicates

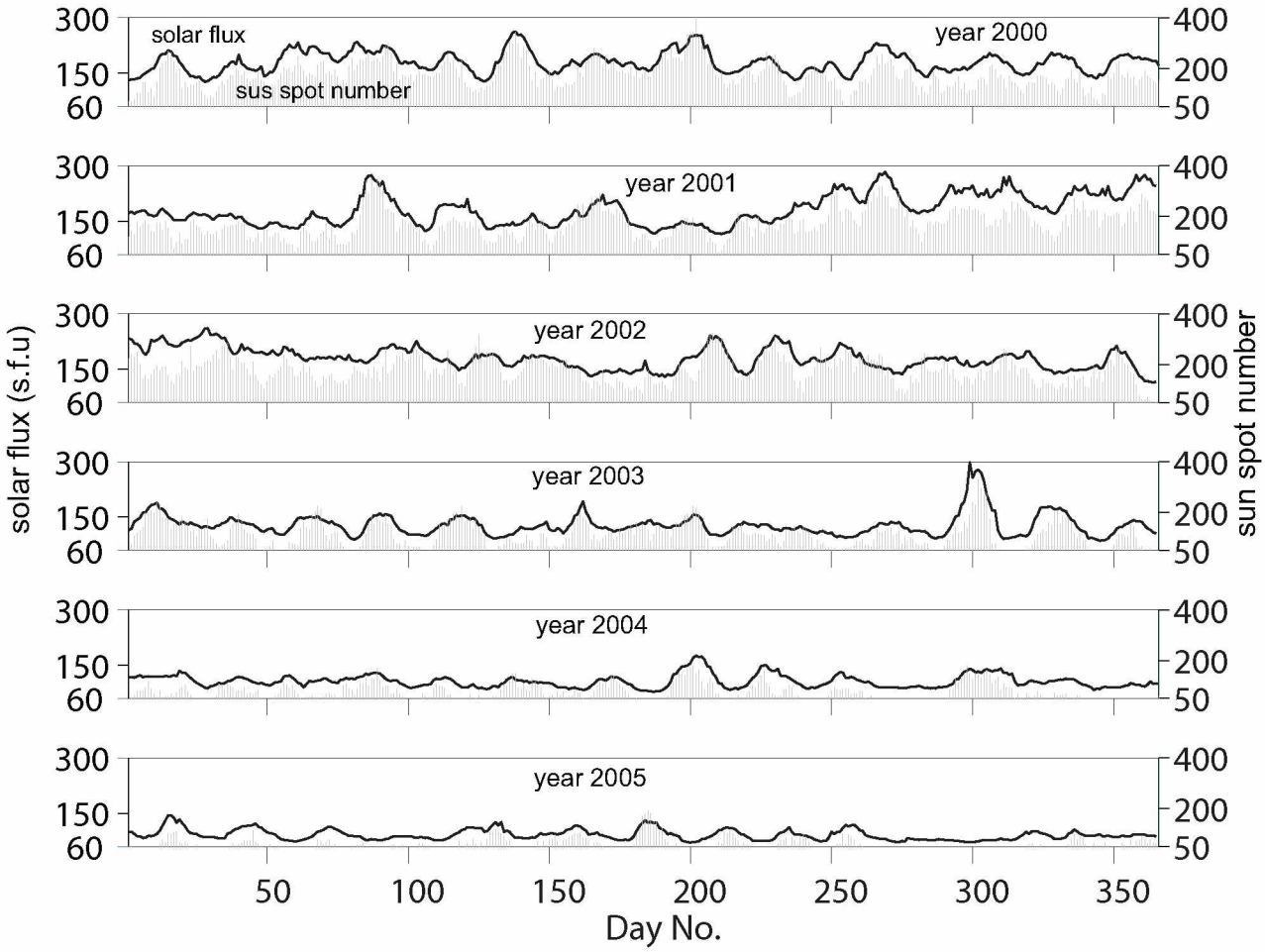

Figure 3.1. Solar conditions during the 2000-2005 period. The solid curve represents the solar flux variation and the grey lines indicate the sun spot number.

a minor storm; and Kp>6 indicates a major storm. As Kp increases, the severity of the storm increases. The Dst provides a quantitative measure of geomagnetic disturbance. During quiet periods the Dst value typically varies between -20 to 20 nT. Values of -20 to -50 nT indicate moderate conditions in the magnetosphere; -100 nT$\lesssim$Dst$\lesssim$-50 nT indicates a minor geomagnetic storm; and Dst$\lesssim$-100 nT indicates a major storm. During a typical geomagnetic storm, the level of Dst remains above its typical value for a period of 2–3 hours. This is called the storm onset. The onset phase is not necessarily seen for all geomagnetic storms. The onset phase is followed by a sudden decrease in the value of Dst, which is called the development of the main phase of the storm. The magnitude decrease represents the severity of the disturbance. The approximately twelve days of time for Dst to get back to its typical value is the recovery phase of the storm. In the year 2000 there were fifteen major (Kp$\geqslant$ 6 and/or Dst< -100 nT) geomagnetic storms, two of

which were super storms with Dst going below -250 nT and Kp of -9 or greater. In 2001 there were twelve major geomagnetic storms: two were super storms and one was an extreme storm with Dst close to -400 nT and Kp of -9. In 2002 there were eleven major geomagnetic storms. In 2003 there were six major geomagnetic storms, three of which were extreme with Dst below or close to -350 nT and Kp -9 or greater. In 2004 there were six major geomagnetic storms, and one out of those was an extreme case where Dst went below -350 nT and Kp of -9. In 2005 there were nine major geomagnetic storms, two of which were severe with Dst below -200 nT and a Kp of 8. It can be seen from Figure 3.2 that the magnetospheric conditions are quite variable and years 2003 and 2004 are relatively quiet compared with other years.

A survey of WM echoes during geomagnetically disturbed conditions was performed and WM sounding data were available for $\sim$40 geomagnetic storms. The WM sounding data were not available for all the storms because either there were no active soundings during the storm time or frequencies in the WM sounding range were not transmitted.

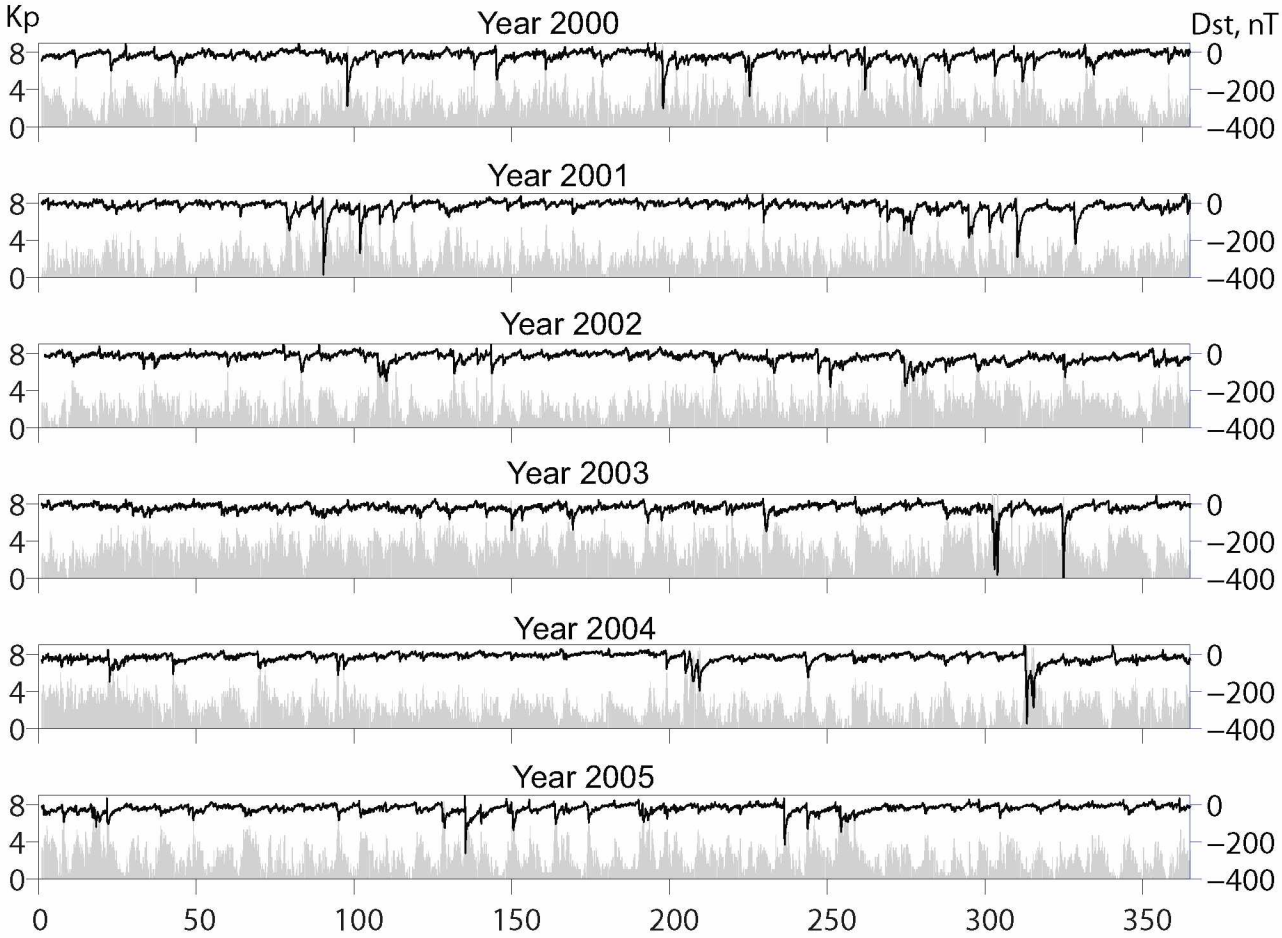

Figure 3.2. Geomagnetic conditions during the 2000-2005 period. The black curve represents Dst and the grey bars represent Kp.

3.1.3 Examples of quiet and disturbed periods

Figure 3.3 shows an example of a quiet to moderate period. If geomagnetically quiet/moderate conditions prevail for two or more days, it is called a quiet to moderate period. In Figure 3.3 there is one quiet period (days 339–344) and two moderate periods, one preceding the quiet period and one following. Analysis of whistler mode echoes observed during quiet to moderate periods allows determination of nominal field-aligned electron and ion densities against which storm time variations can be compared.

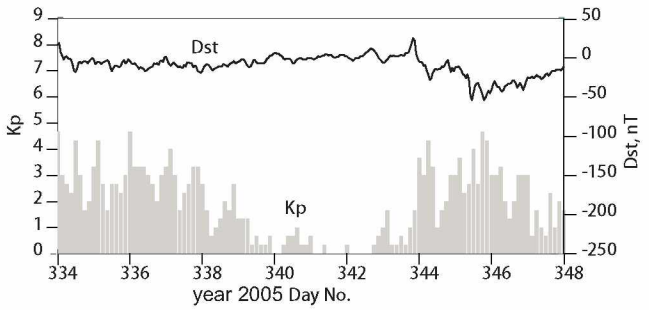

Figure 3.3. Example of a geomagnetically quiet to moderate period. The ∼5 day quiet period (Day #339–344) is preceded and followed by geomagnetically moderate activity.

Figure 3.4 shows examples of disturbed periods. A disturbed period includes the onset, main and recovery phases of one or more geomagnetic storms (Kp>-5 and Dst<-50 nT). Figure 3.4a shows an example of a disturbed period that includes one moderate geomagnetic storm. The storm is preceded (days 91–94) and followed (98–100) by a quiet period. Figure 3.4b shows another example of a disturbed period that includes two geomagnetic storms. These two storms occurred in a period of five days.

As noted earlier there were ∼40 geomagnetic storms for which WM data were available. From these was selected one prolonged, 31 day, disturbed period (24 August to 24 September 2005; Day #228–280) that included one severe storm (24 August), two major storms (31 August, 11-14 September), 5 moderate storms (02–03 September, 04 September, 10 September, 15 September) and one minor storm (18 September) was selected to determine electron density, ion composition, and FAI occurrence and properties as a function of L-shell during onset, main, and recovery phases of the storms. Figure 3.5 shows the variation of Kp and Dst during this disturbed period. Geomagnetic storms that occurred during this period are shown by arrows. This 31 day disturbed

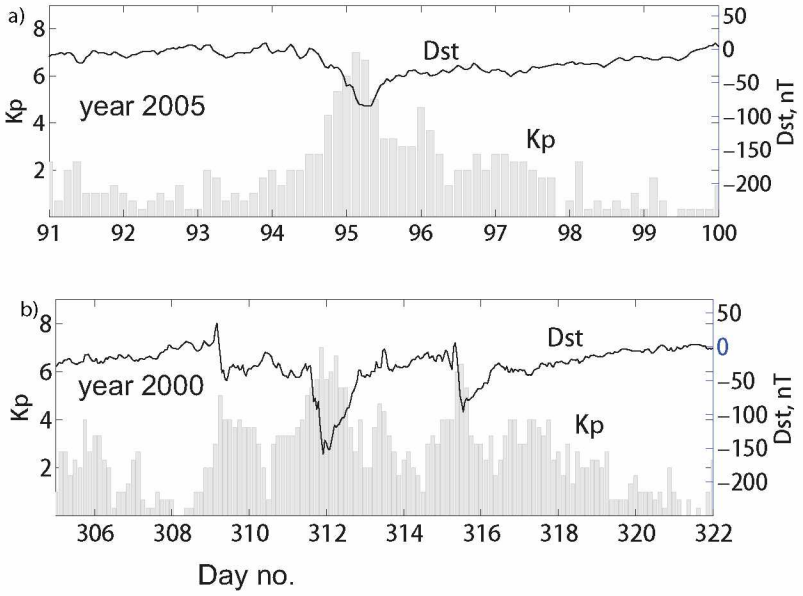

Figure 3.4. Examples of disturbed periods. Top panel shows disturbed period that included a moderate storm. Bottom panel shows disturbed period that included two storms that occurred in succession.

period was preceded by a week long quiet-moderate period (16–23 August 2005) and followed by a quiet-moderate period of 2 weeks (24 September - 06 October 2005). This selected time period of 52 days (16 August to 06 October 2005) had many advantageous features, including whistler mode echoes that allowed measurements of both plasma density and ion composition. In addition, complementary in situ electron and ion density data from DMSP (850 km) and CHAMP (350 km) satellites, and vertical sounding data from the network of ground ionosondes was available.

3.2 Interplanetary, solar, and geomagnetic conditions during the 16 August to 24 September 2005 storm activity

The solar and interplanetary origin of intense geomagnetic storms has been widely studied [e.g., Tsurutani et al., 1992; Gonzalez et al., 1999; Echer et al., 2008]. Figures 3.6, 3.7, and 3.8, respectively show the interplanetary, solar, and geomagnetic observations that resulted in 24 Aug 2005, 31 August 2005, and 10–15 September 2005 geomagnetic disturbances. The information on interplanetary conditions during these geomagnetic disturbances was obtained from NASA website (http://omniweb.gsfc.nasa.gov/form/dx1.html). The geomagnetic and solar conditions are obtained from the NOAA website (http://spidr.ngdc.noaa.gov/). The information on CMEs and solar flares

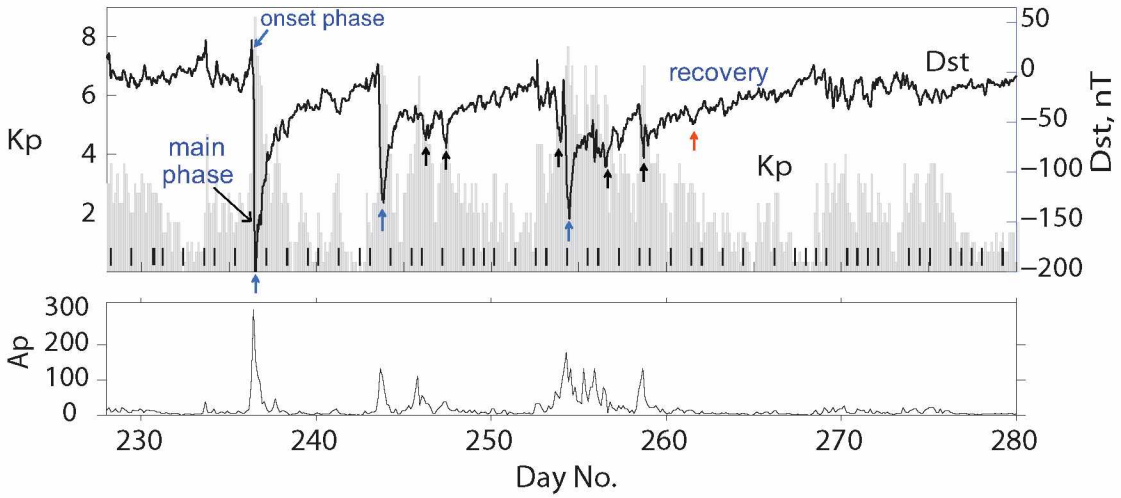

Figure 3.5. Variation of Kp, Dst and Ap during the 16 August to 06 October 2005 (Day #228-280) period. This period included one severe, two major, four moderate and one minor geomagnetic storm. This 52 day long period is selected to determine variations in electron density and ion composition as a function of geomagnetic storm activity.

is obtained from the NASA website (http://umbra.nascom.nasa.gov/newsite/data.html).

The severe geomagnetic storm recorded on 24–25 Aug 2005, with a Kp maximum of -9 and a Dst index of -216 nT, was known to be result of interplanetary shock caused by coronal mass ejection [Echer et al., 2008]. The Dst (See Figure 3.6 second panel from bottom) was observed to maintain a quiet response from 18 August to 20 August (days 228–232). On 21 August (Day #233) Dst increased to 32 nT and shortly afterwards Kp value increased to -5, indicating disturbed conditions. This increase in Kp and Dst coincides with increased proton density. Sun spot number increased and did solar flux during this period. During the 22 August to early 24 August 2005 period, Dst again remained quiet . This quiet period was followed by the onset phase of the 24 August 2005 storm, Dst increased to 30 nT. Around the same time IMF Bz value reached -40 nT while the solar wind speed increased to over 700 km/s. The proton density increased to 56 /cc and there was an excitement of proton temperature to higher magnitude. The electric field increased to 27 mV/m. Shortly afterwards, the Kp value increased to 7 and then to 9, and the Kp value remained at minor- to- severe storm levels until early 25 August.

The major geomagnetic storm recorded on 31 August 2005, a storm with a Kp maximum of -7 and a Dst index of -131 nT, was known to be the result of a corotating interplanetary region or high speed solar wind streams [Echer et al., 2008]. The Dst remained quiet from 25 to 30 August

2005. At the end of 30 August, the Dst increased to -6 nT indicating the onset phase of the 31 August storm. At the onset IMF Bz value was 18.6 nT, and solar wind speed increased to 512 km/s. Proton density increased to 27 /cc. There was little increase in proton temperature. The electric field increased to 6 mV/m. There were no sunspots during this period, and the solar flux remained close to 90 indicating quiet solar conditions. Although the storm onset was at the close of 30 August, it developed toward the middle of 31 August and reached the level of a major magnetic storm.

Following the major storm on 31 August 2005 there were two moderate storms, one on 03 September with a Kp maximum of 5+ and Dst index of -68 nT, the other on 04 September with a Kp maximum of -5 and Dst index of -76 nT. Note that Kp indicated moderate storm levels by the close of 02 September 2005. At the time of Kp increase, IMF Bz was 8 nT while the solar wind speed increased to 659 km/s. The Kp remained high on 03 September. The proton density remained almost the same while proton temperature decreased. The electric field decreased to -5.36 mV/m. On 04 September around the moderate storm time, no significant changes in interplanetary conditions were observed. The solar wind speed increased to 743 km/s.

The geomagnetic storms recorded during the 10–12 September period were a result of CMEs, associated with the large solar flares of this period. An increased sunspot number and solar flux form $\sim$90 to $\sim$120 were observed during this period. On 09 September the solar wind speed jumped from 350 to 500 km/s and the IMF Bz dipped to -9 nT. In the proton density an increase to 24 /cc was seen prior to the increase in solar wind speed and the dip in IMF Bz. There was an excitement in proton temperature to higher values. The electric field decreased to -5 mV/m. On 10 September the Kp index increased to 5, Dst decreased to -70 nT. On 11 September, the Bz decreased to -6.4 nT and the maximum solar wind speed was 1059 km/s. No increase in proton density was seen, but there was excitement in proton temperature to higher values. The electric field decreased to -3.6 mV/m. The Kp reached a peak value of 9 and Dst reached a minimum of -147 nT. Later, on 12 September, the IMF Bz value dipped to -10 nT and the solar wind speed increased from 700 to 993 km/s. No increase in proton density was seen, but there was excitement in proton temperature to higher values. The electric field decreased to -6.5 mV/m. The Kp index reached a value of -6.

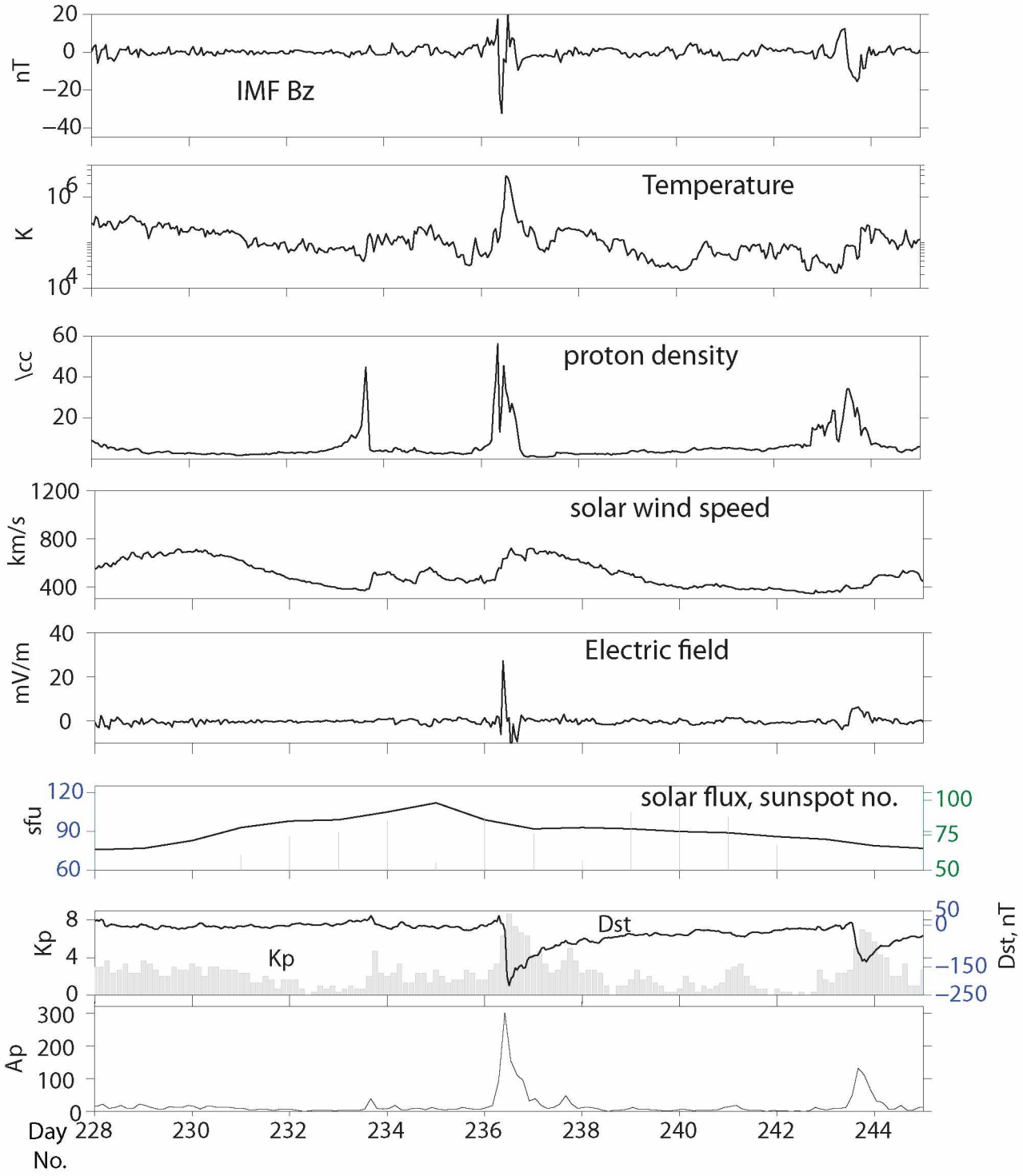

Figure 3.6. Variation of interplanetary conditions, solar parameters, and geomagnetic conditions during the 16 August (Day #228) to 02 September (Day #245) period.

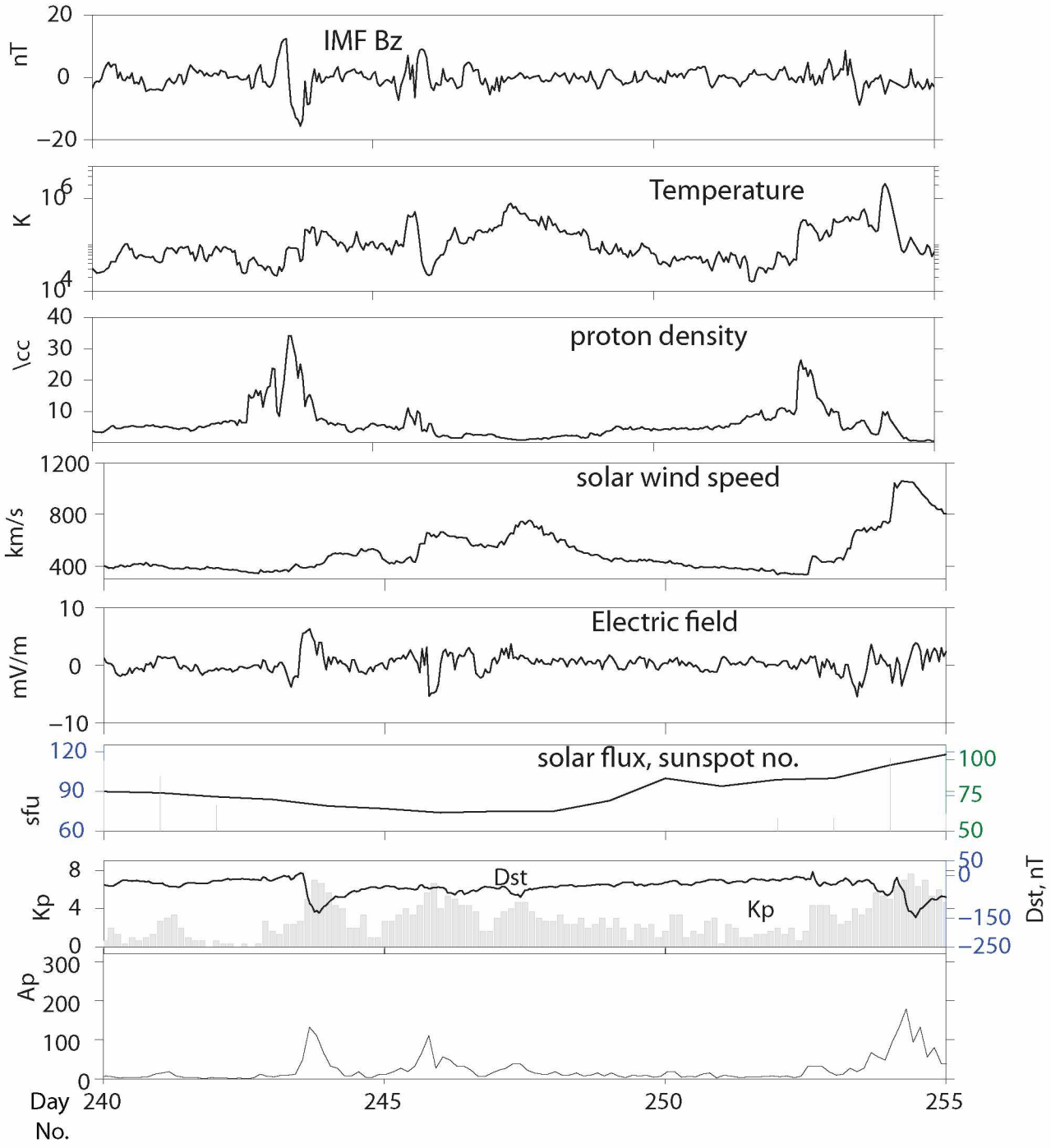

Figure 3.7. Variation of interplanetary conditions, solar parameters, and geomagnetic conditions during the 28 August (Day #240) to 12 September (Day #255) period.

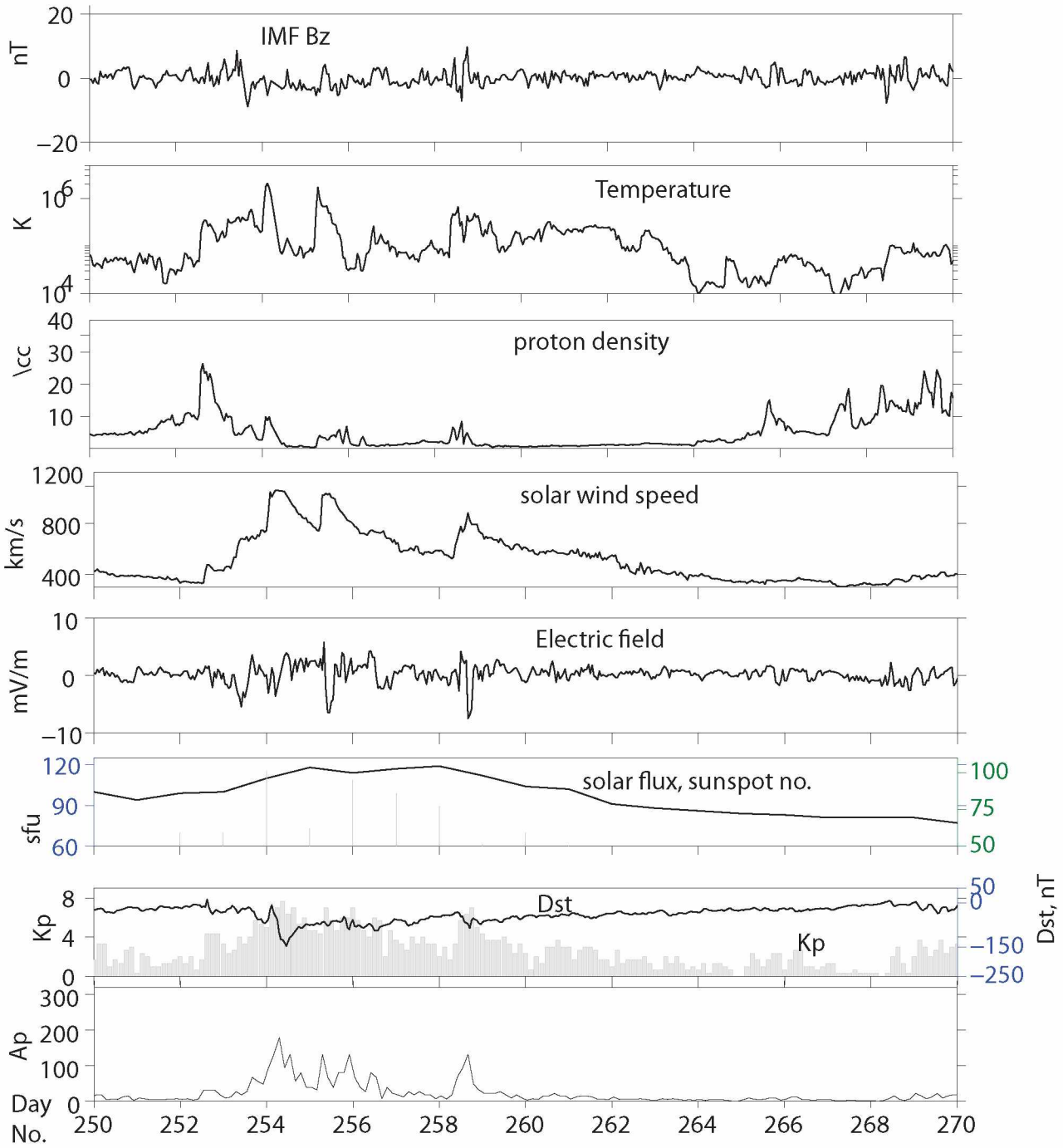

Figure 3.8. Variation of interplanetary conditions, solar parameters, and geomagnetic conditions during the 07 September (Day #250) to 27 September (Day #270) period.

On 15 September 2005 there was another moderate storm, a result of CME, with a Kp maximum of 7 and a Dst minimum of -78 nT. At the time of the storm, the solar wind speed rose from 550 to 862 km/s, and IMF Bz dipped to -7 nT. No increase in proton density was seen but there was increase in proton temperature. The electric field decreased to -7 mV/m.

On 18 September the Dst indicated a minor geomagnetic disturbance, but no significant changes in interplanetary or solar conditions were seen.

3.3 Occurrence patterns of whistler mode echoes

In the following subsections occurrence patterns in space and time of whistler mode echoes observed during the 16 August to 06 October 2005 period are discussed.

3.3.1 Locations of IMAGE in magnetic meridional plane during the 16 August to 06 October 2005 period when WM echoes were observed

Figure 3.9a shows the locations of IMAGE in the magnetic meridional plane when whistler mode (WM) echoes were observed during the 16 August to 06 October 2005 period. Red and green dots, respectively, indicate the locations of IMAGE when MR and SR echoes were observed. There were 101 WM echoes observed for L<10 during the day-time (13-15 MLT) and 48 WM echoes observed for L<10 during the night-time (2-4 MLT). There were 30 echoes observed for L>10. In this chapter WM echoes observed inside the plasmasphere below L=2.4 are analyzed. Figure 3.9b shows locations of IMAGE in the magnetic meridional plane when WM echoes were observed below L=2.4.

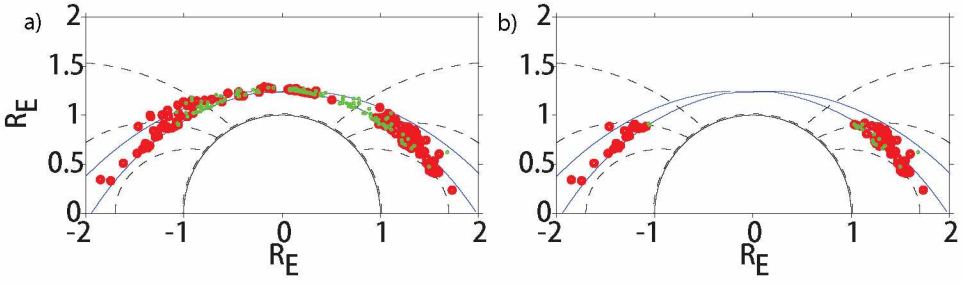

Figure 3.9. Locations of IMAGE in the magnetic meridional plane during the 16 August to 06 October 2005 period when WM echoes were observed

3.3.2 Locations of IMAGE in equatorial plane during Aug 16-Oct 06 period when WM echoes were observed

Figure 3.10a shows the locations of IMAGE in the equatorial plane when whistler mode (WM) echoes were observed during the 16 August to 06 October 2005 period. Red and green dots, respectively, indicate locations of IMAGE when MR and SR echoes were observed. Figure 3.10b shows locations of IMAGE in the equatorial plane when WM echoes were observed below L=2.4.

As seen in Figures 3.9 and 3.10 WM echo data on the night-side (MLT 2-4) is sparse. This is because of the IMAGE satellite orbit. As discussed in Chapter 2, WM echoes were observed at altitudes below 5000 km. The altitude of IMAGE is greater on the night-side compared to the day-side and hence fewer echoes were observed. Note that the night-side WM echo data are noisy compared to that of the day-side, challenging the identification of echoes on the night-side as well as the measurements of time delay versus frequency. For most of the night-side cases, the upper cutoff of MR echo is unclear.

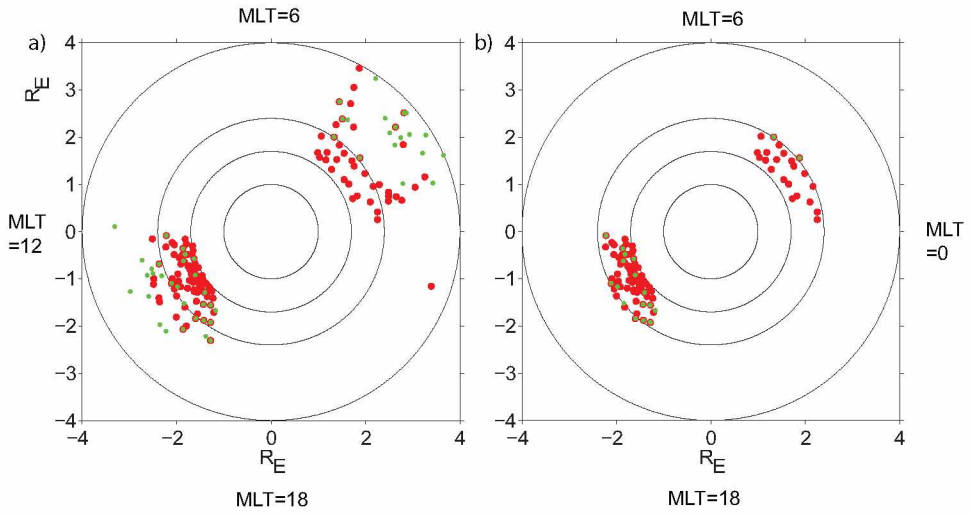

Figure 3.10. Locations of IMAGE in equatorial plane during 16 August to 06 October 2005 period when WM echoes were observed

3.3.3 Temporal pattern of WM echoes observed during Aug 16-Oct 06 period on day-side and night-side

Figures 3.11 and 3.12 show, respectively, temporal patterns of WM echoes observed for L<3.5 as a function of geomagnetic activity, as indicated by Kp, Ap and Dst indices, for the 16 August to 06 October 2005 period.

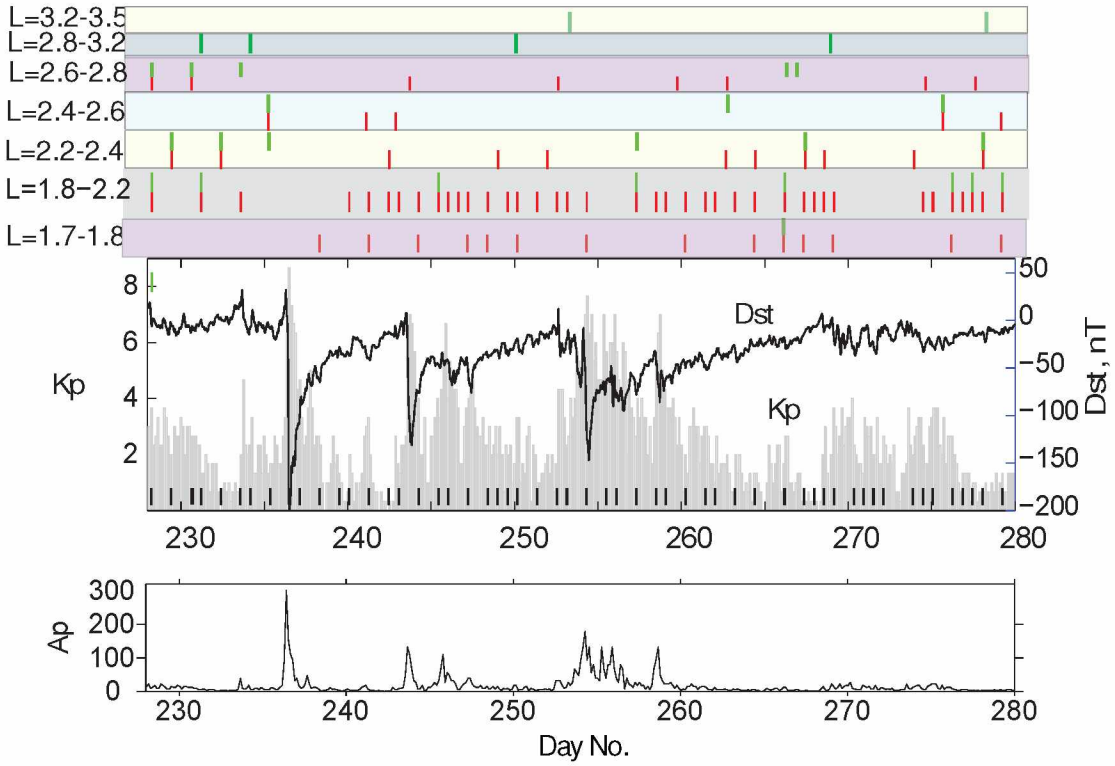

Figure 3.11. Temporal pattern of WM echoes observed on the day-side in the L-shell range 1.7-3.5 during the period 16 August (Day #228, 15 MLT) to 07 October 2005 (Day #280, 13 MLT) as a function of geomagnetic activity. Also shown are the variation of geomagnetic indices Kp (gray bars), Dst (black curve), and Ap (bottom panel). The black lines on the time axis indicate times when 6-63 kHz transmissions from IMAGE were made. From these VLF/LF transmissions WM echoes result. The red vertical lines on the top axis indicate presence of MR echoes; green lines SR echoes. The super storm (Dst<-200 nT) occurred on Day #236, major storms (Dst<-100 nT) on days 243 and 254, moderate storms (Dst<-50 nT) on Day #246, #247, and #258, and a minor storm on Day #261.

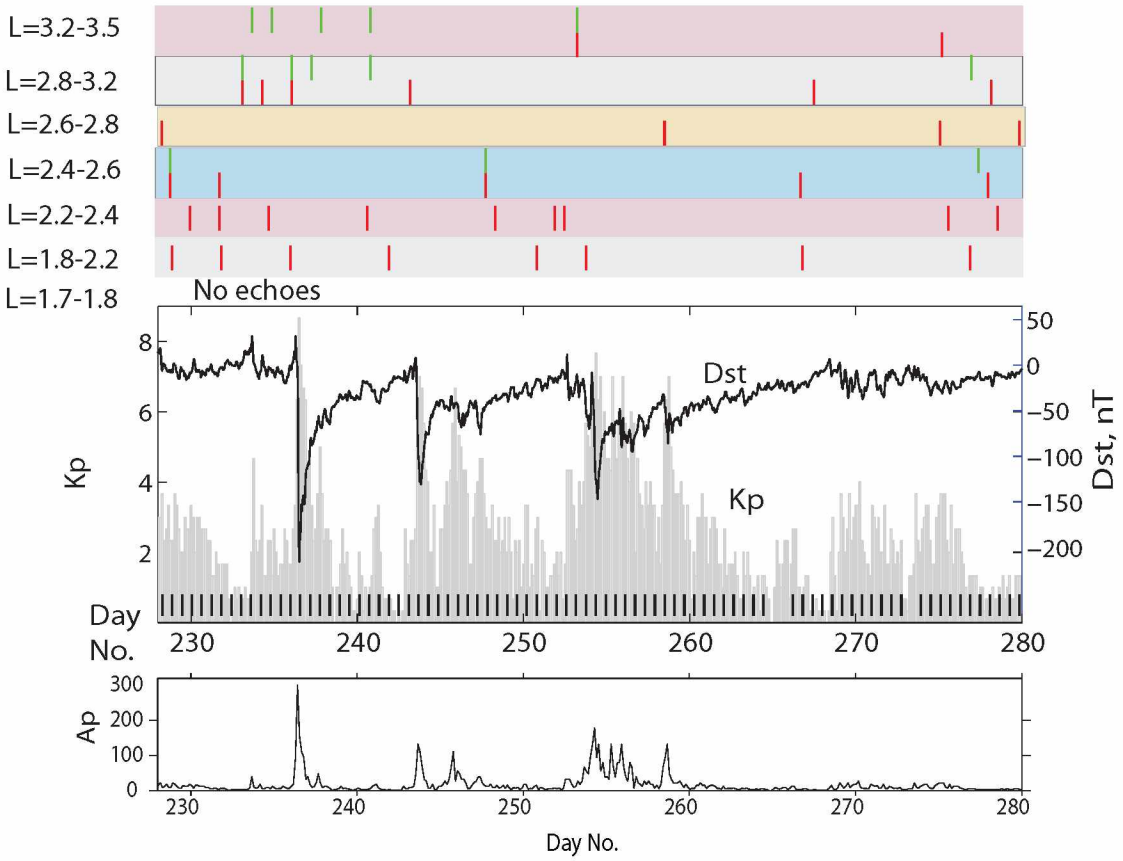

Figure 3.12. Temporal pattern of WM echoes observed on the night-side in the L-shell range 1.7-3.5 during the period 16 August (Day #228, 2 MLT) to 07 October 2005 (Day #280, 4 MLT) as a function of geomagnetic activity. Also shown are the variation of geomagnetic indices Kp (gray bars), Dst (black curve), and Ap (bottom panel). The black lines on the time axis indicate times when 6-63 kHz transmissions from IMAGE were made. From these VLF/LF transmissions WM echoes result. The red vertical lines on the top axis indicate presence of MR echoes; green lines SR echoes. The super storm (Dst<-200 nT) occurred on Day #236, major storms (Dst<-100 nT) on days 243 and 254, moderate storms (Dst<-50 nT) on Day #246, #247, and #258, and a minor storm on Day #261.

3.4 Measurements of locations of plasmapause, cutoffs of MR echoes, and locations of large scale FAIs

3.4.1 Variation of plasmapause on day-side and night-side during the 16 August-06 October 2005 period

Upper hybrid emissions observed in the passive recording of naturally occurring waves on IMAGE were used to determine plasmapause (L_{pp}) location during quiet and disturbed periods. Figure 3.13 shows variation of plasmapause location as a function of geomagnetic activity for the 16 August to 06 October 2005 period. The black vertical bars represent L_{pp} obtained from the passive recording of naturally occurring waves on IMAGE. As can be noted from Figure 3.13 the length of the black bars representing the possible range of L_{pp} varies. This length depend on the time between successive passive recording on IMAGE. When the gap between two passive recordings is large, the satellite moves greater distances, hence the range of L_{pp} will be large.

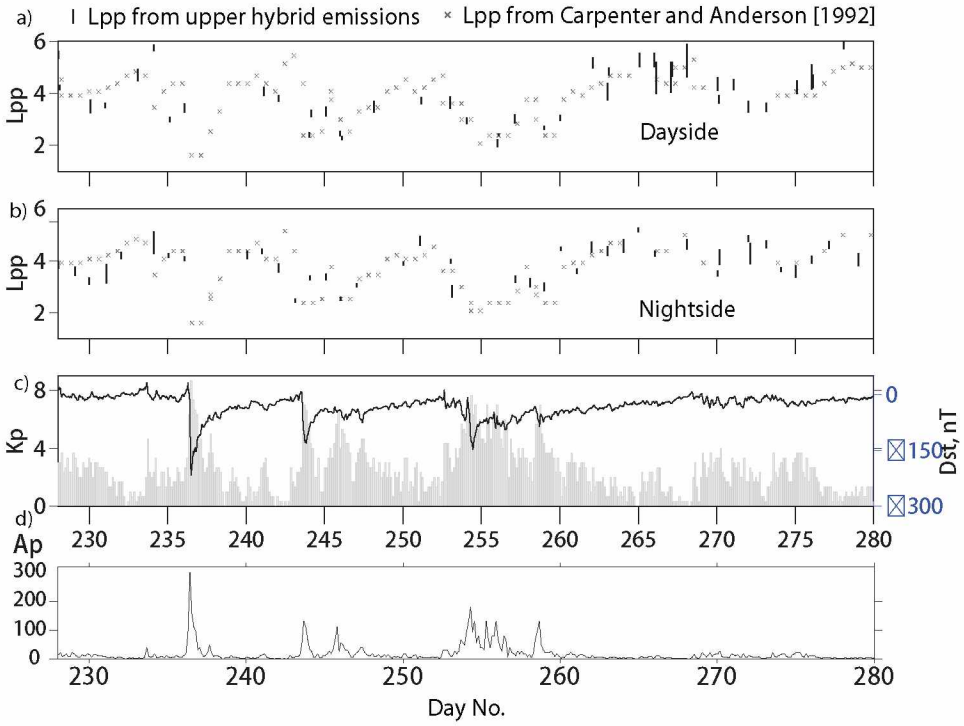

Figure 3.13. Variation of plasmapause location as a function of geomagnetic storm activity obtained from RPI passive recordings and that predicted by Carpenter and Anderson [1992] empirical model.

On the day-side (Figure 3.13a) during the quiet period preceding the storm, L_{pp} location increased from ~3.8 to ~5.8. During the onset phase (Day #235) of the severe storm that occurred on

24 August (Day #236), L_{pp} moved to ~3. During the main phase of the storm, L_{pp} was not available. Before the onset phase (Day #242) of second major storm on 31 Aug 2005 (Day #243) L_{pp} was ~ 4. Plasmapause location roughly moved to L=2.3 during the onset phase. It then increased to ~3.5 during the main phase, and then decreased to ~2.3 during the early recovery phase of the storm. Before the onset phase (Day #252), of the moderate storm on 10 September (Day #253) L_{pp} was ~4. Plasmapause continuously decreased from 4 to L~2.1 during the 09 September to 11 September period (days 252–254). During the quiet period following the storm, L_{pp} was ~ . On the night-side the location of L_{pp} showed similar variation to that on the day-side. In short, (1) on the day-side, plasmapause moved from L~4.5 during the quiet time to L~2.4 during the disturbed time; (2) on the night-side, plasmapause moved from L~4 during the quiet time to L~2.5 during the disturbed time.

With grey cross marks, Figure 3.13 also shows the locations of L_{pp} obtained using the Carpenter and Anderson [1992] empirical model given as $L_{pp} = 5.6 - 0.46(K_{p,max})$, where $K_{p,max}$ is the maximum in Kp in the past 24 hours. The trend in the variation of L_{pp} obtained from the empirical model is in agreement with that obtained from upper hybrid emissions. The minimum L_{pp} obtained form the empirical model was 1.8 on both day-side and night-side on day #236 (main phase of the first major storm). The maximum difference in L_{pp} obtained from f_{uh} and that from the empirical model is about 1L on Day #243 on the night-side and on Day #261 on the day-side.

3.4.2 Variation of lower and upper cutoffs of MR echoes as a function of geomagnetic storm activity

As demonstrated in section 2.5, the upper cutoff, $f_{MR,max}$, of an MR echo is close to but lower than $f_{lh,max1}$ along $\mathbf{B_0}$. Figure 3.14 shows variation of lower ($f_{MR,min}$) and upper cutoffs ($f_{MR,max}$) of MR echoes, which give the local f_{lh} and the maximum f_{lh} along $\mathbf{B_0}$, as a function of geomagnetic activity for the 16 August to 06 October period. Typically, f_{lh}calculated from independently obtained values of f_{pe} and f_{ce}, is within 0.3–0.6 kHz of measured $f_{MR,min}$ [Sonwalkar et al., 2011a] and, as discussed in Chapter 2, maximum in f_{lh} along $\mathbf{B_0}$ was found to be greater than but within a few hundred Hz of $f_{MR,max}$ and close to $f_{OI,min}$. Thus $f_{MR,max}$ can be used to place a lower bound on $f_{lh,max1}$.

Measurement of $f_{MR,max}$ is significant because it determines the upper frequency cutoff of nonducted WM waves, of manmade or natural origin, that are magnetospherically reflected and can remain trapped in the magnetosphere. It also provides an indirect measure of the O^+/H^+ transition height where O^+ and H^+ ions are in equal numbers. The mid-latitude O^+/H^+ transition height is of importance because it corresponds to the transition from the main ionosphere to the plasmasphere [Sonwalkar et al., 2011a; Lemaire and Gringauz, 1998]. As seen from Equation (1) and its discussion in Chapter 2; section 2.1.1, $f_{lh,max1}$ occurs when m_{eff} starts increasing rapidly. This can also be noticed in Figure 2.9a. Assuming f_{ce} and f_{pe} roughly the same, a lower value of $f_{lh,max1}$ indicates increase in m_{eff} and implies an increase in the number of heavy ions and thereby an increase in O^+/H^+ transition height.

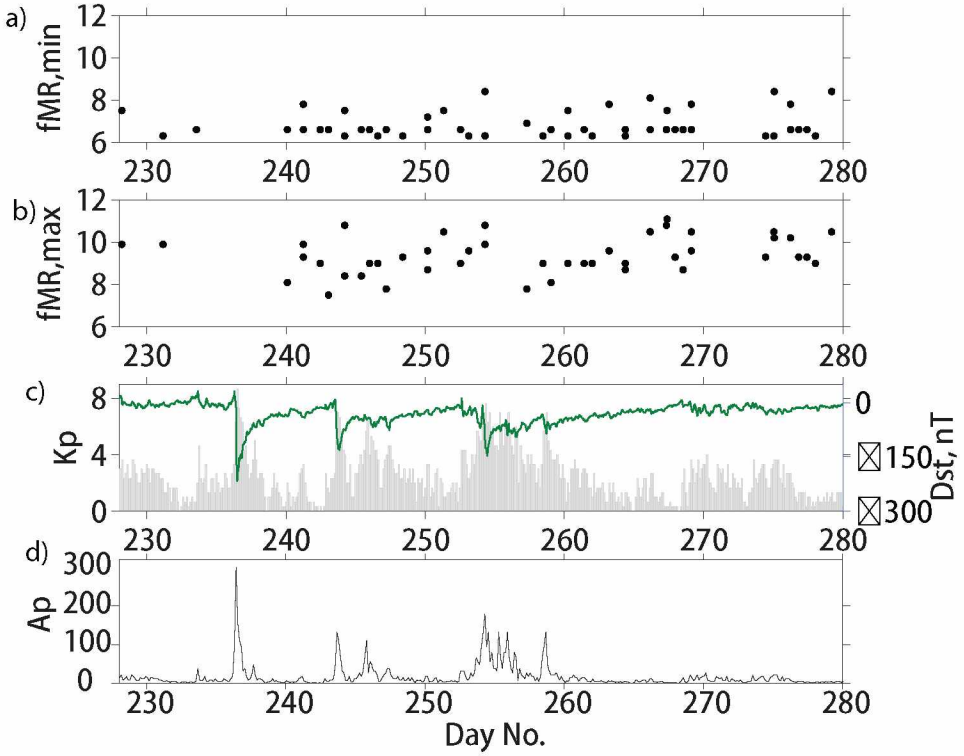

Figure 3.14. Variation of lower and upper cutoffs of MR echoes as a function of geomagnetic storm activity

In Figure 3.14 the lower cutoffs (Figure 3.14a) do not show any pattern with geomagnetic activity. This is expected since f_{lh} decreases with altitude and the echoes were observed at a range of altitudes below 4000 km, the variation in f_{lh} will be random. The upper cutoffs (Figure 3.14b) show a decrease during the early recovery period of the storms, followed by a recovery. The

average upper cutoff during quiet periods is on the order of 10 kHz. The decrease in the upper cutoffs during storm recovery phase is indicative of increase in the transition height or heavy ions during storm time.

3.4.3 Locations of large scale irregularities as obtained from patchy SR echoes during the 16 August to 06 October 2005 period

At all latitudes including low- and mid-latitudes, plasmapause, auroral, and polar regions FAIs occur [Kelley, 2009; Schunk and Nagy, 2000; Hunsucker and Hargreaves, 2003]. They are generated by various processes including plasma instabilities, particle precipitation, and plasma drifts occurring in the ionosphere [Kelley, 2009]. These plasma processes are enhanced during disturbed solar and geomagnetic conditions, leading to the generation of plasma density structures. Measurement of irregularities is important because they contribute to the fading of high frequency trans-ionospheric signals and to the degradation of ground-satellite communications.

As noted in section 2.2.2 of Chapter 2 large scale FAIs can deflect the ray paths of echoes and can lead to no detection of echoes. These large scale FAIs can lead to patchy echoes (absence of echoes at some frequencies). Since WM waves propagate close to the field lines, measuring frequencies at which echoes are absent and obtaining the L-shell of the satellite when those frequencies were transmitted gives the field lines along which large scale FAIs are present. Figure 3.15 shows the field lines along which large scale FAIs are present during quiet and disturbed periods. The locations of these FAIs are obtained from the measurements of patchy SR echoes observed during the 6 August to 06 October 2005 period. As can be noted from the figure, large scale FAIs are present on the day-side as well as the night-side during both quiet (top panel) and disturbed periods (bottom panel). Relative to quiet time, FAIs are more on the night-side during disturbed periods. It is well-known from the literature that FAIs respond to geomagnetic storms. For example, Pfaff et al. [2008] found close relation between development of a storm as indicated by Dst and the increased ambient density and the region of irregularities. Mendillo [2006] often found large increases in the mid-latitude ionospheric density and TEC in the local dusk sector during magnetic storms.

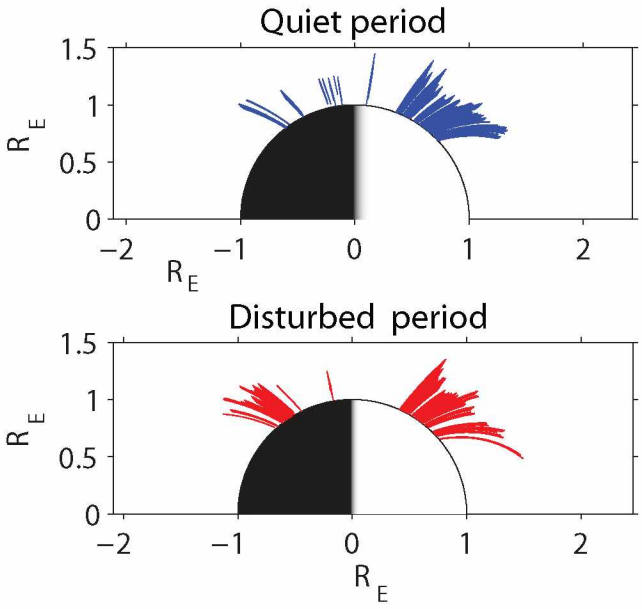

Figure 3.15. Locations of large scale irregularities during geomagnetically quiet and disturbed periods

3.5 Field-aligned electron density and ion composition at 1.7<L<2.4 as a function of geomagnetic storm activity

3.5.1 Baseline electron densities at different L shells on day-side and night-side

As noted in Chapter 1, geomagnetic storms can dramatically change plasma density and composition. Measurement of field-aligned plasma density and composition is critical to understanding the dynamic processes that determine distribution of plasma along a field line. To study the storm time variations in the plasma density and composition, a subset of 63 whistler mode echoes from the day-side and ∼18 whistler mode echoes from the night-side observed in the 1.7<L<2.4 L-shell range during 16 August to 06 October 2005 were selected . These L-shells remain within the plasmasphere throughout the 53-day period because the minimum plasmaspause location observed was L=2.4, obtained from the passive measurements.

By applying the whistler mode radio sounding method to echoes observed during the two quiet periods, one preceding and the other following the disturbed period, average density models and ion composition at different L-shells was determined. Figure 3.16 shows average electron density along different L-shells. At altitudes below 1500 km, electron density did not show any trend in

variation with L (Figure 3.16a). Electron density increased from L=1.8 to L-2.0 and decreased from L=2.0 to 2.2. Electron density at L=2.2 and 2.4 is within 1–2%. At altitudes above 1500 km, average electron density decreased with L (Figure 3.16b).

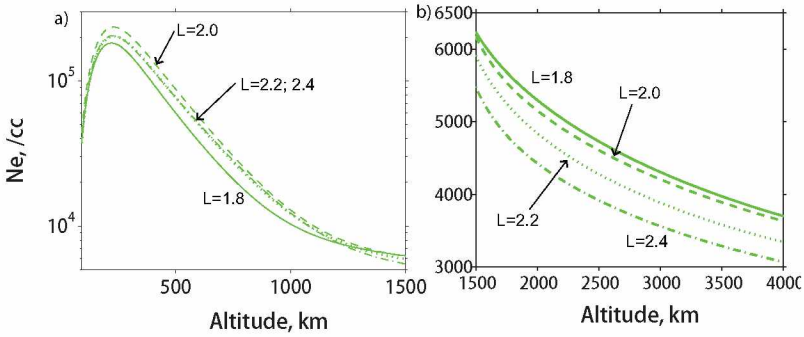

Figure 3.16. Quiet time field-aligned average electron density at different L on the day-side. (a) Electron density below 1500 km. (b) Electron density above 1500 km. At altitudes below 1500 km, the average quiet time N_e did not show any trend in variation with L. Above 1500 km, N_e decreased with L.

Figures 3.17–3.19 show, respectively, variation in average α_{H^+}, α_{He^+} and α_{O^+} ion concentrations with L. Average α_{H^+} decreased with L from 1.8–2.2, and it is almost the same at L=2.2 and 2.4. Average α_{He^+} at L=1.8 and 2.0 is comparable, it increased from L=2.0 to 2.2. Average α_{He^+} at L=2.2 and 2.4 is comparable. Average α_{O^+} increased from L=1.8 to 2.0 and it remained almost the same in the L shell range 2.0 to 2.4.

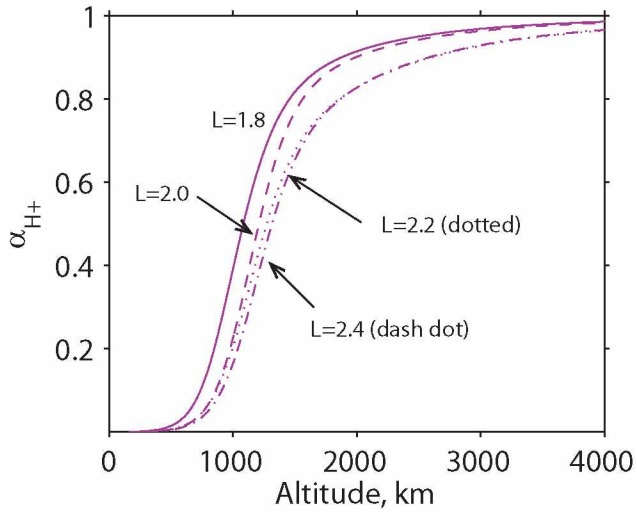

Figure 3.17. Quiet time average field-aligned α_{H^+} at different L on the day-side. The average α_{H^+} decreased with L.

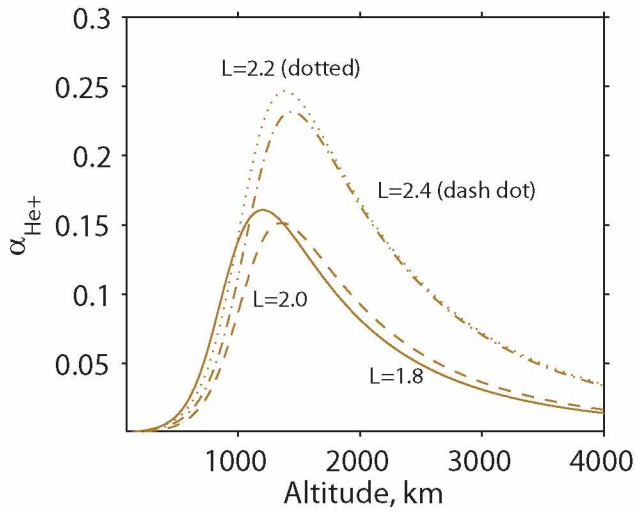

Figure 3.18. Quiet time average field-aligned α_{He^+} at different L on the day-side. The average α_{He^+} did not show any trend in variation with L.

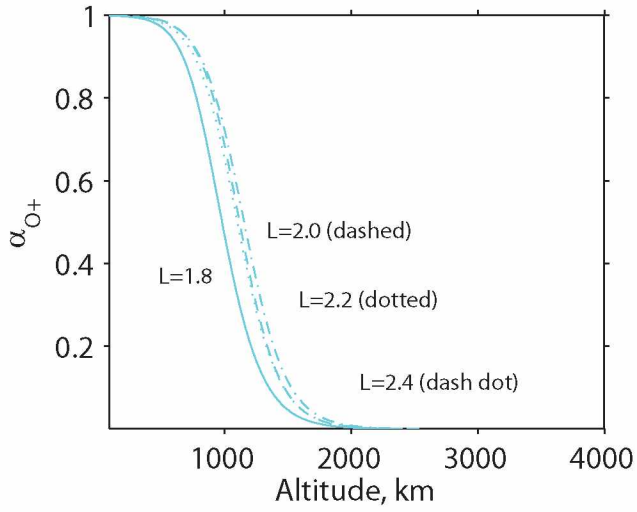

Figure 3.19. Quiet time average field-aligned α_{O^+} at different L on the day-side. The average α_{O^+} increased with L.

On the night-side during quiet periods (Figure 3.12) there were: (1) no echoes observed in the L-shell range 1.7–1.8; and (2) only four cases observed in the L-shell range 1.9–2.2. Of these four cases, three were in the quiet period preceding the storm period, and one followed the storm period. All three cases observed during the quiet period before the disturbed period were noisy, and it was not possible to obtain electron and ion densities reliably. (3) There were three echoes observed in the L-shell range 2.2–2.4 during the quiet period preceding the storm period and two

echoes during the quiet period following the storm period. The latter two cases were noisy, and it was not possible to obtain electron and ion densities reliably.

Figure 3.20 shows field-aligned electron density for the four quiet time cases: three observed during the quiet period before the storm in the L-shell range 2.2–2.4 and one observed during the quiet period after the storm in the L-shell range 1.8–2.2. Figure 3.20(a) shows N_e below 1500 km and Figure 3.20(b) shows N_e above 1500 km. The electron density did not show any trend in variation with L. The N_e at the F2 peak on all four days was different. Also note that the scale height with which N_e decreases is high on August 18 (Day #230) relative to other quiet days. Of the four days, the minimum N_e at the F2 peak was on 16 August (Day #228), and the maximum N_e at the F2 peak, about three times that of 16 August, was on 18 August (Day #230). The N_e above 1500 km altitude also did not show any trend in L-shell. The electron density obtained on 16 August (Day #228) and that on 19 August (Day #231) was almost the same (within 5%). The electron density obtained on 18 August (Day #230) was within 10% of that on 03 October (Day #276). The N_e on all four days was within 30–40%.

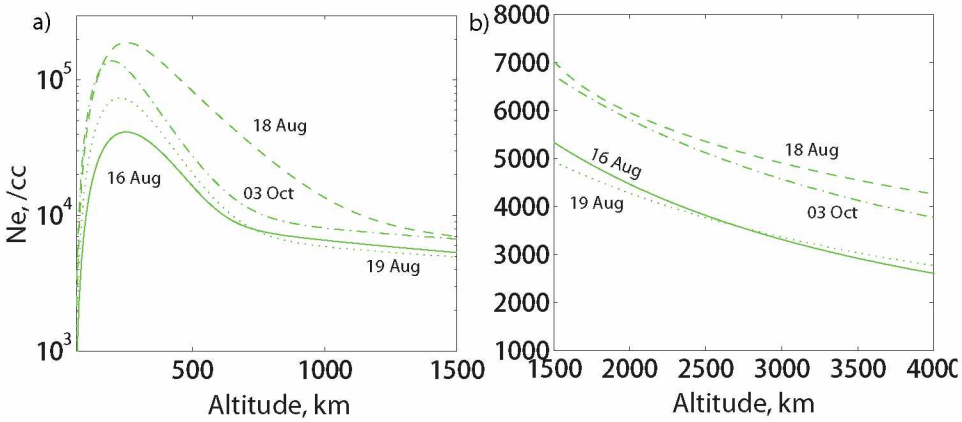

Figure 3.20. Field-aligned electron density obtained during quiet time on the night-side. (a) Electron density below 1500 km. (b) Electron density above 1500 km.

Figure 3.21 shows ion composition obtained from the four quiet cases observed on the night-side. The ion compositions obtained from three cases (18 August, 19 August, and 03 October) were similar. Relative to the ion composition obtained from these three cases, on 18 August (Day #230, dashed curve) α_{H^+} was substantially low, and α_{He^+} and α_{O^+} were high.

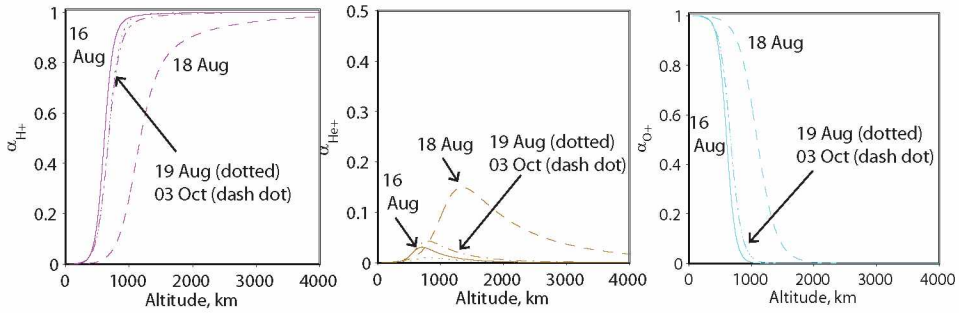

Figure 3.21. Field-aligned ion composition obtained during quiet time on the night-side. From left to right is α_{H^+}, α_{He^+}, and α_{O^+}.

3.5.2 Variation of field-aligned electron density and ion composition during the 23-30 August 2005 disturbed period that included a severe storm

During the 23–30 August 2005 disturbed period, a severe storm occurred on 24 August 2005 (Day #236). On 24 August Dst minimum was -220 nT (at 12 UT) and Kp maximum was -9. The onset of 24 August 2005 storm was at 7 UT (Dst increased to 32 nT) and main phase (decrease in Dst) started at 10 UT. Figure 3.22(a) shows the temporal pattern of WM echoes observed in the L-shell range 1.7-2.45 during the 16 August to 02 September 2005 period. After the main phase of the storm, the first WM echo (labeled N) was observed on 26 Aug 2005 (Day #238), but that case was noisy: electron and ion densities could not be obtained reliably. On 23 August 2005 (labeled Q1) an SR echo was observed at 08:34 UT. The electron density obtained from this case is shown by red curve in Figures 3.22(b) and 3.22(c). Figures 3.22(b) and 3.22(c) show electron densities (solid curve) obtained below 1500 km and above 1500 km during the recovery period of the 24 August 2005 storm.

Relative to the electron density obtained on 23 August 2005 (Q1), the electron densities obtained at all altitudes during the recovery period are either close or greater indicating recovery of electron density. For altitudes above 1500 km the electron density at L$\sim$2 was within 20% and the electron density at L$\sim$2.3 was within 5%. On 31 August 2005 (R4), electron density obtained at L=2 and 2.4 are respectively $\sim$ 2 times and 1.5 times greater than the electron density obtained on 23 August 2005.

Figures 3.23, 3.24, and 3.25 respectively show the variation of α_{H^+}, α_{He^+}, and α_{O^+} during the 23 August to 31 August 2005 period. The red curves in these figures indicate ion composition

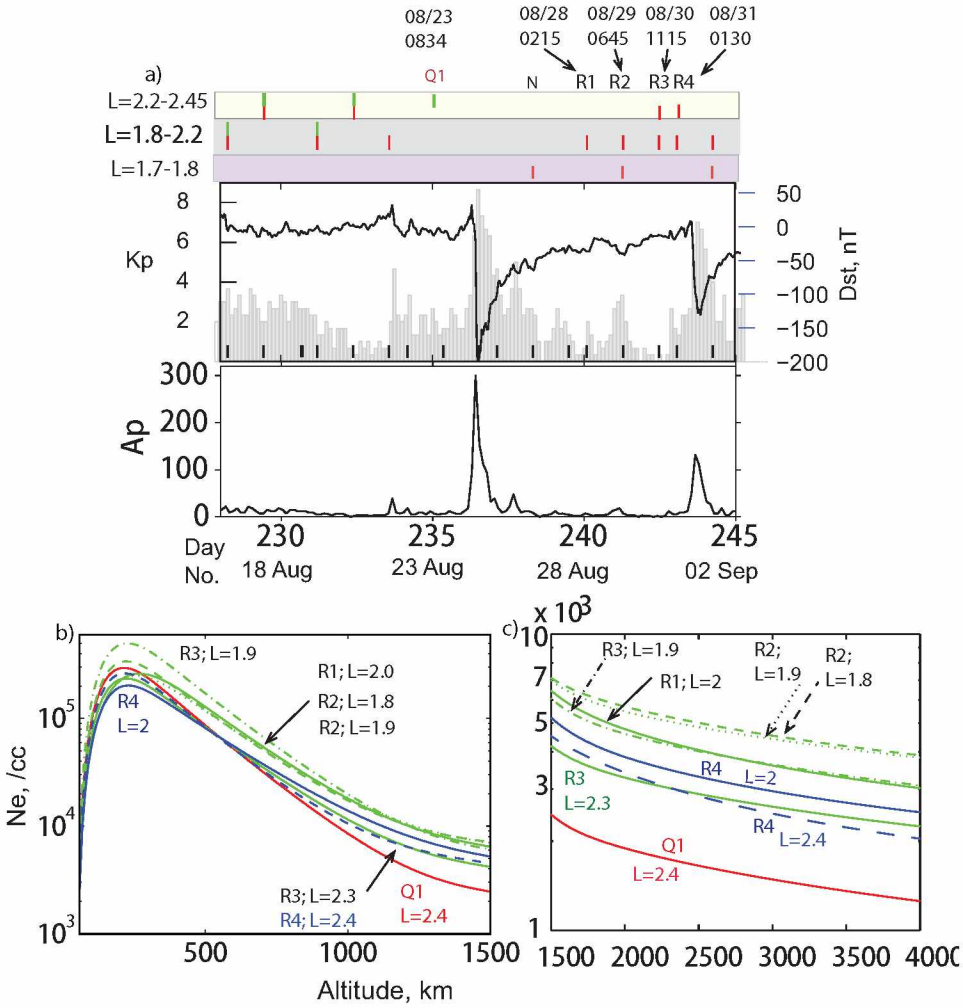

Figure 3.22. Variation of the electron density during the recovery phase of 24 August 2005 severe storm.

obtained on 23 August 2005. The blue curves represent ion composition on 31 August 2005 at L=2 (solid curve) and L=2.4 (dashed curve).

There was substantial decrease in α_{H^+}, relative to ion composition obtained on 23 Aug 2005, on 28 Aug 2005 (R1). The α_{H^+} on R2 and R3 is comparable to that on 23 August 2005. On 31 August 2005 (R4) there was decrease in α_{H^+}. On 28 August 2005 (R1) there was substantial increase in α_{He^+}. The α_{He^+} on R2 and R3 is comparable to that on 23 August 2005. On 31 August 2005 (R4) there was increase in α_{He^+}. On all four days α_{O^+} is comparable to that on Q1. It is speculated that the decrease in α_{H^+} and increase in α_{He^+} on 31 Aug 2005 (R4) could be because of another major storm that occurred on 31 August 2005 with onset was $\sim$ 11 UT. The R4 case is in the onset phase of the major storm on 31 August 2005.

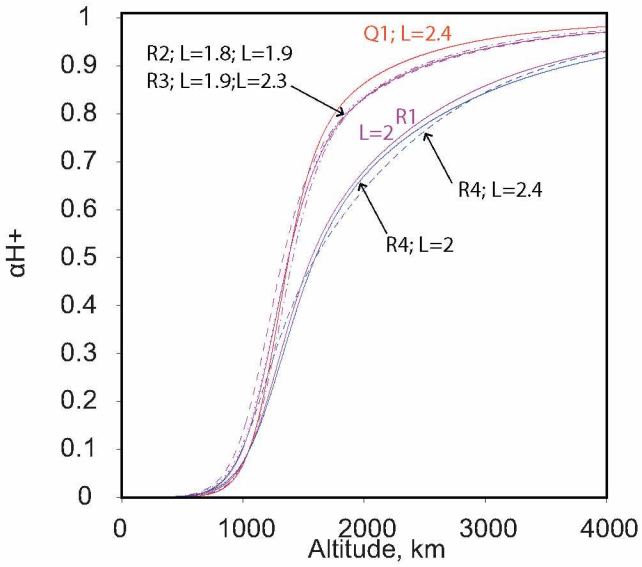

Figure 3.23. Variation of the α_{H^+} during the recovery phase of the 24 August 2005 severe storm.

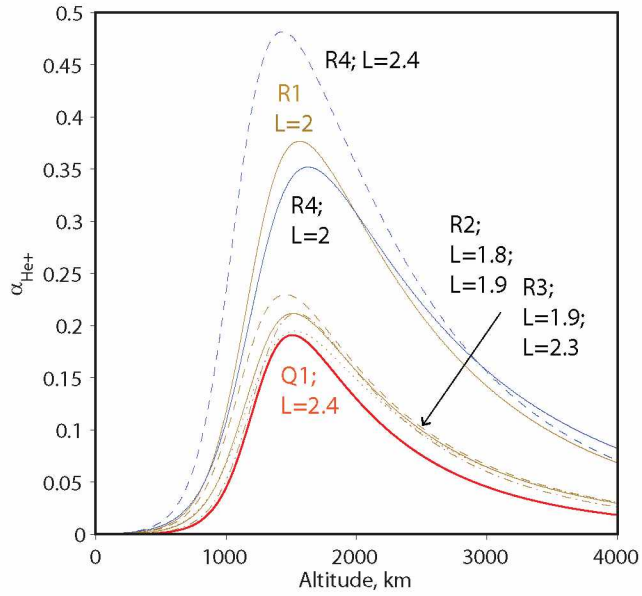

Figure 3.24. Variation of the α_{He^+} during the recovery phase of the 24 August 2005 severe storm.

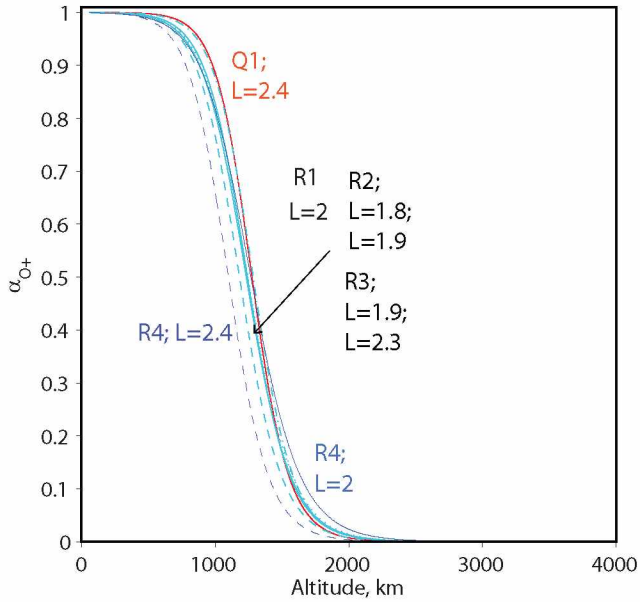

Figure 3.25. Variation of the α_{O^+} during the recovery phase of the 24 August 2005 severe storm.

Figure 3.26 shows the temporal pattern of WM echoes observed on the night-side in the 1.7-.4 L-shell range during the 16 August to 02 September 2005 period. As can be seen from the figure, two MR echoes are observed during the recovery period of the 24 August 2005 storm, but both cases are noisy and electron and ion densities could not be measured reliably.

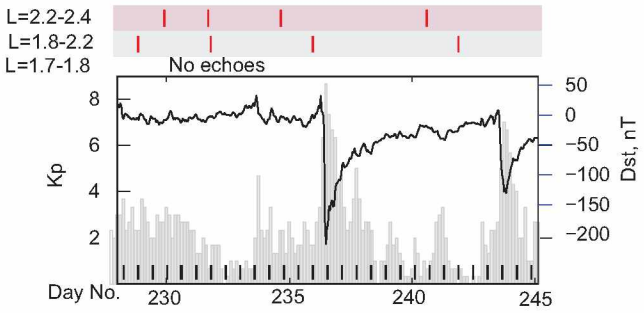

Figure 3.26. Temporal pattern of echoes on the night-side during the 16–31 August 2005 period. Both the cases observed during the recovery phase of the 24 August storm were noisy and reliable electron density and ion composition could not be obtained.

From the WM radio sounding results, the variations of field-aligned N_e and α_i resulting from the 24 August 2005 storm can be summarized as follows: the day-side densities recovered by or before 28 August 2005, within four days of the storm. On 28 August, the α_{H^+} was lower and α_{He^+} was greater than the quiet time values preceding the storm, which indicates that these ions

did not recover after the disturbance. On 29 August, five days after the storm, α_{H^+} and α_{He^+} were comparable to quiet values before the storm. The α_{O^+} recovered by 28 August 2005. No whistler mode sounding data was available before 28 August on the day-side to get estimates of density depletions or enhancements during the main and early recovery phases of the storm.

3.5.3 Variation of field-aligned electron density and ion composition during the 30 August-10 September 2005 disturbed period that included one major storm and two moderate storms

Following the severe storm on 24 August 2005, there was another major storm on 31 August 2005 (Day #243). The minimum in Dst on Day #243 was -131 nT (at 20 UT) and the maximum in Kp was 7. The storm onset was on 30 August at the end of the day (18 UT). The storm developed by midday of 31 August 2005 (14 UT). Three days after the major storm, on 03 September (Day #246),there was a moderate storm. The minimum in Dst was -68 nT and the maximum in Kp was 5+. Note that although Dst did not indicate any disturbance on 02 September, Kp indicated moderate geomagnetic disturbance by the close of the 02 September 2005. The moderate storm on 02–03 September was followed by another moderate storm on 04 September (Day #247). The minimum in Dst on 04 September was -76 nT and the maximum in Kp was -5.

Figure 3.27(a) shows the temporal pattern of WM echoes observed during the Day #240–255 period, which included one major and two moderate storms. Given at the top of the figure are the date and time at which these echoes were observed. The vertical bars labeled N indicate noisy echoes that could be used to obtain reliable electron and ion density measurements. Figures 3.27b and 3.27c, respectively, show variation of electron density below and above 1500 km during 31 August to 03 September 2005 (Day #243-246) period. The electron density obtained on 31 August 2005 at ~01:30 UT (O1, O2), during the onset phase of the major storm, at L=2 and 2.4 is shown respectively by solid and dashed red curves. The electron density at the F2 peak on 01 and 02 September (R1, R2) was comparable to that during the onset phase. On 03 September (R3) the electron density at the F2 peak decreased by ~40%. Above 1500 km, relative to onset phase electron density, on 01 September (R1) electron density increased by ~50% and on the second day of recovery (02 September, R2) electron density was comparable. On the third day of recovery (03 September, R3) electron density again increased by ~35%. As noted earlier, on 02 September

at 18 UT Kp indicated moderate disturbance and on 03 September there was a moderate storm as indicated by Dst. The case R3 was observed in between these two disturbances of 02 and 03 September. It is probable that the decrease in the N_e at F2 peak and increase in N_e at altitudes above 1500 km is due to the plasma flowing up from the ionosphere to plasmasphere in the early phases of the storm. It should be noted that enhancement of electron densities in the plasmasphere during the storm recovery phase were not observed earlier until recently by Chi et al. [2005].

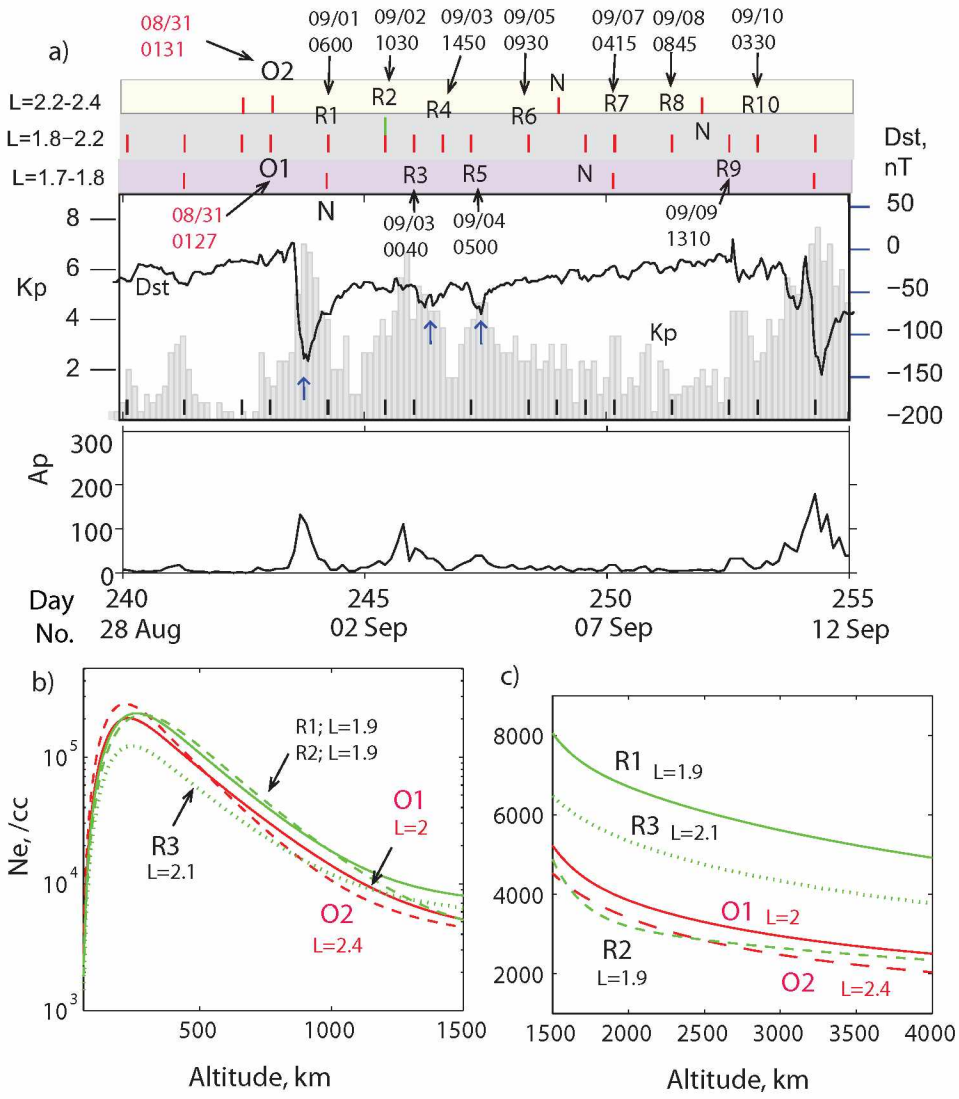

Figure 3.27. Variation of field-aligned electron density on the day-side during the recovery phase of 31 August 2005 storm. (a) Temporal pattern of WM echoes during the 28 August to 11 September 205 period. (b) Variation of N_e below 1500 km during the 31 August-03 September 2005 period. (c) Variation of N_e above 1500 km during the 31 August-03 September 2005 period.

Figure 3.28 shows the variation of electron density during the 03 September to 10 September disturbed period (Day #246-253). The top panel shows N_e variation during the recovery of moderate storm on 03 September, bottom two panels shows N_e variation during the recovery of 04 September moderate storm. In Figures 3.28(a) and 3.28(b) the red dash dot curve represents electron density obtained on 03 September at 00:40 UT (R3). Relative to the electron density obtained on R3, on R4 (03 September; 1450 UT) N_e at all altitudes increased. The N_e increased by $\sim$40% at the F2 peak and by $\sim$30% at altitudes above 1500 km. On 04 September (R5), N_e at the F2 peak increased further (almost 2 times) where as N_e at altitudes above decreased by about $\sim$45%.

In Figures 3.28(c) and 3.28(d) the red dash dot curve represents electron density obtained on 04 September at 05:00 UT (R5) before the moderate storm on the same day occurred. Relative to the densities on R5, on R6 (05 September; 09:30 UT) electron density below 1500 km was comparable. Above 1500 km, electron density increased by $\sim$20%. On 07 September (R7), there were two WM echoes observed one at L=1.8 and other at L=2. At both L-shells electron density at the F2 peak decreased and electron density above 1500 km increased indicating plasma flow from the ionosphere to the plasmasphere.

Figures 3.28(e) and 3.28(f) show electron density obtained during the 08–10 September 2005 period. In red dashed and dotted curves indicate electron density obtained on R7 at L=1.8 and L=2. Below 1500 km, relative to the densities on R7, the F2 peak densities increased on 08 September (R8) and 09 September (R9) and decreased on 10 September (R10). The N_e above 1500 km continued to increase indicating refilling state of the plasmasphere. Note that on 10 September there was a moderate storm (Dst,min=-70 nT at 22 UT). Since case R10 falls in the onset phase of the moderate storm on 10 September the increase in electron density could be the result of the storm.

Figure 3.29 shows the variation of ion composition during the 31 August to 10 September 2005 period. The red solid and dashed curves in the top panel, respectively, represent ion composition at L=2 and L=2.4 during the onset phase of 31 August 2005 major storm.

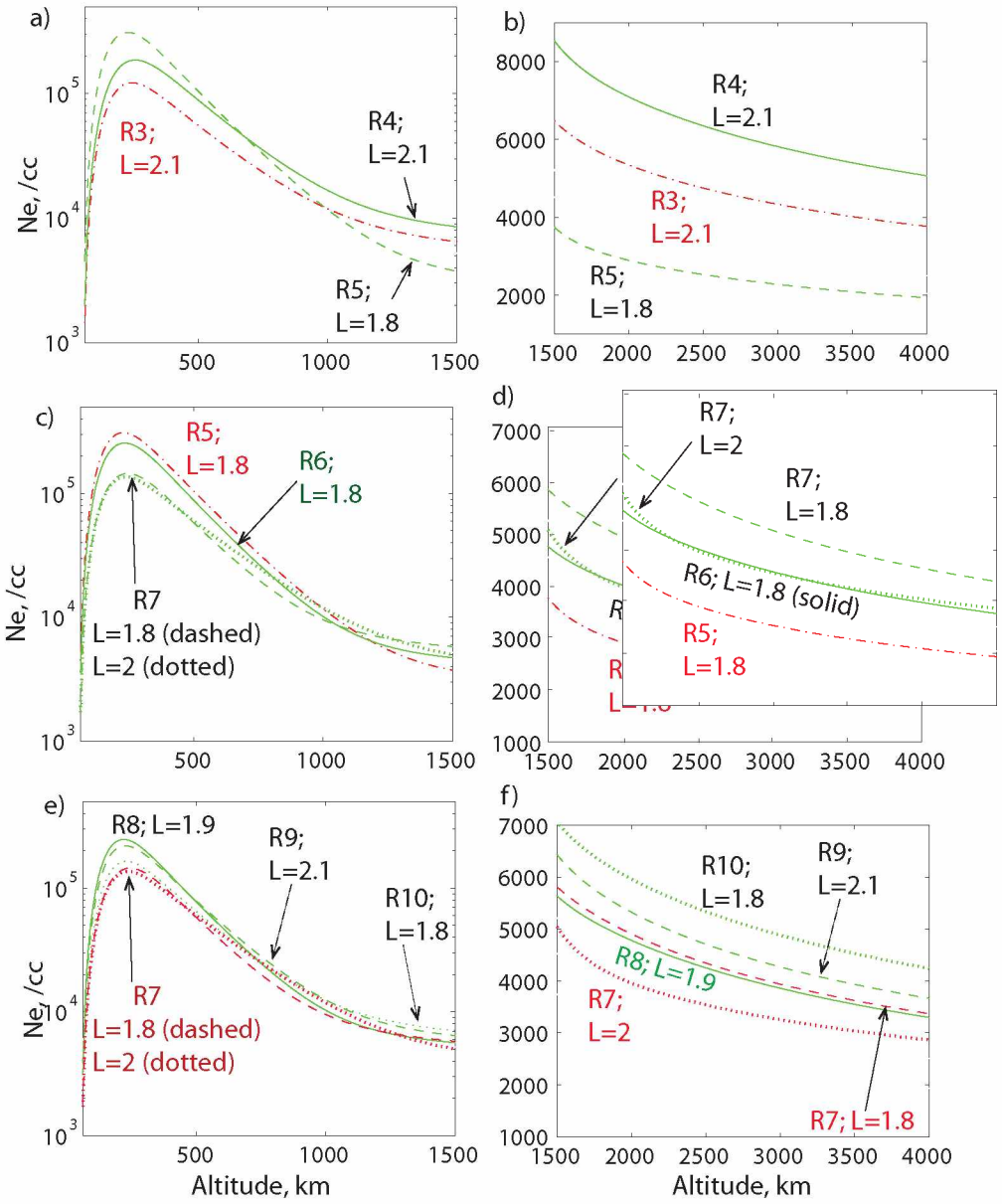

Figure 3.28. Variation of the field-aligned electron density on the day-side during the 03–10 September 2005 disturbed period. The top panel shows N_e variation during the recovery phase of 03 September moderate storm. Bottom two panels show N_e variation during the recovery phase of 04 September moderate storm.

The top panel shows the variation of α_i during the 01–03 September 2005 period, recovery phase of the major storm on 31 August 2005. Relative to the α_i during the onset phase: α_{H^+} was higher on all three days (R1, R2, R3); α_{He^+} was low on all three days; α_{O^+} was comparable on the first (R1) and third day (R3) and was higher on second day (R2). The α_{H^+} increased on the first day of recovery (01 September; R1) and then decreased on the second day (02 September; R2). On the third day α_{H^+} increased at altitudes below 1500 km and decreased at altitudes above 1500 km. The α_{He^+} decreased substantially on R1 and it increased on R2 and R3. The α_{O^+} was comparable to that during onset phase on R1, it increased on R2 and then decreased to that on R1 on 03 September (R3).

The second panel shows the variation of α_i on 03 and 04 September 2005, recovery phase of the moderate storm on 03 September 2005. Note that 02 September was also a disturbed day as per Kp. The α_i on R3 falls in the onset phase of 03 September 2005 moderate storm or recovery of 02 September 2005 moderate storm. The red dash dot curves in this panel represent α_i on R3. Relative to the α_i obtained on R3: α_{H^+} on R4 (03 September 450 UT) was comparable at altitudes below 1500 km and it increased above 1500 km. On R5 (04 September) α_{H^+} decreased at altitudes below 1500 km and above 1500 km it was comparable to that on R4; α_{He^+} on R4 (03 September 04:50 UT) was comparable at altitudes below 1500 km and it decreased above 1500 km. On R5 (04 September) α_{He^+} decreased at altitudes below 1500 km and above 1500 km it was comparable to that on R4; α_{O^+} on R5 (03 September 04:50 UT) was comparable. On R5 (04 September) α_{O^+} increased at altitudes below 1500 km and above 1500 km it was comparable to that on R5;

The third panel shows the variation of α_i during the 05–07 September 2005 period, recovery phase of 04 September 2005 moderate storm. The red dash dot curves in this panel represent α_i on R5 (04 September before the storm). Relative to the ion compositions obtained on R5: α_{H^+} increased at altitudes on R6 (05 September). On R7 (07 September; L=1.8) α_{H^+} at altitudes below 1500 km was comparable to that on R6 and it decreased at altitudes above 1500 km and is comparable to that on R5. On 07 September at L=2 (R7) α_{H^+} is comparable to that on R5. The α_{He^+} deceased at altitudes above 1500 km on R6. It increased at all altitudes on R7 at L=1.8. On September 07 at L=2 (R7) it α_{He^+} was comparable to that on R5. The α_{O^+} decreased on R6 (L=1.8) at altitudes below 2000 km, and it further decreased on R7 at L=1.8.On R7 at L=2 (07 September) α_{O^+} was comparable to that on R5 at L=1.8.

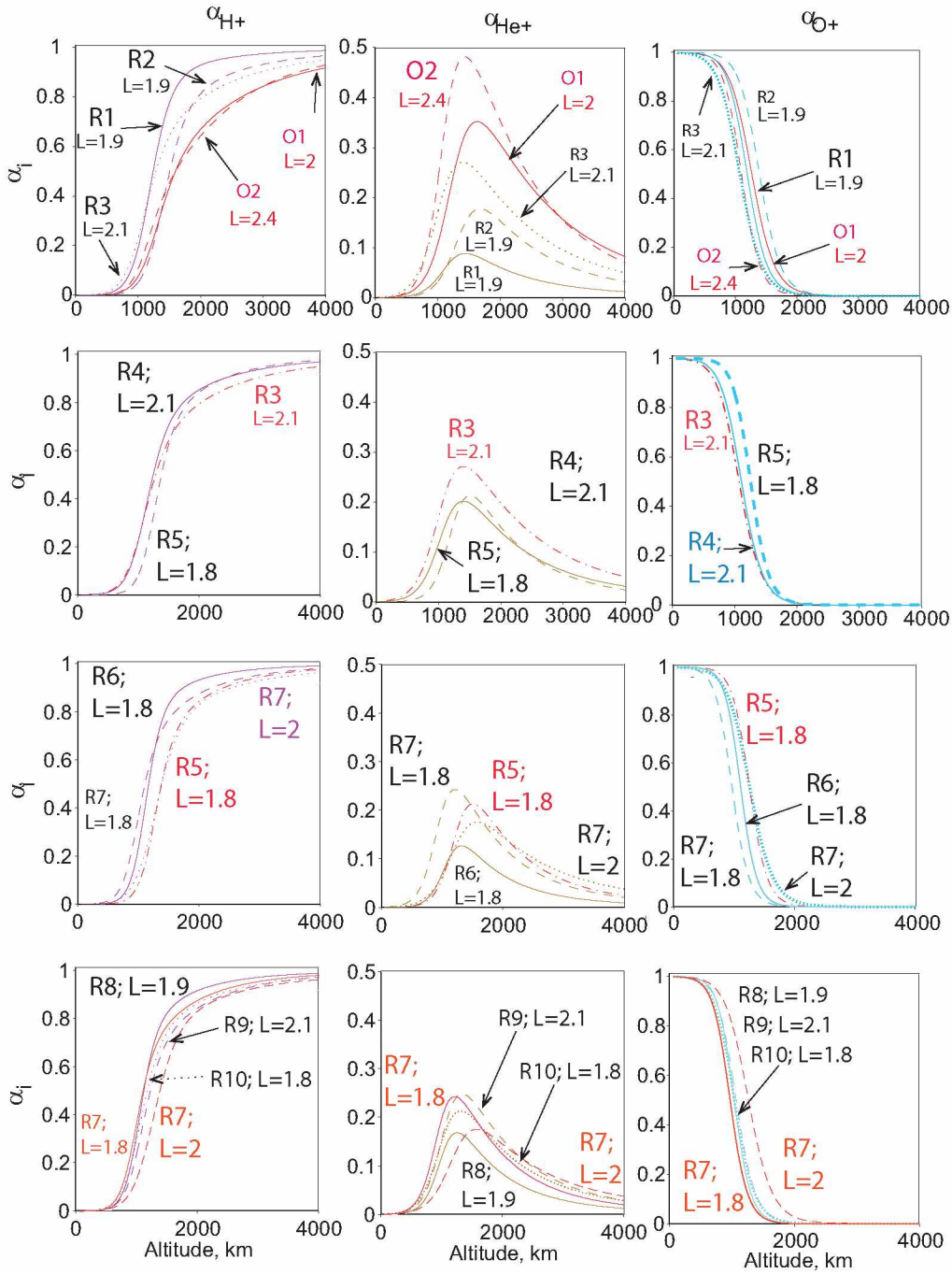

Figure 3.29. Variation of field-aligned ion composition on the day-side during the 03–10 September 2005 disturbed period. The top panel shows the variation of α_i during the 01–03 September 2005 period. The second panel shows the variation of α_i on 03 and 04 September 2005. The third panel shows the variation of α_i during the 05–07 September 2005 period. The bottom panel shows the variation of α_i during the 08–10 September 2005 period.

The bottom panel shows the variation of α_i during the 08–10 September 2005 period. The red solid and dashed curves in this panel, respectively, represent α_i on 07 September at L=1.8 and L=2 (R7). Relative to the ion compositions obtained on R7: α_{H^+} increased on R8 (September 08) at altitudes greater than 1500 km. The α_{H^+} on R9 (09 September) and R10 (10 September) is almost the same, at lower altitudes it is greater than that on R6 and altitudes above 1500 km it is comparable to that on R7. The α_{He^+} on R8 (08 September) decreased at altitudes greater than 1500 km. On 08 September at altitudes above 1500 km and on R9 (09 September), and R10 (10 September) at altitudes it is comparable. α_{O^+} was roughly the same on all three days, R10, R11, and R2. It is lower than the α_{O^+} on R6 at altitudes below $\sim$1500 km and was comparable above.

Figure 3.30 shows the variation of electron density on the night-side during the 01–10 September 2005 period. Figure 3.30(a) shows that only one WM echo was observed on 01 September at 2042 UT during the recovery phase of the 31 Aug 2005 major storm. In Figures 3.30(b-d), the red solid and dashed curves, respectively, represent the quiet time maximum and minimum electron density obtained on quiet days (16 August and 18 August 2005) on the night-side. The N_e obtained on 01 September 2005 falls between these two curves indicating that the N_e recovered from the 31 August 2005 disturbance. After the two moderate storms on 03 and 04 September 2005, WM echoes were observed on 05, 07 , 08, 09, and 10 September 2005. However, the cases on 05 and 09 September (labeled N in Figure 3.30(a)) were noisy, and reliable electron and ion densities could not be obtained. Figures 3.30(c) and 3.30(d), respectively, show variation of N_e below and above 1500 km during the 07 to 10 September 2005 period. The N_e at the F2 peak remained within the quiet time maximum and minimum F2 peak values on all days. The scale height with which electron density falls off is greater on R2 (07 September 2005 L=2.3). At altitudes above 1500 km, on R2 electron density was 10-40% lower than the minimum quiet time N_e. On R3 (07 September; L=1.9) N_e is comparable to minimum quiet time N_e. The electron density on R4 (08 September L=2.3) and R5 (10 September L=1.9), respectively, is comparable to minimum and maximum electron density during quiet time. The variations in N_e indicate there was significant loss of plasma (more than 40%) on the night-side after the two moderate storms, one on 03 September and the other on 04 September, and that the plasmasphere was in refilling stage on 07 September.

Figure 3.31 shows variation of ion composition during the 01–10 September 2005 period on the night-side. The red solid and dashed curves, respectively, represent the quiet time maximum

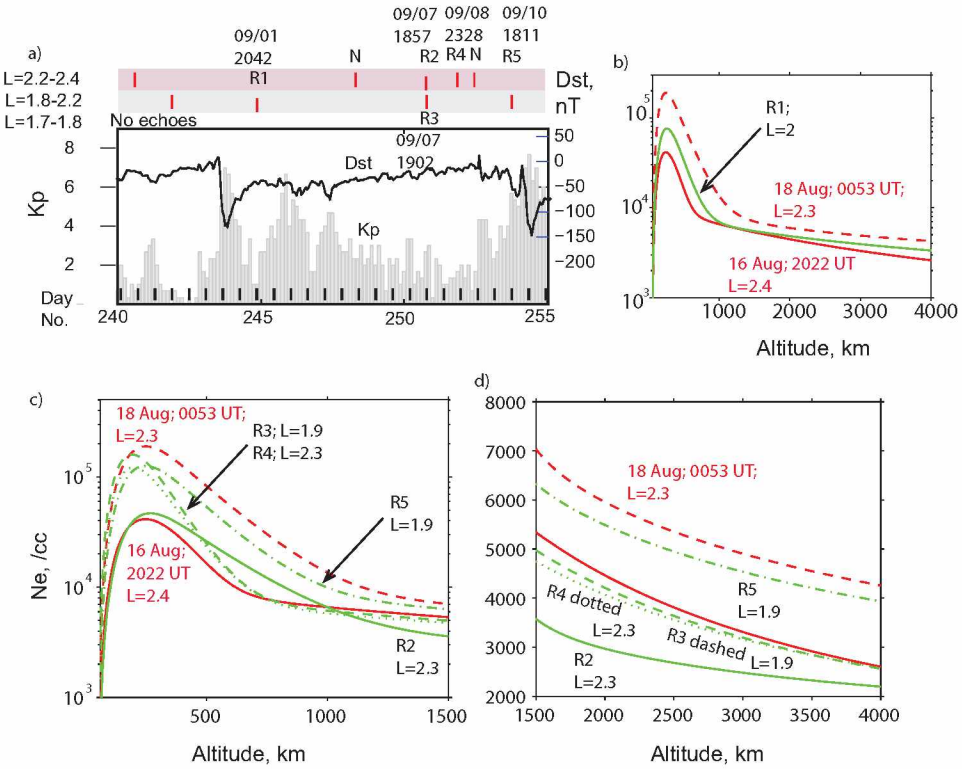

Figure 3.30. Variation of field-aligned electron density on the night-side during the 30 August to 10 September disturbed period.

and minimum ion concentrations. The top panel shows the ion composition obtained on R1 (01 September 2005). The ion concentrations obtained on this day fall between the maximum and minimum ion concentrations obtained during quiet time, indicating that ions recovered from the storm. The bottom panel shows the ion concentrations obtained during the 07–10 September 2005 period, recovery period after the 03 September and 04 September 2005 moderate storms. Relative to the quiet time ion concentrations, on 07 September at L=2.3 (R2) there was decrease in α_{H^+}, increase in α_{He^+} at all altitudes. The α_{O^+} increased at altitudes above ~1200 km. On R3 and R4 α_{H^+} increased, α_{He^+} decreased and α_{O^+} decreased. On R5, α_{H^+} decreased, α_{He^+} and α_{O^+} increased. The case R5 (10 September 2005; 18 UT) is observed during the main phase of another moderate storm on 10 September 2005. It is probable that the change in the ions on R5 is due to the moderate storm activity on 10 September 2005.

The field-aligned electron density and ion composition variations resulting from the 31 Aug 2005 disturbance and the two moderate storms that followed it on 02–03 September and 04 September 2005 can be summarized as follows:

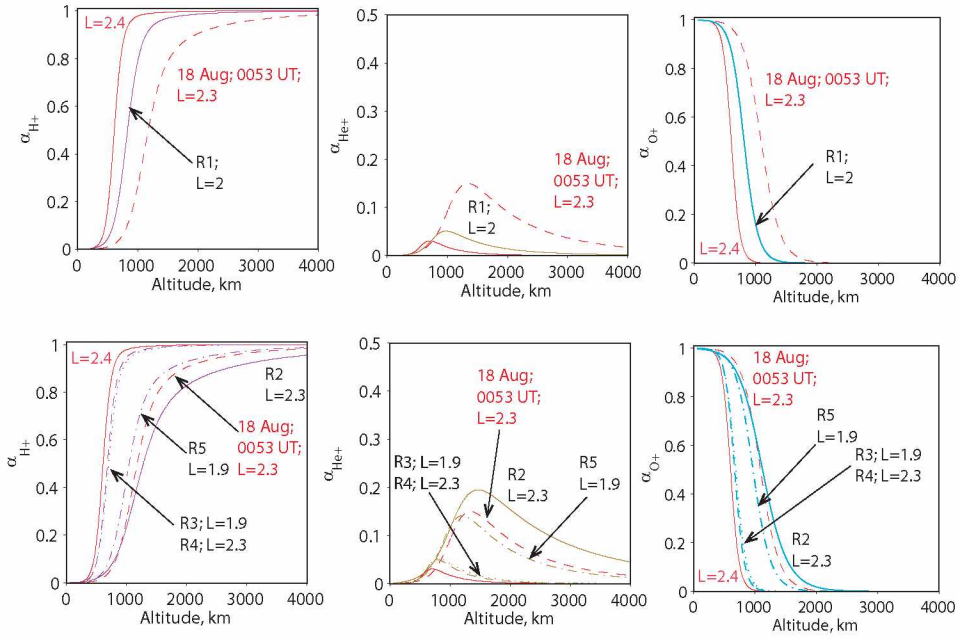

Figure 3.31. Variation of field-aligned ion composition on the night-side during the 30 August to 10 September disturbed period.

On the day-side, an enhancement in electron density at all altitudes was observed in the onset phase of the major storm on 31 August 2005. During the recovery phase, below 1500 km, N_e remained comparable to that during the onset phase. Relative to the N_e during the onset phase, above 1500 km, the electron density increased on the first day (01 September) followed by a decrease on the second day (02 September). By the close of the second day there was another moderate disturbance, followed by another moderate disturbance on 03 September. After the disturbance on 02 September but before the one on 03 September, a decrease in electron density at the F2 peak and an increase in electron density above 1500 km was observed. During the recovery phase of 03 September storm, the N_e at the F2 peak as well as the N_e above 1500 km increased on the first day; on the second day (04 September) N_e above 1500 km decreased. On 04 September, there was another moderate disturbance, which did not seem to effect the electron density. The electron density continued to increase on next 4 days (05–09 September) indicating the refilling of the plasmasphere.

On the day-side, α_{H^+} decreased in the onset phase of the major storm on 31 August 2005. It increased on the first day after disturbance and decreased on the second day. The α_{He^+} increased in the onset phase, decreased on the first day, and increased on the second day of recovery phase. The

α_{O^+} was not affected in the onset phase and on the first day of recovery phase. It increased on the second day. After the 02 September storm but before the 03 September storm, α_{H^+} remained low, α_{He^+} increased and α_{O^+} decreased. During the recovery of 03 September storm, α_{H^+} increased at all altitudes on the first day and it decreased at altitudes below 1500 km on the next day (04 September). The α_{He^+} decreased on the first day and remained the same on the next day. The α_{O^+} did not show any variation on the first day; it increased on the next day. On 04 September, there was another moderate disturbance that did not seem to effect the ions. The α_{H^+} increased and α_{O^+} decreased indicating their recovery. The α_{He^+} did not show any trend.

On the night-side, both electron density and ions recovered within a day (01 September 2005) after the major storm on 31 August 2005. After the moderate storms on 02, 03, and 04 September, neither the electron or ions recovered until 07 September 2005. On 07 September the electron density above 1500 km was about 40% lower than quiet time, the α_{H^+} was lower, α_{He^+} and α_{O^+} were greater than quiet time values. The electron density and all ions recovered to their quiet time values on 08 September, four days after the 04 September storm.

3.5.4 Variation of field-aligned electron density and ion composition during the 10 September to 24 September 2005 disturbed period that included one major, two moderate, and one minor storm

The 10–24 September 2005 disturbed period included one major storm, two moderate storms and a minor storm. Figure 3.32(a) shows the geomagnetic conditions using Kp and Dst during this period. Shown in this figure are WM echoes (red and green vertical bars) observed as a function of storm activity. The numbers at the top/bottom of labeled WM echoes give the date and time in UT when the WM echoes were observed.

On 10 September 2005 there was a moderate storm (Dst minimum is -70 nT at 22 UT; Kp maximum is -6). This moderate storm is followed by a major storm on 11 September (Dst minimum -147 nT, at 11 UT and Kpmax is 8-). The disturbed conditions that started on 11 September 2005 remained for 3 consecutive days until 14 September 2005. The Dst started recovering on 14 September 2005 but another moderate storm occurred on 15 September 2005 (Dst minimum -86 nT at 17 UT; Kp maximum is 7). Following this moderate storm there was another minor storm on 18 September 2005 (Dst minimum is -52 nT at 12 UT; Kp maximum is 3).

Figures 3.32(b) and 3.32(c), respectively, show variation in electron density below and above 1500 km during the 10–14 September 2005 period. The red curve in these figures represents the electron density obtained on 10 September 2005 at ~03:30 UT during the onset phase of the 10 September 2005 moderate storm. Relative to the density in the onset phase, on 11 September (R1, R2), below 1000 km N_e increased. The increase was maximum (about 2 times that during onset) at the F2 peak. Above ~1000 km N_e was comparable (within 10–12%) to that in the onset phase. On 14 September (R3, R4) below ~ 1000 km N_e was comparable to that in the onset phase. Above 1000 km, electron density decreased by ~ 35-40% at L=1.85 and by ~50% at L=2.3. Figure 3.33 shows the variation of electron density during the 15–23 September 2005 period. The top panel shows the electron density variation during the 15 September to 17 September 2005 period (R5-R8): main and recovery phase of the 15 September 2005 moderate storm. The red solid and dashed curves in the top panel indicate the electron density obtained on 14 September 2005 at L=1.85 (R3) and 2.3 (R4). Relative to R3 and R4, N_e increased on 15 September (R5) at all altitudes. The case R5 was observed around the beginning of the main phase of the 15 September storm. On 16 September (R6) N_e below 1500 km was comparable to that on 14 September (R3). On 17 September (R7, R8) N_e below 1500 km increased. Above 1500 km, electron density on R6, R7, R8 was lower than that during the main phase and was greater that during the recovery of major storm (R3). The densities on R6, R7 and R8 were very close (within 5%) indicating recovered densities.

The middle panel of Figure 3.33 shows the variation in electron density during the 17–20 September 2005 period that included the recovery period of 18 September minor storm. The red solid and dashed curves in Figures 3.33(c) and 3.33(d) indicate the electron density obtained on 17 September 2005 at L=1.7 (R7) and L=1.9 (R8). During the 18–23 September period N_e below ~1000 km remained comparable to that on R7 and R8. Above 1000 km, on 18 September (R9) during the main phase of the storm N_e was comparable to that on R7 and R8. Relative to N_e on R7 and R8, on 19 September at 1 UT (R10) N_e increased by ~35-40%. On 19 September at 15 UT (R11) N_e further increased by ~5%. On 20 September (R12) N_e was comparable to that on R7.

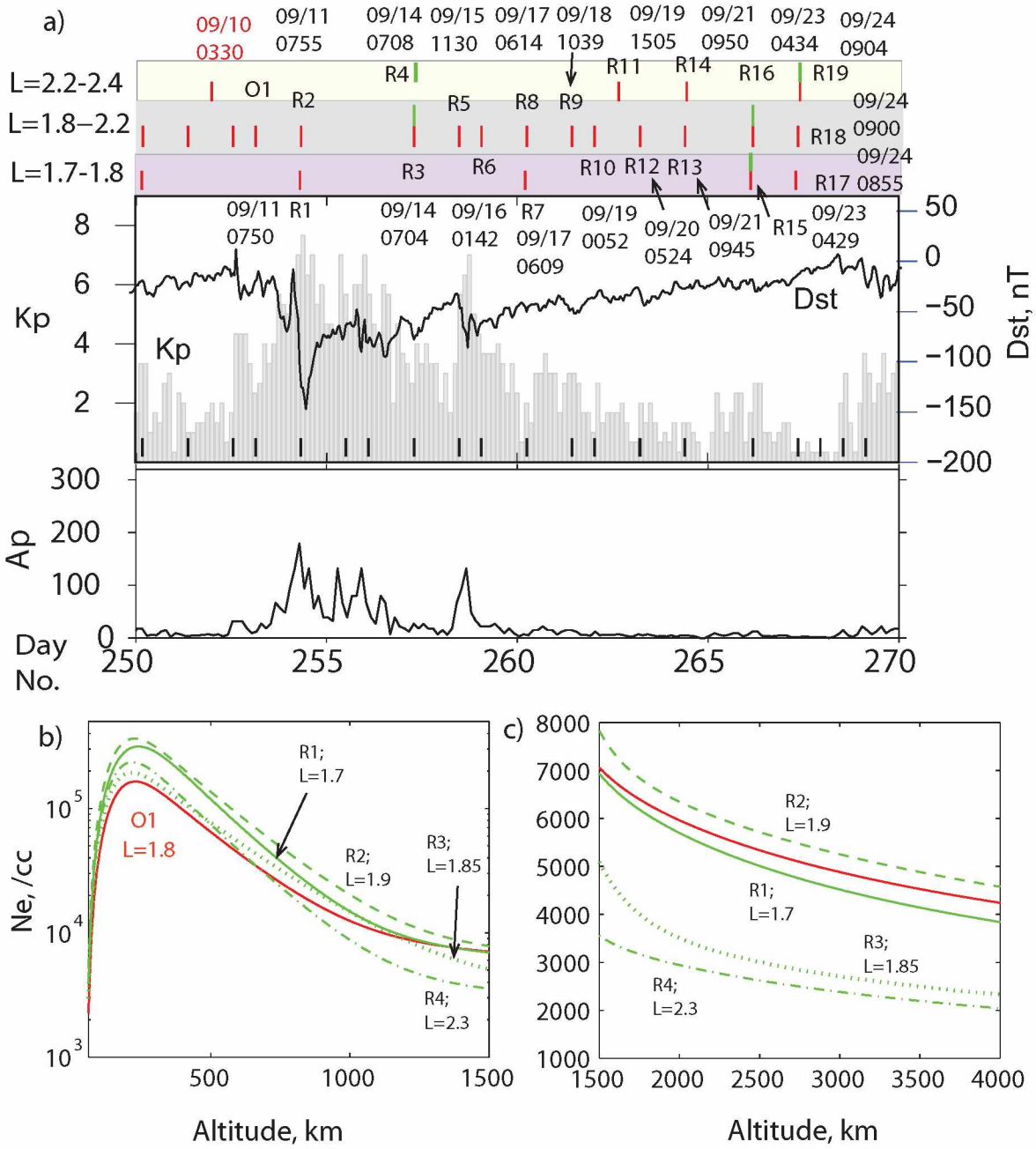

Figure 3.32. Variation of the field-aligned electron density on the day-side during the 11–14 September 2005 period. (a) Shows the temporal pattern of WM echoes during the 10–23 September 2005 period. (b) Variation of N_e below 1500 km during the 11–14 September 2005 period. (c) Variation of N_e above 1500 km during the 11–14 September 2005 period.

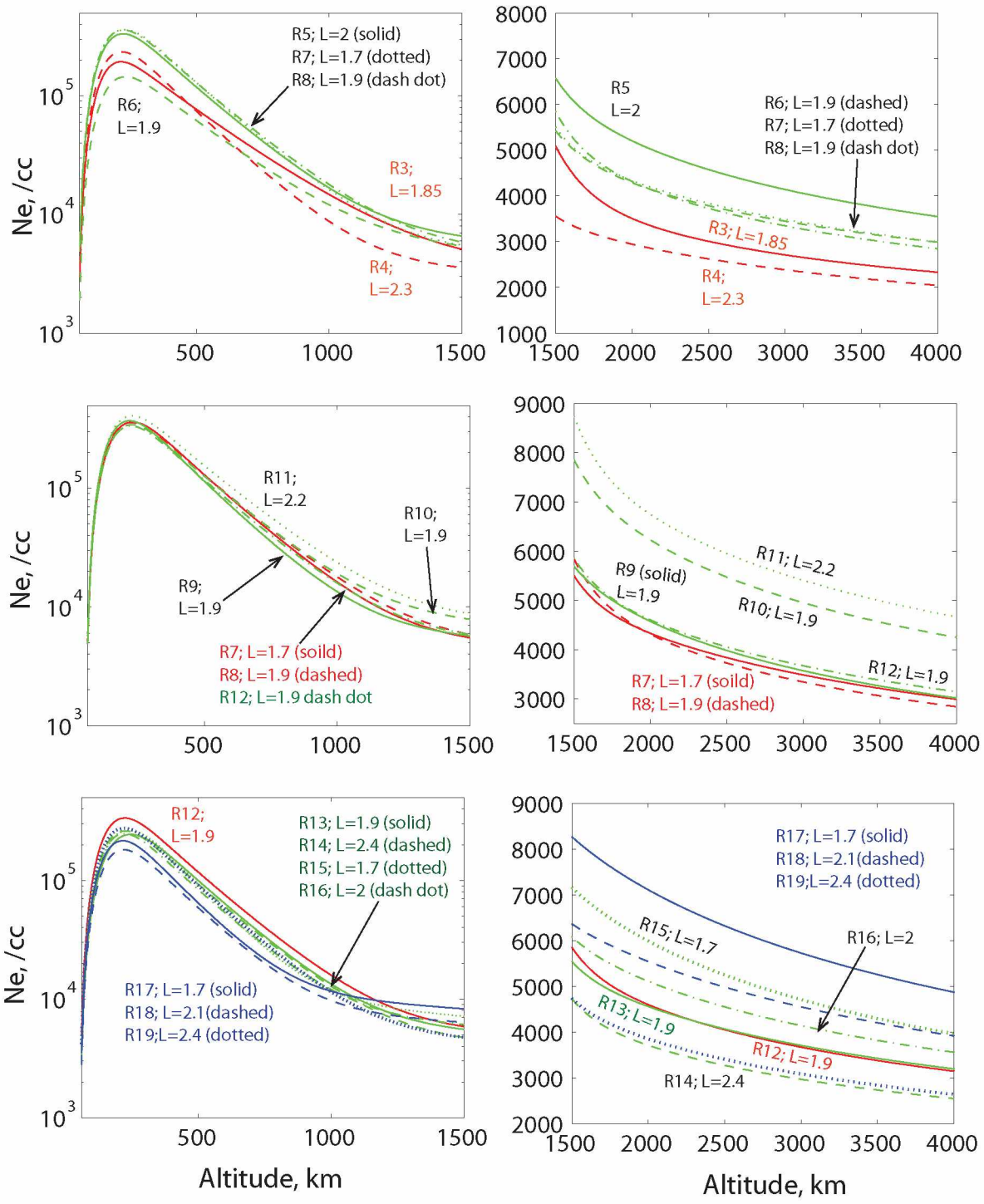

Figure 3.33. Variation of field-aligned electron density on the day-side during the 15–23 September 2005 period. The top panel shows the electron density variation during the 15–17 September 2005 period. The middle panel shows the electron density variation during the 17–20 September 2005 period. The bottom panel shows the electron density variation during the 20–23 September 2005 period.

The bottom panel shows the variation of electron density during 20–23 September 2005. The red curve in Figures 3.33(e) and 3.33(f) represents electron density on 20 September 2005 (R12). Below ~1000 km the electron density obtained during the 21–23 September 2005 is lower than that on 20 September 2005. The electron density below 1000 km did not vary much (within 30% at F2 peak on all days) during this period. Above 1000 km, on 21 September 2005 at L=1.9 (R13) the density is comparable to that on R12. On 20 September at L=2.4 (R14) N_e is ~15% lower than that at L=1.9 (R13). On 23 September (R15, R16) electron density increased. On 24 September 2005 (R17, R8, R19) N_e further increased indicating refilling stage of the plasmasphere.

Figure 3.34 shows the variation of ion composition during the 10–24 September 2005 period. In the top panel, the red solid curve represents ion composition on 10 September 2005 obtained during the onset phase on 10 September 2005. Relative to the ion composition on 10 September 2005: On 11 September (R1, R2) α_{H^+} remained comparable. On 14 September (R3, R4) α_{H^+} decreased at lower L-shell (R3) and remained about the same as R1, R2 at higher L (R4). On 11 September α_{He^+} was comparable to that on 10 September at lower L-shell (R1) but decreased at higher L (R2). On 14 September α_{He^+} increased at lower L (R3) and altitudes above 1500 km at and was greater than that on 10 September 2005. At higher L (R4) α_{He^+} was about the same as on 11 September. On 11 September α_{O^+} was comparable to that on 10 September at lower L (R1) and increased at higher L (R2). On 14 September α_{O^+} increased at lower L (R3) and it remained about the same as that on 11 September at higher L (R4).

The second panel in Figure 3.34 shows the variation of ion composition during the 15–17 September 2005 period. The solid and dashed red curves, respectively, represent ion compositions on 14 September 2005 at lower (L=1.85) and higher L (L=2.3). All the ions remained close to or within the red curves indicating that the moderate storm on 15 September 2005 did not affect the ions.

The third panel in Figure 3.34 shows the variation of ion composition during the 18–20 September 2005 period. The solid and dashed red curves, respectively, represent ion compositions on 17 September 2005 at L=1.7 and L=1.9. All the ions during this period remained within the solid and dashed curves indicating that the minor storm on 18 Sep 2005 did not affect the ions.

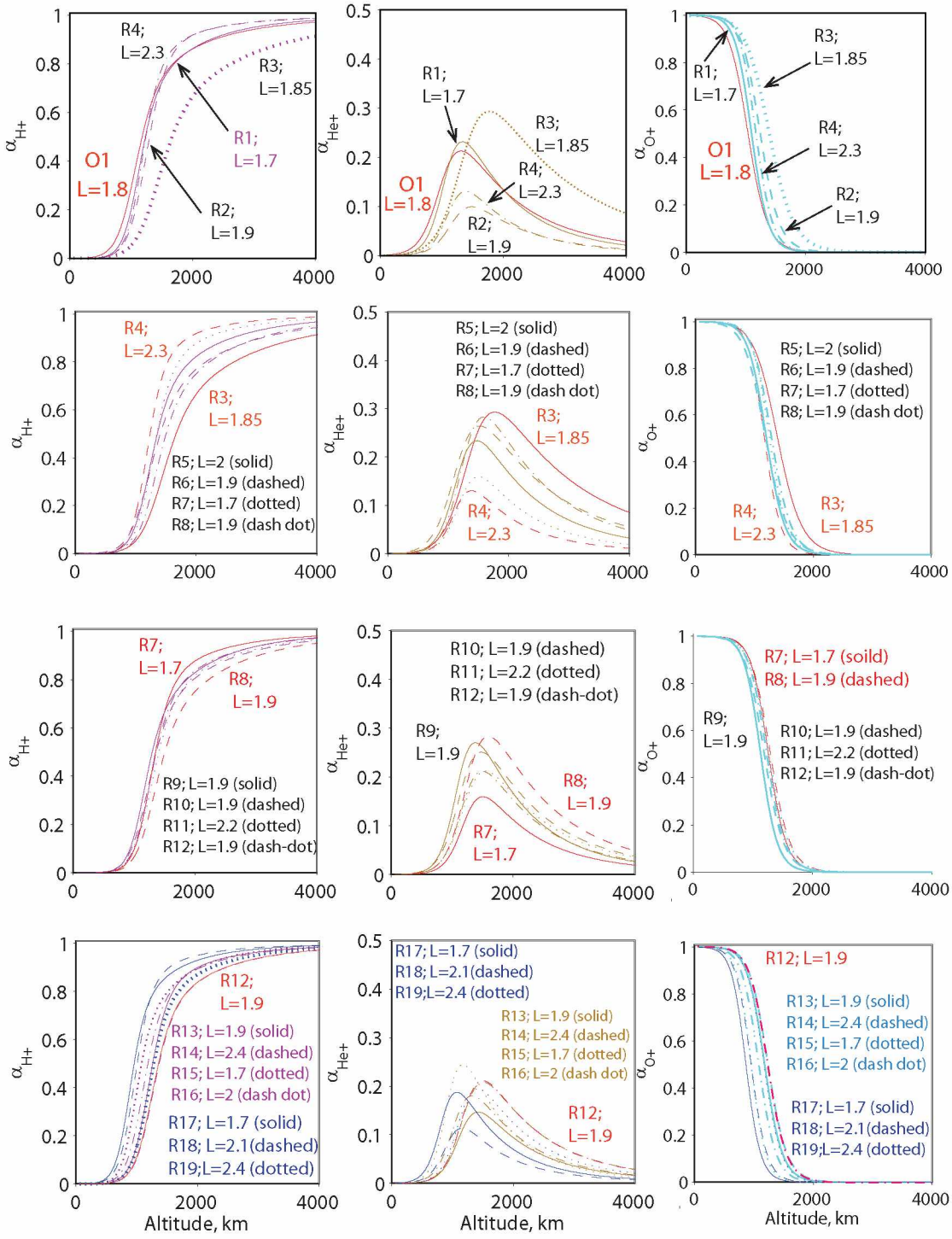

Figure 3.34. Variation of the day-side ion composition during the 10–24 September 2005 period. The top panel shows the variation of ion composition during the 10–14 September 2005 period. The second panel shows the variation of ion composition during the 15–17 September 2005 period. The third panel shows the variation of ion composition during the 18–20 September 2005 period. The bottom panel shows the variation of ion composition during the 21–24 September 2005 period.

The bottom panel in Figure 3.34 shows the variation of ion composition during the 21–24 September 2005 period. The red solid curve represents α_i on 20 September 2005 (R12). From 21 to 23 and 24 September α_{H^+} increased and α_{O^+} decreased at a given L-shell. The α_{He^+} did not show any trend.

Figure 3.35(a) shows that only one WM echo was observed in the L-shell range 1.7-2.4 on the night-side during the 11–24 September 2005 disturbed period (Day #254-267). This echo was observed on 23 September 2005, five days after the minor storm on 18 September 2005. Figures 3.32(b-e) show that both the electron density and ion composition on this day were within the quiet time values shown by red curves.

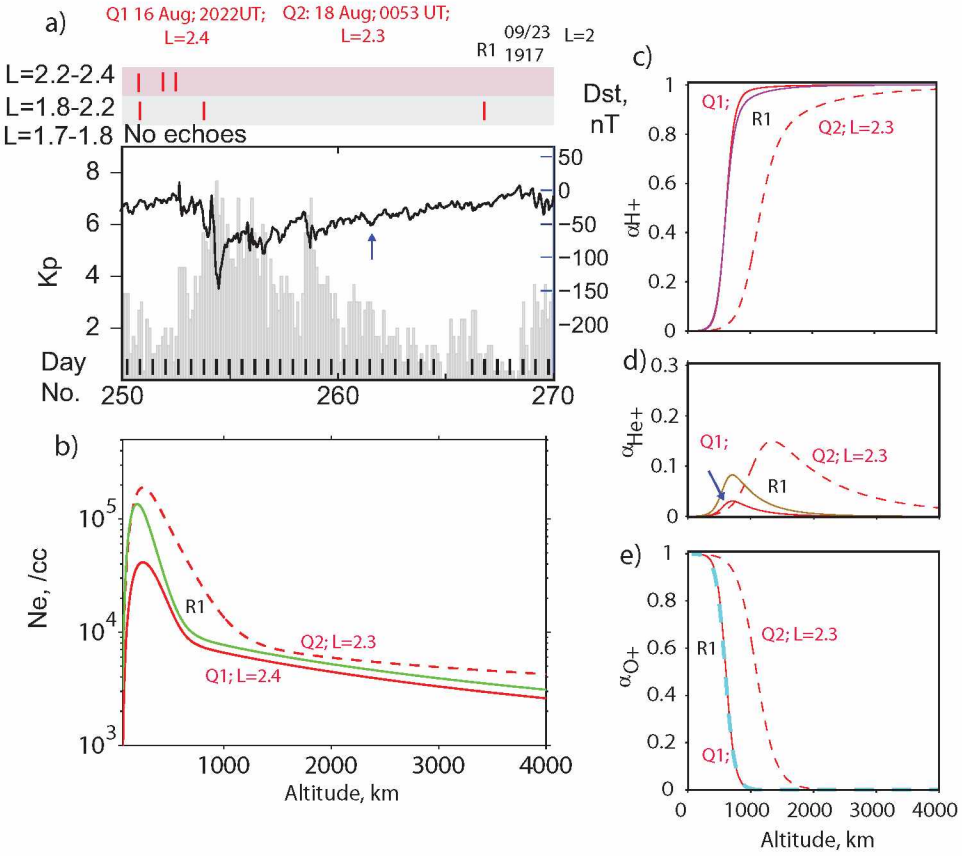

Figure 3.35. Field-aligned electron density and ion composition on 23 September 2005, five days after the minor storm, on the night-side

The day-side electron density and ion composition variations resulting from the major, moderate, and minor storms during the 10–18 September 2005 period can be summarized as follows. In the onset phase of the moderate storm on 10 September 2005, electron density at F2 peak de-

creased. Electron density above 1500 km increased. During the main phase of 11 September major storm, N_e at the F2 peak increased. Electron density above 1500 km remained close to the N_e during the onset of 10 September storm. Three days after the major storm, on 14 September a decrease in N_e at a range of L-shells (1.85-2.3) was observed. On 15 September, at the beginning of the main phase of another moderate storm electron density increased at all altitudes followed by a decrease in N_e at all altitudes on the next day (16 September). On the following day (17 September) N_e at the F2 peak increased and N_e above 1500 km remained the same as that on 16 September. The minor storm on 18 September did not affect N_e at the F2 peak. The electron density above 1500 km remained the same as that on 17 September during the main phase of the storm but it increased on the next day (19 September) and remained high for at least next 14 hours. On 20 September electron density decreased relative to that before the 18 September storm.

The day-side ion composition did not vary during the onset phase of the moderate storm on 10 September. The α_{H^+} was not affected during the main phase of 11 September storm. It decreased at lower shells on 14 September (3 days after major storm) and remained the same as that on 10 September at higher L. The α_{He^+} decreased at higher L-shells during the main phase of 11 September storm and it decreased at lower L-shells during the recovery period (14 September). The α_{O^+} increased at higher L-shells during the main phase of 11 September storm and it increased at lower L-shells during the recovery period (14 September). The moderate on 15 September and minor storm on 18 September did not affect the ions. The α_{H^+} increased and α_{O^+} decreased on 15 September and later indicating their recovery. The α_{He^+} did show any trend.

3.5.5 Variation of electron density and ion composition at various altitudes

Electron density and ion composition vary smoothly with altitude. Therefore, plots of N_e and α_i at various altitudes provide another way to study the variations in N_e and α_i as a function of storm activity. Figure 3.36 shows variation of electron density at 1000, 2000, and 3000 km as a function of geomagnetic storm activity. Figure 3.36 shows: (1) Electron density values after the severe storm were greater than the average quiet time values. (2) There was enhancement in electron density during the onset and main phase of the major and moderate storms. (3) The enhancement is followed by depletion in the early recovery period of the storm.

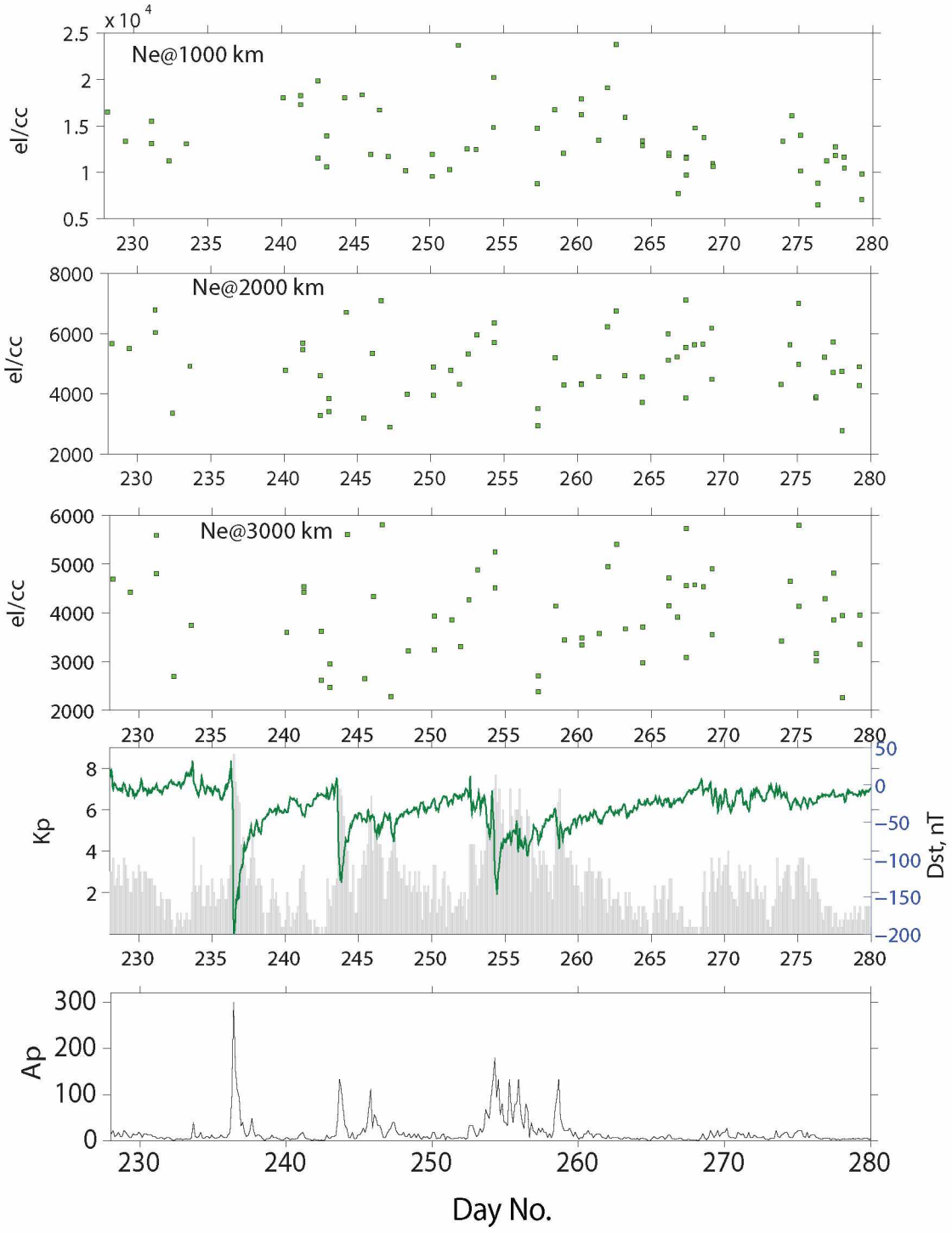

Figure 3.36. Variation of electron density at 1000 km, 2000 km and 3000 km as a function of geomagnetic storm activity

Figures 3.37–3.39 respectively show variation of α_{H^+}, α_{He^+} and α_{O^+} at 1000 and 2000 km as a function of storm activity. These figures show: (1) the α_{H^+} decreased during the onset phase of all major storms and remained low until the early recovery period of storms and then increased, (2) the α_{He^+} increased during onset and main phase of all major storms and then decreased and (3) the α_{O^+} increased during the early recovery phase and decreased during during the recovery phase of storms.

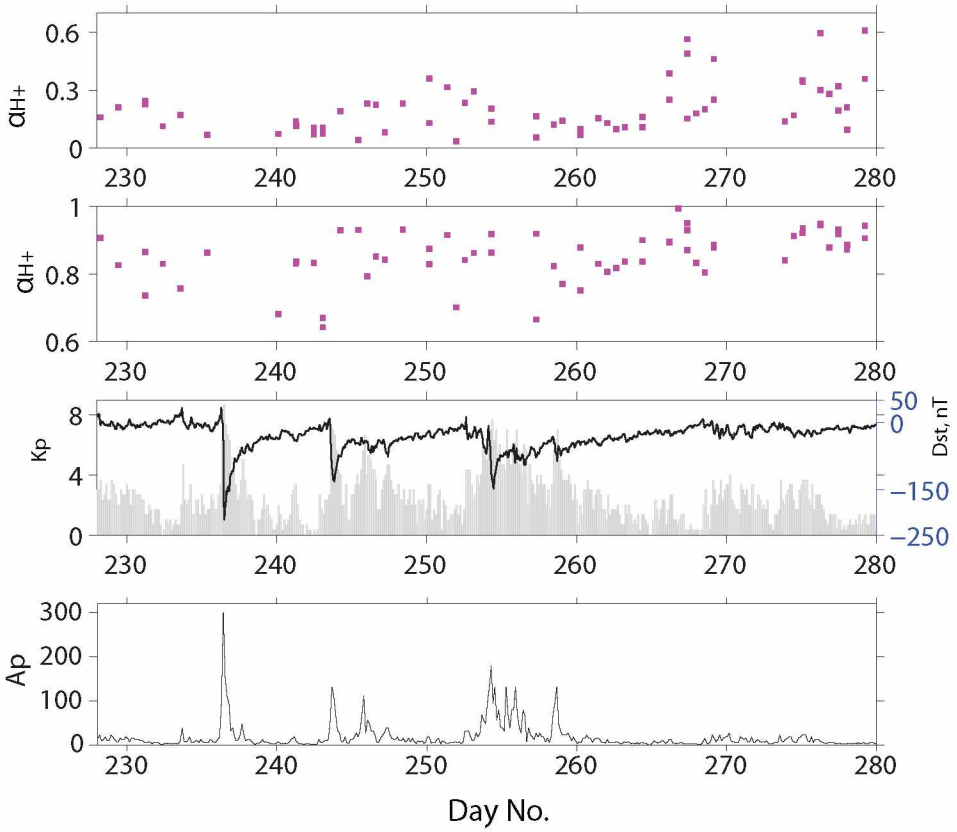

Figure 3.37. Variation of α_{H^+} at 1000 km and 2000 km as a function of geomagnetic storm activity

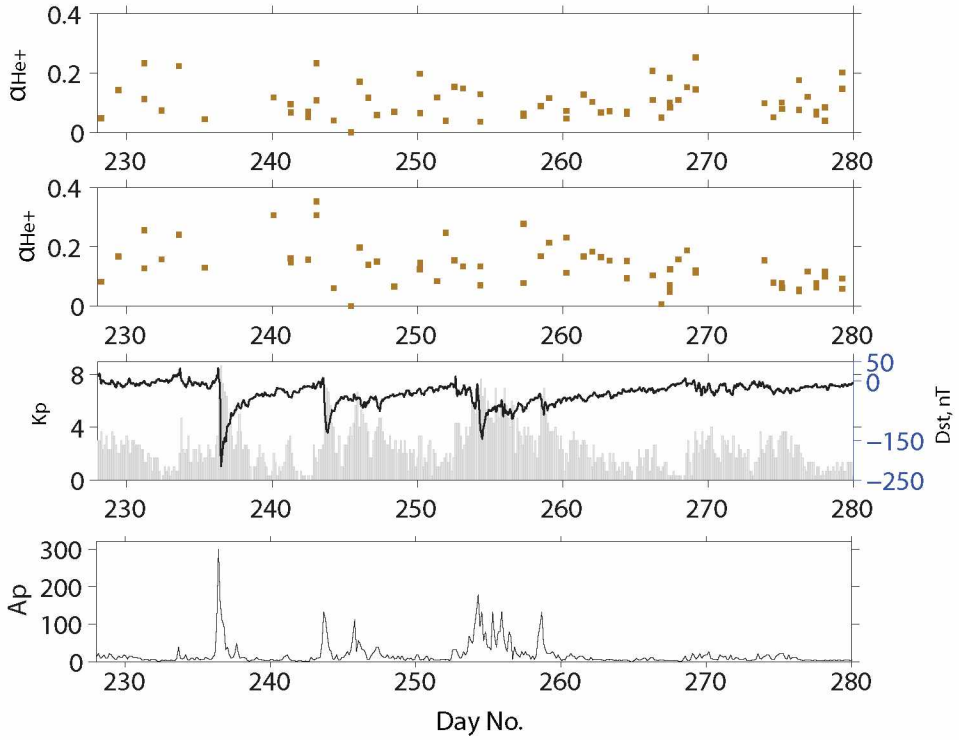

Figure 3.38. Variation of α_{He^+} at 1000 km and 2000 km as a function of geomagnetic storm activity

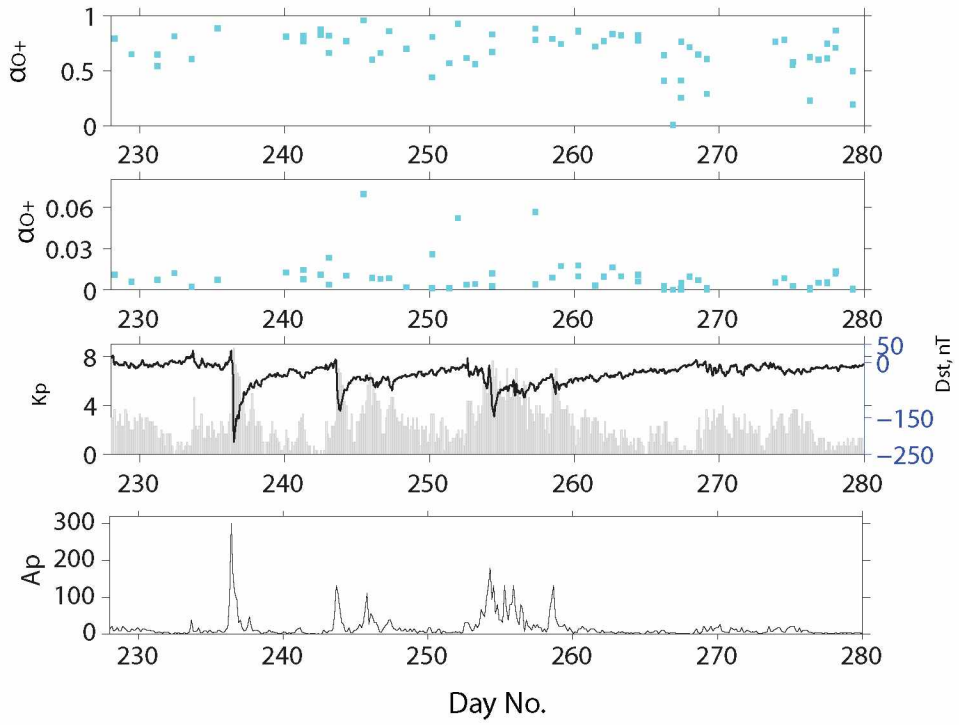

Figure 3.39. Variation of α_{O^+} at 1000 km and 2000 km as a function of geomagnetic storm activity

3.5.6 Variation of electron density at F2 peak and O^+/H^+ transition height during the 16 August-06 October 2005 period

This subsection presents the variation of the F2 peak, upper transition height (light ion to heavy ion) and O^+/H^+ transition height as a function of geomagnetic activity.

Geomagnetic storms can dramatically alter the F2 region density in the ionosphere [e.g., Liu et al., 2010; Mansilla, 2007; Danilov, 2001 and references therein]. The maximum electron density at the F2 peak, NmF2, may increase or decrease, respectively, termed as positive and negative ionospheric storms during these geomagnetic disturbances [Mansilla, 2007].

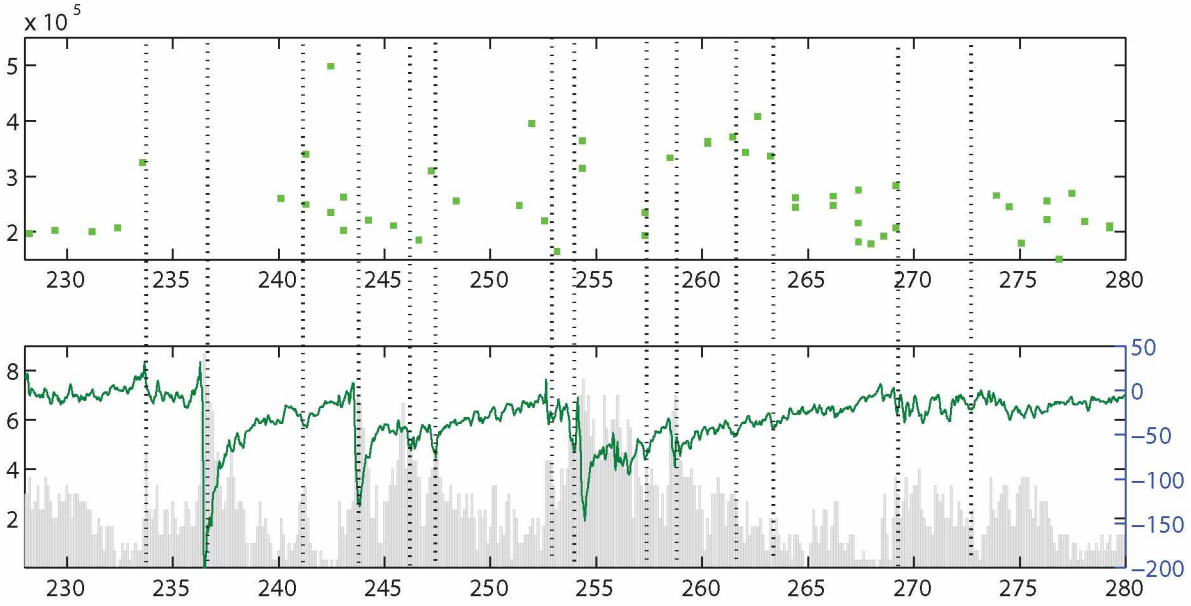

Figure 3.40. Variation of the electron density at F2 peak as a function of geomagnetic storm activity.

Figure 3.40 shows the electron density at the F2 peak for the 16 August to 06 October 2005 period. The average quiet time F2 peak before the storm is about 2×10^5 and that after the storm in about 2.5×10^5. The N_e at F2 peak varied with changes in Kp and/or Dst. For e.g., on Day #254 Dst indicated quiet conditions but Kp was -5 indicating minor storm, an increase in F2 peak was observed. On Day#242 both Dst and Kp indicated quiet conditions but there was a slight dip in Dst indicating geomagnetic disturbance; an increase in the F2 peak was observed around the same time. In 31 August and 10 September storm cases increase in the F2 peak was observed during the onset phase followed by a decrease during the early recovery phase of storms. The N_e at F2 peak remained high during the 15–20 September 2005 disturbed period that included a moderate and minor storm. Enhancements in electron density at the F2 peak during the onset phase of have been observed earlier at low-mid latitudes [e.g. Chi et al., 2000; Berube et al., 2005].

Figure 3.41 shows the variation of upper transition height as a function of geomagnetic activity. Upper transition height is the altitude at which light ions (H^+) are equal to heavier ions (He^+, O^+). The average upper transition height during quiet time before the disturbed period is about 1300 km and that after the disturbed period is about 1200 km. Before the beginning of the major storm on 31 August and moderate storms on 10 September and 15 September an increase, $\sim$300-400km, in upper transition height was observed. The upper transition height remained high during the early recovery period of all storms and then decreased to average quiet time value.

Figure 3.42 shows the variation of O^+/H^+ transition height as a function of storm activity. The average O^+/H^+ transition height is about 1200 km. An increase in the transition height (200-300 km) in the onset phase and during the recovery phases of the storms was observed. The O^+/H^+ transition height on the first day of recovery is lower than that during the onset phase. The O^+/H^+ transition height continuously increased for 2 days or more during the recovery phase of all storms and then decreased to the average quiet time value. Both the variation of upper transition height as well as O^+/H^+ transition height suggest an increase in heavy ion concentration during the onset and recovery phases of major, moderate and minor storms.

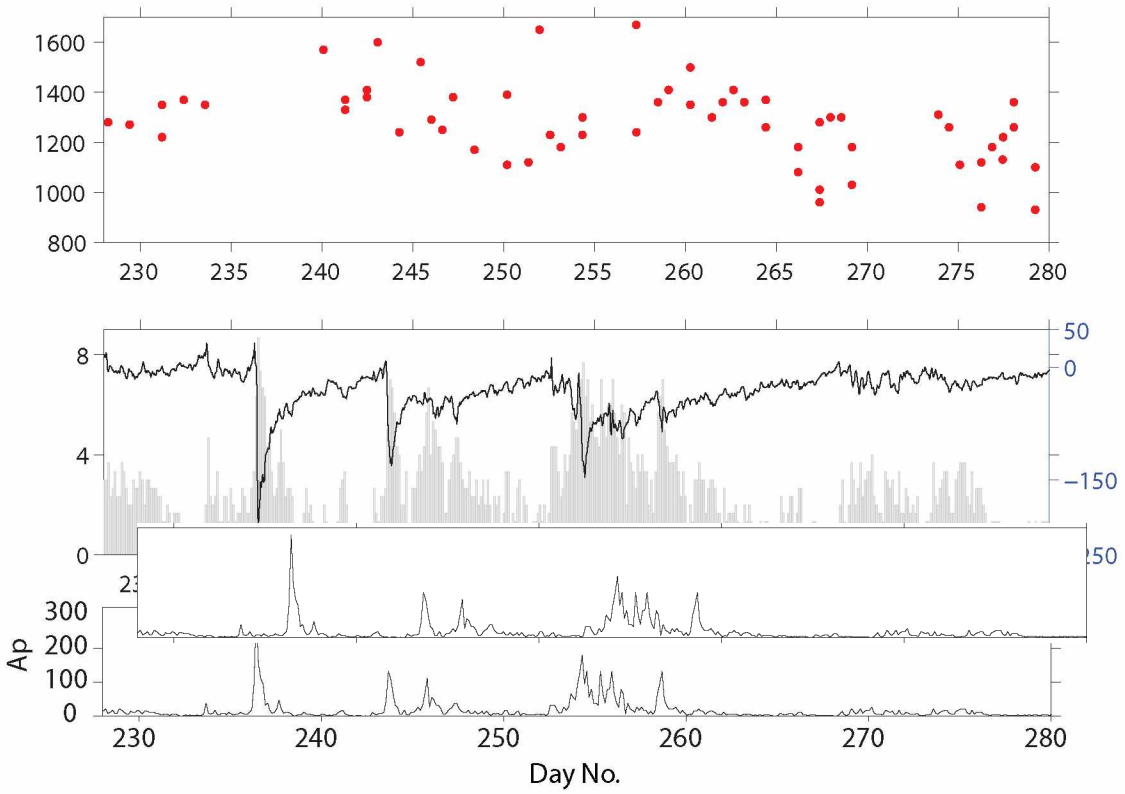

Figure 3.41. Variation of the upper transition height (light ion to heavy ion) as a function of geomagnetic storm activity.

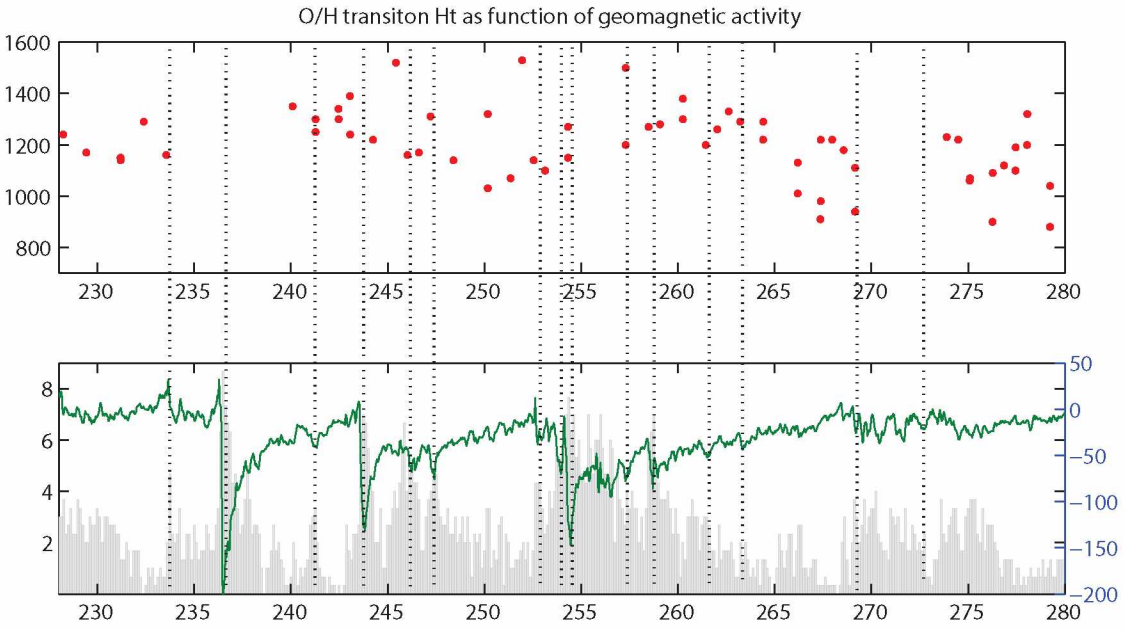

Figure 3.42. Variation of the O^+/H^+ transition height as a function of geomagnetic storm activity.

3.6 Variation of plasma parameters as obtained from other satellites and bottomside sounding as a function of storm activity

In this section the response of plasma parameters including electron density, ion composition, O^+/H^+ ratio (proxy for O/H transition height) as obtained from CHAMP, DMSP F-13, and DMSP F-15 satellites, and bottomside sounding is presented. These data sets provide complementary information to that obtained from WM sounding.

3.6.1 Electron density at 350 km as a function of geomagnetic activity from the CHAMP satellite

As noted earlier in Chapter 2, CHAMP satellite is in a circular near-polar orbit(87° inclination) sampling the ionospheric plasma at $\sim$350 km. Figures 3.43 and 3.44, respectively, show electron density obtained from CHAMP on day-side and night-side as a function of geomagnetic activity for the 53 day period (Day #228-280, 2005).

The average electron density on day-side during the quiet time is $\sim 1.5\times10^5$ /cc. CHAMP data showed enhancement in electron density with geomagnetic activity. For example, on Day #234 Kp increased to 5 (Dst indicated quiet time) indicating disturbed conditions and CHAMP data showed increase in N_e. On Day #242 Kp indicated moderate geomagnetic conditions and there was a dip in Dst from -20 nT to -42 nT, around the same time an increase in N_e from CHAMP data is noticeable. CHAMP data showed an increase in N_e at the beginning of the main phase of all major, moderate and minor geomagnetic storm. The level of enhancement in N_e is correlated to the intensity of the geomagnetic activity. Relative to the quiet time average density, CHAMP data showed an enhancement of $\sim$4 or more for major storms, $\sim$2.6–4 for moderate storms, and $\sim$2 for minor storms.

The average electron density on the night-side from CHAMP during quiet time is $\sim 1.0\times10^5$ /cc, sightly lower than day-side average quiet time density. The spread in N_e on a given day is more on the night-side relative to the day-side. As a result, variations in N_e for minor disturbances is not clear. CHAMP data showed enhancement in N_e during the onset phase of all major storms. The enhancement in N_e is followed by depletion during the main phase for two major storms (Day #236 and Day #254-256). In the case of the major storm on Day #242, no depletion was observed. Enhancement in N_e was observed during the onset phase of all moderate storms, excepting for

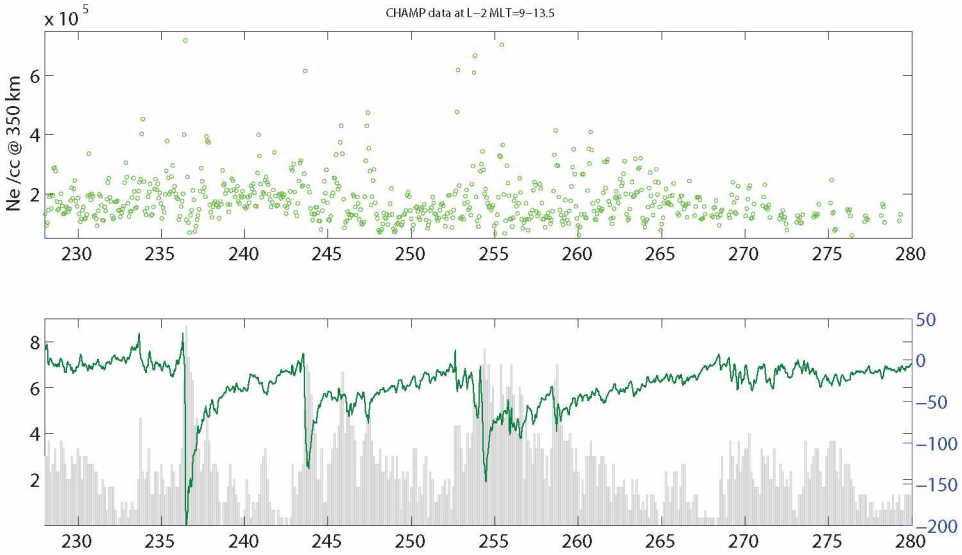

Figure 3.43. Variation of the day-side electron density at 350 km as obtained from the CHAMP satellite.

the one on Day #247 (04 September). The latter strom did not affect N_e. No decrease in n_e was observed during the main phase of moderate storms. CHAMP data showed correlation between the level of enhancement during the onset phase and the intensity of geomagnetic activity. Relative to quiet time average night-side density, an enhancement of $\sim$2 or more for major storms and $\sim$2 for moderate storms is found.

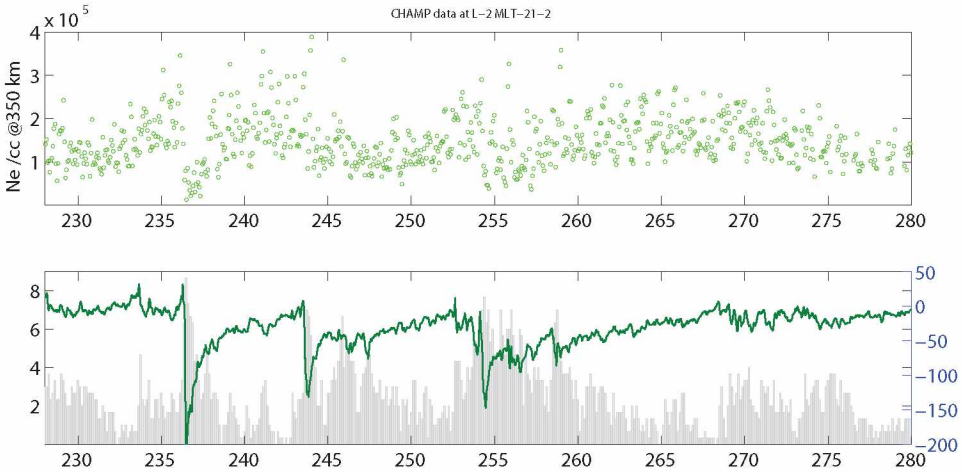

Figure 3.44. Variation of the night-side electron density at 350 km as obtained from the CHAMP satellite.

3.6.2 Electron density and ion composition at 850 km as a function of geomagnetic activity from the DMSP satellites

The DMSP spacecraft are in circular polar orbits (fixed in local time) sampling the ionospheric plasma at about 850 km. The orbital period of DMSP spacecraft is 90 min. DMSP-F13 satellite is in a 0545-1745 local time orientation and DMSP-F15 satellite is in a 0930-2130 local time orientation. Figure 3.45 and 3.46, respectively, show electron density and ion composition variation at L=2 and 2.5 and at MLT $\sim$ 17 (duskside) as obtained from DMSP-F13 spacecraft data. Figures 3.47 and 3.48, respectively, show electron density and ion composition variation at L=2 and 2.5 and at MLT $\sim$ 9 (dawnside) as obtained from DMSP-F15 spacecraft data.

The DMSP spacecraft data showed increase in N_e during the onset phase of all three major storms on both dawnside (MLT$\sim$9) and duskside (MLT$\sim$17) at both L-shells, 2 and 2.5. The moderate and minor disturbances did not affect N_e on the duskside (Figure 3.45 and 3.46) but an increase in N_e in the onset phase was observed on the duskside. On both dawnside and duskside, DMSP data showed, a decrease in α_{H^+} and an increase in α_{O^+} during the main phase of the storms. An increase in heavy ions during storm time is reported earlier by Horwitz et al., 1984 and Berube et al., 2005. The α_{He^+} from DMSP did not show any trend in variation with geomagnetic activity. These variations in electron density and ion composition obtained from DMSP data are consistent with WM sounding results.

As noted earlier transition height is one of the important parameters as it roughly indicates the transition from O^+ dominated ionosphere to H^+ dominated plasmasphere. The O^+/H^+ ratio from DMSP at 850 km can serve as a proxy for transition height. An increase in O^+/H^+ ratio indicates increase in transition height and vice versa. Figures 3.49 and 3.50 show, respectively, the variation in O^+/H^+ ratio on the duskside and dawnside as a function of geomagnetic activity. The figures indicate an increase in O^+/H^+ ratio indicating an increase in O^+/H^+ transition height during the main phase of all major storms. The time period for which the O^+/H^+ ratio remained high is different for all three storms. The moderate and minor storms did not affect the O^+/H^+ ratio. Whistler mode sounding results also showed an increase in the transition height during the onset,main and recovery phase of major storms.

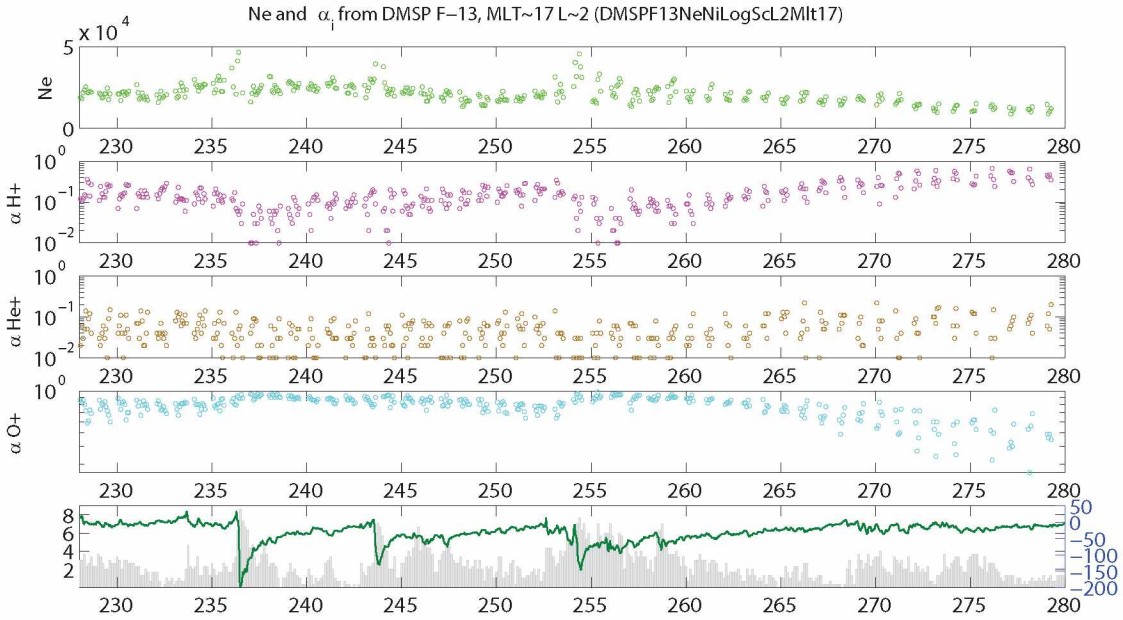

Figure 3.45. Variation of the duskside (MLT∼17) plasma density and composition at 850 km and L=2 as obtained from the DMSP-F13 satellite.

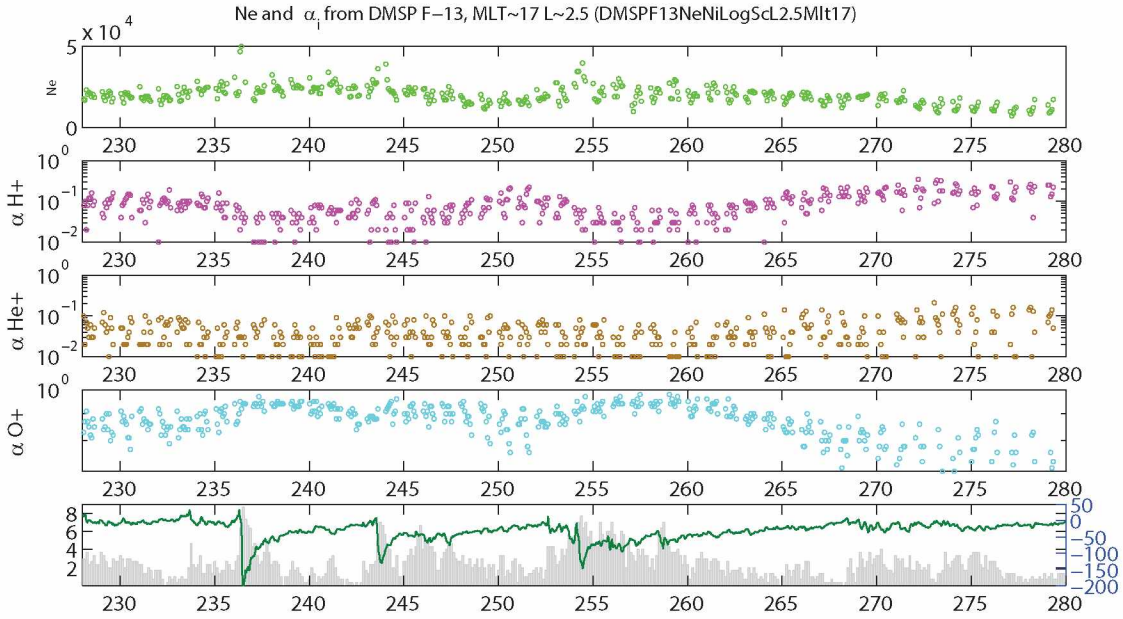

Figure 3.46. Variation of the duskside (MLT∼17) plasma density and composition at 850 km and L=2.5 as obtained from the DMSP-F13 satellite.

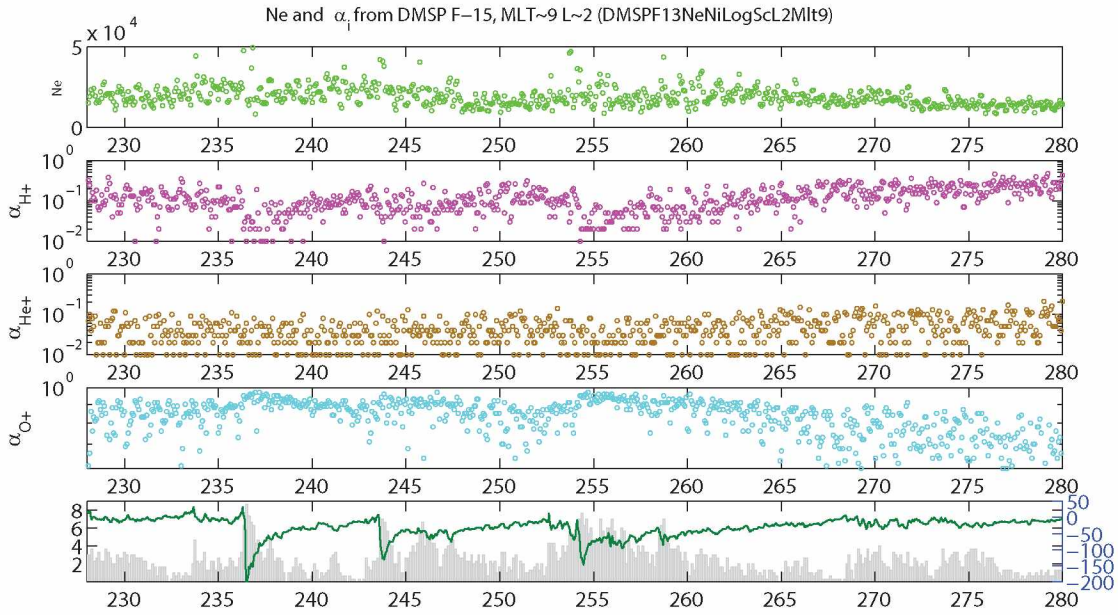

Figure 3.47. Variation of the dawnside (MLT~9-10) plasma density and composition at 850 km and L=2 as obtained from the DMSP F-15 satellite.

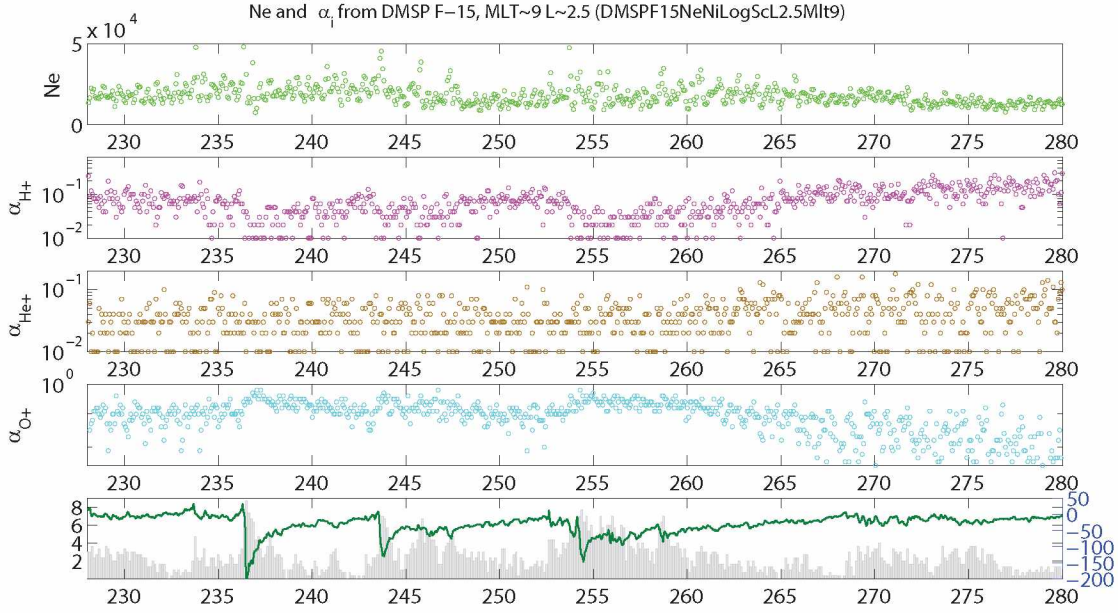

Figure 3.48. Variation of the dawnside (MLT~9-10) plasma density and composition at 850 km and L=2.5 as obtained from the DMSP F-15 satellite.

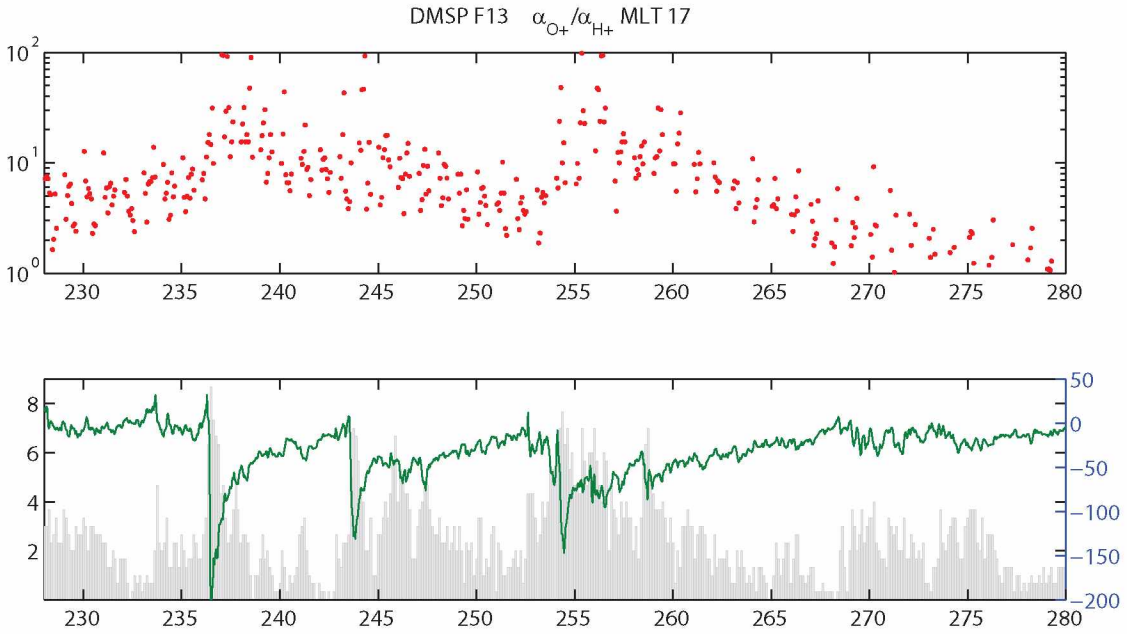

Figure 3.49. Variation of the O^+/H^+ ratio at 850 km and at MLT∼17 as obtained from the DMSP F-13 satellite.

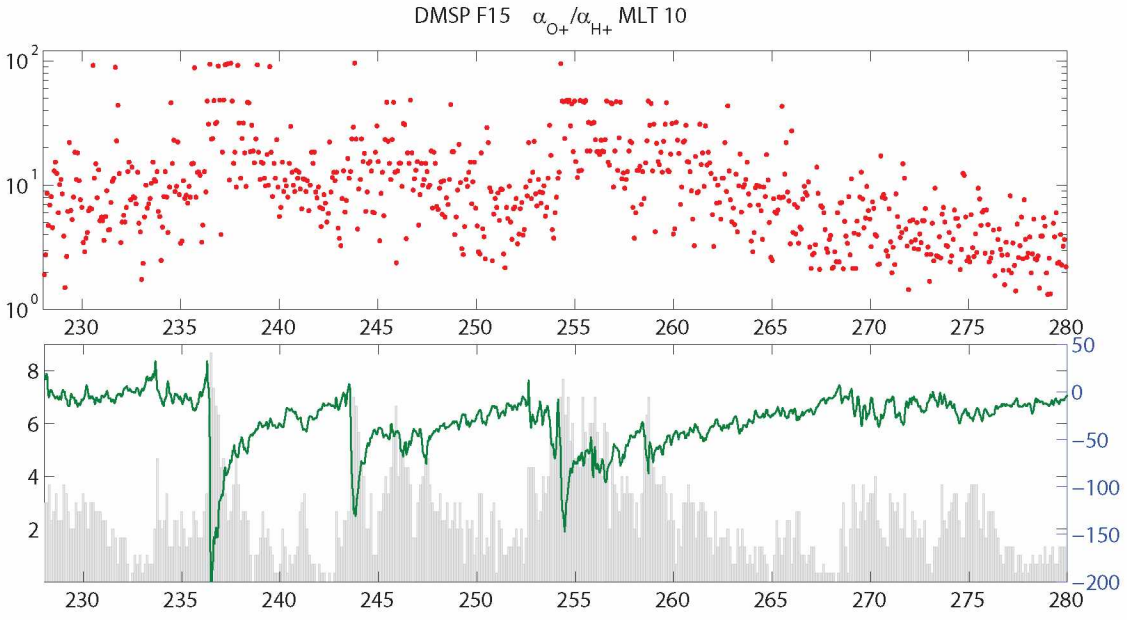

Figure 3.50. Variation of O^+/H^+ ratio at 850 km and at MLT∼10 as obtained from the DMSP F-15 satellite.

3.6.3 Electron density at F2 peak as a function of geomagnetic activity from ground based Ionosonde stations

Bottomside sounding results were used to study the variation in electron density at the F2 peak during geomagnetic storms for decades. The reaction of the ionosphere as seen at different ionosonde stations may be quite different during the same storm depending on the station coordinates, local time, and some other parameters [Liu et al., 2010]. Figures 3.51–3.53 show variation of day-side plasma frequency at the F2 peak at L$\sim$1.85, L$\sim$2 and L$\sim$2.35 as obtained from different ionosonde stations. Figures 3.54–3.57 show the plasma frequency at the F2 peak from the same stations on the night-side.

Figure 3.51 shows f_{pe} at F2 peak from Rostov and Pt. Arguello ionosonde stations for the 53 day period of 16 August to 05 October 2005. The f_{pe} obtained from station Rostov did not show any significant variation with geomagnetic activity. The f_{pe} oscillated between $\sim$5 and 6 MHz during the Day #233-264 period, it increased $\sim$6.5 MHz on Day #265 and remained about the same though the Day #265-280 period. The f_{pe} obtained from Pt. Arguello station showed decrease ($\sim$3.5 MHz) at the beginning of the main phase of 24 August 2005 (Day #236) storm. Although both Kp and Dst indicated quiet to moderate geomagnetic conditions, there was sudden increase in f_{pe} to $\sim$8 MHz on Day #240; recovery phase of 24 August 2005 storm. The f_{pe} increased from $\sim$6 to 8 MHz during the main phase of 31 August 2005 storm (Day #243). The f_{pe} oscillated between 8 and 4 MHz during the 10–14 September 2005 disturbed period and it remained high , $\sim$8 MHz, during the 15–20 September 2005 disturbed period.

Figure 3.52 shows day-side f_{pe} at the F2 peak at L$\sim$2 as obtained from Petropavlovsk and Novosibirsk ionosonde stations. The f_{pe} obtained from these two stations did not show any significant variation with geomagnetic activity. The f_{pe} obtained from both stations oscillated between $\sim$5 and 6 MHz during the Day #230-260 period. It then gradually increased to $\sim$7 MHz by Day #280.

Figure 3.53 shows day-side f_{pe} at F2 peak obtained from Tomsk, Wallops, and Bear Lake ionosonde stations. These stations are located, respectively, at L-shells of 2.14, 2.23 and 2.35. At all three stations f_{pe} first decreased then increased during the 24 August 2005 storm activity. The f_{pe} from Tomsk and Wallops stations oscillated between 5 and 6.5 MHz during the 31 August to 05 September 2005 disturbed period. Bear Lake station data was not available for this period. During

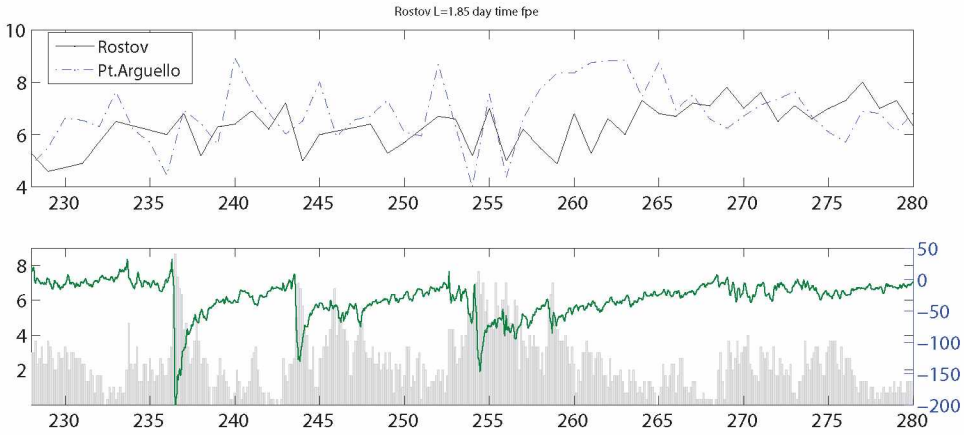

Figure 3.51. Variation of the day-side N_e at F2 peak at L=1.8 and 1.85, respectively, as obtained from Rostov and Pt.Arguello ionosonde stations

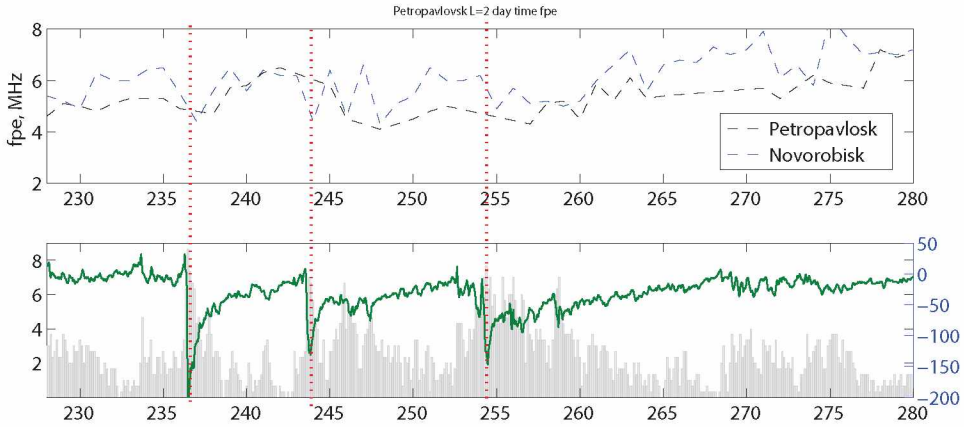

Figure 3.52. Variation of the day-side N_e at F2 peak at L$\sim$2 as obtained from Petropavlovsk and Novosibirsk ionosonde stations

the 10 to 20 September 2005 (day#253–263) disturbed period, the f_{pe} at Tomsk did not show any variation. The f_{pe} at Wallops decreased from $\sim$6 to 4 MHz during the 11 September 2005 storm main phase and then increased to $\sim$8 MHz on 14 September 2005. The f_{pe} at Wallops remained high ($\sim$8 MHz) until 06 October 2005. The f_{pe} at Bear lake data increased from $\sim$6 to 8 MHz during the onset phase of 10 September 2005 moderate storm and it decreased to $\sim$4 MHz during the main phase of the 11 September storm. On 14 September (Day #257) f_{pe} increased to $\sim$8 MHz and it remained about the same till 06 October 2005 (Day #280) .

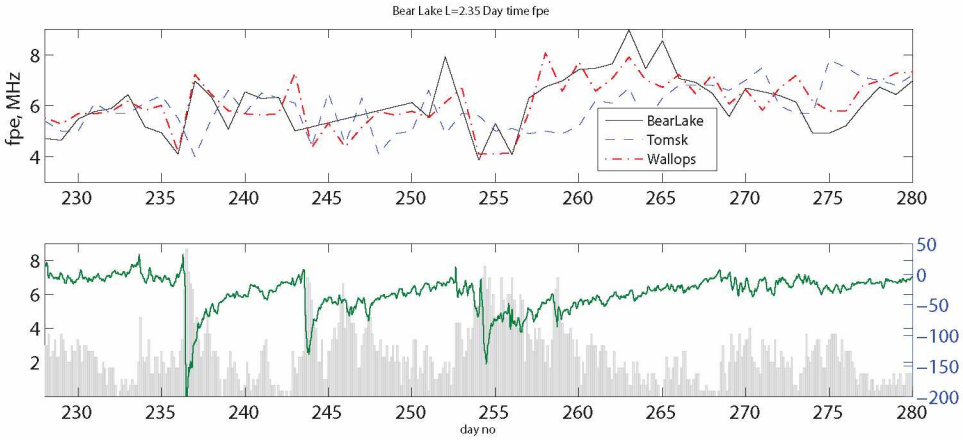

Figure 3.53. Variation of the day-side N_e F2 peak at L=2.13, 2.24 and 2.35, respectively, as obtained from Tomsk, Wallops, and Bear Lake ionosonde stations

Figure 3.54 shows the variation of f_{pe} at the F2 peak at L$\sim$1.8 on the night-side from Rostov and Pt. Arguello ionospnde stations. The f_{pe} at Pt. Arguello decreased from $\sim$5 to $\sim$2 MHz during the main phase of the 24 August 2005 storm (Day #236). It oscillated between $\sim$3.5 and 4 MHz for the rest of the period (Day #236-280) and did not respond to other storms. The f_{pe} at Rostov decreased from $\sim$6 MHz to 4 MHz during the main phase of 24 August storm. It recovered to $\sim$6 MHz before the onset of 31 August storm. It oscillated between 4 and 6 MHz during the 31 August to 04 September 2005 disturbed period. The stroms that occurred during the 10–20 September 2005 period did not affect f_{pe} at Rostov.

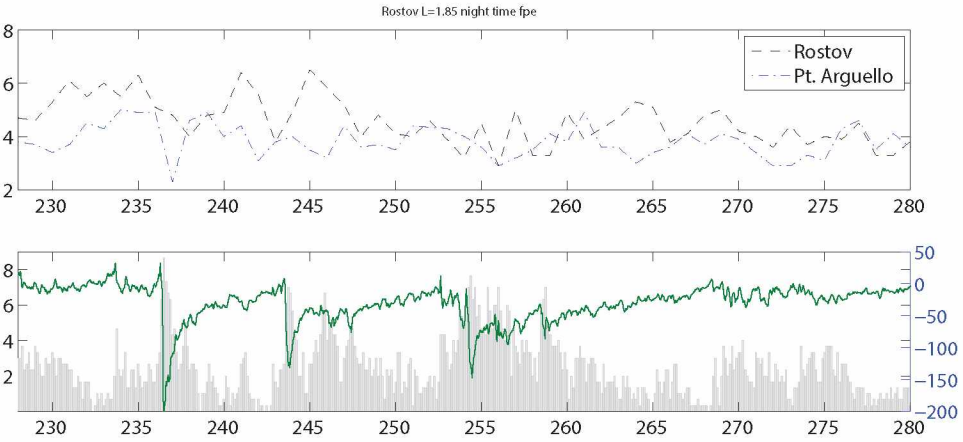

Figure 3.54. Variation of the day-side N_e at F2 peak at L=1.8 and 1.85, respectively as obtained from Rostov and Pt. Arguello ionosonde stations.

Figure 3.55 shows the variation of f_{pe} at the F2 peak at L$\sim$2 from Petropavlovsk and Novosibirsk stations on the night-side. The f_{pe} from both stations decreased from $\sim$4.5 to $\sim$2 MHz during the main phase of 24 August 2005 storm and from $\sim$4.5 to $\sim$3 MHz during the main phase of 31 August 2005 storm. The f_{pe} at Petropavlovsk did not respond to other storms that occurred during the 03 to 19 September 2005 period. The moderate storms on 03, 04 September did not affect f_{pe} at Novosibirsk. The f_{pe} decreased from $\sim$4 to 3 MHz during the main phase of 10 September 2005. It increased from $\sim$3 Mhz to 5 MHz during the main phase and decreased from 5 Mhz to 2 MHz during the recovery phase of 11 September 2005 storm followed by a gradual increase to 4 MHz. The moderate and minor storms during the 15–20 September 2005 period did not affect f_{pe} at Novosibirsk.

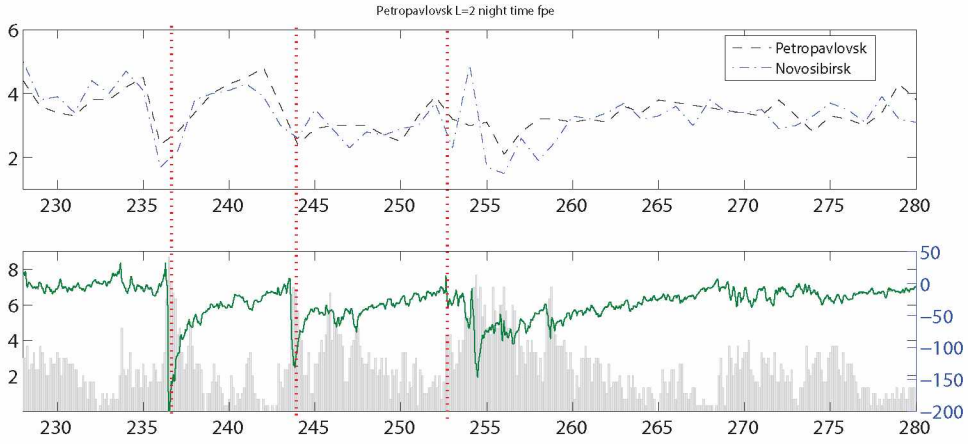

Figure 3.55. Variation of the day-side N_e at F2 peak at L$\sim$2 as obtained from Petropavlovsk and Novosibirsk ionosonde stations.

Figure 3.56 shows the night-side f_{pe} at the F2 peak obtained from Tomsk, Wallops, and Bear Lake Ionosonde stations. The f_{pe} obtained from all three stations decreased from $\sim$4 MHz to 2 MHz during the recovery phase of 24 August 2005 (Day#236) storm followed by a gradual increase to 4 MHz. The other geomagnetic storms that occurred during the Day #243-280 period did not affect f_{pe} at these stations.

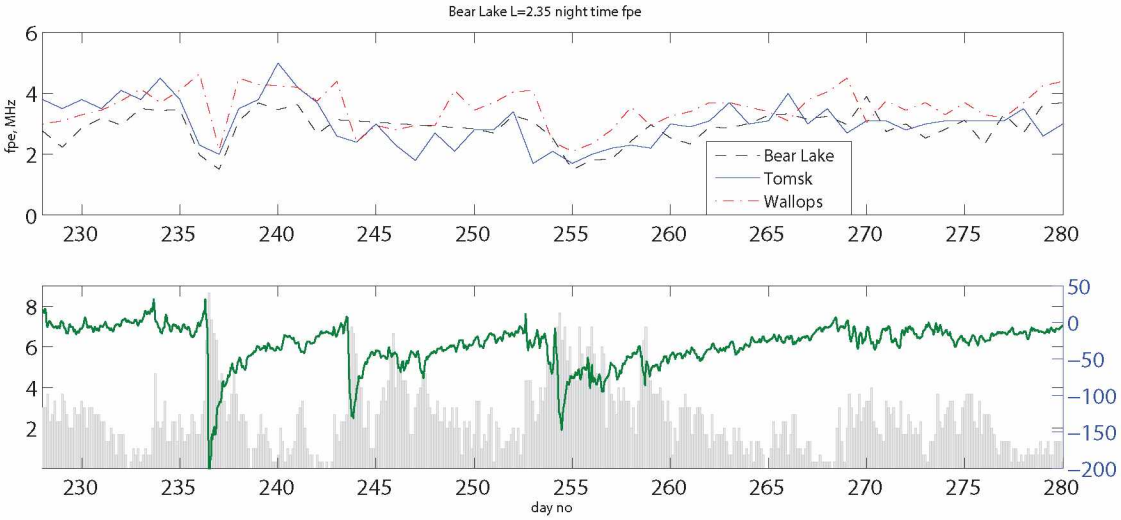

Figure 3.56. Variation of the day-side N_e at F2 peak at L=2.13, 2.24 and 2.35, respectively, as obtained from Tomsk, Wallops, and Bear Lake ionosonde stations.

3.7 Comparison of the electron density and ion composition obtained from WM sounding with insitu measurements from other satellites, bottomside sounding results, and predictions from empirical model

In this subsection we compare WM radio sounding results obtained during the 16 August to 06 October 2005 period with in situ measurements from the DMSP and CHAMP satellites and predictions from IRI-2012 empirical model. Figure 3.57 shows comparison of electron density and ion composition obtained from WM sounding (green, magenta, brown, and cyan squares) with in-situ measurements from DMSP (blue squares) and IRI-2012 predictions (red cross) at 850 km. The Figure shows that the WM sounding results are in general agreement with DMSP measurements except for one case on Day #254. On this day relative to WM sounding results, DMSP measured higher electron density and α_{H+}, and lower α_{O^+}. IRI-2012 predictions of N_e, α_{H^+} and α_{O+} are in general agreement with WM sounding results. But IRI predictions of α_{He^+} (almost 0) are substantially low relative to WM sounding results.

Figure 3.58 shows comparison of electron density obtained from WM sounding (green curve) at 350 km with in situ measurements from CHAMP (blue squares) and IRI-2012 predictions (red cross). The Figure shows that the WM sounding results are in general agreement ($\sim$20%) with CHAMP measurements during geomagnetically quiet to moderate periods. Some discrepancies between WM sounding results and CHAMP were observed during the disturbed period. In the

onset phase of 31 August 2005 storm WM sounding measurements showed increase in N_e but CHAMP data did not. In the onset phase of moderate storms on 03 and 04 September 2005 CHAMP data showed increase in N_e but WM measurements did not. During the recovery period of 18 September 2005 storm CHAMP data showed decrease in N_e but WM measurements did not. Except for these four cases WM sounding results and CHAMP measurements are in good agreement.

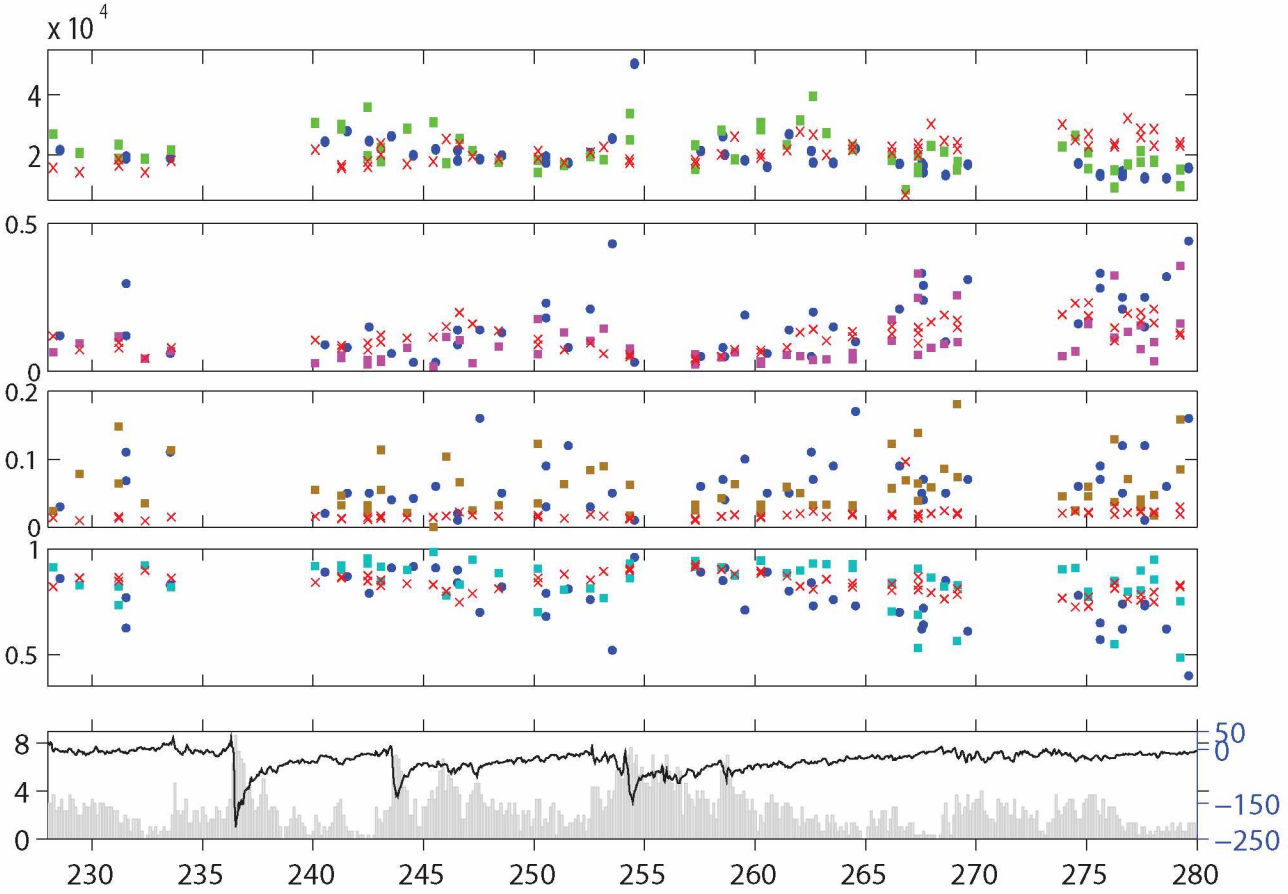

Figure 3.57. Comparison of the electron density and ion composition obtained from WM sounding at 850 km with in situ measurements from the DMSP satellite and predictions from IRI-2012 model.

Relative to WM sounding results IRI overestimated N_e at 350 km. The difference between IRI predictions of N_e and WM sounding results is more (roughly 2 times) during the 24 September-06 October 2005 period. The trend in the variation of N_e predicted by IRI is also different than that obtained form WM. For e.g., on 03 September WM sounding results showed decrease in N_e whereas IRI showed increase in N_e. Similarly after the moderate storm on 05 September, WM sounding results indicated decrease in N_e whereas IRI predicted increase in N_e. Luhr and Xiong [2010] also found that IRI model overestimates N_e by 50-60% relative to CHAMP measurements; CHAMP measurements are in better agreement with WM sounding results than IRI indicating that IRI-2012 model needs improvement for better predictions of N_e during quiet as well as disturbed periods.

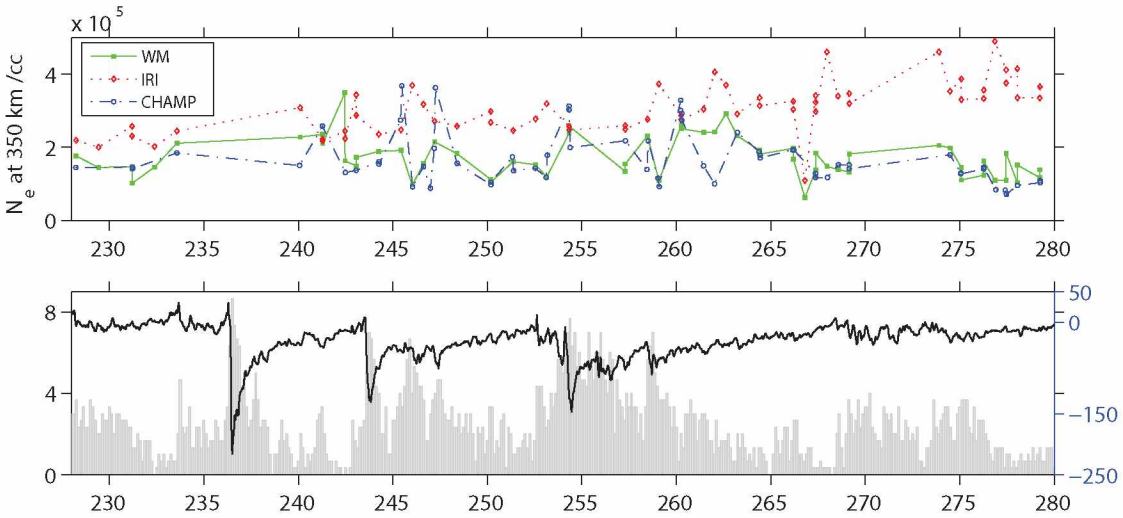

Figure 3.58. Comparison of the electron density obtained from WM sounding at 350 km with in situ measurements from the CHAMP satellite and predictions from IRI-2012 model.

Figure 3.59 shows comparison of N_e at the F2 peak obtained from WM sounding with that obtained from nearby Ionosonde stations and that predicted by IRI-2012 model. Relative to WM sounding results both bottomside sounding results and IRI predictions overestimated N_e at the F2 peak. Relative to WM sounding results IRI predictions agree better with bottomside sounding results. This is consistent, because IRI empirical model uses data from all ionosonde station. The trend in the variation of N_e obtained from WM sounding and bottomside sounding is similar excepting on Day #265 where bottomside sounding indicated increase in N_e at F2 peak but WM sounding results did not.

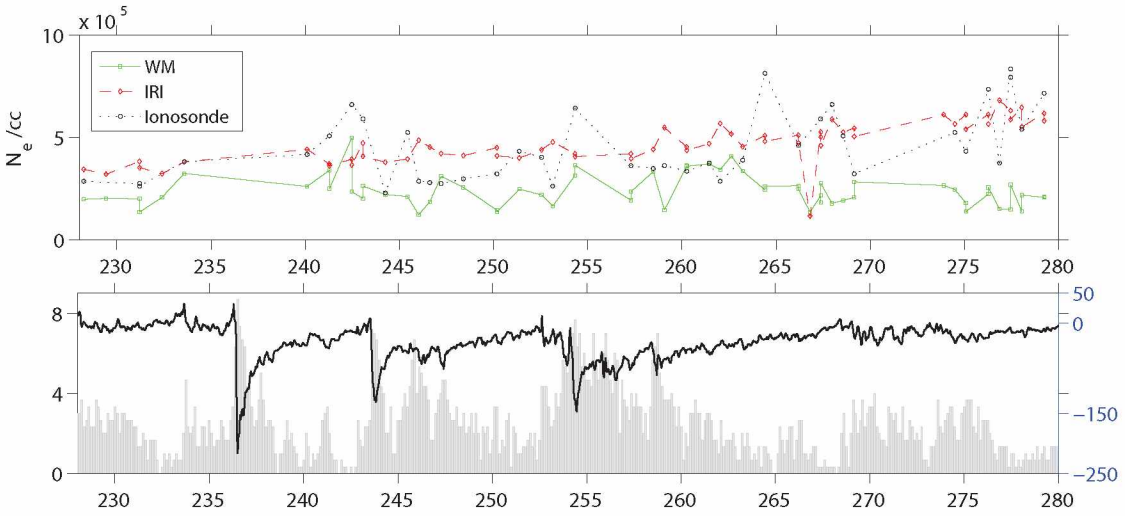

Figure 3.59. Comparison of the N_e at F2 peak obtained from WM sounding with that obtained from bottomside sounding and that predicted by IRI-2012.

Figure 3.60 shows comparison of O^+/H^+ transition height obtained from WM sounding with that predicted by IRI-2012 empirical model. Both WM sounding results and IRI predictions show increase in O^+/H^+ transition height during disturbed period and are in general agreement.

3.8 Summary, discussion and conclusions

3.8.1 Summary of major results

Whistler mode radio sounding from the IMAGE satellite during 16 August to 06 October 2005, covering three major (24 August, 31 August, 11 September), four moderate (02-03 September, 04 September, 10 September, 15 September), and one minor (18 September) storms, has permitted the first measurements of plasmaspheric field-aligned electron and ion densities (L=1.7-∼2.4) below ∼4000 km on the day-side (MLT∼13-15) and the night-side (MLT∼2-4) as a function of geomagnetic storm activity. Indices Kp, Ap and Dst and the sunspot number and solar flux parameters were used to determine the geomagnetic and solar conditions during this period. The interplanetary conditions were determined using IMF Bz, proton density, temperature, interplanetary electric field and solar wind speed. The whistler mode sounding results were augmented by observations from CHAMP, DMSP satellites, and ground ionosonde stations during the same period.

The salient features of storm time variations in plasma density and compostion presented below are based on certain reasonable assumptions that were based on past work [e.g., Lemaire and

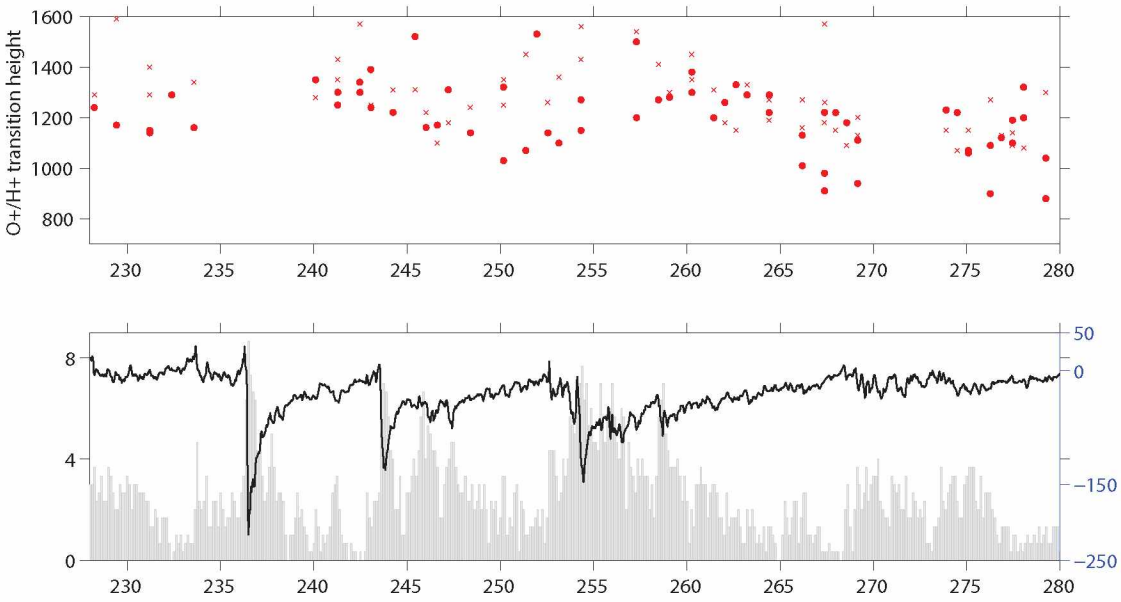

Figure 3.60. Comparison of the O^+/H^+ transition height obtained from WM sounding with those predicted by IRI-2012 empirical model.

Gringauz, 1998; Berube et al., 2005]: (1) under quiet conditions and similar MLT's electron density in the L-shell range 1.8–2.2 changes of the order 20% or less; (2) electron density decreases with L; (3) α_{H^+} decreases with L; (4) α_{O^+} increases with L. On the day-side WM echo data, roughly at least one per orbit, were available only in the L-shell range 1.8–2.2 to study plasma density and composition variations as function of storm activity. On the night-side, WM echo data were available only at L$\sim$2.3 during the recovery phase of the moderate storm on 04 September 2005. The summary of variations in field-aligned plasma parameters inside the plasmasphere as a function of geomagnetic storm activity presented below therefore are true at L$\sim$2 on the day-side and at L$\sim$2.3 on the night-side.

1. As a result of geomagnetic disturbances, the plasmapause moved from Lpp$\sim$4.5 during the quiet time to Lpp$\sim$2.4 during the disturbed time. On the night-side, plasmapause moved from Lpp$\sim$4 during the quiet time to Lpp$\sim$2.5 during the disturbed time.

2. When storms affected plasma parameters, electron density, relative ion concentrations, and O^+/H^+ transition height underwent temporal changes as a function of geomagnetic storm activity, and each species has different temporal behavior thus indicating different recovery times.

3. On the day-side, when major and moderate or moderate storms occurred in succession in an interval of roughly less than a day, the latter storms had little or no effect on electron density and ion composition. On the night-side, WM echo data was sparse and the affect of storms that occurred in succession on electron density and ion composition could not be studied.

4. On the day-side, the minor storm did not effect ions. On the night-side no WM echo data was available during the minor storm activity.

5. The WM sounding results on the day-side showed an increase in the O^+/H^+ transition height by ~200-300 km during the onset, main and early recovery phases of the storms. Data from DMSP (~850 km) on the dawn and duskside showed increase in O^+/H^+ ratio during the onset, main, and recovery phases of storms. This is indicative of an increase in O^+/H^+ transition height.

6. On the day-side, variations in the electron density below the O^+/H^+ transition height were different than those above. For example, the minor storm on 18 September did not effect N_e at F2 peak but enhancement in N_e was observed above O^+/H^+ transition height. The ion composition did not show any general trend with respect to O^+/H^+ transition height.

7. On the day-side, WM sounding results indicated an increase in N_e at F2 peak during the onset/main phase followed by a decrease in F2 peak during the recovery phase. Consistent with WM sounding results, in situ measurements from CHAMP at ~350 km and from DMSP at ~850 km, respectively, showed increase in N_e beginning main phase and onset phase of all major and moderate storms. The CHAMP satellite data correlation between the level of enhancement in N_e at ~350 km and the strength of the geomagnetic disturbance.

8. On the day-side and above 1500 km, WM sounding results showed an enhancement in N_e in the onset and main phase followed by depletion in the early recovery phase of all major and moderate storms excepting the 04 September 2005 moderate storm. The latter storm did not effect N_e above 1500 km. In the minor storm case, there was no onset phase; an enhancement in N_e during the recovery phase was observed.

9. When ions were effected by storm, on the day-side, decrease in α_{H^+} was observed in the early phases of storms (onset, main, and first one to two days of recovery); increase in α_{O^+}

was observed in the recovery phase of the storm; The α_{He^+} varied in a complex manner. Increase in α_{He^+} in the onset phase and decrease in α_{He^+} in the recovery phase was more common. The variations in α_{H^+} and α_{O^+} ion composition obtained from DMSP were consistent with those obtained from WM sounding results. The α_{He^+} from DMSP did not show any trend.

10. On the night-side, at L$\sim$2.3 WM sounding results showed decrease in N_e above 1500 km in the recovery phase of the 04 September moderate storm. Not sufficient WM data was available to study the plasma density and composition variations in the case of other storms and at altitudes below 1500 km and other L-shells as a function of storm activity.

11. On the night-side in situ measurements from CHAMP at $\sim$350 km showed increase in N_e during the onset phase of all major and moderate storms excepting the 04 September 2005 moderate storm. The increase in N_e is followed by depletion only in the case of 24 August and 11 September major storms. The 04 September 2005 storm did not affect N_e at 350 km. The level of enhancement in N_e at $\sim$350 km showed correlation to the strength of the geomagnetic disturbance. The DMSP satellite data showed increase in N_e at $\sim$850 km during the onset phase of only major storms. Other storms did not affect N_e at 850 km.

12. The apparent recovery times of electron density and ion composition at L$\sim$2.3 on the day-side are different than those on the night-side.

The temporal variations of field-aligned electron density and ion composition presented here coupled with a physics-based model allow: (1) investigation of the role of thermospheric winds, dynamo electric fields, and storm time electric fields in causing the variations and (2) the testing of current theories and the validating of physics-based models of thermosphere-ionosphere-magnetosphere coupling.

3.8.2 Discussion

3.8.2.1 Reduction in the plasmapause radius

Consistent with past work, plasmapause measurements obtained from RPI passive recording indicate reduction in the plasmapause radius during disturbed geomagnetic conditions. The past work

indicated that the plasmapause position on the night-side (22 to 06 MLT) was closely correlated with the average magnetic activity over the preceding 2 to 6-hour period [Chappell et al., 1970a; 1970b] where as the plasmapause position on the day-side (06 to 15 MLT) did not immediately respond to changes in magnetic activity, but its position depended instead on the level of activity present when that region previously corotated through the night-side region [Chappell et al., 1971]. The day-side and night-side measurements of L_{pp} obtained from RPI passive recordings showed the shrink and recovery of plasmapause around similar time. No lag in the response of the plasmapause on the day-side was noticeable from RPI passive resording. Possible reason for not observing the difference in the response of day-side and night-side plasmapause to geomagnetic activity is insufficient temporal resolution plasmapause measurements. The resolution of L_{pp} measurements is 14.2 hrs (IMAGE orbital period) or greater. The plasmapause measurements obtained from RPI are consistent with that obtained from Carpenter and Anderson [1992] empirical model.

3.8.2.2 On the response of electron density and ion composition to geomagnetic storms

Whistler mode sounding results show day-side enhancement in N_e at F2 layer in the storm onset phase followed by a depletion in the recovery phase. The maximum electron density of F2 layer, may increase or decrease, respectively, termed as positive and negative ionospheric storms during these geomagnetic disturbances [Mansilla, 2007]. The reaction of the ionosphere as seen at different ionospheric stations may be quite different during the same storm depending on the station coordinates, local time, and other parameters [Liu et al., 2010]. Negative ionospheric storm effects are most often seen in the morning sector and positive storm effects in the afternoon and evening sectors. Also, at mid-latitudes, positive storm effects are more often seen, or last longer in winter, and negative storm effects prevail in summer [Buonsanto 1999]. WM sounding results indicated increase in F2 peak followed by a decrease, a positive ionospheric storm followed by a negative ionospheric storm. Past studies have shown that winds created by heating at high latitudes will lead to positive storms at mid-latitudes [e.g. Jones and Rishbeth, 1971] and negative storms at mid-latitudes are explained by changes in neutral composition [e.g. Davies and Ruster 1976].

WM sounding results, in the altitude range of $\sim$1000-4000 km, showed enhanced day-side field-aligned electron densities inside the plasmasphere (L$\sim$1.9-2.1) in the onset or main or on the first day of recovery phase followed by depletion in the recovery phase of major and moder-

ate storms. Although enhancements in N_e were commonly observed in the F2 peak and at low latitudes from TEC measurements, incoherent scatter radar measurements, and GPS [Jones and Rishbeth 1971; Foster and Rideout 2005; Foster et al., 2002; Chi et al., 2005], enhancements in electron density in the plasmasphere were not commonly observed [Chi et al., 2005]. Depletion in the electron density inside the plasmasphere due to geomagnetic storms is a more common phenomenon that was reported in the past [Park 1970; Chi et al., 2000; Berube et al., 2005; Reinisch et al., 2004; Obana et al., 2010]. Whistler mode sounding results showed commonly an enhancement in plasmaspheric field-aligned electron density in the ~1000-4000 km altitude range during the onset and main phase by a depletion and recovery in the case of major and moderate storms. In minor storm case only enhancement in N_e was observed. We believe because of the temporal resolution of WM data (~14.2 hrs) decrease in N_e following enhanced N_e may not have been observed in the minor storm case . Consistent with WM sounding results, Chi et al., 2005 reported enhanced electron density in the mid-latitude region following the 30 Oct 2003 Halloween geomagnetic storm. The density enhancements lasted for few hours. WM sounding results showed that the density enhancements lasted for a day or more (See Figures 3.37, 3.28, 3.32 and 3.33). These enhancements suggest an up-flow of plasma from ionosphere to plasmasphere in the early stages of storm and then loss of plasma to the ionosphere in the recovery phase.

Whistler mode sounding results show decrease in α_{H^+} during early stages of storm (onset or main phase). It remained low during the first and/or second day of the recovery phase. An increase in O^+ in the recovery phase was observed. Whistler mode sounding results of ions are consistent with past measurements, a decrease in the α_{H^+} in the mid-latitude topside ionosphere [Banks et al., 1971] and increase in heavy ions at mid-latitudes and in the outer regions of the plasmasphere [Horwitz et al., 1984; Fraser et al., 2005; Berube et al., 2005; Obana et al., 2010] were observed earlier. Past observations indicate that no trend in α_{He^+} was observed during storm time [Darrouzet et al., 2009]. WM sounding results indicate complex variation of α_{He^+}; increase in α_{He^+} in the onset phase and decrease in α_{He^+} in the recovery phase was more common. The past observations of ion variations resulting due to storms are based on in situ measurements [e.g. Horwitz et al., 1984] or ground based magnetometer measurements [e.g. Berube et al., 2005] that give information on the overall changes in mass density at a field line or coordinated ground and space measurements [Dent et al., 2006]. Field-aligned plasma density and composition measurements are critical to

the understanding of the dynamic processes that effect the ionospheric-plasmaspheric composition along a field line. Whistler mode sounding measurements of field-aligned plasma density and composition will be useful for better understanding of the plasma flow from ionosphere to magnetosphere and vice versa that is important for thermosphere-ionosphere-magnetosphere coupling as well as for testing the predictions from various physics-based models.

Storm time neutral winds and electric fields are generally considered as the two main sources that cause variations in plasma density and composition. During geomagnetic storms, the disturbed solar wind compresses the Earths magnetosphere, and intense electric fields are mapped along geomagnetic field lines to the high latitude ionosphere. At the same time, energetic particles precipitate to the lower thermosphere and below, expanding the auroral zone, and increasing ionospheric conductivities. Intense electric currents couple the high latitude ionosphere with the magnetosphere, and the enhanced energy input causes considerable heating of the ionized and neutral gases. The resulting expansion of the thermosphere produces pressure gradients that drive strong neutral winds. These disturbed neutral winds flow from high latitudes to mid- and low- latitudes where they alter the neutral composition, and move the plasma up and down magnetic field lines, changing thermospheric composition [Jones and Rishbeth, 1971; Buonsanto, 1999; Balan et al., 2013]. Also, the electric fields of solar origin can penetrate to lower latitudes [e.g. Rastogi, 1977]. The penetration of these electric fields is very fast and they have been called "prompt penetrating electric fields" or PPEFs. Disturbed neutral winds also cause F region electric fields by the disturbance dynamo mechanism [Blanc and Richmond, 1980]. These electric fields redistribute the plasma, affecting production and loss rates. Dawn to dusk PPEFs are known to cause positive ionospheric storms on the day-side and negative ionospheric storms on the night-side. Day-side PPEFs also cause oxygen ion uplift [Tsurutani et al., 2008].

Figure 3.61 shows the variation of interplanetary electric field and thermospheric neutral winds as function of geomagnetic activity during the 16 August to 06 October 2005 period. The interplanetary electric field data used for the plot shown in Figure 3.61(a) was obtained from NASA website (http://omniweb.gsfc.nasa.gov/form/dx1.html). The interplanetary electric field is a derived quantity. It is the product of solar wind speed and meridional component of interplanetary magnetic field (Bz) in the Geocentric Solar Magnetospheric (GSM) system. There were substantial variations, increase or decrease, in the electric field at the time of all major and moderate storms.

Figure 3.61b shows the neutral wind speed at ~350 km at L=2 (λ_m ~43°) and L=4 (λ_m ~59°) field lines as obtained from CHAMP. The STAR accelerometer on the CHAMP satellite allows determination of neutral wind speed [Sutton et al., 2005]. The blue curve represents the wind speed at L=2 and red at L=4 at MLTsim12. There was substantial increase in the wind speed at L=2 at the time of intense storm on 24 Aug 2005. Changes in the wind speed were observed at L=4 during the disturbance time in the case of all major storms. Whistler mode sounding results of the positive ionospheric storms followed by negative ionospheric storms, enhancements seen in the plasmasphere in the early stages of storm, and increased α_{O^+} during the storm recovery phase may be due to the plasma redistribution and changes in the thermospheric composition resulting from both neutral winds and electric fields of solar origin. Further work involving physics-based models simulations of WM sounding results are needed to determine the role of neutral winds and dynamo and storm time electric fields in causing the variations in electron density and ion composition.

The response of the electron density and ions to geomagnetic storms must depend on the previous state of the magnetosphere. For example, the most dramatic plasmasphere erosion events are precipitated by exceptionally large convection enhancements that follow prolonged intervals of quiet geomagnetic conditions. If the convection increase is mild, and/or the plasmasphere has very recently been eroded, little or no erosion may occur [Goldstein, 2006]. In the study presented here, the moderate storms on 04 September and 15 September and the minor storm on 18 September occurred after a series of major and/or moderate storms, and they had little or no effect on the electron density and ions. We speculate that this may be a result of recently eroded plasmasphere. Future work involving reproduction of WM sounding results using physics based model simulations is needed to explain the response of electron density and ions to geomagnetic storms that occur in succession.

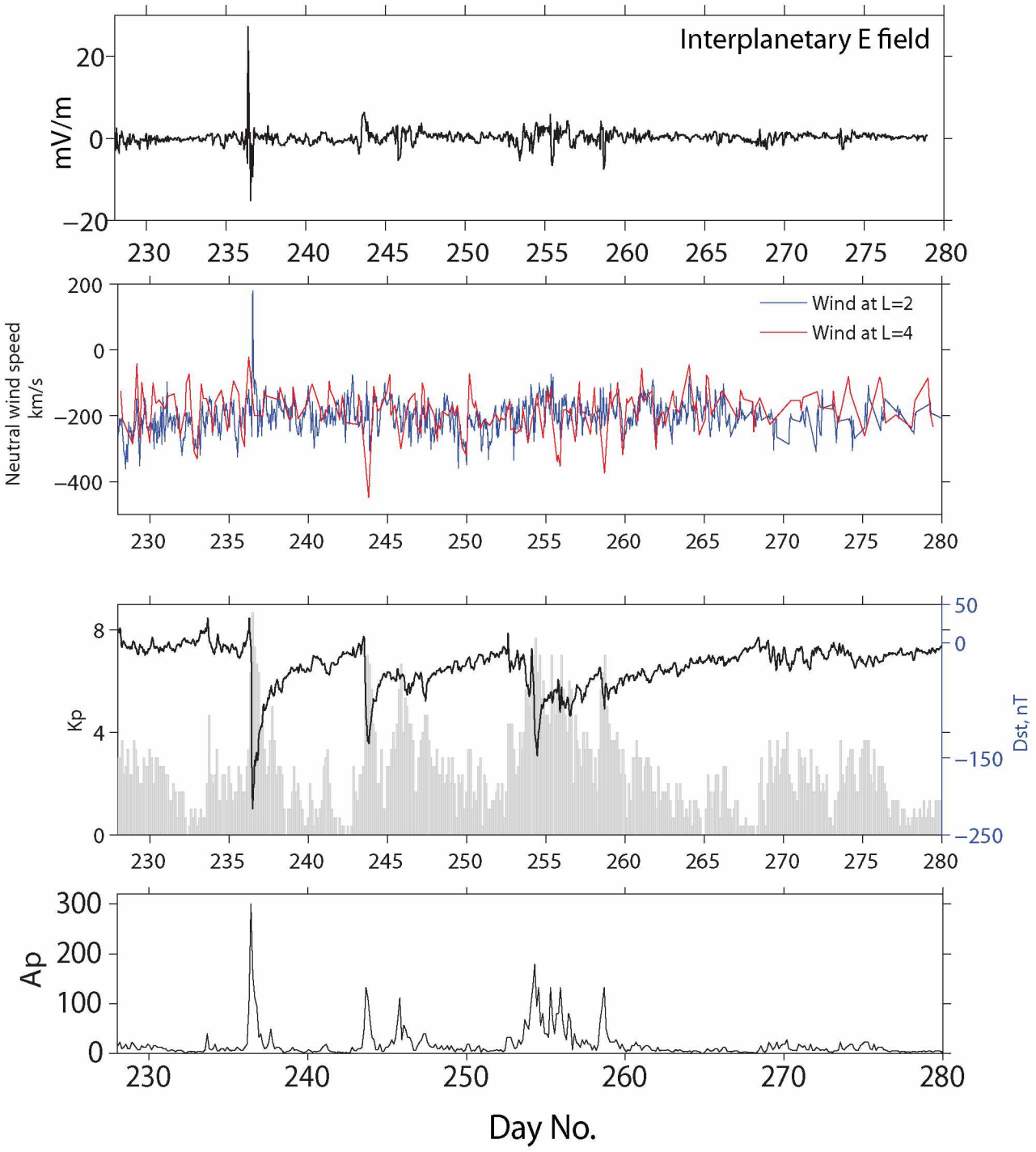

Figure 3.61. Variation of interplanetary electric field and thermospheric wind during the 16 August to 06 October 2005 period

The recovery times of electron and ion densities may depend on the rate of energy input from solar origin into the earth's magnetosphere. For example, when a high amount of energy is input over short duration (as with the storm on 24 August 2005) the ionosphere and plasmasphere may respond impulsively and the response could also decay faster. Whereas, if a small amount of energy is input over long duration (as with the 01–03 September or 10–14 September 2005 storms) the ionosphere and plasmasphere may respond slowly but the decay could be longer. In this context, measurements of the rate of energy release during CMEs and or high speed streams seem useful to predict the severity of space weather events [Balan et al., 2013].

3.8.2.3 Contribution of thermal O^+ inside the plasmasphere to O^+ rich ring current during storm time

As noted above, WM radio sounding results as well as DMSP in situ measurements indicate an increase in O^+ during the storm main phase and recovery phase. The enhanced O^+ decreases later in the recovery phase. The source of these ions is the ionosphere. During storm time the plasmaspheric thermal electrons get heated. The resultant heat is conducted down to the underlying ionosphere and it raises the temperatures of ionospheric ions and electrons. This results in increases of the scale height of ionospheric plasma causing upward diffusion of O^+ ions. These enhanced O^+ ions should be observed in the ring current population as warm O^+. In fact, Hamilton et al. [1988] found greatly increased concentrations of O^+ in the ring current during disturbed periods. Daglis et al. [1999a, 1999b] showed that ionospheric origin ions contribute a large part of ring current particles during large storms. Fu et al., 2001 using CRRES data for four selected storms found energetic particle enhancements at very low equatorial altitudes (L=3–4) during large storms with significant delays relative to the storm sudden commencement times. They also found that fractional number density of O^+ ions increases with the intensity of the storm. We believe observing the spatial and temporal variations of the density of ions (H^+, He^+, O^+) will shed light on understanding the role they play in controlling the properties of the ring current.

3.8.2.4 Comparison of WM sounding results with other satellite measurements, bottomside sounding results and empirical model predictions

Whistler mode sounding results are compared with in situ measurements from other satellites, bottomside sounding results, and empirical model predictions. Electron density obtained from the DMSP (~850 km) and CHAMP (~350 km) satellites was within ~20-30% of that from WM sounding. Ion compositions obtained from DMSP were within ~0.5-2 times of that from WM sounding at respective altitudes. The bottomside sounding results from ionosonde stations consistently overestimated electron density at F2 peak by ~2-3 times relative to WM sounding results. Predictions from GCPM and IRI-2012 models overestimated electron density at lower altitudes relative WM sounding results. The difference is maximum at the F2 peak where the N_e obtained from GCPM and IRI is roughly 2-3 times that from WM sounding. This is consistent because IRI-2012 uses N_e obtained from bottomside sounding and GCPM uses IRI model to predict N_e at lower altitudes. GCPM and Ozhogin et al. [2012] predictions of electron density above 2000 km are within ~30% of WM sounding results. Relative to WM sounding results, GCPM overestimates N_{H^+} and N_{O^+} by ~1.4 and ~2 times, respectively, at lower altitudes and IRI substantially underestimated α_{He^+} (almost 0) at all altitudes. Empirical model predictions of ions are based on limited amount of available data on ion measurements. Furthermore, the ion measurements are either in situ or from incoherent scatter radar that may not represent field aligned ion densities. Whistler mode sounding of N_e and α_i can be used to develop new empirical models of field-aligned electron density and ion composition. These new empirical models can be used in the development of physics-based models as well as for testing and validating physics-based models.

3.8.3 Conclusions

The WM sounding has permitted first measurements of field-aligned electron density and ion composition inside the plasmasphere as a function of geomagnetic storm activity. Whistler mode sounding results indicated that the electron density, relative ion concentrations, and O^+/H^+ transition height underwent temporal changes as a function of geomagnetic storm activity, and each species has different temporal behavior, thus indicating different recovery times. Also, the recovery times of electron density and ion composition on the day-side is different than that on the

night-side. The variations in the plasma parameters obtained from WM sounding results are consistent with the past observations and in situ measurements from CHAMP and DMSP. Based on the past knowledge and the measurements of thermospheric neutral wind and interplanetary electric field it appears both winds and electric fields may have contributed to the temporal variations of electrons and ions. Further work involving coupled WM sounding results and physics-based model simulations will allow investigation of the role of thermospheric winds, dynamo electric fields, and PPEF in causing the storm time variations in electron density and ion composition. Such studies will also test current theories and validate physics-based models of thermosphere-ionosphere-magnetosphere coupling.

Chapter 4

Summary, Discussion, Future Work and Conclusions

4.1 Summary

Observations of magnetospherically and specularly reflected whistler mode echoes by RPI/IMAGE has permitted for the first time measurement of field-aligned electron density, ion composition, ion effective mass and field-aligned irregularities [Sonwalkar et al., 2004; Sonwalkar et al., 2011a; Sonwalkar et al., 2011b]. The WM radio sounding method involves an iterative procedure. In this method, a ray tracing density model is assumed and simulations are carried out to calculate $t_g - f$ and cutoffs for each of the observed echoes. The calculated $t_g - f$ is then compared with the measured ones. If the time delays and cutoffs do not agree, a new density model is assumed and the process is repeated until a match is obtained. Sonwalkar et al. [2011b] demonstrated the WM radio sounding method, but certain important aspects of it including: (1) an efficient approach to adjust the density model during the iterative process; (2) uncertainties in the measurement of effective ion mass; and (3) augmentation of WM sounding results with near simultaneous in situ measurements from other satellites and/or bottomside sounding results were not adequately addressed.

In Chapter 2 of this thesis, a systematic and iterative procedure for implementing the WM radio sounding method is presented. This procedure was demonstrated with a case study. The measurement of effective ion mass depends on the number of ion species assumed in the ray tracing density model. This assumption leads to uncertainty in the measurement of m_{eff}. The uncertainty in m_{eff} was illustrated with two different density models that explain observed WM echo features. For one model it was assumed that the magnetospheric plasma is composed of three ions (H^+, He^+, and O^+; three ion model). For the other it was assumed that the plasma is composed of two ions (H^+ and O^+; two ion model). Once m_{eff} was obtained, individual ion concentrations were determined using the equation of m_{eff} and that the sum of fractional abundance of all ion species is equal to 1. In the two ion model case, there is no uncertainty in the measurement of ions once m_{eff} is obtained. However, in the three ion model case additional assumptions are needed to determine individual ion concentrations. Also discussed in Chapter 2 is the uncertainty in the measured ion composition when three ion species are assumed in the density model.

To cover larger altitude ranges and choose one amongst many density models that can explain observed echo features, whistler mode radio sounding results can be augmented with near-simultaneous in situ measurements from other satellites and bottomside sounding results . Magnetospherically reflected WM echoes allow measurement of plasma density and composition from satellite altitude down to ~1500 km. Specularly reflected WM echoes allow measurement of plasma density from satellite altitude down to 90 km. Magnetospherically reflected WM echoes accompanied by specularly reflected WM echoes allow measurement of both electron density and ion composition from satellite altitude down to 90 km. When only MR or SR echoes were observed, as discussed in Chapter 2, there can be large uncertainties in the measurement of N_e at altitudes below ~1500 km. In such cases in situ measurements from DMSP, CHAMP, and/or bottomside sounding results from ground based ionosonde stations can be used to augment whistler mode sounding results below ~1500 km. This method of augmenting WM sounding results was discussed in Chapter 2.

In Chapter 3, the WM radio sounding method was applied to determine, for the first time, the response of plasmaspheric field-aligned electron and ion densities to several geomagnetic storms that occurred in succession during the 16 August to 06 October 2005 period. The Kp and Dst indices and the sunspot number and solar flux parameters were used to determine the geomagnetic and solar conditions during this period. The interplanetary conditions were determined using IMF Bz, proton density, temperature, interplanetary electric field, and solar wind speed.

Using WM radio sounding data from IMAGE, the variation of plasmaspheric field-aligned electron density and ion composition was determined during the onset, main and recovery phases of geomagnetic storms. The variations in the plasma density and composition were obtained in the L-shell range 1.7–2.4 on the day-side for all storms and at L~2.3 on the night-side for one moderate storm. The WM radio sounding results were augmented by in situ measurements from DMSP, CHAMP, and measurements from ground based ionosonde stations. The following results were found as a function of geomagnetic storm activity: (1) The plasmapause moved from Lpp~4.5 during the quiet time to Lpp~2.4 during the disturbed time. (2) On the day-side at L~2 when major and moderate or two moderate storms occurred in succession in an interval of roughly less than a day, the latter storms had little or no effect on the electron density and/or ion composition. (3) When storms affected the plasma parameters on both day-side and night-side the electron

density, relative ion concentrations, and O^+/H^+ transition height underwent temporal changes as a function of geomagnetic storm activity, and each species had different temporal behavior thus indicating different recovery times. (4) On the day-side, the O^+/H^+ transition height increased by ~200-300 km during the onset, main, and early recovery phases of the storms. (5) Variation in the electron density below the O^+/H^+ transition height was different from that above. (6) Electron density at F2 peak increased during the onset or main phase of storms followed by a decrease in the recovery phase. (7) Electron density above 1500 km increased either in the onset or on the first day of recovery phase followed by a decrease. (8) α_{H^+} decreased during the onset, main and/or early recovery phases of storms; α_{O^+} increased in the early recovery phase of the storm; α_{He^+} varied in a complex manner but an increase in α_{He^+} in the onset phase and decrease in α_{He^+} in the recovery phase was more common. (9) On the night-side, WM sounding results showed decrease in N_e above 1500 km in the recovery phase of the 04 September moderate storm. Not sufficient WM data was available to study the plasma density and composition variations in the case of other storms and at altitudes below 1500 km and other L-shells as a function of storm activity. (10) Variations in plasma parameters measured by CHAMP (350 km) and DMSP (850 km) were in agreement with those obtained from whistler mode sounding.

The WM sounding measurements of field-aligned plasma density and composition presented here will lead to better understanding of plasma flow from the ionosphere to the magnetosphere and vice versa that is important for thermosphere-ionosphere-magnetosphere coupling, as well as for testing the predictions from various physics-based models.

4.2 Discussion

The WM radio sounding method has many advantages over free space and Z mode sounding methods from RPI/IMAGE. The N_e measurements along $\mathbf{B_0}$ by R-X and L-O mode (free space modes) sounding by RPI are possible only down to ~2000–3000 km because of the spatial resolution of the 3.2 ms pulse [Reinisch et al., 2004]. The N_e measurements along $\mathbf{B_0}$ by Z mode sounding are limited to altitudes above ~1000 km, the minimum reflection altitude of Z mode waves transmitted by RPI/IMAGE [Sonwalkar et al., URSIGA 2014b; Carpenter et al., 2003]. Neither free space mode sounding nor Z mode sounding permits the measurement of ion composition. Whistler mode radio sounding is a powerful new method that provides measurement of both field-aligned electron

density and ion composition from the satellite altitude (<5,000 km) down to 90 km, including the important region of transition from the O^+dominated ionosphere to the light ion regime above.

4.3 Recommendations for future work

The rich whistler mode echo data set and the new whistler mode radio sounding method provide many opportunities for future research.

First, the whistler mode sounding method discussed here can be improved in several ways. Used as tool in the WM radio sounding method, the Stanford 2D ray tracing density model, has sufficient parameters that provide flexibility to adjust and obtain desired N_e but not ion composition. The density model assumes that scale heights of ions are inversely proportional to their atomic mass resulting in rapid decrease of He^+ and O^+ above Rbase ($\sim$1000 km). This is the result of assuming the same temperature for all ion species in the density model. It is therefore suggested that results from past ion measurements and recent empirical models should be used to construct a new parametric ray tracing density model for use in determining ion composition and electron density from whistler mode sounding. One more way to strengthen WM sounding method would be to augment the WM sounding results with results from empirical models that provide electron density at the equator [e.g., Carpenter and Anderson, 1992]. Such a method will provide electron density measurements from the equator down to 90 km.

Second, the study presented here on the evolution of plasma parameters as a function of storm activity can be extended to other regions of the magnetosphere including the plasmapause, auroral, and high latitude regions. Approximately 2500 WM echoes observed on IMAGE at all latitudes and MLT's [Sonwalkar et al., URSIGA 2014a] are available for this study. Theoretical explanation of the plasmapause phenomenon, as a boundary or as a boundary layer [Carpenter and Lemaire, 2004], its evolution with time, associated erosion processes, and various features such as plumes remains poorly understood. Earlier theoretical work included studies of the stability of the plasmapause profile (e.g., Richmond [1973]; Lemaire [1975]), and more recently, theoretical work has included development of physics-based fluid and kinetic models of the plasmasphere and its erosion and recovery (e.g., Pierrard et al. [2009] and references therein). Further progress toward understanding the erosion processes would clearly depend upon the ability of the observations to cover larger regions of the plasmasphere boundary, including underlying the ionospheric plasma,

so as to elucidate its topology. For example, Pierrard and Voiculescu [2011] have recently coupled the 3D dynamic model of the plasmasphere developed by Pierrard and Stegen (2008) with the ionospheric IRI model with encouraging results. However, IRI suffers from a serious drawbacks: its ion composition model is built from measurements with large uncertainties [Bilitza and Reinisch, 2008]; its electron density model overestimates by 50-60% near the F2 peak [Luhr and Xiong, 2010]; it is limited to <2000 km. A better ionospheric model is needed to couple with the plasmaspheric model. Whistler mode sounding results will provide a better plasma model (<5000 km), including electron density and ion composition, to couple with an overlying plasmaspheric model, and thus improve the predications of simulations. On the other hand, simulation predications can be compared with specific WM sounding results when direct measurements are not available.

During storm times, energetic particles from the plasmasheet guided along magnetic field lines are precipitated in the auroral ionosphere. The particle precipitation can effectively ionize the F-region and elevate ionospheric ion supply to higher topside altitudes. Subauroral polarization streams (SAPS), westward ion flows equatorward of the auroral boundary in the night-side, result from differences in the electron and ion precipitation from the plasmasheet; due to the low conductivity equatorward of the auroral region, this results in polarized electric fields, driving eastward ion flows. Less frequent are latitudinally narrow (1-3°) regions of fast ion drift (over 1000 m/s) in the pre-midnight region. These particular enhancements result from recombination chemical reactions that locally deplete ion density, leading to larger polarization electric fields and larger ion drifts [Anderson et al., 1993]. Whistler mode sounding results on plasma density and composition obtained in the auroral region will be useful for understanding the physics of the auroral processes. They will also improve physics-based models (e.g., DyFk) that are used to study the ion outflow in this region.

Knowledge of high latitude plasma density and composition is important because they are intimately tied to the physics of the auroral acceleration processes, including auroral precipitation, visible and radar aurora, and magnetic storm and substorm activity [e.g., Kelley, 2009; Schunk and Nagy, 2000). Plasma density and composition are important parameters in many theories of auroral acceleration and polar ion outflow, two key processes at high latitude [e.g., Hargreaves, 1992]. Whistler mode echoes observed in the high latitude region provide an excellent opportunity to study plasma density and composition in the high latitude region.

Whistler mode sounding can provide the distributions of plasma density irregularities in space and time throughout the plasmasphere [Sonwalkar et al., 2004; Sonwalkar et al., 2011b]. The generation of plasma density structures is an important manifestation of the injection of energy and momentum originating at the sun into the earth's atmosphere and physical processes occurring in the underlying neutral atmosphere and in the overlying ionosphere and magnetosphere. FAIs occur at all MLT in all parts of the magnetosphere [Kelley, 2009; Schunk and Nagy, 2000; Hunsucker and Hargreaves, 2003] and are generated by various processes including plasma instabilities, particle precipitation, and plasma drifts occurring in the ionosphere [Kelley, 2009]. These plasma processes are enhanced during disturbed solar and geomagnetic conditions, leading to the generation of plasma density structures. Thus FAIs are one of the key indicators of space weather and of physical processes occurring as a result of changing space weather conditions.

The large number of WM echoes observed under quiet as well as disturbed conditions provide a new method to study FAI dependence on geomagnetic activity at higher altitudes. Measurement of FAIs at higher altitudes are not directly accessible to low altitude satellites or the ground radars. Geomagnetic storms can dramatically alter the plasma density and density structures in the ionosphere. For example, the observations from ionospheric sounding, DMSP satellites and GPS TEC during the 2003 Halloween storm indicate that the equatorial ionospheric irregularities or plasma bubbles (EPBs) extend to the Argentinean station Rawson (λ_m=33.1° S) and map at the magnetic equator at an altitude of about 2500 km [Sahai et al., 2009]. Huang et al., [2009] have shown that EPBs develop during main phase of the storm and are suppressed during the recovery phase for several hours to days. Observations from the DEMETER satellite (710 km) have provided a general framework showing how low-, mid-, and subauroral-latitude plasma density structures and associated electric field irregularities respond to geomagnetic storms [Pfaff et al., 2008]. These authors found a close relation between the development of a storm as indicated by Dst and the increased ambient density and the region of irregularities. Using the data from ROCSAT satellite, Su et al. [2006] distinguished the mid- and low-latitude irregularities on the basis of solar and geomagnetic disturbances.

At low altitudes, IMAGE has observed VLF ground transmitter signals on almost every RPI plasmagram. The transmitted power of the VLF ground transmitted signals is hundreds of kilowatts and the bandwidth is a few hundred Hz. These observations of VLF ground transmitter

signals by RPI can be used to detect small scale FAIs. The signal from the transmitter propagates in the Earth-ionosphere waveguide. A part of this signal couples to the ionosphere as a wave propagating in the whistler mode. In the presence of small scale (10 m–1 km) FAI, the VLF signals are forward scattered. The scattered waves containing a range of wave normals lead to spectrally broadened (f$\sim$1-2 kHz) signals on a moving satellite [Bell et al., 1983; Bell and Ngo, 1988, 1990]. These spectrally broadened signals can be used to detect FAI. Note that the FAI that lie between the ground and the IMAGE are illuminated by RPI signals at large wave normal angle coming down and ground transmitter signals at relatively small wave normal angles (roughly vertical) from below. Thus simultaneous observations of diffuse WM echoes and spectrally broadened transmitter signals could potentially be a new diagnostic method to study FAI.

Comparison of WM sounding results with the data from past missions allows determination of how accurately the statistical data represents field-aligned measurements and comparison of plasma parameters obtained by different techniques. Data on the plasma density and composition is available from past missions including Alouette-1 (Altitude range$\sim$1000 km) and Alouette-2 (Altitude range$\sim$500–3000 km), AE-c,-d,-e (Altitude range$\sim$150–4000 km), ISIS-1 (Altitude range$\sim$500–3500 km) and ISIS-2 (Altitude range$\sim$1400 km) topside sounders, and OGO-6 (Altitude range$\sim$400–1100 km) spacecraft covering the period 1962–1979. The WM sounding results can also be compared with incoherent scatter radar data that provides plasma density and composition from about 90–1000 km. The results from such comparisons can be used to improve measurement techniques.

Whistler mode sounding measurements of field-aligned electron and ion densities, combined with simulations using a physics-based thermosphere-ionosphere-magnetosphere dynamics model (e.g., SAMI2), provide a unique approach to study the role of thermospheric winds, dynamo electric fields, and PPEFs in modifying the ionosphere-magnetosphere. Such studies also validate and improve physics-based models of magnetosphere-ionosphere-thermosphere coupling. The SAMI2 [Huba et al., 2000] models plasma and chemical evolution of seven ion species in the altitude range 85 km–20,000 km in the low-mid latitude region. The model solves electron and ion (H^+, He^+ and O^+) temperature and momentum equations and takes into account ExB drift. It uses an offset tilted dipole magnetic field model. The inputs to SAMI2 include F10.7 flux, Ap, and scaling factors for neutral wind, ExB drifts, neutral densities that are specified by empirical models. The outputs from

SAMI2 include ion densities, ion drift velocities, neutral winds, and ExB drifts. Preliminary studies [Sonwalkar et al., AGU 2013] comparing SAMI2 simulation results with field-aligned electron and ion densities obtained from whistler mode sounding demonstrate that such studies can potentially provide information on neutral density, wind, and electric field. It can also be used to validate and improve the performance of the SAMI2 model. Such a study, however, poses many challenges that need to be addressed in the future: (1) The solution found for the tuning parameters that allows SAMI2 to match the whistler mode data may not be unique. (2) SAMI2 by default uses the Scherliess and Fejer [1999] (SF) empirical model to specify electric fields. The magnitudes and time evolutions of the electric fields at L=2–3 are not expected to follow that SF empirical model. Therefore, a new electric field model is needed to specify the ExB drifts and improve SAMI2. (3) Storm time electric fields that are of solar origin are not included in SAMI2. The SMAI2 model has to be combined with other existing models, such as the Rice Convection Model to take into account the effect of disturbed time electric fields. How these challenges can be addressed is beyond the scope of this work.

4.4 Conclusions

Whistler mode sounding has permitted the first measurements of field-aligned electron density and ion composition inside the plasmasphere as a function of geomagnetic storm activity. Whistler mode sounding results show that the electron density, relative ion concentrations, and O^+/H^+ transition height undergo temporal changes as a function of geomagnetic storm activity, and each species has a different temporal behavior thus indicating of different recovery times. The apparent recovery times of electron density and ion composition on the day-side is different than that on the night-side. The variations in the plasma parameters obtained from WM sounding results are consistent with past observations. In the past, in order to study the variations in plasma density and composition at a range of altitudes, it was necessary to piece together data obtained on multiple satellites and from the ground. Such coordinated measurements were infrequent and did not provide the field-aligned plasma distributions that are critical to understand the physical processes that influence plasma flow along field lines during disturbed conditions. Whistler mode sounding allows study of the dynamics of field-aligned electron density and ion composition as function of geomagnetic storm activity in the $\sim$5000 km to 90 km altitude range, including the important

region of transition from the O^{+}dominated ionosphere to the light ion regime above. The temporal variations of field-aligned electron density and ion composition obtained from WM sounding coupled with physics-based models provide a unique way to investigate the role of thermospheric winds, dynamo electric fields, and storm time electric fields in causing the variations in electron density and ion composition. Such studies will also test current theories and validate physics-based models of thermosphere-ionosphere-magnetosphere coupling.

References

Anderson, P. C., W. B. Hanson, R. A. Heelis, J. D. Craven, D. N. Baker, and L. A. Frank (1993), A proposed production model of rapid subauroral ion drifts and their relationship to substorm evolution, J. Geophys. Res., 98(A4), 6069-6078.

Angerami, J. J., and J. O. Thomas (1964), Studies of planetary atmosphere: 1. The distribution of electrons and ions in the Earth's exosphere, J. Geophys. Res., 69, 4537.

Balan, N., Y. Otsuka, M. Nishioka, J. Y. Liu, and G. J. Bailey (2013), Physical mechanisms of the ionospheric storms at equatorial and higher latitudes during the recovery phase of geomagnetic storms, J. Geophys. Res., 118, 2660-2669, doi:10.1002/jgra.50275.

Balsiger, H., P Eberhardt, J. Geiss, and D.T. Young (1980), Magnetic storm injection of 0.9- to 16 keV/ e solar and terrestrial ions into the high-altitude magnetosphere, J. Geophys. Res., 85(A4), 1645-1662.

Banks, P. M., A. F. Nagy, and W. I. Axford (1971), Dynamical behavior of thermal protons in the mid-latitude ionosphere and magnetosphere, Planet. Space Sci., 19, 1053.

Barrington, R. E., J. S. Belrose, and G. L. Nelms (1965), Ion composition and temperature at 1000 km as deduced from simultaneous observations of a VLF plasma resonance and topside sounding data from the Alouette I satellite, J. Geophys. Res., 70, 1647-1664.

Barrington, R. E., J. S. Belrose, and W. E. Mather (1966), A helium whistler observed in the Canadian satellite Alouette 2, Nature London, 210, 80-81.

Baugher, C. R., C. R. Chappell, J. L. Horwitz, E. G. Shelley, D. T. Young (1980), Initial thermal plasma observations from ISEE 1, Geophys. Res. Lett., 7, 657.

Bell, T. F., H. G. James, U. S. Inan, and J. P. Katsufrakis (1983), The apparent spectral broadening of VLF transmitter signals during transionospheric propagation, J. Geophys. Res., 88, 4813.

Bell, T. F., and H. Ngo (1988), Electrostatic waves stimulated by coherent VLF signals propagating in and near the inner radiation belt, J. Geophys. Res., 93, 25992618.

Bell, T. F., and H. D. Ngo (1990), Electrostatic lower hybrid waves excited by electromagnetic whistler mode waves scattering from planar magnetic-field-aligned plasma density irregularities, J. Geophys. Res., 95, 149.

Benson, R. F., V. A. Osherovich, J. Fainberg, and B. W. Reinisch (2003), Classification of IMAGE/RPI-stimulated plasma resonances for the accurate determination of magnetospheric electron density and magnetic field values, J. Geophys. Res., 108(A5), 1207, doi:10.1029/2002JA009589.

Benson, R. F., P. A. Webb, J. L. Green, L. Garcia, and B. W. Reinisch (2004), Magnetospheric electron densities inferred from upper-hybrid band emissions, Geophys. Res. Lett., 31, L20803, doi:10.1029/2004GL020847.

Benson, R. F. (2010), Four decades of space-borne radio sounding, Rad. Sci. Bull., 333, 24-44.

Berube, D., M. B. Moldwin, and J. M. Weygand (2003), An automated method for the detection of field line resonance frequencies using ground magnetometer techniques, J. Geophys. Res., 108(A9), 1348, doi:10.1029/ 2002JA009737.

Berube, D., M. B. Moldwin, S. F. Fung, and J. L. Green (2005), A plasmaspheric mass density model and constraints on its heavy ion concentration, J. Geophys. Res., 110, A04212, doi:10.1029/2004JA010684.

Bilitza, D., and B. W. Reinisch (2008), International Reference Ionosphere 2007: Improvements and new parameters, Adv. Space Res., 18, 599-609.

Bilitza, D., D. Altadill, Y. Zhang, C. Mertens, V. Truhlik, P. Richards, L. -A. McKinnell, and B. W. Reinisch (2014), The International Reference Ionosphere 2012 A model of international collaboration, J. Space Weather Space Clim., 4, A07.

Blanc, M., and A. D. Richmond (1980), The Ionospheric Disturbance Dynamo, J. Geophys. Res., 85, 16691686.

Brice, N. M., and R. L. Smith (1965), Lower hybrid resonance emissions, J. Geophys. Res., 70, 71.

Brinton, H. C., R. A. Pickett, and H. A. Taylor (1969), Diurnal and seasonal variation of atmosphericio n composition;C orrelation with solar zenith angle, J. Geophys. Res., 74, 4064.

Buonsanto, M.J. (1999), Ionospheric Storms A Review, Space Sci. Rev., 88, 563.

Carpenter D. L. (1966), Whistler studies of the plasmapause in the magnetosphere. 1. Temporal variations in the position of the knee and some evidence on plasma motions near the knee. J. Geophys. Res.,71, 693-709.

Carpenter, D. L., and R. R. Anderson (1992), An ISEE/whistler model of equatorial electrondensity in the magnetosphere, J. Geophys. Res., 97(A2), 1097-1108.

Carpenter, D. L., B. L. Giles, C. R.Chappell, P. M. E. Decreau, R. R. Anderson, A. M. Persoon, A. J. Smith, Y. Corcuff, and P. Canu (1993), Plasmasphere dynamics in the duskside bulge region: A new look at old topic, J. Geophys. Res., 98, 19243-19271, doi:10.1029/93JA00922.

Carpenter, D. L., V. S. Sonwalkar, R. A. Helliwell, M. Walt, U. S. Inan, M. Ikeda, and D. L. Caudle (1997), Probing properties of the magnetospheric hot plasma distribution by whistler mode wave injection at multiple frequencies: Evidence of spatial as well as temporal wave growth, J. Geophys. Res., 102(A7), 355-362.

Carpenter, D. L., M. A. Spasojevic, T. F. Bell, U. S. Inan, B. W. Reinisch, I. A. Galkin, R. F. Benson, J. L. Green, S. F. Fung, and S. A. Boardsen (2002), Small-scale field-aligned plasmaspheric density structures inferred from the Radio Plasma Imager on IMAGE, J. Geophys. Res., 107(A9), 1258, doi:10.1029/2001JA009199.

Carpenter, D. L., T. F. Bell, U. S. Inan, R. F. Benson, V. S. Sonwalkar, B. W. Reinisch, and D. L. Gallagher (2003), Z-mode sounding within propagation "cavities" and other inner magnetospheric regions by the RPI instrument on the IMAGE satellite, J. Geophys. Res., 108, 1421, doi:10.1029/2003JA010025.

Carpenter D. L. and J. Lemaire (2004), The Plasmasphere Boundary Layer, Annales Geophysicae , 22, 4291-4298.

Carpenter, D. L., T. F. Bell, D. Chen, D. Ng, C. Baran, B. W. Reinisch, and I. Galkin (2007), Proton cyclotron echoes and a new resonance observed by the Radio Plasma Imager instrument on the IMAGE satellite, J. Geophys. Res., 112, A08208, doi:10.1029/2006JA012139.

Chappell, C. R., K. K. Harris, and G.W. Sharp (1970a), A study of the influence of magnetic activity on the location of the plasmapause as measured by OGO 5, J. Geophys. Res., 75, 50.

Chappell, C. R., K. K. Harris,a nd G. W. Sharp (1970b), The morphology of the bulge region of the plasmasphere, J. Geophys. Res., 75, 3848.

Chappell, C. R., K. K. Harris, and G. W. Sharp (1971), The dayside of the plasmasphere, J. Geophys. Res., 76, 7632.

Chappell, C. R. (1974), Detached plasma regions in magnetosphere, J. Geophys. Res., 79(13), 18611870, doi:10.1029/JA079i013p01861.

Chi, P. J., C. T. Russell, S. Musman, W. K. Peterson, G. Le, V. Angelopoulos, G. D. Reeves, M. B. Moldwin, and F. K. Chun (2000), Plasmaspheric depletion and refilling associated with the September 25, 1998 magnetic storm observed by ground magnetometers at L = 2, Geophys. Res. Lett., 27(5), 633-636.

Chi, P. J., C. T. Russell, J. C. Foster, M. B. Moldwin, M. J. Engebretson, and I. R. Mann (2005), Density enhancement in plasmasphere-ionosphere plasma during the 2003 Halloween Superstorm: Observations along the 330th magnetic meridian in North America, Geophys. Res. Lett., 32, L03S07, doi:10.1029/2004GL021722.

Clilverd, M. A., A. J. Smith, and N. R. Thomson (1991), The annual variation in quiet time plasmaspheric electron density determined from whistler mode group delays, Planet. Space Sci., 39, 1059 1067.

Cooke, D. L., W. Turnbull, C. Roth, A. Morgan, and R. Redus (2003), Ion drift-meter status and calibration, in: First Champ Mission Results for Gravity, Magnetic, and Atmospheric Studies, edited by: Reigber, C., Luhr, H., and Schwintzer, P., Springer, New York, 212219.

Craven, P. D., D. L. Gallagher, R. H. Comfort (1997), Relative concentration of He+ in the inner magnetosphere as observed by the DE1 retarding ion mass spectrometer. J. Geophys. Res., 102, 2279.

Daglis, I. A., The role of magnetosphere-ionosphere coupling in magnetic storm dynamics, in Magnetic Storms (1997), Geophys. Monogr. Ser., vol.98, edited by B. T. Tsurutani et al., AGU, Washington D.C., 107-116.

Daglis, I. A., W. Baumjohann, J. Geiss, S.Orsini, E. Sarris, M. Scholer, B. T. Tsurutani, D. Vassiliadis (1999a), Recent advances open questions and future directions in solar-terrestrial research Phys. Chem. Earth, 5-28.

Daglis, I . A., G. Rasotakis, E . Sarris ,Y . Kamide, S . Livi, B. Wilken, Variations of the ion composition during a large magnetic storm and their consequences (1999b), Phys. Chem. Earth, 24, 229-232.

Danilov, A.D., (2001), F2-region response to geomagnetic disturbances, J. Atoms. Sol. Terre. Phys. 63, 431.

Darrouzet F, D. L. Gallagher,N Andr, D. L. Carpenter, I. Dandouras, P. M.E. Dcrau, J De Keyser, R. E. Denton, J.C. Foster, J. Goldstein, M. B. Moldwin, B.W. Reinisch, B. R. Sandel, and J. Tu (2009), Plasmaspheric density structures and dynamics: properties observed by the CLUSTER and IMAGE missions, Space Sci. Rev. 145, 55-106.

Davies, K., and R. Rster (1976), Theoretical studies of storm effects in ionospheric total electron content, Planet. Space Sci., 24, 867.

De La Beaujardiere, O., et al. (2004), C/NOFS: A mission to forecast scintillations, J. Atmos. Sol. Terr. Phys., 66, 1573- 1591, doi:10.1016/ j.jastp.2004.07.030.

Dent, Z. C., I. R. Mann, J. Goldstein, F. W. Menk, and L. G. Ozeke (2006), Plasmaspheric depletion, refilling, and plasmapause dynamics: A coordinated ground-based and IMAGE satellite study, J. Geophys. Res., 111, A03205, doi:10.1029/2005JA011046.

Denton, R. E., and D. L. Gallagher (2000), Determining the mass density along magnetic field lines from toroidal eigenfrequencies, J. Geophys. Res., 105(A12), 27717.

Denton, R. E., E. G. Miftakhova, M. R. Lessard, R. Anderson, and J. W. Hughes (2001), Determining the mass density along magnetic field lines from toroidal eigenfrequencies: Polynomial expansion applied to CRRES data, J. Geophys. Res., 106, 29915 29924.

Denton, R. E., Y. Wang, P. A. Webb, P. M. Tengdin, J. Goldstein, J. A. Redfern, and B. W. Reinisch (2012), Magnetospheric electron density long-term (>1 day) refilling rates inferred from passive radio emissions measured by IMAGE RPI during geomagnetically quiet times, J. Geophys. Res., 117, A03221, doi:10.1029/2011JA017274.

Echer, E., W. D. Gonzalez, B. T. Tsurutani, and A. L. C. Gonzalez (2008), Interplanetary conditions causing intense geomagnetic storms (Dst≤100 nT) during solar cycle 23 (19962006), J. Geophys. Res., 113, A05221, doi:10.1029/2007JA012744.

Edgar, B. C. (1976), The lower and upper frequency cutoffs of magnetospherically reflected whistlers, J. Geophys. Res., 81, 205-211.

Evans, J. V., and J. M. Holt (1978), Nighttime proton fluxes at Millstone Hill, Planet. Space Sci., 26(8), 727744.

Farrugia, C. J., D. T. Young, J. Geiss, H. Balsiger (1989), The composition temperature and density structure of cold ions in the quiet terrestrial plasmasphere: GOES 1 results, J. Geophys. Res., 94(11), 865.

Fejer, B. G., and M. C. Kelley (1980), Ionospheric irregularities, Rev. Geophys., 18(2), 401-454.

Foster, J. C., P. J. Erickson, A. J. Coster, J. Goldstein, and F. J. Rich (2002), Ionospheric signatures of plasmaspheric tails, Geophys. Res. Lett., 29(13), 1623, doi:10.1029/2002GL015067.

Foster, J. C., A. J. Coster, P. J. Erickson, F. J. Rich, and B. R. Sandel (2004), Stormtime observations of the flux of plasmaspheric ions to the dayside cusp/magnetopause, Geophys. Res. Lett., 31, L08809, doi:10.1029/2004GL020082.

Foster, J. C., and W. Rideout (2005), Mid-latitude TEC enhancements during the October 2003 Superstorm, Geophys. Res. Lett., 32 , L12S04, doi:10.1029/ 2004GL021719.

Fraser, B. J., J. L. Horwitz, J. A. Slavin, Z. C. Dent, and I. R. Mann (2005), Heavy ion mass loading of the geomagnetic field near the plasmapause and ULF wave implications, Geophys. Res. Lett., 32, L04102, doi:10.1029/ 2004GL021315.

Fu S. Y., B. Wilken, Q. G. Zong, and Z. Y. Pu (2001), Ion composition variations in the inner magnetosphere: Individual and collective storm effects in 1991, 106, A12, 29683-29704.

Gallagher, D. L., P. D. Craven, and R. H. Comfort (2000), Global core plasma model, J. Geophys. Res., 105(A8), 18819-18833.

Goldstein, J., R. E. Denton, M. K. Hudson, E. G. Miftakhova, S. L. Young, J. D. Menietti, and D. L. Gallagher (2001), Latitudinal density dependence of magnetic field lines inferred from Polar plasma wave data, J. Geophys. Res., 106(A4), 6195-6201.

Goldstein, J. (2006), Plasmasphere response: tutorial and review of recent imaging results, Space Sci. Rev., 124, 203, doi:10.1007/s11214-006-9105-y.

Gonzalez, W. D., B. T. Tsurutani, and A. L. Clua de Gonzalez (1999), Interplanetary origin of magnetic storms, Space Sci. Rev., 88, 529 562.

Grande, M., Perry, C. H., Blake, J. B., Chen, M., Fennell, J., Roeder, J. L., et al. (1996), Evolution of the ring current ion population, as observed by the CRRES/MICS instrument, Workshop on the Earth's Trapped Particle Environment, Taos/NM USA, Woodbury, New York: AIP Conference Proceedings, 383, 137-143.

Grew, R. S., F. W. Menk, M. A. Clilverd, and B. R. Sandel (2007), Mass and electron densities in the inner magnetosphere during a prolonged disturbed interval, Geophys. Res. Lett., 34, L02108, doi:10.1029/ 2006GL028254.

Groves, K., M. Lee, and S. Kuo (1988), Spectral broadening of VLF radio signals traversing the ionosphere, J. Geophys. Res., 93, 14,68314,687.

Gurnett, D. A., and S. D. Shawhan (1966), Determination of hydrogen ion concentration electron density and proton gyrofrequency from the dispersion of proton whistlers, J. Geophys. Res., 71, 741-754.

Hamilton, D. C., G. Gloekler, F. M. Ipavich, B. Wilken, and W. Stuedmann (1988), Ring current development during the great geomagnetic storm of February, J. Geophys. Res., 93(A12), 14343.

Hargreaves, J. K. (1992), The solar-terrestrial environment, Cambridge Atmospheric and space science series, Cambridge University Press, Cambridge.

Haselgrove, J. (1955), Ray theory and a new method for ray tracing, paper presented at Conference on the Physics of the Ionosphere, Phys. Soc. of London, London, 355364.

Helliwell, R. A. (1965), Whistlers and Related Ionospheric Phenomena, Stanford University Press, Stanford, California.

Helliwell, R. A. (1988), VLF wave stimulation experiments in the magnetosphere from Siple Station, Antarctica, Reviews of Geophysics, 26, 551.

Horwitz, J. L., R. H. Comfort, and C. R. Chappell (1984), Thermal ion composition measurements of the formation of the new outer plasmasphere and double plasmapause during storm recovery phase, Geophys. Res. Lett., 11(8), 701-704, doi:10.1029/GL011i008p00701.

Horwitz, J. L., R. H. Comfort, P. G. Richards, M. O. Chandler, C. R. Chappell, P. Anderson, W. B. Hanson, and L. H. Brace (1990), Plasmasphere-ionosphere coupling: 2. Ion composition measurements at plasmaspheric and ionospheric altitudes and comparison with modeling results, J. Geophys. Res., 95(A6), 79497959, doi:10.1029/JA095iA06p07949.

Huang, C. Y., W. J. Burke, and C. S. Lin (2009), Two observed consequences of penetration electric fields, J. Atmos. Solar Terr. Phys., 71, 1614-1622.

Huba, J. D., G. Joyce, and J. A. Fedder (2000), Sami2 is Another Model of the Ionosphere (SAMI2): A new low-latitude ionosphere model, J. Geophys. Res., 105, 2303523054.

Hunsucker, R. D, and J. K. Hargreaves (2003), The high-latitude ionosphere and its effects on radio propagation, Cambridge University Press.

Inan, U. S., T. F. Bell, R. A. Helliwell, and J. P. Katsufrakis (1981), A VLF transmitter on the space shuttle, Adv. Space Res., 1, 235.

James, H. (1978), Wave propagation experiments at medium frequencies between two ionospheric satellites: 2. Whistlermode pulses, Radio Sci., 13, 543-558.

Jones, K. L., and H. Rishbeth (1971), The origin of storm increases of mid-latitude F-layer electron concentration, J. Atmos. Terr. Phys., 33, 391401.

Kelley, M. (2009), The Earth's Ionosphere: Plasma Physics and Electrodynamics, Int. Geophys. Ser., 96, 2nd ed., Elsevier, Amsterdam.

Kennel, C. F., and H. E. Petschek (1966), Limit on stably trapped particle fluxes, J. Geophys. Res., 71, 1.

Kimura, I. (1966), Effects of ions on whistler-mode ray tracing, Radio Science 1, 269.

Kintner, P. M., et al., (2008), Midlatitude Ionospheric Dynamics and Disturbances, Geophys. Monogr. Ser., AGU, Washington, D. C., 181, 327.

Kletzing, C. A., F. S. Mozer, and R. B. Torbert (1998), Electron temperature and density at high latitude, J. Geophys. Res., 103, 14837.

Klobuchar, J. A., (1997), Real-time ionospherics science: The new reality, Radio Sc., 32(5), 1943.

Kougblenou, S., G. Lointier, P. M. E. Decreau, J. -G. Trotignon, J. -L. Rauch, X. Valli'eres, P. Canu, A. Masson, and J. Pickett (2011), Lower hybrid resonances stimulated by the four CLUSTER relaxation sounders deep inside the plasmasphere: observations and inferred plasma characteristics, Ann. Geophys., 29, 2003- 2018, doi:10.5194/angeo-29-2003-2011.

Lemaire, J. F. (1975), The mechanisms of formation of the plasmapause, Ann. Geophys., 31, 175-189.

Lemaire, J. F. and K. I. Gringauz (1998), The Earths Plasmasphere, Cambridge University Press, New York.

Li, J. (2004), Measurement of electron density in the Earth's magnetosphere using discrete whistler mode echoes observed on the IMAGE satellite, M.S. thesis, Univ. of Alaska Fairbanks, Fairbanks.

Liemohn, M. W., and A. A. Chan (2007), Unraveling the causes of radiation belt enhancements, Eos Trans. AGU, 88(42), 425426, doi:10.1029/2007EO420001.

Liu, J., B. Zhao, and L. Liu (2010), Time delay and duration of ionospheric total electron content responses to geomagnetic disturbances, Ann. Geophys. 28, 795-805.

Luhr H. and C. Xiong (2010), IRI-2007 model overestimates electron density during the 23/24 solar minimum, Geophys. Res. Lett., 37, L23101, doi:10.1029/2010GL045430.

Lyons, L. R., and D. J. Williams (1984), Quantitative Aspects of Magnetospheric Physics, 231, D. Reidel, Boston.

Mansilla (2007), Ionospheric effects of an intense geomagnetic storm, Stud. Geophys. Geod., 51, 563-574.

Mayaud, P. N. (1980), Derivation, Meaning and Use of Geomagnetic Indices, Am. Geophys. Union, Washington D.C., Geophysical Monograph, 22, doi:10.1029/GM022.

McNamara, L. F., D. L Cooke, C. E. Valladares, and B. W. Reinisch (2007), Comparision of CHAMP and Digisonde plasma frequencies at Jicamarca, Peru, Radio Sci., 42, RS2005, doi:10.1029/2006RS003491.

Mendillo M. (2006), Storms in the ionosphere: Patterns and processes for total electron content, Rev. Geophys., 44, RG4001, doi:10.1029/2005RG000193.

Moldwin M. (2008), An Introduction to Space Weather, Cambridge University Press, New York.

Muldrew, D. G. (1969), Nonvertical propagation and delayedecho generation observed by the topside sounders, Proc. IEEE, 57, 1097-1107.

Nose, M., K. Takahashi, R. R. Anderson, and H. J. Singer (2011), Oxygen torus in the deep inner magnetosphere and its contribution to recurrent process of O^{+}-rich ring current formation, J. Geophys. Res., 116, A10224, doi:10.1029/2011JA016651.

Obana, Y., F. W. Menk, and I. Yoshikawa (2010), Plasma refilling rates for L = 2.3-3.8 flux tubes, J. Geophys. Res., 115, A03204, doi:10.1029/2009JA014191.

Ozhogin, P., J. Tu, P. Song, and B. W. Reinisch (2012), Field-aligned distribution of the plasmaspheric electron density: An empirical model derived from the IMAGE RPI measurements, J. Geophys. Res., 117, A06225, doi:10.1029/2011JA017330.

Ozhogin, P., P. Song, J. Tu, and B. W. Reinisch (2014), Evaluating the diffusive equilibrium models: Comparison with the IMAGE RPI field-aligned electron density measurements, J. Geophys. Res. Space Physics, 119, 4400-4411, doi:10.1002/2014JA019982.

Park, C.G. (1970), Whistler observations of the interchange of ionization between the ionosphere and the protonosphere, J. Geophys. Res., 75, 22.

Park, C. G. (1974), Some features of plasma distribution in plasmasphere deduced from antarctic whistlers, J. Geophys. Res., 79(1), 169-173.

Persoon, A. M., D. A. Gurnett, and S. D. Shawhan (1983), Polar cap electron densities from DE 1 plasma wave observations, J. Geophys. Res., 88, 10123-10136.

Pfaff, R. F, C. Liebrecht, J. -J. Berthelier, M. Malingre, Michel Parrot, and J. -P. Lebreton (2008), DEMETER satellite observations of plasma irregularities in the topside ionosphere at low, middle, and sub-auroral latitudes and their dependence on magnetic storms, Midlatitude Ionospheric Dynamics and Disturbances, Geophys. Monograph Series, 181, 297-310, doi:10.1029/181GM27.

Pierrard, V., and K. Stegen (2008), A three-dimensional dynamic kinetic model of the plasmasphere, J. Geophys. Res., 113, A10209, doi:10.1029/2008JA013060.

Pierrard, V., J. Goldstein, N. Andr, V. K. Jordanova, G. A. Kotova, J. F. Lemaire, M. W. Liemohn, and H. Matsui (2009), Recent progress in physics-based models of the plasmasphere, Space Sci. Rev., 145(1-2), 193-229, doi:10.1007/s11214-008-9480-7.

Pierrard, V., and M. Voiculescu (2011), The 3D model of the plasmasphere coupled to the ionosphere, Geophys. Res. Lett, 38, L12104, doi:10.1029/2011GL047767.

Rastogi, R. G. (1977), Geomagnetic storms and electric fields in the equatorial ionosphere, Nature, 268, 422.

Reddy, A., and V. S. Sonwalkar, Observations and analysis of whistler mode echoes during quiet and disturbed periods: measurement of the electron density and ion effective mass as a function of geomagnetic cctivity, AGU Fall 2011 Meeting, 05-09 December 2011, San Francisco, abstract # SM13D-2117.

Reddy, A., and V. S. Sonwalkar, Electron and ion density variation below 4000 km along the L$\sim$2 flux tube as a function of geomagnetic activity: A study using whistler mode echoes observed by RPI/IMAGE, AGU Fall 2012 Meeting, 03-07 December 2012, San Francisco, abstract # SM41A-2196.

Reinisch, B. W., D. M. Haines, K. Bibl, G. Cheney, I. A. Galkin, X. Huang, S. H. Myers, G. S. Sales, R. F. Benson, S. F. Fung, J. L. Green, W. W. L. Taylor, J. L. Bougeret, R. Manning, N. Meyer-Vernet, M. Moncuquet, D. L. Carpenter, D. L. Gallagher, and P. H. Reiff (2000), The Radio Plasma Imager Investigation on the IMAGE Spacecraft, Space Sci. Rev., 91, 319-359.

Reinisch, B. W., I. A. Galkin, G. Khmyrov, A. Kozlov, and D. F. Kitrosser (2004), Automated collection and dissemination of ionospheric data from the digisonde network, Adv. Radio Sci., 2, 241-247.

Rich, F., and M. Hairston (1994), Largescale convection patterns observed by DMSP, J. Geophys. Res., 99, 3827-3844.

Richmond, A. (1973), Self-induced motions of thermal plasma in the magnetosphere and the stability of the plasmapause, Radio Sci., 8(11), 1019-1027.

Sahai, Y., F. Becker-Guedes, P. R. Fagundes, A. J. de Abreu, R. de Jesus, V. G. Pillat, J. R. Abalde, C. R. Martinis, C. Brunini, M. Gende, C. -S. Huang, X. Pi, W. L. C. Lima, J. A. Bittencourt, and Y. Otsuka (2009), Observations of the F-region ionospheric irregularities in the South American sector during the October 2003 "Halloween Storms, Ann. Geophys., 27, 4463-4477, doi:10.5194/angeo-27-4463-2009.

Sandel, B. R., and M. H. Denton (2007), Global view of refilling of the plasmasphere, Geophys. Res. Lett., 34, L17102, doi:10.1029/2007GL030669.

Saxton, J. M., and A. J. Smith (1989), Quiet time plasmaspheric electric fields and plasmasphere ionosphere coupling fluxes at L = 2.5, Planet. Space Sci., 37(3), 283-293.

Scherliess, L., and B. G. Fejer (1999), Radar and satellite global equatorial F region ver-

tical drift model, J. Geophys. Res., 10, 6829.

Schulz, M. (1996), Eigenfrequencies of geomagnetic field lines and implications for plasma-density modeling, J. Geophys. Res., 101(A8), 17385.

Schunk R. W. and A. F. Nagy (2000), Ionospheres, Cambridge University Press.

Shawhan, S. D., and D. A. Gurnett (1966), Fractional concentration of hydrogen ions in the ionosphere from VLF proton whistler measurement, J. Geophys. Res., 71, 47-59.

Siefring C. L., P. A. Bernhardt, P. A. Roddy, and D. E. Hunton, (2009), Comparisons of equatorial irregularities measurements from C/NOFS: TEC using CERTO and CITRIS with in-situ plasma density, Geophys. Res. Lett., 36, L00C08, doi:10.1029/2009GL038985.

Smith, R. L. (1960), The use of nose whistlers in the study of the outer ionosphere, Stanford Electronics Labs. Tech. Rept. 6, contract AF 18 (603)-126, Stanford University, July.

Smith, R. L., and J. J. Angerami (1968), Magnetospheric properties deduced from the OGO-1 observations of ducted and nonducted whistlers, J. Geophys. Res., 73, 1.

Sonwalkar, V. S., D. L. Carpenter, R. A. Helliwell, M. Walt, U. S. Inan, D. L. Caudle, and M. Ikeda (1997), Properties of the magnetospheric hot plasma distribution deduced from whistler mode wave injection at 2400 Hz: Ground-based detection of azimuthal structure in magnetospheric hot plasmas, J. Geophys. Res., 102(A7), 14363-14380.

Sonwalkar, V. S., and J. Harikumar (2000), An explanation of ground observations of auroral hiss: Role of density depletions and meter-scale irregularities, J. Geophys. Res., 105, 18867.

Sonwalkar, V. S., X. Chen, J. Harikumar, D. L. Carpenter, and T. F. Bell (2001), Whistlermode wave injection experiments in the plasmasphere with a radio sounder, J. Atmos. Sol. Terr. Phys., 63, 1199-1216.

Sonwalkar, V. S., D.L. Carpenter, T. F. Bell, M.A. Spasojevic, U. S. Inan, J. Li, X. Chen, A. Venkatasubramanian, J. Harikumar, R. F. Benson, W. W. L. Taylor, and B. W. Reinisch (2004), Diagnostics of magnetospheric electron density and irregularities at altitudes <5000km using whistler and Z mode echoes from radio sounding on the IMAGE satellite, J. Geophys. Res., 109, A11212.

Sonwalkar, V. S. (2006), The influence of plasma density irregularities on whistler-mode wave propagation, Lect. Notes Phys., Springer-Verlag, Berlin Heidelberg, 687, 141-191.

Sonwalkar, V. S., D. L. Carpenter, A. Reddy, R. Proddaturi, S. Hazra, K. Mayank, and B. W. Reinisch (2011a), Magnetospherically reflected, specularly reflected, and backscattered whistler mode radiosounder echoes observed on the IMAGE satellite: 1. Observations and interpretation, J. Geophys. Res., 116, A11210, doi:10.1029/2011JA016759.

Sonwalkar, V. S., A. Reddy, and D. L. Carpenter (2011b), Magnetospherically reflected, specularly reflected, and backscattered whistler mode radio sounder echoes observed on the IMAGE satellite: 2. Sounding of electron density, ion effective mass (m_{eff}), ion composition (H^+, He^+, O^+), and density irregularities along the geomagnetic field line, J. Geophys. Res., 116, A11211, doi:10.1029/2011JA016760.

Sonwalkar, V. S., A. Reddy, S. Hazra, K. Mayank, and D. L. Carpenter (2012), Whistler- and Z-mode radio sounding of electrons, ions, irregularities, ducts and cavities in the magnetosphere, 39th COSPAR Scientific Assembly, July 14-22, Mysore, India.

Sonwalkar, V. S., S. Hazra, K. Mayank, A. Reddy, Y. Liu, and D. L. Carpenter (2013),

Measurement of field aligned electron and ion densities and ducts from the whistler and Z mode radio sounding from IMAGE, AGU Fall 2013 Meeting, abstract # SM53A-2210, 9-13 December 2013, San Francisco.

Sonwalkar, V. S., A. Reddy, and S. Hazra (2014a), Whistler mode radio sounding from IMAGE of field aligned electron and ion densities in the plasmasphere below 4000 km, URSI GASS, Paper # 1812, August 16-23, 2014, Beijing, China.

Sonwalkar, V. S., K. Mayank, and A. Reddy (2014b), Z Mode Radio Sounding from IMAGE of Field Aligned Electron Density and Ducts, URSI GASS, Paper # 1907, August 16-23, 2014, Beijing, China.

Sonwalkar, V. S., A. Reddy, K. Mayank, S. Hazra and D. L. Carpenter (2014c), Recent results from the whistler- and Z-mode radio sounding from the IMAGE satellite, AGU 2014 Fall Meeting, abstract # SM31C-4211, 15-19 December 2014, San Francisco, California, USA.

Storey, L. R. O. (1953), An investigation of whistling atmospherics, Phil. Trans. Roy. Soc. Lond., 246, 113-141.

Su, S. -Y., C. H. Liu, H. H. Ho, and C. K. Chao (2006), Distribution characteristics of topside ionospheric density irregularities: Equatorial versus midlatitude regions, J. Geophys. Res., 111, A06305, doi:10.1029/2005JA011330.

Sutton, E. K., J. M. Forbes, and R. S. Nerem (2005), Global thermospheric neutral density and wind response to the severe 2003 geomagnetic storms from CHAMP accelerometer data, J. Geophys. Res., 110, A09S40, doi:10.1029/2004JA010985.

Takahashi, K., R. E. Denton, R. R. Anderson, and W. J. Hughes (2006), Mass density inferred from toroidal wave frequencies and its comparison to electron density, J. Geophys. Res., 111, A01201, doi:10.1029/2005JA011286.

Takahashi, K., S. Ohtani, R. E. Denton, W. J. Hughes, and R. R. Anderson (2008), Ion composition in the plasma trough and plasma plume derived from a Combined Release and Radiation Effects satellite magnetoseismic study, J. Geophys. Res., 113, A12203, doi:10.1029/2008JA013248.

Tarcsai, G. (1985), Ionosphereplasmasphere electron fluxes at middle latitudes obtained from whistlers, Adv. Space Res., 5(4), 155-158.

Taylor Jr., H. A., H. C. Brinton, and C. R. Smith (1965), Positive ion composition in the magnetoionosphere obtained from the Ogo-A satellite, J. Geophys. Res., 70(23), 57695781, doi:10.1029/JZ070i023p05769.

Titova, E. E., V. I. Di, V. E. Yurov, O. M. Raspopov, V. Y. Trakhtengertz, F. Jiricek, and P. Triska (1984), Interaction between VLF waves and the turbulent ionosphere, Geophys. Res. Lett., 11(4), 323326.

Tsurutani, B. T., W. D. Gonzalez, F. Tang, and Y. T. Lee (1992), Great magnetic storms, Geophys. Res. Lett., 19, 73.

Tsurutani, B. T., et al. (2008), Prompt penetration electric fields (PPEFs) and their ionospheric effects during the great magnetic storm of 3031 October 2003, J. Geophys. Res., 113, A05311, doi:10.1029/2007JA012879.

Webb, P. A., R. F. Benson, and J. M. Grebowsky (2006), Technique for determining midlatitude O+/H+ transition heights from topside ionograms, Radio Sci., 41, RS6S34, doi:10.1029/2005RS003391.

Yeh, H. -C., and J. C. Foster (1990), Storm time heavy ion outflow at midlatitude, J. Geophys. Res., 95(A6), 7881.

Young, D. T., H. Balsiger, and J. Geiss (1982), Correlations of magnetospheric ion composition with geomagnetic and solar activity, J. Geophys. Res., 87, 9077-9096.

Appendix A

In addition to time delays, the ray-tracing simulations provide quantitative information on wave characteristics along the echo ray path including wave-normal angle, refractive index, wavelength, group velocity, amount of group delay accrued as a function of distance along the ray path, MR echo reflection altitude, f_{lh} at this altitude, and details of the magnetospheric and specular reflections. This information, coupled with the satellite motion and the transmission format, explains many features of the observed echoes.

This appendix discusses the initial, reflection, and arrival parameters for MR and SR whistler mode echoes obtained from ray tracing calculations for the 22 October 2005 case assuming three ion model (Model 3).

Tables A.1 to A.3 respectively give ray parameters, at initial, reflection and arrival points for MR echoes. Tables A.4-A.7 give ray parameters, at initial, reflection and arrival points for OI-SR echoes. And Tables A.8-A.11 give ray parameters, at initial, reflection and arrival points for NI-SR echoes.

Table A.1. Initial ray parameters of 22 Oct 2005 MR echo ray tracing. Table includes the frequency (f), altitude(Alt), geomagnetic latitude (Mlat), L shell value (L), wave normal angle (θ), resonance cone angle (θ_{res}), Gendrin angle (θ_{gen}), local f_{lh} ($f_{lh,local}$), ray direction(θ_{ray}),refractive index (μ)and effective ion mass at the location of satellite

f (kHz)	Alt (km)	Mlat (°)	L	θ (°)	θ_{res} (°)	θ_{gen} (°)	$f_{lh,local}$ (kHz)	θ_{ray} (°)	μ
6.6	3410	31.92	2.1309	90.57	90.44	90.99	6.25	-179.67	294
7.2	3408	31.94	2.13168	91.03	90.75	91.55	6.26	-179.52	166
7.8	3406	31.96	2.13246	91.41	90.98	91.99	6.26	-179.45	123
8.4	3404	31.99	2.13324	91.77	91.17	92.37	6.27	-179.42	100
9	3402	32.01	2.13403	92.07	91.35	92.72	6.27	-179.36	88
9.15	3402	32.01	2.13403	92.09	91.4	92.81	6.27	-179.3	88
9.3	3401	32.03	2.13442	92.03	91.44	92.89	6.27	-179.15	95

Table A.2. Ray parameters at reflection point; 22 Oct 2005 MR echo ray tracing. Table includes the frequency (f), reflection altitude (RefAlt), geomagnetic latitude (Mlat),L shell value(L), time delay (t_g), f_{lh} ($f_{lh,ref}$), ray direction(θ_{ray}),refractive index (μ)and effective ion mass at the reflection point of the ray

f (kHz)	RefAlt (km)	Mlat (°)	L	t_g (ms)	$f_{lh,ref}$ (kHz)	μ	m_eff
6.6	3129	33.22	2.1309	45.8	6.75	310	1.04
7.2	2697	35.20	2.13168	47.1	7.57	192	1.06
7.8	2311	36.92	2.13246	49.1	8.34	155	1.1
8.4	1949	38.52	2.13324	52.4	9.06	136	1.16
9.0	1574	40.14	2.13403	60.4	9.73	130	1.26
9.15	1471	40.59	2.13403	68.3	9.85	135	1.32
9.3	1396	40.91	2.13442	93.1	9.99	148	1.4

Table A.3. Ray parameters at arriving point for 22 Oct 2005 MR echo ray tracing. Table includes the frequency (f), L shell value(L), time delay (t_g), wave normal angle (θ), resonance cone angle (θ_{res}), ray direction(θ_{ray}), and refractive index (μ) at the location of satellite

f (kHz)	L	t_g (ms)	θ(°)	θ_{res}(°)	θ_{ray}(°)	μ
6.6	2.13089	89	89.42	89.54	-0.354	290
7.2	2.13169	93	88.95	89.24	-0.49	162
7.8	2.13248	98	88.55	89.01	-0.55	120
8.4	2.13324	104	88.18	88.82	-0.56	98
9.0	2.13403	120	87.88	88.64	-0.61	85
9.15	2.13415	136	87.86	88.6	-0.68	86
9.3	2.13446	185	87.94	88.56	-0.84	93

Table A.4. Initial ray parameters of 22 Oct 2005 OI-SR echo ray tracing. Table includes the frequency (f), altitude(Alt), geomagnetic latitude (Mlat), L shell value (L), wave normal angle (θ), resonance cone angle (θ_{res}), ray direction(θ_{ray}), and refractive index (μ) at the location of satellite

f (kHz)	Alt (km)	Mlat (°)	L	θ(°)	θ_{res}(°)	θ_{ray} (°)	μ
9.6	3400	32.05	2.13495	-88.04	-88.48	1.09	109
9.9	3399	32.07	2.13548	-87.86	-88.4	-1.07	97
10.2	3398	32.08	2.13601	-87.72	-88.32	1.09	90
11.4	3393	32.15	2.13813	-87.21	-88.01	1.19	74
14.4	3379	32.33	2.14377	-86.11	-87.31	1.49	53
16.2	3371	32.43	2.14703	-85.49	-86.91	1.68	46
17.7	3366	32.51	2.14937	-84.99	-86.58	1.83	42
18.9	3361	32.58	2.15144	-84.58	-86.32	1.94	39
22.2	3348	32.76	2.15718	-83.53	-85.63	2.28	32
33.3	3310	33.28	2.17442	-80.01	-83.37	3.27	21

Table A.5. Ray parameters at the point of incidence at the earth ionosphere boundary for 22 Oct 2005 OI-SR echoes. Table includes the frequency (f), reflection altitude(RefAlt), geomagnetic latitude (Mlat), L shell value (L), time delay (t_g), incidence wave normal angle (θ_1), refractive index at the point of incidence(n_1), angle w.r.to vertical (δ_1), $n_1 sin(\delta_1)$, Angle between B and vertical ($AngB_0$) and resonance cone angle (θ_{res})

f (kHz)	RefAlt (km)	Mlat (°)	L	t_g ms	θ_1 (°)	n_1	δ_1 (°)	$n_1 sin(\delta_1)$	$AngB_0$ (°)
9.6	90	46.43	2.1354	114	-89.06	213.4	65.5	194.3	25.42
9.9	90	46.45	2.13630	92	-88.97	198.57	65.6	180.9	25.42
10.2	90	46.46	2.13702	83.9	-88.7	162.02	65.9	147.9	25.39
11.4	90	46.5	2.13998	71.2	-88.11	117.2	66.6	107.5	25.31
14.4	90	46.6	2.14789	62.6	-87.78	101.5	66.9	93.4	25.26
16.2	90	46.66	2.1527	60.72	-87.46	91.36	67.3	84.3	25.23
17.7	90	46.7	2.15644	59.7	-87.25	84.43	67.6	78.0	25.19
18.9	90	46.75	2.16019	59	-86.67	70.6	68.2	65.6	25.11
22.2	90	46.86	2.16888	57.9	-84.61	44.72	70.6	42.2	25.82
33.3	90	47.23	2.19904	55.7	-89.06	213	65.5	194.3	25.42

Table A.6. Ray parameters at the point of reflection at the earth ionosphere boundary for 22 Oct 2005 OI-SR echoes. Table includes the frequency (f), resonance cone angle (θ_{res}), reflection wave normal angle(θ_2), refractive index at the point of reflection(n_2), angle of incidence w.r.to vertical (δ_2), $n_2 sin(\delta_2)$

f (kHz)	θ_{res} (°)	θ_2 (°)	n_2	δ_2 (°)	$n_2 sin(\delta_2)$
9.6	89.66	89.07	216.8	63.66	194.3
9.9	89.64	88.99	202	63.57	180.9
10.2	89.62	88.71	165.5	63.32	147.9
11.4	89.54	88.05	121	62.74	107.5
14.4	89.36	87.81	105.2	62.55	93.4
16.2	89.27	87.53	95.2	62.30	84.3
17.7	89.19	87.35	88.3	62.16	78.0
18.9	89.12	86.72	74.5	61.62	65.6
22.2	89.95	84.24	48.99	59.41	42.2
33.3	89.66	89.07	216.8	63.66	194.3

Table A.7. Ray parameters at arriving point for 22 Oct 2005 OI-SR echoes. The table includes frequency (f), L shell value(L), time delay (t_g), wave normal angle (θ), resonance cone angle (θ_{res}), ray direction(θ_{ray}), and refractive index (μ) at the location of satellite

f (kHz)	L	t_g (ms)	θ(°)	θ_{res}(°)	θ_{ray}(°)	μ
9.6	2.13487	228.5	-91.95	-91.52	178.92	110.3
9.9	2.13551	184.1	-92.12	-91.61	178.9	99
10.2	2.13598	167.8	-92.25	-91.69	178.88	92.32
11.4	2.13814	141.9	-92.73	-91.99	178.76	75.95
14.4	2.14376	124.1	-93.79	-92.7	178.4	55.83
16.2	2.14707	119.9	-94.37	-93.1	178.19	48.8
17.7	2.14943	117.6	-94.84	-93.42	178	44.32
18.9	2.15237	116.2	-95.21	-93.68	177.86	41.19
22.2	2.1573	113.4	-96.18	-94.38	177.43	35.01
33.3	2.1747	108.4	-99.31	-96.63	176.04	23.39

Table A.8. Initial ray parameters of 22 Oct 2005 NI-SR echo ray tracing. Table includes the frequency (f), altitude(Alt), geomagnetic latitude (Mlat), L shell value (L), wave normal angle (θ), resonance cone angle (θ_{res}), ray direction(θ_{ray}), and refractive index (μ) at the location of satellite.

f (kHz)	Alt (km)	Mlat (°)	L	θ(°)	θ_{res}(°)	θ_{ray} (°)	μ
6	3411.74	-31.89	2.13	21.94	-	10.35	12.47
6.6	3410.13	-31.92	2.13	21.92	89.56	10.31	11.91
7.5	3407.23	-31.95	2.13	21.93	89.13	10.28	11.21
8.7	3403.37	-32.01	2.13	21.94	88.73	10.23	10.45
9.6	3400.16	-32.05	2.13	21.88	88.48	10.17	9.97
9.9	3398.87	-32.07	2.14	21.88	88.40	10.15	9.82
10.2	3397.59	-32.08	2.14	21.87	88.32	10.14	9.68
11.4	3392.45	-32.15	2.14	21.85	88.01	10.07	9.18
14.4	3378.99	-32.34	2.14	21.76	87.31	9.91	8.22
16.2	3371.31	-32.44	2.15	21.70	86.91	9.81	7.78
17.7	3365.88	-32.51	2.15	21.66	86.58	9.73	7.46
18.9	3361.09	-32.58	2.15	21.62	86.32	9.67	7.23
22.2	3348.02	-32.76	2.16	21.51	85.63	9.48	6.71
33.3	3310.25	-33.28	2.17	21.20	83.37	8.88	5.59

Table A.9. Ray parameters at the point of incidence at the earth ionosphere boundary for 22 Oct 2005 NI-SR echoes. Table includes the frequency (f), reflection altitude(RefAlt), geomagnetic latitude (Mlat), L shell value (L), time delay (t_g), incidence wave normal angle (θ_1), refractive index at the point of incidence(n_1), angle w.r.to vertical (δ_1), $n_1 sin(\delta_1)$, and Angle between B and vertical ($AngB_0$)

f (kHz)	RefAlt (km)	Mlat (°)	L	t_g	θ_1 (°)	n_1	δ_1 (°)	$n_1 sin(\delta_1)$	$AngB_0$ (°)
6	90	-42.01	1.84	111.41	29.05	29.20	0	0	29.03
6.6	90	-42.04	1.84	106.34	29.01	28.11	0	0	29.01
7.5	90	-42.06	1.84	99.87	29.00	26.61	0	0	29.00
8.7	90	-42.09	1.84	92.88	28.99	24.47	0	0	28.97
9.6	90	-42.13	1.84	88.58	28.92	23.22	0	0	28.94
9.9	90	-42.14	1.84	87.24	28.91	23.20	0	0	28.93
10.2	90	-42.15	1.84	85.97	28.91	22.67	0	0	28.92
11.4	90	-42.19	1.85	81.47	28.87	21.41	0	0	28.88
14.4	90	-42.32	1.85	72.86	28.78	19.14	0	0	28.78
16.2	90	-42.39	1.86	68.92	28.72	18.03	0	0	28.72
17.7	90	-42.44	1.86	66.10	28.68	17.15	0	0	28.67
18.9	90	-42.48	1.86	64.13	28.64	16.67	0	0	28.63
22.2	90	-42.61	1.87	59.53	28.53	15.48	0	0	28.53
33.3	90	-42.99	1.90	49.73	28.22	12.70	0	0	28.20

Table A.10. Ray parameters at the point of reflection at the earth ionosphere boundary for 22 Oct 2005 NI-SR echoes. Table includes the frequency (f), resonance cone angle (θ_{res}), reflection wave normal angle(θ_2), refractive index at the point of reflection(n_2), angle of incidence w.r.to vertical (δ_2), $n_2 sin(\delta_2)$

f (kHz)	θ_{res} (°)	θ_2 (°)	n_2	δ_2 (°)	$n_2 sin(\delta_2)$
6		29.01	29.20	0	0
6.6	89.93	29.01	28.11	0	0
7.5	89.80	29.00	26.61	0	0
8.7	89.70	28.95	24.46	0	0
9.6	89.63	28.95	23.23	0	0
9.9	89.61	28.94	23.20	0	0
10.2	89.59	28.93	22.67	0	0
11.4	89.51	28.88	21.41	0	0
14.4	89.34	28.78	19.14	0	0
16.2	89.23	28.72	18.03	0	0
17.7	89.15	28.67	17.15	0	0
18.9	89.08	28.63	16.67	0	0
22.2	88.91	28.53	15.48	0	0
33.3	88.32	28.19	12.69	0	0

Table A.11. Ray parameters at arriving point for 22 Oct 2005 NI-SR echoes. The table includes frequency (f), L shell value(L), time delay (t_g), wave normal angle (θ), resonance cone angle (θ_{res}), ray direction(θ_{ray}), and refractive index (μ) at the location of satellite

f (kHz)	L	t_g (ms)	θ(°)	θ_{res}(°)	θ_{ray}(°)	μ
6	2.13	222.79	21.90	90.00	10.33	12.47
6.6	2.13	212.64	21.93	89.56	10.31	11.91
7.5	2.13	199.70	21.93	89.13	10.27	11.21
8.7	2.13	185.76	21.90	88.73	10.21	10.45
9.6	2.14	177.12	21.92	88.48	10.18	9.97
9.9	2.14	174.46	21.91	88.40	10.16	9.82
10.2	2.14	171.94	21.90	88.32	10.15	9.69
11.4	2.14	162.95	21.86	88.01	10.08	9.19
14.4	2.14	145.68	21.76	87.31	9.91	8.22
16.2	2.15	137.81	21.71	86.91	9.81	7.78
17.7	2.15	132.20	21.67	86.58	9.74	7.46
18.9	2.15	128.23	21.63	86.32	9.67	7.24
22.2	2.16	119.03	21.53	85.62	9.49	6.71
33.3	2.17	99.46	21.17	83.37	8.86	5.58